comp.
[illegible]

DOE/ET/21017-T1

SOLAR HEATED-AIR CAVITY RECEIVER DEVELOPMENT (SHARE)

Final Report

1 December 1981

Philip O. Jarvinen

Massachusetts Institute of Technology
Lincoln Laboratory
Lexington, Massachusetts 02173

Prepared for
THE U.S. DEPARTMENT OF ENERGY
UNDER CONTRACT NO. ET-78-S-02-4878

Additional copies available from the National Technical Information Service, U.S. Department of Commerce, Springfield, Virginia 22161.

Price: Paper Copy $14.00
Microfiche $ 3.00

COO-4878-15

Distribution Category UC 62

SOLAR HEATED-AIR CAVITY RECEIVER DEVELOPMENT (SHARE)

Final Report

1 December 1981

Philip O. Jarvinen

Massachusetts Institute of Technology
Lincoln Laboratory
Lexington, Massachusetts 02173

Prepared for
THE U.S. DEPARTMENT OF ENERGY
UNDER CONTRACT NO. ET-78-S-02-4878

ABSTRACT

An advanced ceramic dome cavity receiver is discussed which heats pressurized gas to temperatures in the range from 1800°F (1000°C) to 2400°F (1300°C) for use in solar Brayton power systems of the dispersed receiver/dish or central receiver type. Optical, heat transfer, structural, and ceramic material design aspects of the unique receiver are reported and the development and experimental demonstration of a high-temperature seal between the pressurized gas and the high-temperature silicon carbide dome material is described.

TABLE OF CONTENTS

LIST OF FIGURES

List of Figures (con'd)

List of Figures (con'd)

LIST OF TABLES

1.0 INTRODUCTION

Studies of advanced receivers for solar thermal heated-air Brayton power systems have been under way at MIT Lincoln Laboratory since 1975. Results of these studies published in References 1 and 2 show that the ceramic-domed cavity receiver concept is a promising approach for central receiver and dispersed-dish solar thermal electric systems. The receiver concept that is presented utilizes ceramic dome elements to form the interior walls of cavity-type receivers. The ceramic domes are individually cooled by impingement-jet heat-transfer techniques. The impinging air is heated to temperatures in the range from 1800°F (1000°C) to 2400°F (1300°C) when it comes in contact with the hot ceramic dome. A regenerative open-cycle/solar gas turbine approach is chosen since it offers higher overall thermal efficiency than a simple cycle and because peak efficiency is achieved at a pressure ratio of only 4 to 1, which minimizes design considerations of the pressurized receiver.

In May 1978, MIT Lincoln Laboratory was funded to develop this novel concept for solar heated-air receivers by the U.S. Department of Energy (DOE). Funding of $249,680 was provided for the year ending 1 May 1979. At the request of DOE, the program was focused on the development of a high-temperature seal between the pressurized air and the high-temperature, ceramic-dome material. The program also included a number of other tasks as shown in Table I. The overall program included the development and analysis of conceptual designs for ceramic-dome receivers, the selection of dome/seal materials, dome structural analysis, studies of existing mechanical sealing methods, the selection and implementation of a preferred sealing approach and, finally, the experimental demonstration of that sealing approach in ceramic hardware of a physically significant size (judged at this time to be one-foot-diameter seals).

The report which follows describes progress made on a number of elements in the developmental program, including ceramic-dome stress calculations, metalization of ceramics, selection of a preferred receiver/dome sealing approach, mechanical seal leak measurements, and the experimental demonstration of seals on ceramic domes to one-foot diameters.

TABLE I

SCHEDULE AND MAJOR TASKS FOR SOLAR HEATED-AIR CAVITY RECEIVER DEVELOPMENT (SHARE)

	Major Tasks	M	J	J	A	S	O	N	D	J	F	M	A
1	Conceptual Design Studies and Scaling Laws	▭△											
2	Analysis of Conceptual Designs		▭	▭	▭	▭	▭	▭	▭	▭	▭	▭	▭△
3	Dome/Sealing Materials	▭	▭	▭△									
4	Dome Structural Analysis	▭	▭	▭△									
5	Studies of Existing Mechanical Seal Methods	▭	▭	▭△									
6	Analysis, Design, and Fabrication of Preferred Mechanical Seal				▭	▭	▭	▭	▭	▭△			
7	Alternative Seal Studies	▭	▭	▭	▭	▭	▭	▭	▭	▭	▭	▭	▭△
8	Design, Fabricate, and Build Ceramic Dome/Seal Test Fixture				▭	▭	▭	▭	▭	▭△			
9	Test Ceramic Domes under Pressure/ Temperature Loading										▭	▭	▭△

1.1 Solar Heated-Air Cavity Receiver Concept

The essence of the heated-air ceramic—domed receiver is shown in Fig. 1, which illustrates the application of domed ceramic elements to form the walls of a 1-MW bench model-size receiver. In this approach, the ceramic domes face convex side outward from the cavity toward the pressure forces created by the airflow which is to be heated (insert, Fig. 1). The domes carry the pressure loads by going into overall compression; a preferred condition for ceramic materials which are six to eight times stronger in compression than in tension. The concave sides of the domes face toward the interior of the cavity and are heated by concentrated sunlight entering through the cavity aperture. Heat is conducted through the dome walls and is absorbed into the airflow on the convex side of the dome through an impingement heat-transfer scheme which utilizes numerous impinging air jets directed inward against the back sides of the domes (Fig. 1). The heated air is then collected in a manifold and piped to the turbine where mechanical work is generated and electrical energy is produced.

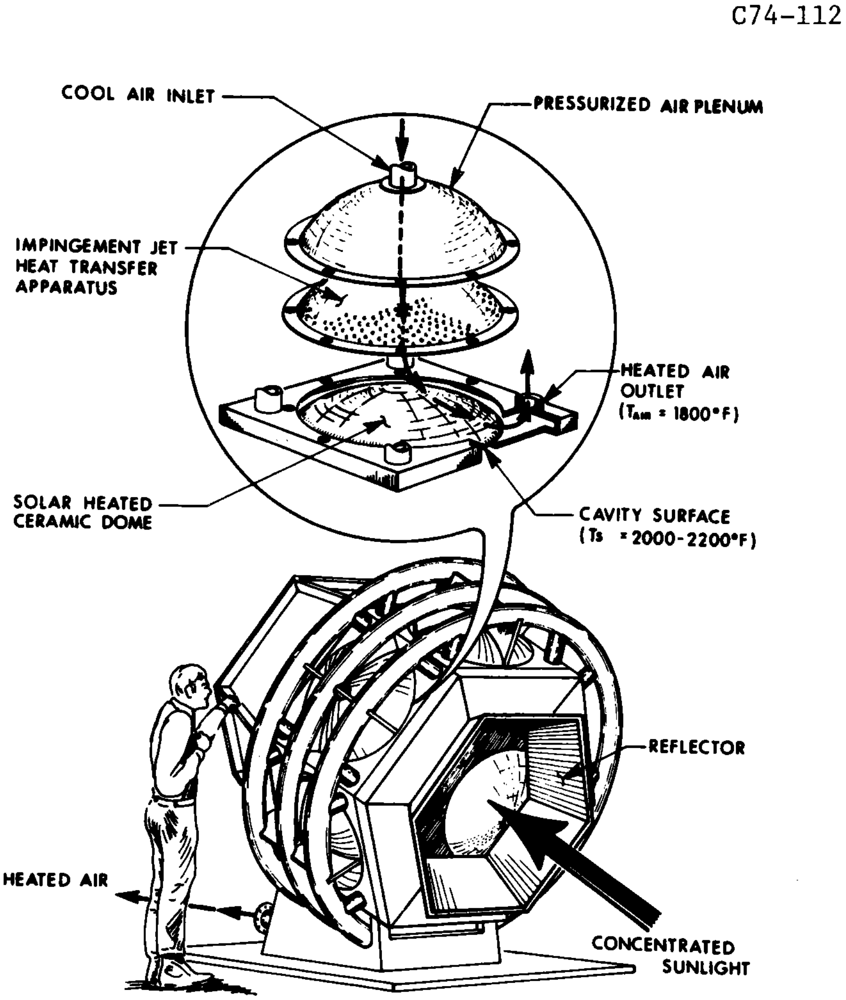

Figure 1. A concept for a 1-MW_t, solar heated-air, ceramic-domed, cavity receiver test unit.

The ceramic dome receiver approach offers a number of engineering advantages, including a non-windowed cavity design, the use of impingement-jet heat-transfer methods which are three to six times more effective for the same pressure drop than alternative heat-transfer methods, the utilization of ceramic dome materials in compression (rather than tension) to support the pressure forces, a maximum material operating temperature limit as high as 3000°F (1650°C), and a mechanical configuration in which stresses due to differential thermal expansion between metal and ceramic components are eliminated.

1.2 Ceramic Dome Receiver Applications

Ceramic dome cavity receivers are applicable to large central tower systems, dispersed-dish systems, or fuel/chemical systems that require a pressurized working fluid, typically a gas, to be heated to temperatures above those attainable with metal receivers.

An example of ceramic domes applied to a combined-cycle solar central receiver hybrid power system of the type considered in Reference 3 is offered in Figs. 2 through 4. In Fig. 2, the tower configuration, the heliostat field layout and the number of cavity receivers on the tower of Reference 3 have been preserved but an alternative ceramic receiver design using ceramic domes in the receiver substation is shown, Fig. 3. In this new approach, ceramic impingement-cooled dome heat exchangers are assembled together to form the rear wall of the receiver. The face of the wall is formed by vertical columns of domes, with individual domes cantilevered from vertical support pipes through which the incoming cool-air supply and outgoing heated-air streams flow, Fig. 4. An example of the piping layout used to couple multiple-ceramic-dome-cavity receivers together is also offered in Fig. 4. In the example receiver shown, the solar flux from the heliostats impinges directly on the face of the ceramic dome modules. A near uniform solar flux distribution is produced across the face of individual dome elements, thus minimizing thermal stress loadings in the ceramic domes.

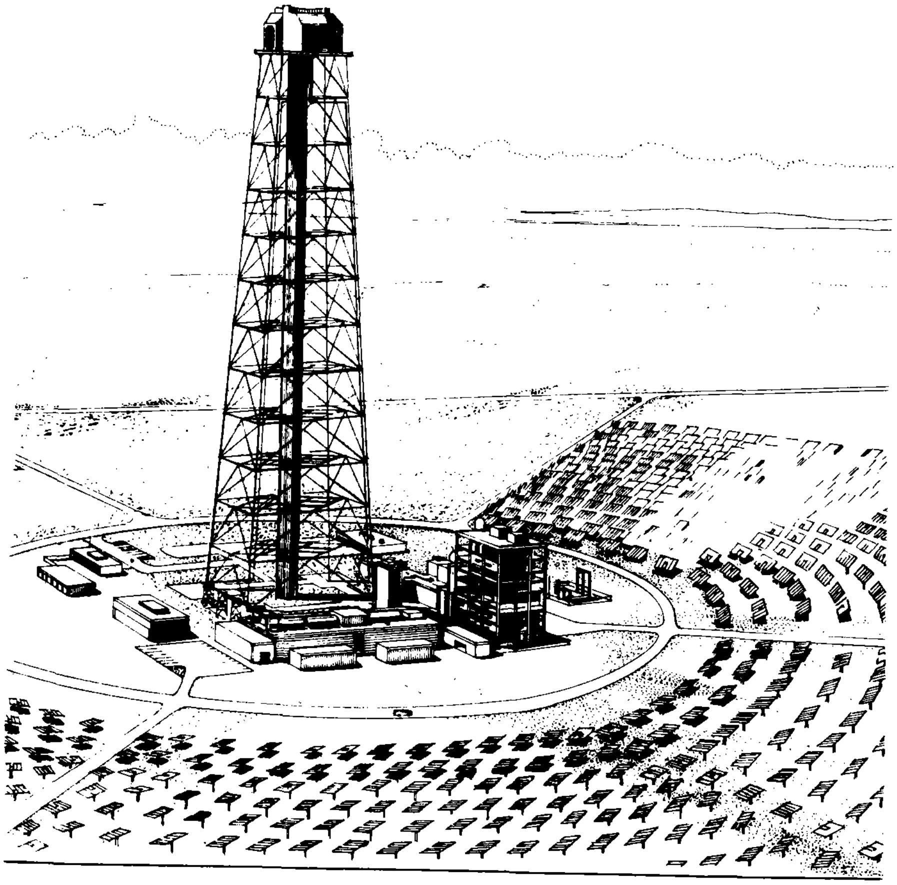

Figure 2. Combined-cycle solar central receiver hybrid power system.[3]

C74-1028

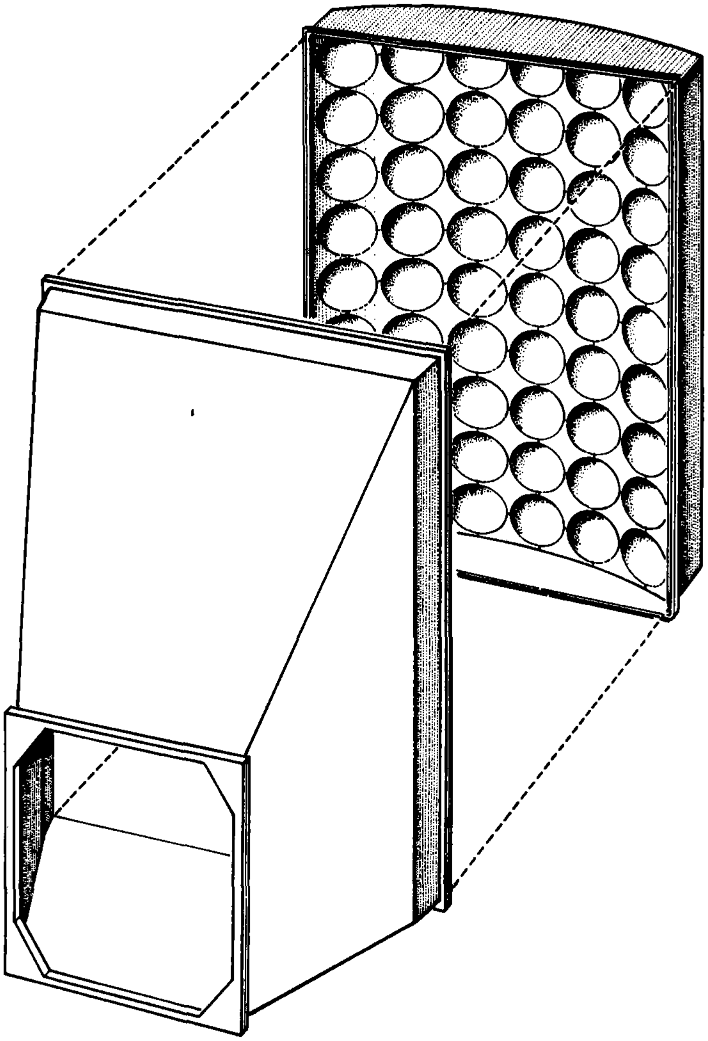

Figure 3. New ceramic dome receiver concept for combined-cycle solar central receiver.

C74-1071

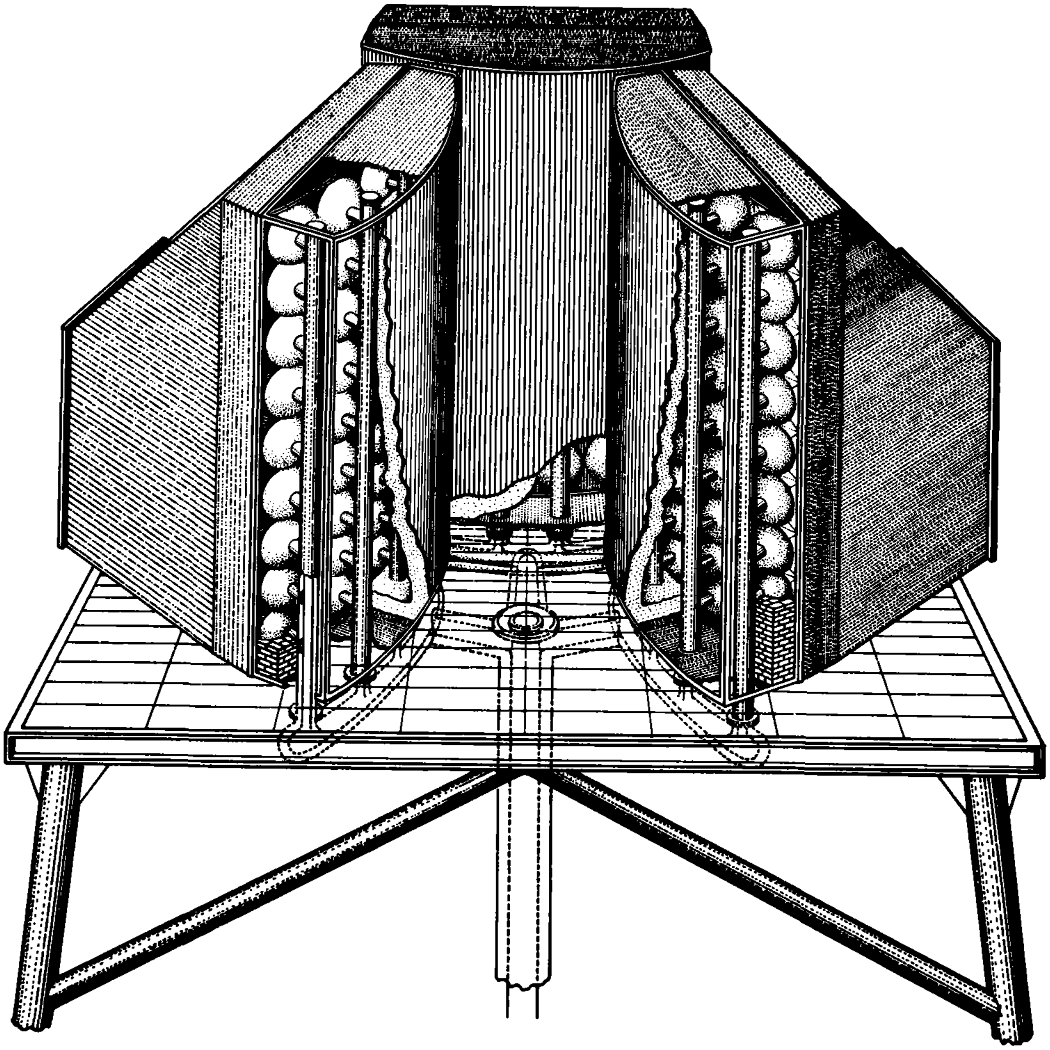

Figure 4. New ceramic dome, combined-cycle cavity receiver design features.

The ceramic dome concept is also applicable to dispersed-dish-type solar systems where the receiver is placed at the focal point of the concentrator. The ceramic dome receiver may be coupled directly to a Stirling engine, as shown in Fig. 5, or may take the form shown in Fig. 6 for solar Brayton applications. The ceramic dome element may be of hemispherical shape, Fig. 5, or shallow dome form, Fig. 6, depending upon the application. In point-focus dish applications, Brayton receivers with up to 75-kW_t capacity may be constructed from single domes at the present time. A single dome of 24-inch span is required and may be fabricated by available techniques. Domes with spans greater than 24 inches cannot be fabricated now due to limitations in the size of existing sintering furnaces. This restraint may be easily removed through the construction of larger sintering furnaces but the ceramic manufacturers have not to date perceived sufficient financial reward to undertake this. Thus, receivers of higher thermal capacity require multiple-dome configurations. Examples of point-focus ceramic receivers of multiple-dome types are shown in Figs. 7 and 8. In Fig. 7, the solar flux impinges directly on the multiple ceramic dome modules and has been designated a direct-type receiver. Figure 8 is an example of a design which depends on a process of absorption on the back wall of the receiver followed by reradiation of the heat to the ceramic heat-transfer modules. This receiver approach has been designated as an indirect-type receiver. As shown in Fig. 9, direct receiver types typically have operating efficiencies a few points higher than indirect receivers. A more detailed explanation of the results shown in Fig. 9 is presented in Appendix A of this report.

C71-958

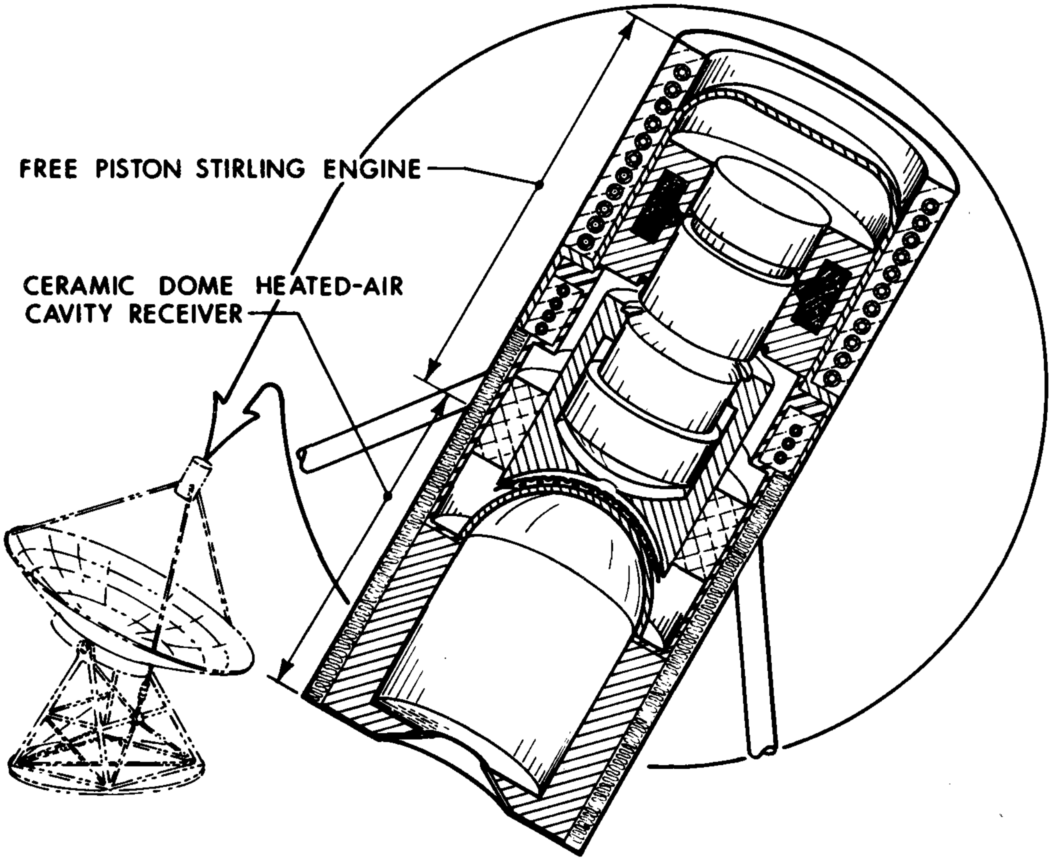

Figure 5. Ceramic dome receiver coupled to a Stirling engine in a dispersed-dish application.

C74-371

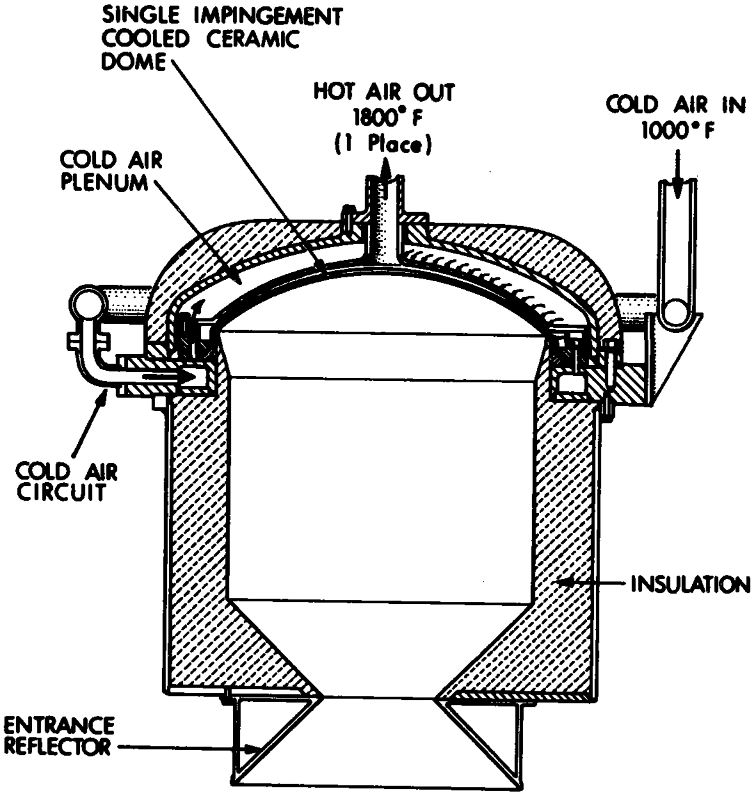

Figure 6. Point-focus ceramic cavity receiver for Brayton systems.

C74-307 (detail)

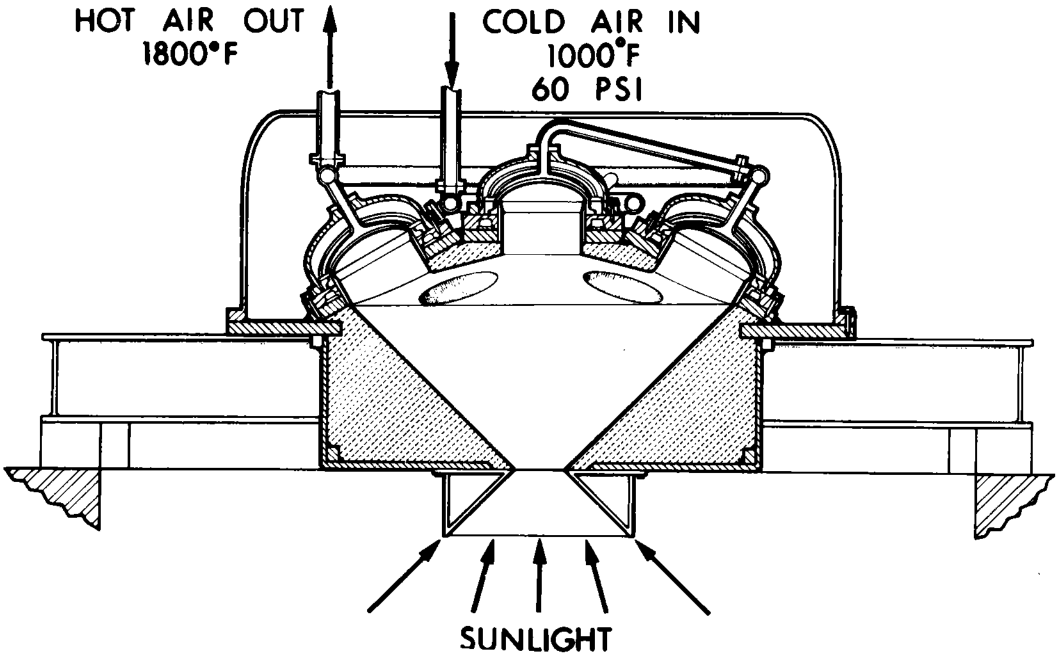

Figure 7. Direct multidome receiver concept.

C74-307 (detail)

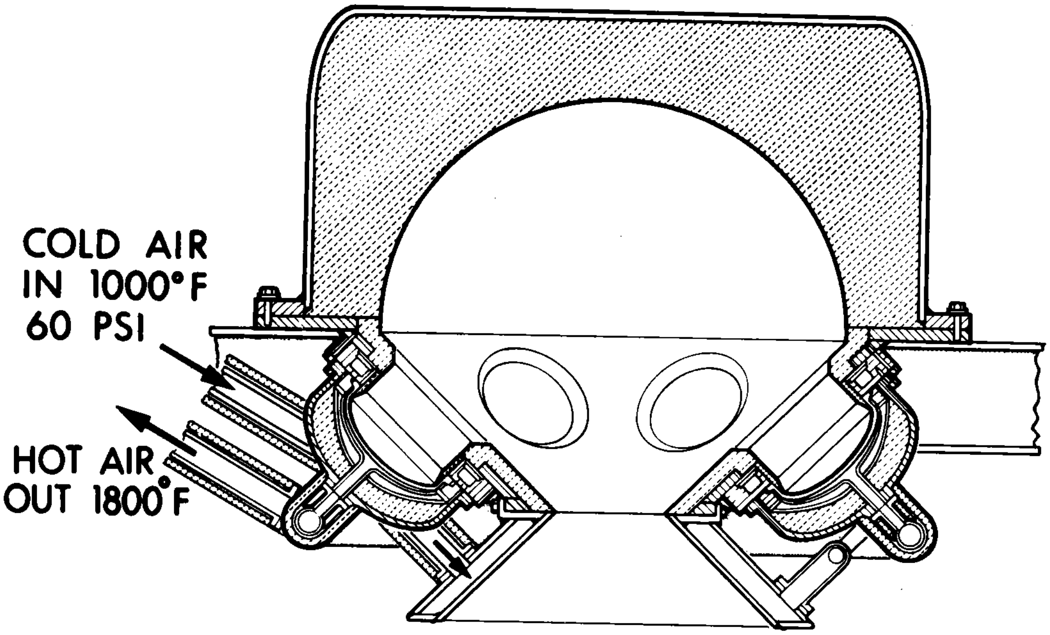

Figure 8. Indirect multidome receiver concept.

C74-459

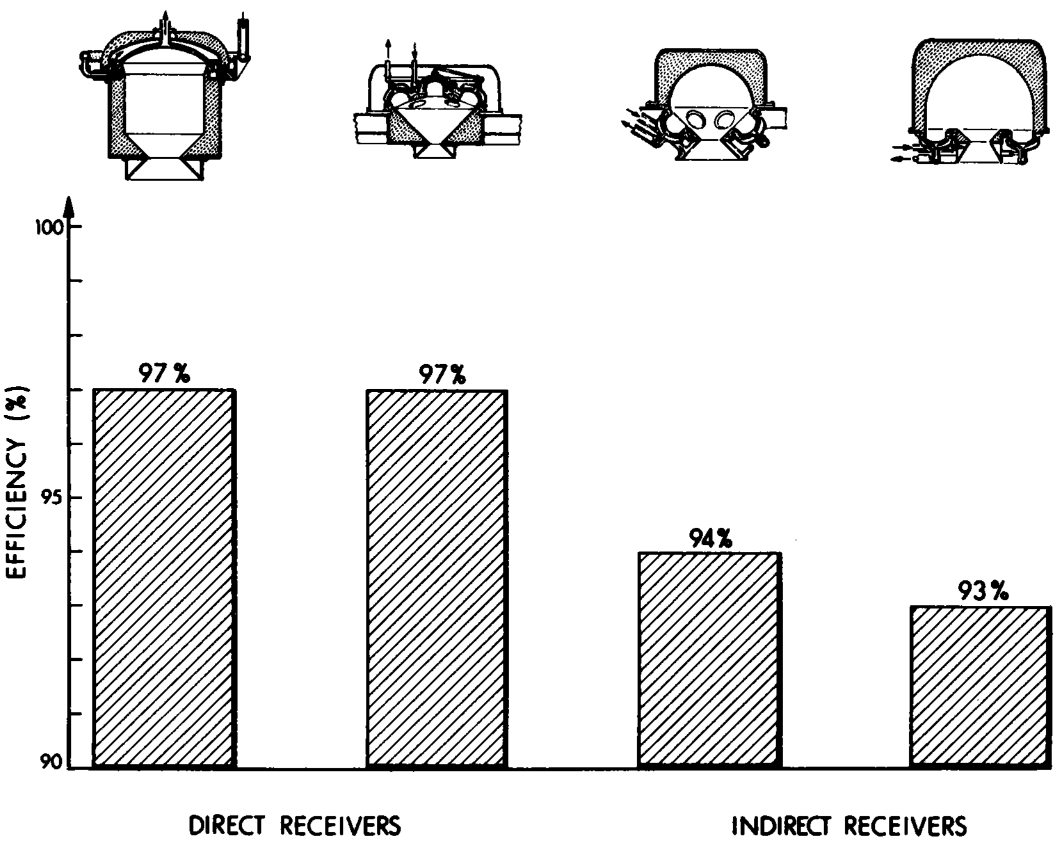

Figure 9. Comparison of the operating efficiencies of direct and indirect point-focus receiver concepts.

1.3 Ceramic Dome Module

The ceramic dome module is the basic receiver building block. An example of a shallow dome version is presented in Fig. 10. The module consists of a cool-air entrance plenum, perforated-impingement jet-plate, silicon carbide dome and an insulating dome support ring (Fig. 11). Impinging jets strike against the solar-heated ceramic dome and remove heat into the airflow by jet action. The ceramic dome sits on an insulating ring and is free to slide on it. The insulating ring, which is also made of ceramic material, provides both a temperature drop between the ceramic dome and the metal support structure and a mechanical path by which the pressure forces on the dome are counteracted by the support structure.

C74-305A

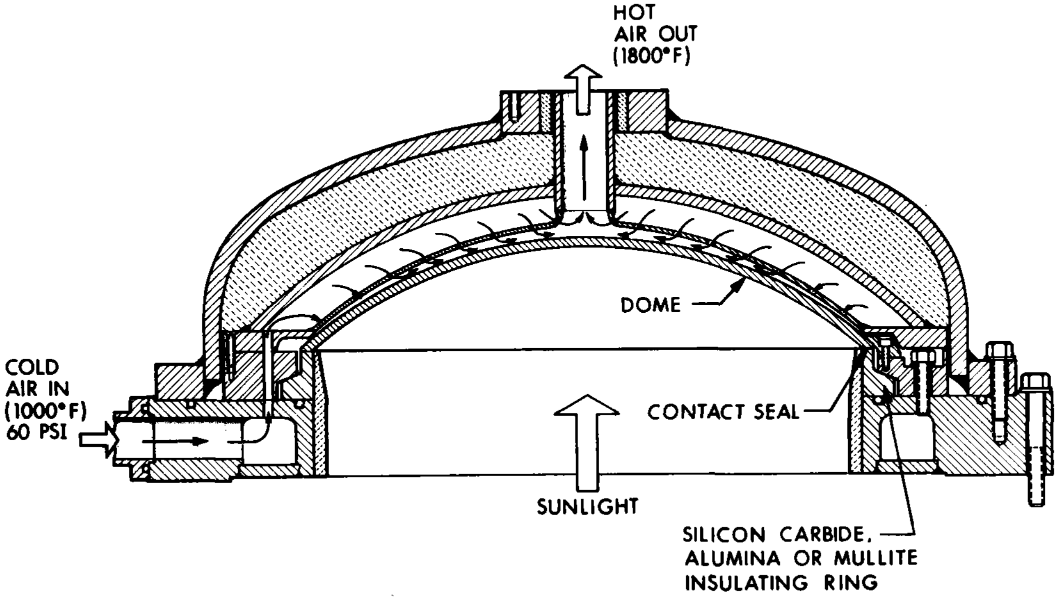

Figure 10. Shallow ceramic dome module.

C74-305A (detail)

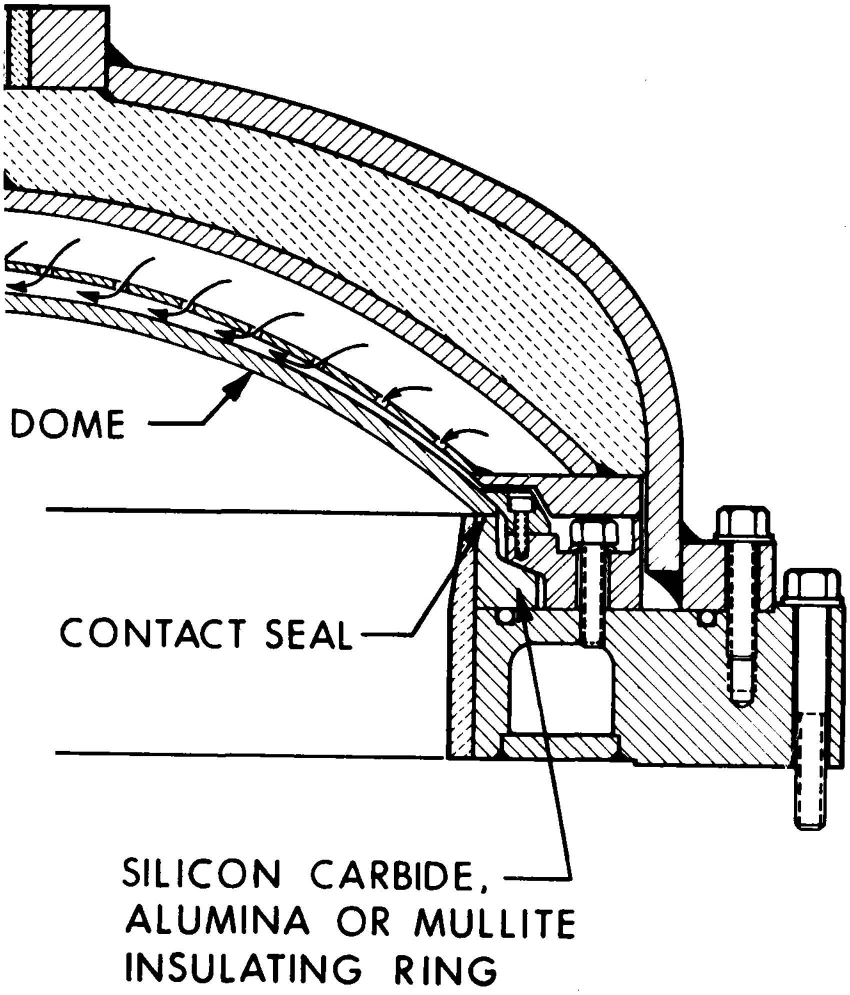

Figure 11. Ceramic dome module support details.

The primary high-temperature seal, a mechanical contact seal, is provided at the sliding interface between the ceramic dome and the insulating ring. A secondary, low-temperature seal is provided at the base of the insulating ring, between the insulating ring and the metal support structure. The primary seal operates at the ceramic dome temperature, typically in the range from 1800°F (1000°C) to 2400°F (1300°C). The insulating ring/ceramic dome support system depicted in Figs. 10 and 11 is an actual representation of the high-temperature seal arrangement that was finally selected and proven at the one-foot-diameter size in experimental tests. Both hemispherical dome and shallow dome/seal geometries were leak tested in the experimental tests reported in Section 7.0. The design goal for the mechanical-contact, high-temperature seal at the dome ring contact surface was a leak rate of 1% (or less) of the total flow impinging on the dome when operating at a pressure differential of four atmospheres and temperatures to 2400°F (1300°C). The goal was easily bettered in the experimental tests.

1.4 Objectives of the Present Program

The main objective of the present program was the development and demonstration of a high-temperature ceramic dome seal. However, the solar heated-air receiver studies also addressed a number of other questions, including:

1. Is it possible to develop a cavity receiver of the ceramic dome type which operates at high conversion efficiency while producing heated air at 1800°F?

2. Can ceramic dome units be designed which will support the pressure and thermal stresses encountered in operation? What type of ceramic material should be used?

3. Can the ceramic dome heat exchanger modules be so positioned in the receiver to receive nearly uniform incident solar and reradiated cavity fluxes to minimize induced thermal stresses?

4. Can a method of support be developed to hold the high-temperature ceramic domes which transmit pressure loads acting on the ceramic dome to a supporting metal structure while simultaneously

insulating that metal structure from the severe dome temperatures and providing an effective high-temperature seal at a four-atmosphere pressure differential?

In the following sections, analytical methods which describe the incident flux distributions inside cavities heated by parabolic concentrators are discussed and results which show that the required degree of flux uniformity in the cavity can be controlled by selecting the proper cavity dimensions and form are presented. Radiative exchange within the cavity and radiative losses through the cavity aperture are then considered. Cavity operating efficiencies are presented. Stress analyses for a variety of ceramic dome/seal configurations are presented next. Both free-standing and clamped-hemispherical and shallow-dome seal geometries are considered. Three different methods for obtaining a high-temperature seal which were successfully implemented in subscale (2-inch-diameter) ceramic hardware are then reported; a glass seal, a brazed seal and a mechanical contact seal. Based on these seal investigations, the mechanical contact seal approach is chosen as the preferred method for demonstration on one-foot-diameter ceramic dome hardware. Finally, experimental demonstration of one-foot-diameter mechanical contact seals is reported.

2.0 SOLAR RADIATION FLUX DISTRIBUTIONS IN CAVITY RECEIVERS

Existing methods for analyzing flux distributions inside cavity receivers for parabolic dispersed-dish systems involve Monte Carlo and Ray Vector techniques that are cumbersome and time consuming. Therefore, as part of the present program, simple analytical methods were developed to describe the incident solar flux distributions in cavity receivers heated by parabolic concentrators for a variety of cavity geometries including elliptical, parabolic, hemispherical and part-hemispherical cavity forms. The methods developed assume perfect optics and provide quick, fairly accurate solutions. Mirror imperfections in the 0-10 milliradian range may be accounted for in the mathematical equations by including a mirror-error constant and numerically integrating the resultant equations. The formulation of the analytical methods and their use in solving practical receiver radiation problems are described in depth in Appendix A. The reader is referred to that section of the report for details as to how the incident radiation calculation methods may be coupled to a cavity radiation exchange model and used to calculate the cavity receiver's internal equilibrium operating temperature profile with ongoing power extraction from the cavity. Sample results calculated for a hemispherical dome-capped cylindrical-cavity receiver and a geometry applicable to the Stirling engine coupled receiver, Fig. 5, are presented below to show that uniform incident flux and uniform operating temperature conditions may be achieved over the dome.

The geometry for a dome-capped cylindrical cavity receiver near the focus of a parabolic concentrator is illustrated in Fig. 12. Reflected sunlight from the parabolic concentrator passes through the cavity entrance and impinges on the cylindrical cavity walls and on the hemispherical end cap. The incident flux distributions on the walls of a 14-inch-diameter cavity placed at the focal point of a 30-foot-diameter, 45-degree rim angle, parabolic dish are shown in Fig. 13 for a dish with perfect optics. The flux impinging on the hemispherical-dome heat exchanger unit is essentially constant, while flux peaks occur on the cavity walls near the rim angle of the concentrator. The resulting temperature distribution within the cavity, after reradiation exchange, is displayed in Fig. 14. This example assumes that heat extraction from the cavity is occurring through the hemispherical dome which is operating at a dome temperature of 1800°F. For the case shown, the equilibrium temperatures on the forward bulkhead which encircles the entrance aperture and on the cavity wall forward of the radiation peak are 2400°F. The maximum cavity temperature of 2800°F occurs in the vicinity of the peak flux on the wall.

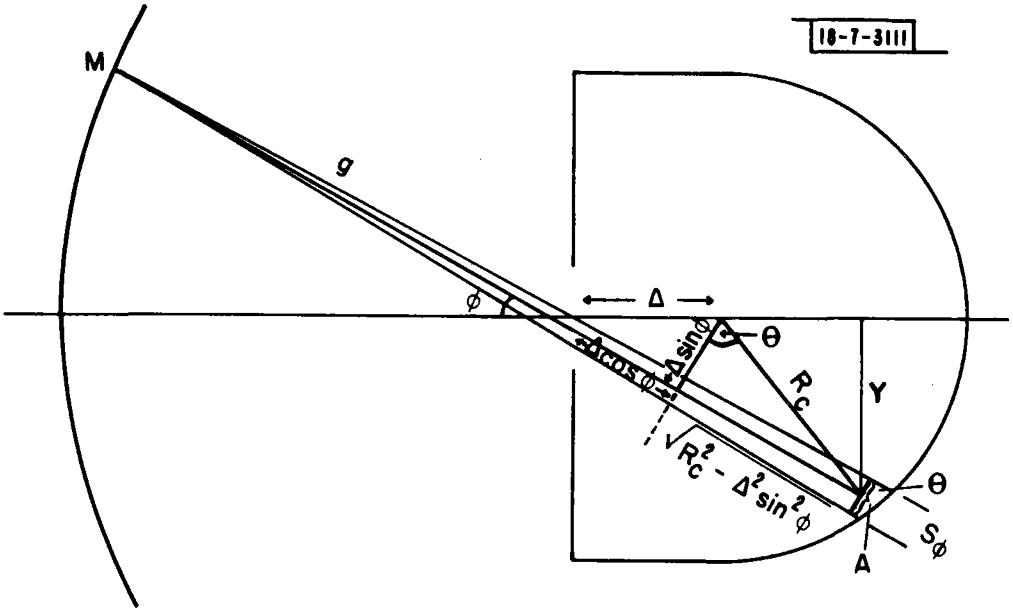

Figure 12. Dome-capped cylindrical-cavity receiver geometry.

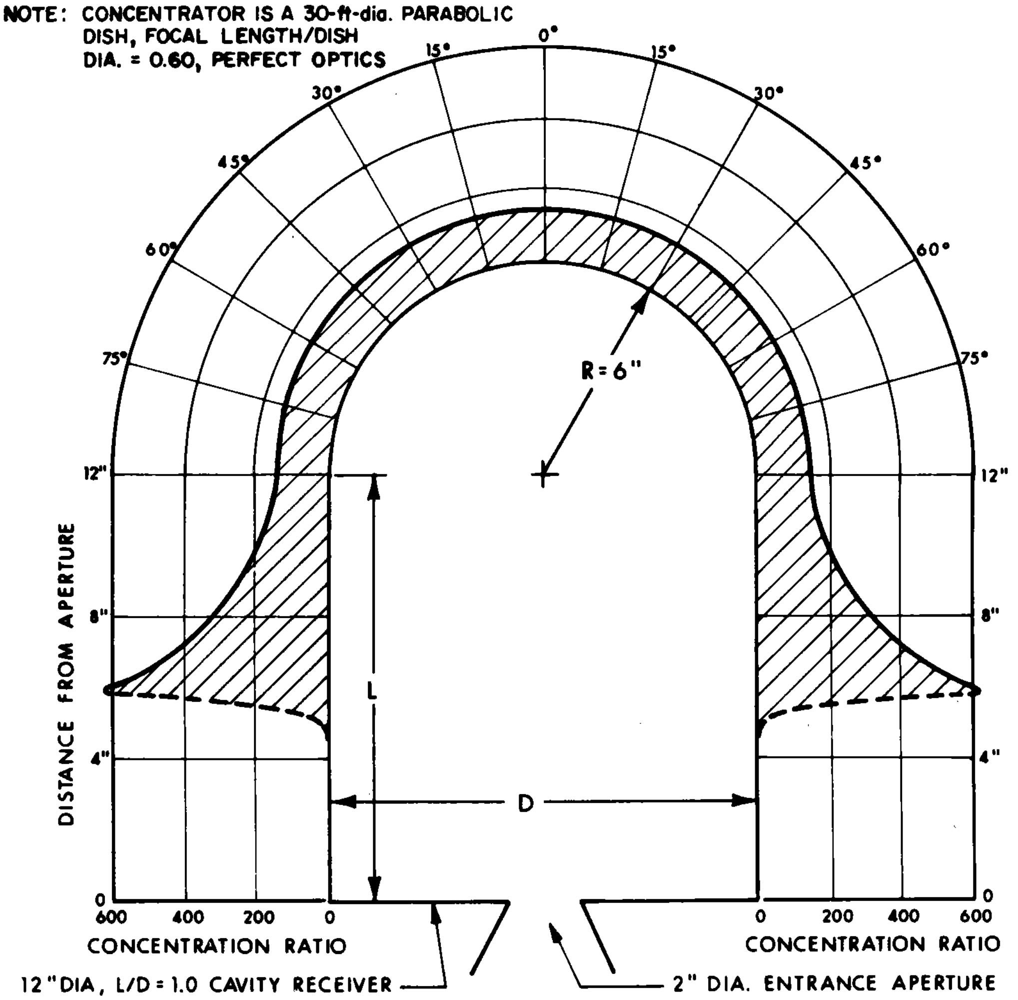

Figure 13. Incident—flux distribution in the receiver.

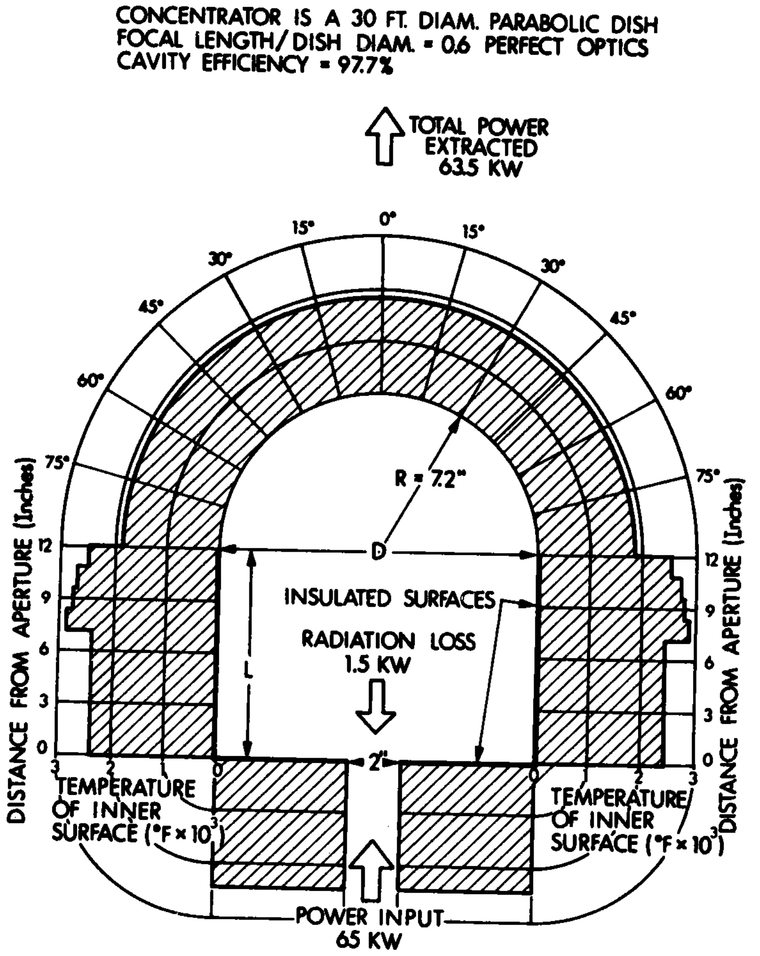

Figure 14. Temperature distribution in the receiver.

The receiver operates at an overall cavity efficiency of 97.7%, where cavity efficiency is defined as the ratio of the integral resultant cavity flux to the incident collector flux. In a practial receiver application with a parabolic concentrator containing mirror errors, the high receiver efficiency (97%) will be reduced, as a larger cavity aperture is necessary to accommodate a broader beam width (caused by mirror error), thereby increasing the losses through the aperture. In addition, specular reflection is estimated to reduce the efficiency by 2%, but even when this and mirror errors up to 10 milliradians are included, the cavity efficiency should still exceed 90%.

3.0 CERAMIC MATERIALS

Silicon carbide was selected as the dome material while silicon carbide (SiC), aluminum oxide (Al_2O_3), and mullite were considered for the insulating ceramic ring. Silicon carbide is preferred for the dome because it has superior properties of thermal conductivity, strength, and thermal shock resistance at elevated temperatures. Two versions of SiC were used in this program; one a siliconized SiC which may be operated satisfactorily in air to a maximum temperature near 2400°F, and the other, a chemical-vapor-deposition (CVD) SiC which potentially can be operated to 3000°F. The siliconized SiC product was produced by Norton Company and the CVD SiC product was fabricated by Materials Technology Corporation (MTC).

Values of thermal conductivity and modulus of rupture (MOR) at 2200°F (1200°C) for two Norton siliconizied SiC materials and MTC CVD SiC are listed in Table II. NC-435 siliconized SiC is a smaller-grained, higher-strength version of NC-430 with a more limited shape-forming capability. During the period of the SHARE contract, NC-435 was available only in plate form with dimensions not exceeding 4 inches. Experimental burst tests by Garrett Corporation of NC-430 and MTC CVD SiC tubes have shown that CVD SiC is 30% stronger than NC-435, Table II.

TABLE II

THERMAL CONDUCTIVITY AND MODULUS OF RUPTURE
OF SiC MATERIALS

(1200°C)

	NC-430	NC-435	MTC* CVD SiC
K Btu/ft^2 hr (°F/ft)	18	--	12
Modulus of Rupture (psi)	38-52000 (3-point)	68000 (4-point)	52-68000+

*Materials Technology Corporation

+Estimate based on Garrett Corporation burst tests of CVD SiC tubes.

The thermal conductivity of NC-430 at elevated temperature exceeds that of metals such as stainless steel. In comparison, aluminum oxide and mullite have thermal conductivities at 1200°C which are a factor of 2 and a factor of 5 to 8 less (depending on the type of mullite), respectively, than SiC; their MORs are substantially less than SiC with mullite being the weaker of the two materials.

NC-430 SiC, NC-435 SiC, MTC CVD SiC, Al_2O_3, and mullite ceramic materials were put to use in the experimental program in a variety of shapes. NC-430 SiC was used in the form of plates, disks, test coupons, domes and insulating rings; NC-435 SiC as disks and test coupons; MTC CVD as test coupons, domes and insulating rings; Al_2O_3 as disks, test coupons, domes and insulating rings, and mullite as test coupons and insulating rings.

Ceramic test coupons were used in the ceramic metalization and brazing portion of the investigation. After metalization, the ceramic/metal couples were heated in a furnace to expected operating temperature levels to test the adhesion qualities of the ceramic-to-metal bond. The metalized coupons were also brazed to each other to form tensile test specimens for brazed-joint strength tests.

The size of the ceramic dome pieces that could be formed from SiC ceramic materials was quite limited at the start of the present contract. Norton Company had fabricated dome-like structures of about 6-inch maximum diameter in NC-430 SiC material. MTC CVD SiC had been produced in plate and disk form only. The situation was better with regard to Al_2O_3 ceramics since missile radomes had been constructed previously in the United States, with dimensions of the order of one-foot diameter and several feet length, so fabrication experience was available. Mullite fabrication was substantially more limited than Al_2O_3, being restricted to plates, sheets rings and disks, with maximum dimensions of not more than a few inches. Thus it was necessary for Lincoln Laboratory to support developmental efforts at Norton Company and MTC to obtain the one-foot-diameter SiC ceramic hardware needed in the present program.

In the course of the program, testing of ceramic hardware was carried out at the 2-inch-diameter, subscale level and the one-foot-diameter, proof-test level. At the 2-inch scale, mechanical seal tests were accomplished with NC-430 SiC, MTC CVD SiC and Al_2O_3 disks and hemispherical domes on insulating rings of Al_2O_3 and mullite. At the 12-inch-diameter scale, NC-430 SiC hemispherical and shallow dome forms were tested on 12-inch-diameter insulating rings of NC-430 SiC, MTC CVD SiC, and Al_2O_3. The 12-inch-diameter NC-430 SiC hemispherical and shallow domes manufactured for Lincoln Laboratory by the Norton Company were the largest dome shapes fabricated by that company up to that time; previous experience being limited to 6-inch-diameter items. Norton Company and MTC were also successful in fabricating 12-inch-diameter insulating rings of NC-430 and MTC CVD SiC, respectively. MTC was unable to deliver 12-inch-diameter CVD SiC domes to Lincoln Laboratory because of problems encountered in separating the CVD SiC dome from its carbon mandrel. This problem was not resolved by MTC during the duration of the SHARE contract. Also 12-inch-diameter insulating rings and plates of Al_2O_3 were delivered to Lincoln Laboratory by GTE Western Gold and Platinum Company (WESGO). Delivery times on the Norton Company NC-430 domes and insulating rings of 12-inch diameter exceeded eight months. MTC CVD SiC and WESGO Al_2O_3 12-inch-diameter parts were delivered three months and six months, respectively, after placement of the order. No contractor could be found who could supply 12-inch-diameter mullite parts.

4.0 HIGH-TEMPERATURE SEAL TECHNOLOGY

Literature searchs of high-temperature seal technology, made at the start of the SHARE Program, showed that the technology necessary to achieve a seal in the temperature range from 1800°F (1000°C) to 2400°F (1300°C) did not exist. Previously, seals had been constructed that would work continuously up to about the 1600°F (875°C) temperature level but nothing had been developed for higher temperatures. Therefore, a program was undertaken to develop the technology that would allow the desired seal to be realized. The philosophy adopted in the program was to attempt to develop three entirely different seal approaches simultaneously in 2-inch-diameter hardware and to select the most promising approach for application to the one-foot-diameter seal tests after about six months elapsed time in the program. Based on the initial literature searches, a mechanical contact seal, a glass seal and a brazed seal were chosen as the most likely candidates. The technology for each of the three seal candidates was successfully developed during the program. The mechanical contact seal was accomplished earliest in time, followed by the brazed ceramic seal and, finally, the glass seal. Based on this development sequence, the mechanical seal approach was chosen as the preferred method for demonstration on one-foot-diameter ceramic dome hardware at the six-month decision point since it appeared to be the most promising and mature option at that time. A description of the three seal options will now be presented along with discussions on supporting technology issues.

4.1 Mechanical Contact Seal

In the mechanical seal approach, a freely supported hemispherical silicon carbide dome (or shallow dome) is mounted on a ceramic insulating ring and the contact area between the dome and ring provides the primary high-temperature seal. A metal O-ring under the insulating ring or a metal diaphragm seal attached to the insulating ring provides a low-temperature seal between the insulating ring and the metal support structure. An example of a 2-inch-diameter seal test unit with this geometry is shown in Fig. 15. This particular unit was assembled from the three components illustrated in Fig. 16. Seal leakage tests were carried out on the 2-inch-diameter hardware by placing the seal within a pressurized vessel, Fig. 17, which it self was then placed inside a laboratory furnace. The complete laboratory test setup is shown in the photograph, Fig. 18, and schematically in Fig. 19. The leak tests were accomplished by pressurizing the space above the dome and by measuring the leakage through the contact seal to the interior space below the dome/ring unit with a mass flow meter. The leakage flow was carried out to the mass flowmeter through a tube, Fig. 15, connected to the interior space. The seal temperature was maintained at the desired setting by the furnace.

The sliding mechanical seal concept was pursued because calculations showed that stresses arising from differential thermal expansion between ceramic and metal parts of a rigid ceramic/metal seal unit at elevated temperature easily exceeded the strength capabilities of the ceramic materials. This can be easily seen from a comparison of the thermal expansion characteristics of SiC, Al_2O_3 and mullite ceramics and some candidate metal materials, Fig. 20. Tungsten metal is seen to have thermal expansion characteristics close to silicon carbide and mullite while kovar, niobium and rhodium closely match the expansion characteristics of aluminum oxide. However, if silicon carbide or aluminum oxide are attached directly to nickel or steel (not shown), excessive stresses are developed in the ceramic and a failure will occur before the seal reaches the desired operating temperature above 1800°F (1000°C).

CP267-4817

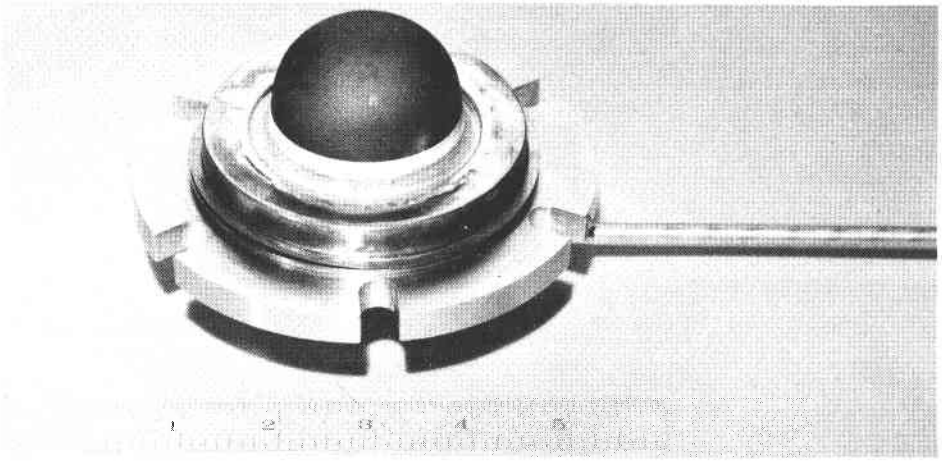

Figure 15. Mechanical contact seal test unit.

CP267-4516

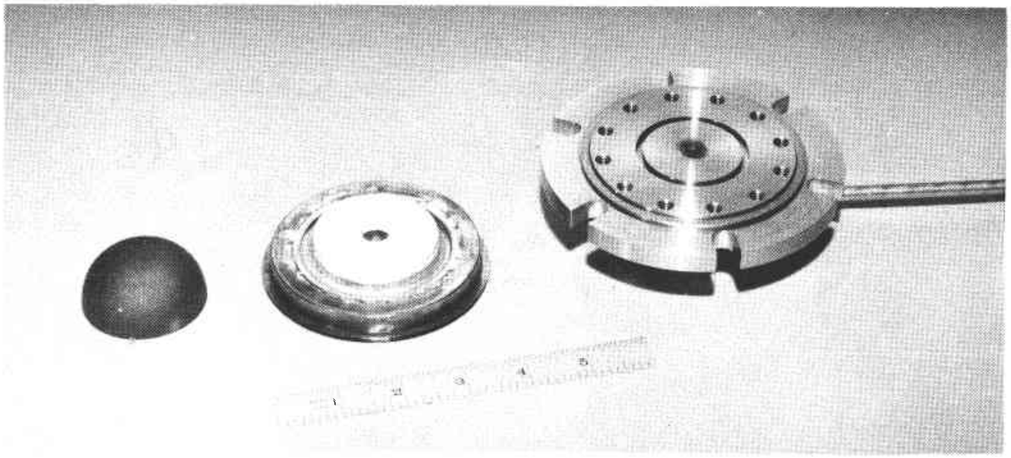

Figure 16. Mechanical contact seal test components.

CP267-4864

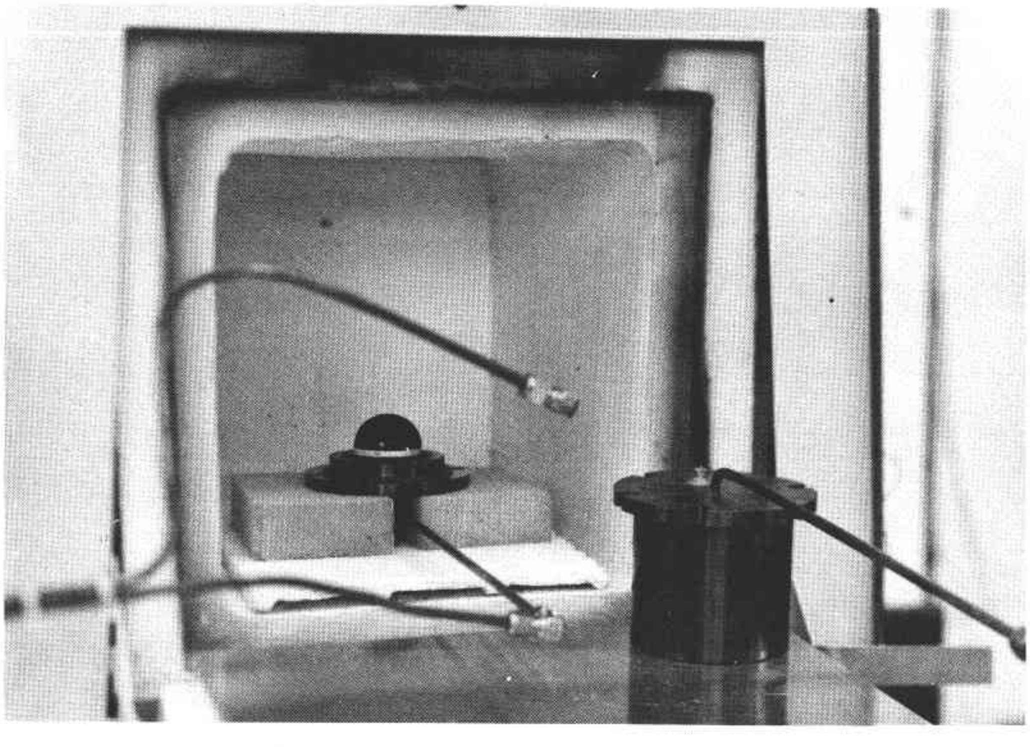

Figure 17. Pressure vessel/seal test unit.

CP267-4863

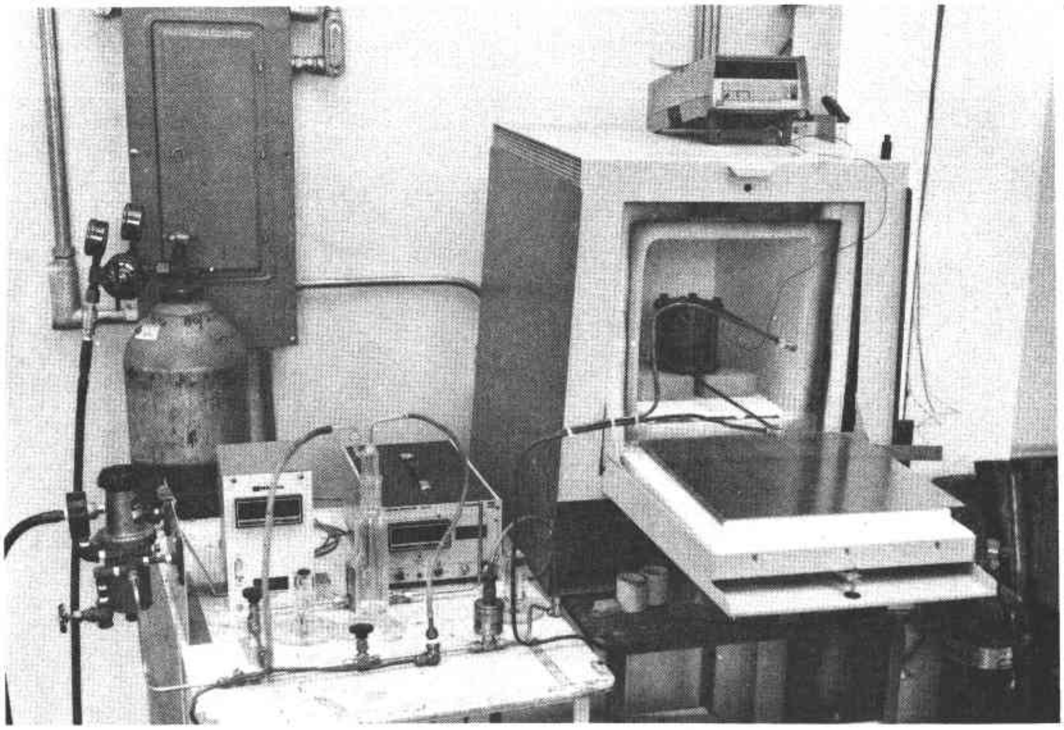

Figure 18. Two-inch-diameter seal test setup.

C71-955

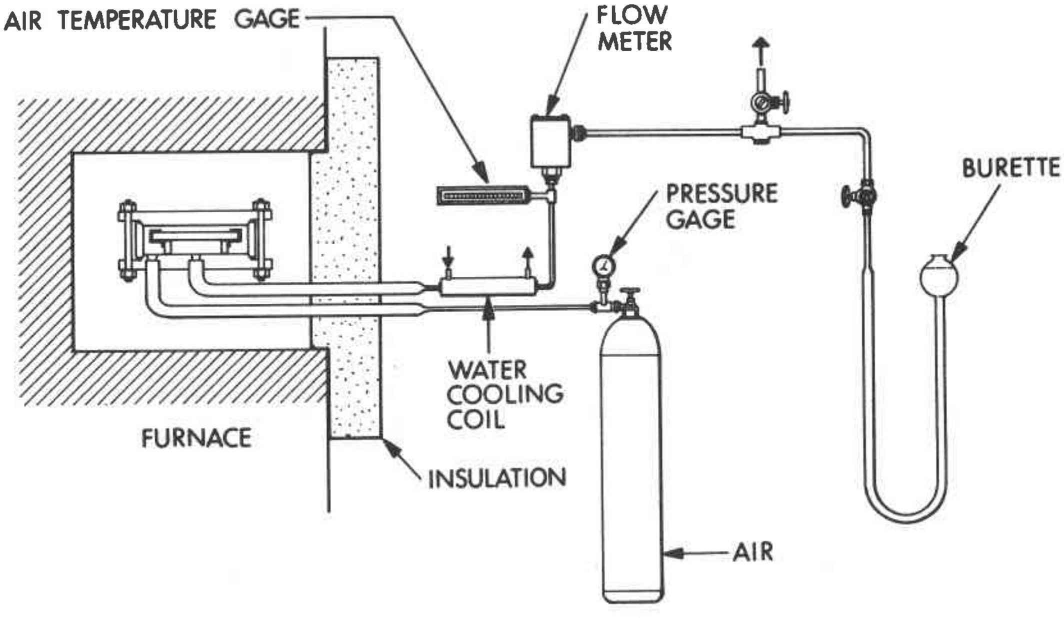

Figure 19. Test setup schematic.

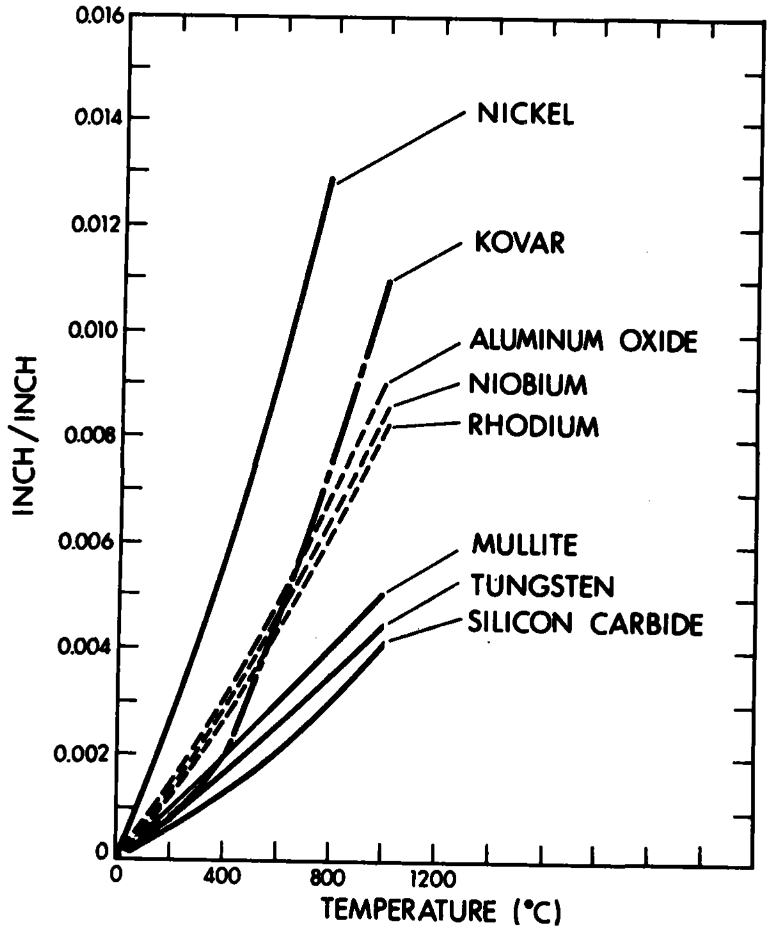

Figure 20. Comparison of the thermal expansion characteristics of ceramic and metals.

Initially leak measurements were taken on a configuration where the dome receiver/seal geometry was modeled by a ceramic disk supported on a short section of tube, Fig. 19. The leak rate through the annular contact seal between the disk and the tube was measured for different surface finishes on the ceramic parts and as a function of the air pressure which forces the disk against the annular seat. Room-temperature leakage measurements for a SiC disk on an alumina tube are shown in Fig. 21 for two different combinations of surface finishes on the ceramic parts; a 6 μ-inch Al_2O_3 ring in combination with a 6 μ-inch or 15 μ-inch SiC disk. The 15 μ-inch finish on the SiC disk and the 6 μ-inch finish on the Al_2O_3 ring are representative of as-received, diamond wheel-ground finishes from ceramic manufacturers. It was not necessary to employ lapped finishes on any of the ceramic parts, because it was found that diamond-ground finishes were adequate. The measured leak rate level at room temperature and 4-atmospheres pressure for a 2-inch diameter was found to be low, only 0.15 cubic feet per hour or less. Leak rate measurements were then made at elevated temperatures and an example of this data is shown in Fig. 22. The low leakage rate at room temperature was found to decrease even further as the temperature was raised. The experimental data was found to obey the leakage rate formula for flat metal contact seals as a function of temperature and pressure:

$$Q_c \alpha = \frac{H^N D}{\mu L T S^{3/2}}$$

where Q_c = leakage rated

H = surface roughness

D = mean seat diameter

μ = viscosity of the leakage gas

L = radial seat land width

T = gas temperature

S = apparent seat stress

N = exponent = 3.0 for metal seals

= 1.6 (measured on ceramic seals)

The only difference in the formula for ceramic parts was found in the value of the exponent N. For ceramic materials in contact, N was measured to be 1.6 rather than the value of 3.0 used for metal surfaces. Subsequent leak measurements taken on hemispherical domes also followed this formula.

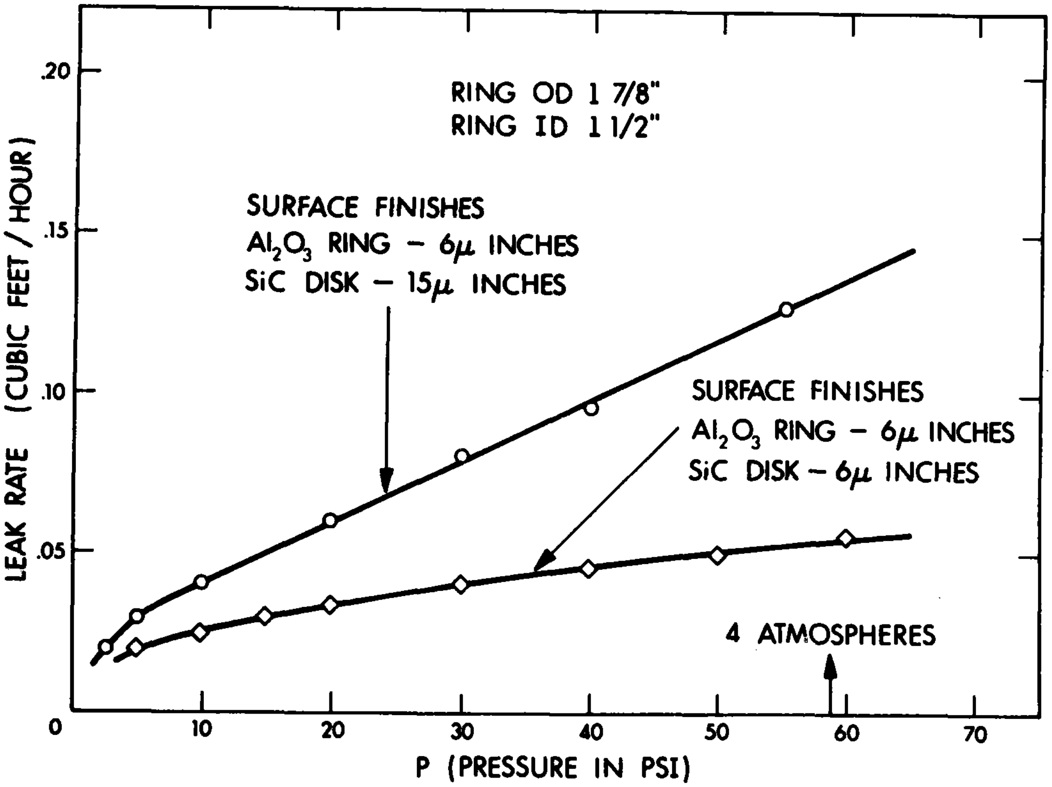

Figure 21. Room-temperature leakage measurements for a SiC disk on an alumina ring.

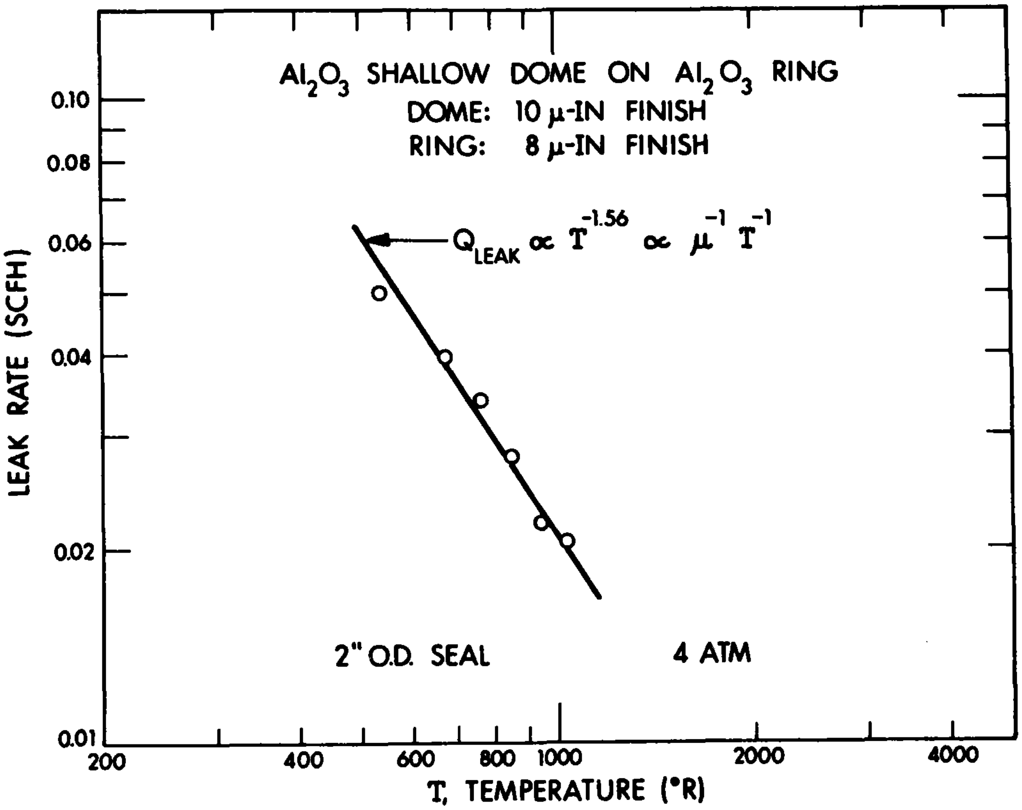

Figure 22. Effect of seal operating temperature on seal leakage rate.

Extrapolations of the subscale leak measurement data to 12-inch-diameter seals were then made, Fig. 23. The data were extrapolated under either of two assumptions: (1) there are no seat stress effects or (2) the seat stress effects follow the flat-metal-contact-seal formula. This comparison shows that the expected leakage rate on a 12-inch-diameter dome at 1800°F will be more than two orders lower than the design goal if seat stress effects are not present in ceramic seals and more than four orders lower if they are. Based on these promising predictions, the mechanical contact seal approach was selected as the preferred method for implementation and further testing in 12-inch-diameter seals.

C71-954

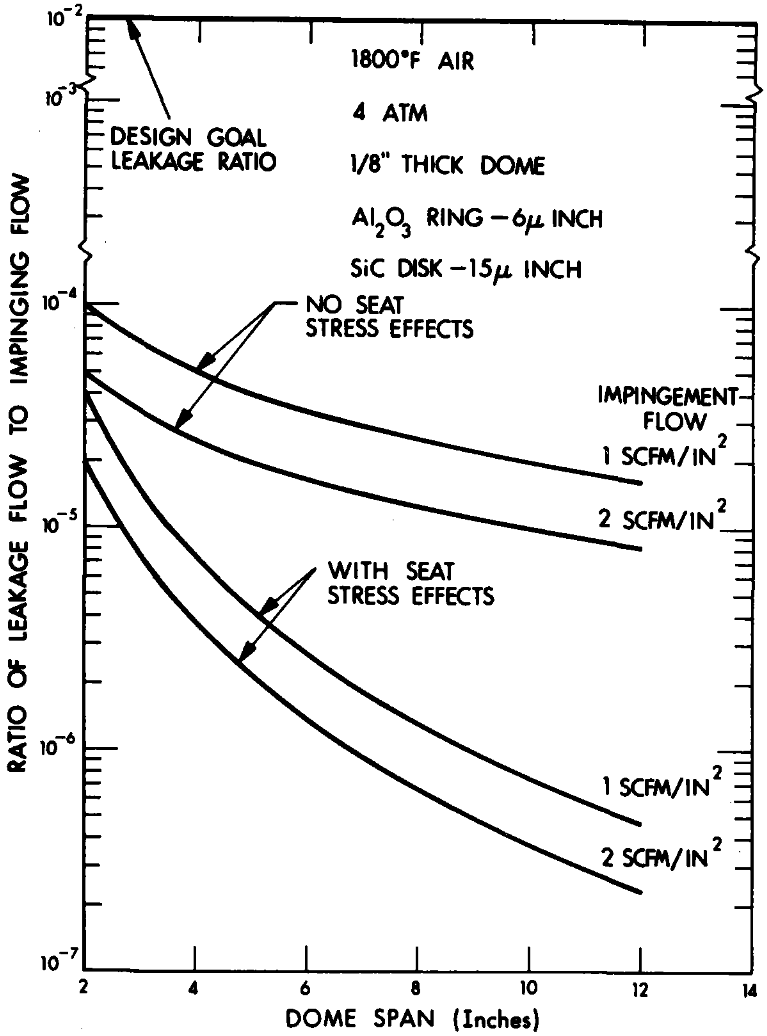

Figure 23. Leakage predictions for larger-diameter contact seals.

4.2 Brazed Ceramic Seal

The brazed ceramic/metal seal concept that was investigated is shown in Fig. 24. The ceramic is metalized and a leak-tight metal diaphragm is brazed to the periphery of the silicon carbide dome. Literature searches into the metalization of silicon carbide for use at temperatures above 1800°F (1000°C) showed that the necessary technology was not available. Therefore an experimental program was undertaken to develop metalization and brazing methods. Vacuum sputtering of the metal coating to the ceramic was chosen as the metalization approach because this technique had not been explored before for use in high-temperature joints for engineering-type applications and appeared to be a promising avenue. Examples of potential uses of metalization techniques in the context of the SHARE program are illustrated in Fig. 25. Development of the approach was shown to be possible.

C71-951A (detail)

Figure 24. Brazed ceramic/metal seal concept.

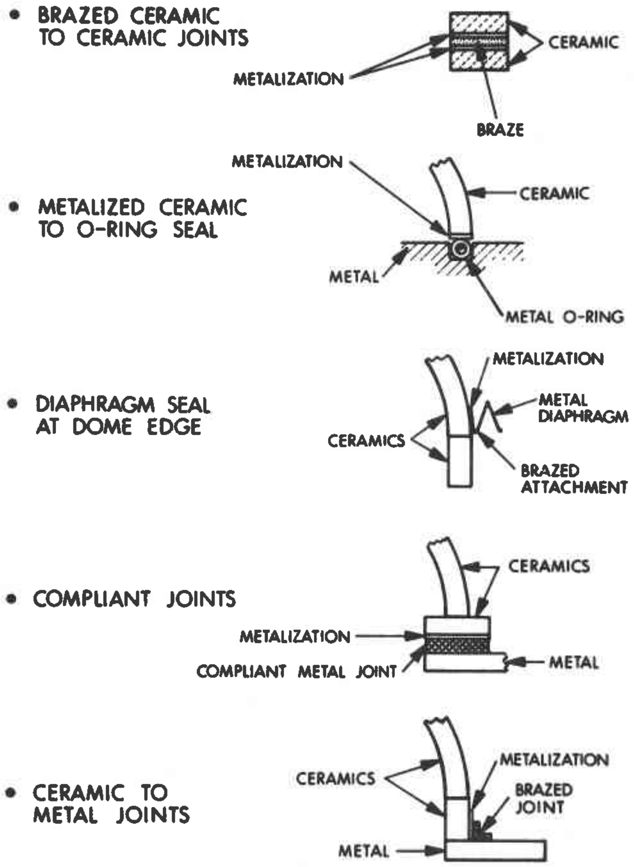

Figure 25. Potential applications for metalization techniques.

The initial attempt at metalization consisted of vacuum sputtering a layer of tungsten (W) onto a 2-inch-diameter disk of NC-430 SiC. Excellent adherence of the coating was observed at room temperature and continued adherence was observed when the disk was heated in 200°C-temperature increments from 600°C to 1200°C (1100°F to 2200°F). The appearance of the 2-inch-diameter, tungsten-coated disk after the 1200°C-temperature cycle is shown in Fig. 26. The dark circular area in the center of the SiC disk is uncoated SiC while the light surrounding area is the coating of tungsten metal. Excellent adherence of the metal and SiC is observed over the entire area vacuum coated with W, and along the circular boundary.

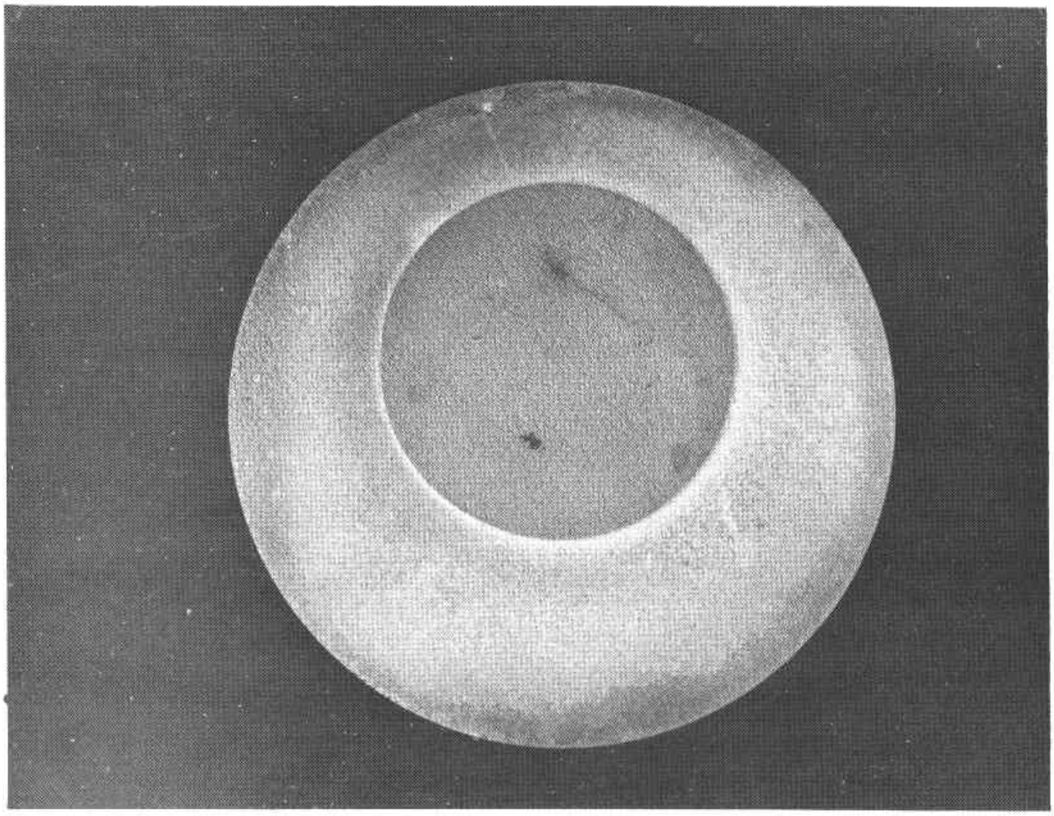

Figure 26. Tungsten-coated SiC disk, after the 1200°C (2200°F)-temperature cycle.

Following the successful metalization of W on SiC, overcoat metalization of the W metal was attempted with nickel to increase the oxidation resistance of the W and to provide a base metal for a brazed joint. Nickel was found to adhere excellently to W at room temperatures and when heated incrementally to 1000°C (1800°F). Figure 27 is a photograph of 1/2-inch-square tungsten (left coupon) and nickel/tungsten-coated (right coupon) SiC coupons after the 1000°C furnace cycle. The nickel coating covers the right half of the right coupon and examination of the vertical nickel/tungsten boundary shows excellent coating adherence. A metalized and brazed SiC joint was then formed by overcoating three pieces of SiC, first with W and then Ni, and then brazing the joint together at 2150°F with an aerospace-type AMS-4783 braze, Fig. 28.

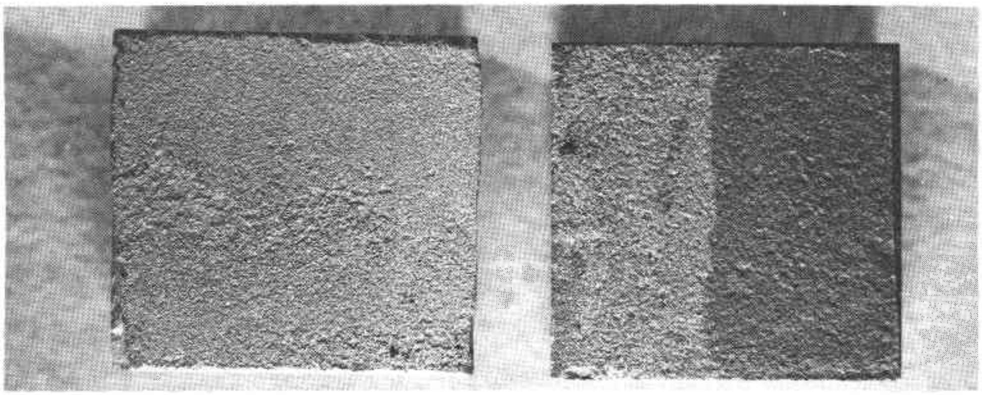

Figure 27. Tungsten and Tungsten/nickel-coated SiC samples, after the 1000°C (1800°F) cycle.

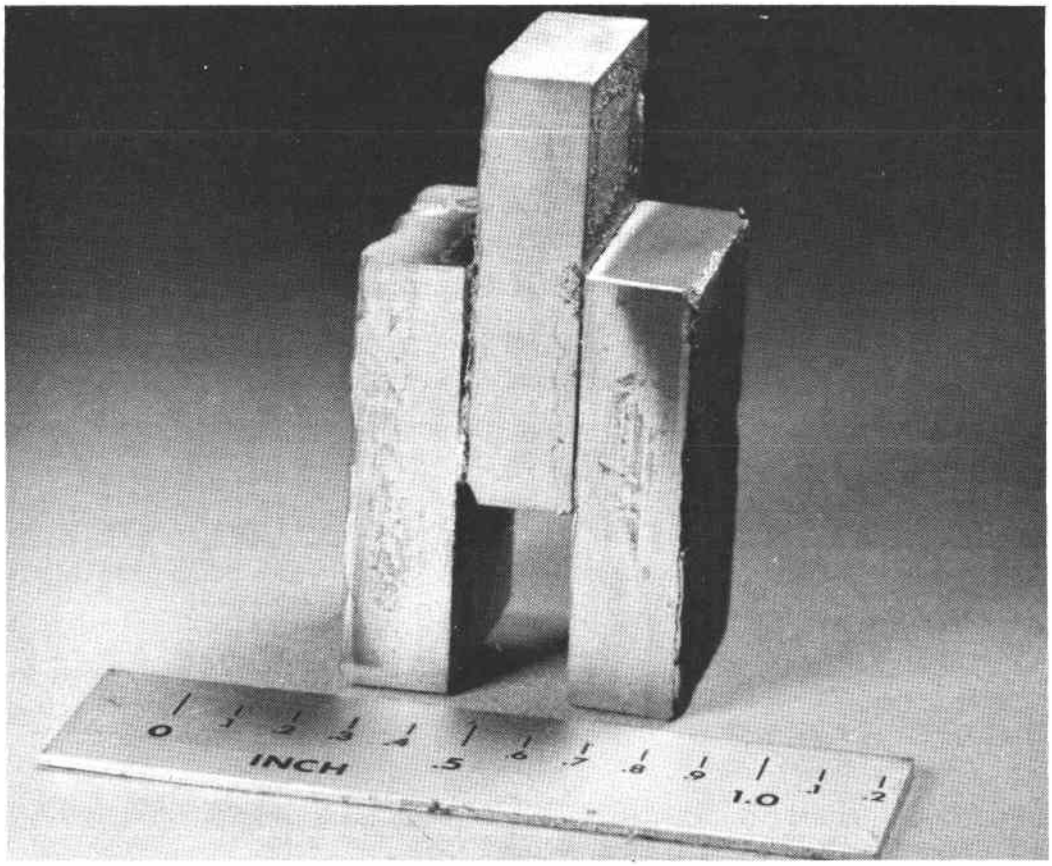

Figure 28. Metalized and brazed SiC joint.

In addition to metalizing W* and W plus Ni* on SiC, the ceramic/metal combinations (couples) listed in Table III were tested for adherence qualities at elevated temperatures. In each case, a ceramic coupon of the type noted was vacuum sputtered with various combinations and thicknesses of the metals. Then each coupon was incrementally heated and examined and photographed after each temperature cycle. A list of ceramics, vacuum-sputtered coatings, and coating thicknesses tried is offered in Appendix B. A particularly good vacuum-sputtered combination, in addition to W and W plus Ni on SiC, was found in the course of these experiments, vacuum-sputtered Ni* on Al_2O_3. This couple showed excellent adherence to 1300°C. A photographic history of a coupon of Al_2O_3 with a vacuum-sputtered coating of Ni is shown in Fig.29 as the temperature is increased to 1300°C. For each temperature, a photograph of the whole coupon is shown on the left and a magnified portion of the coupon is shown at the right. Excellent adherence was observed. This result was unexpected since the literature search made at the outset of the program had shown that metals similar in expansion to Ni, such as copper on Al_2O_3, were unable to survive temperature cycling above the 600-800°C range without deterioration. The success of vacuum-sputtered Ni on Al_2O_3 would allow a metal diaphragm to be brazed directly to an Al_2O_3 insulating ring should that be a desired configuration. Experiments were also conducted of overcoating the exposed edges of brazed metal joints with a layer of CVD SiC for increased oxidation resistance. This also appears to be an excellent approach.

The work described above demonstrated the metalization of ceramics by vacuum-sputtering techniques and the formation of brazed joints between ceramic pieces.

---

*Patent pending.

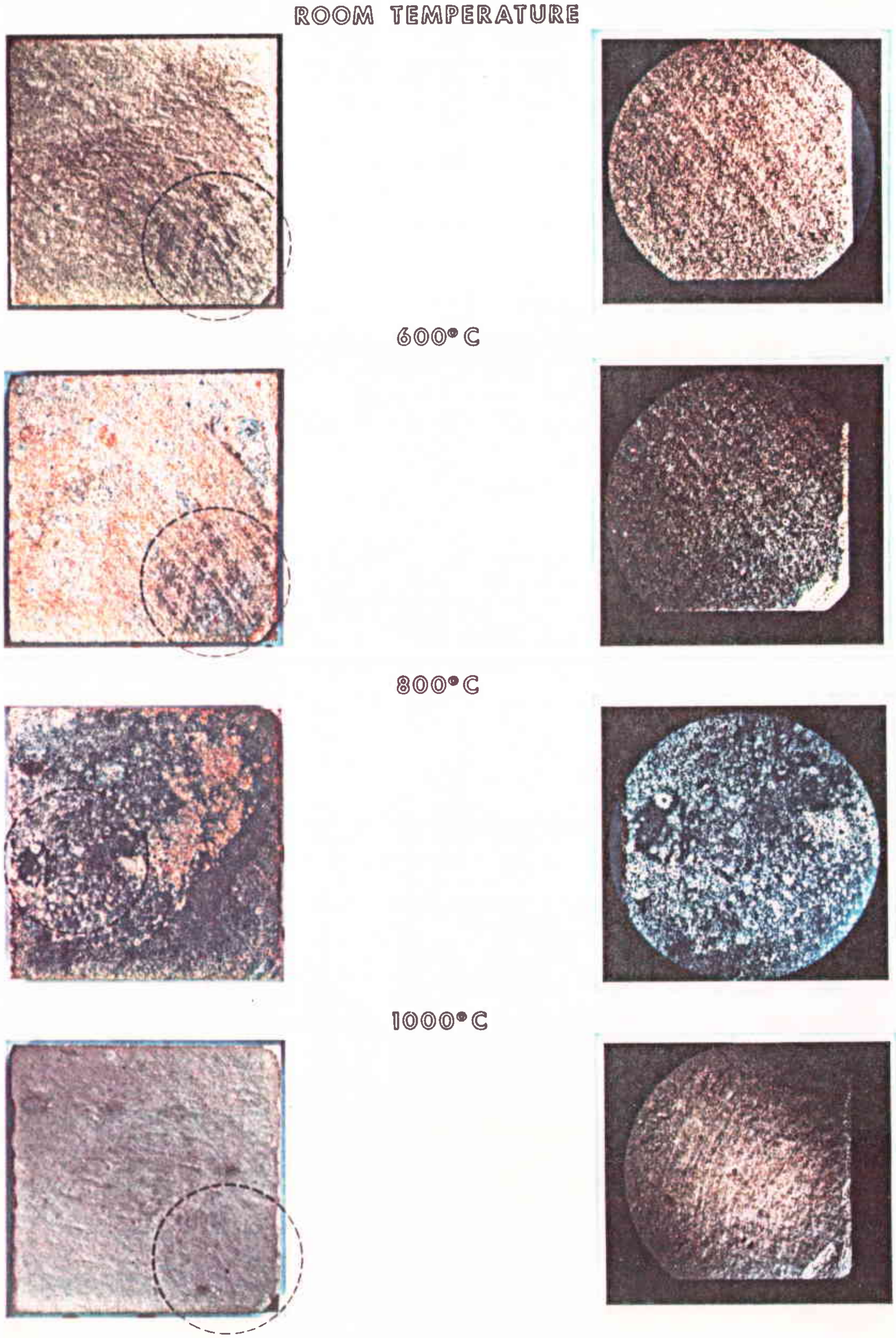

Figure 29. Vacuum-sputtered Ni on Al_2O_3.
Temperature cycling results.

CP267-4808A

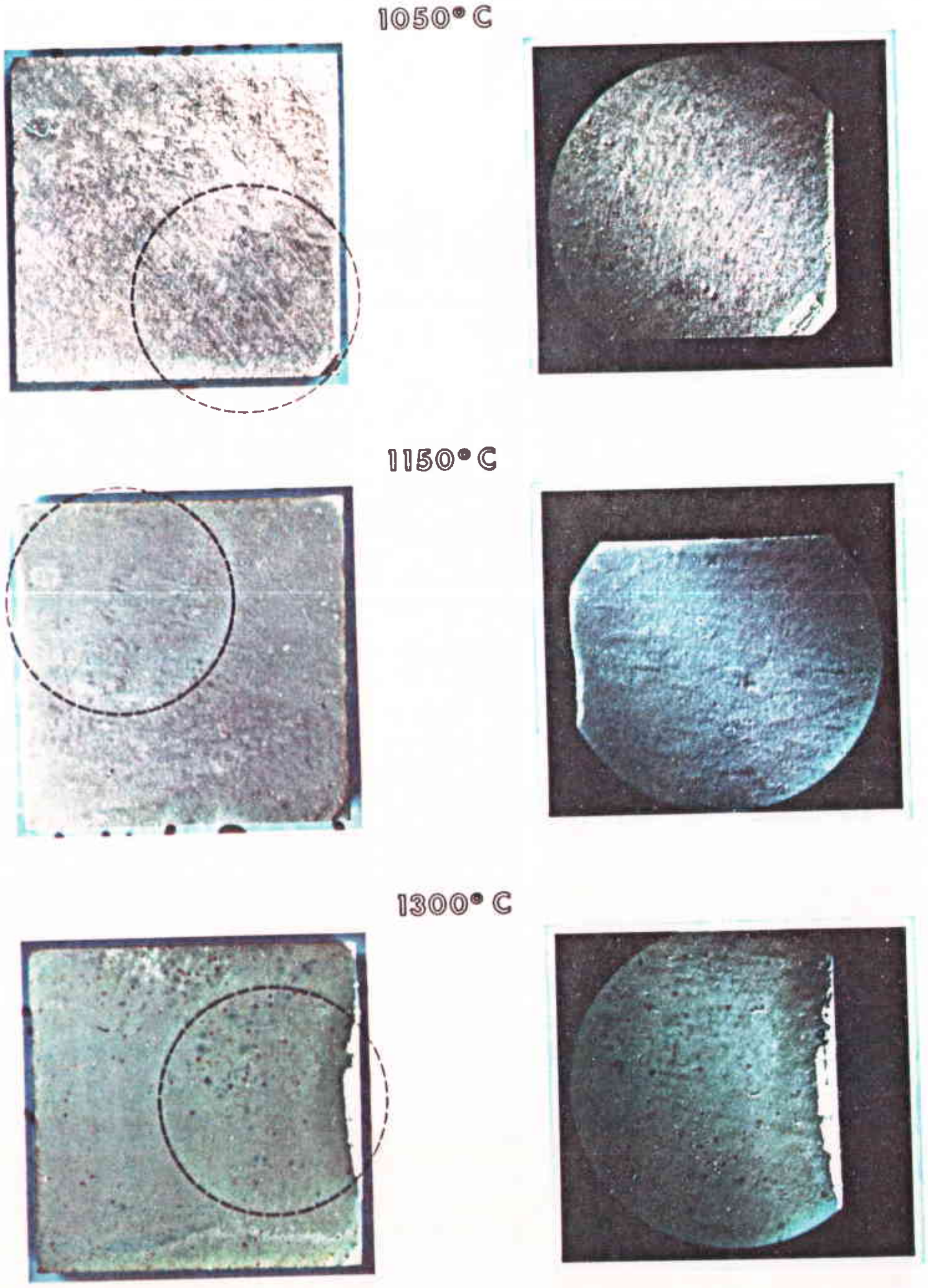

Figure 29 (continued).

TABLE III

CERAMIC/METAL COMBINATIONS (COUPLES) TESTED FOR ADHERENCE QUALITIES

Ceramic Material	Metal Coating			
	Tungsten	Niobium	Nickel	Rhodium
SiC	X			
	X		X	
	X		X	X
Al_2O_3		X		
		X	X	
			X	
Mullite	X			
	X		X	

4.3 Glass Seal

The glass seal portion of the program was carried out on the MIT campus by Professor Kent Bowen and graduate students under subcontract to Lincoln Laboratory. The glass seal approach was successfully demonstrated by forming glass bonds between silicon carbide and mullite ceramic pieces at a temperature of 2200°F (1200°C). An example of the versatility of approach is shown in Fig. 30, where glass has been used to bond two 2-inch-diameter disks of silicon carbide together and then to bond the silicon carbide combination unit to a mullite insulating ring (light color cylinder). The glass seal shown was completed near the end of the SHARE program.

CP267-5039

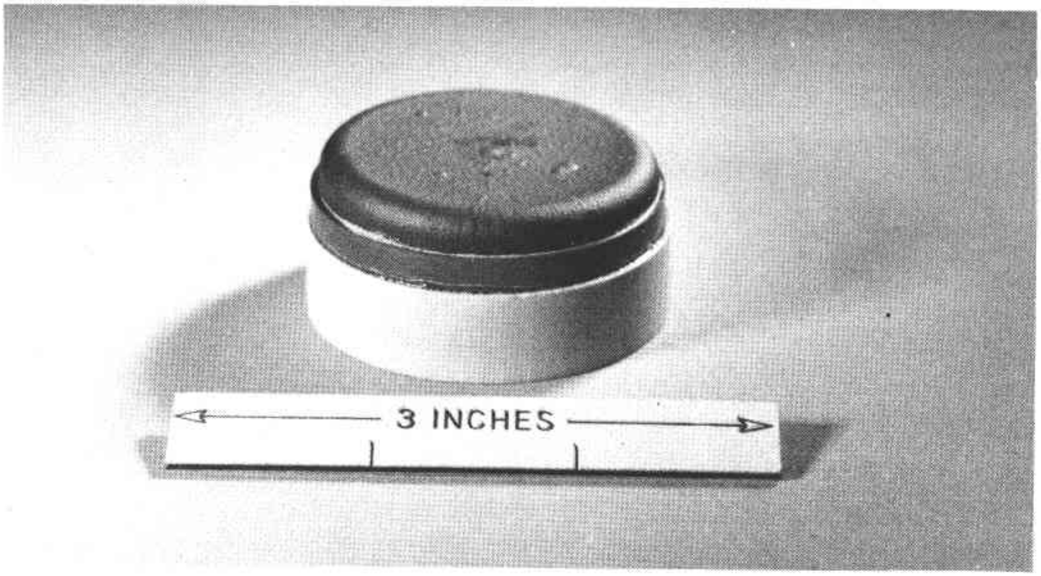

Figure 30. High-temperature glass seal--two-inch diameter.

5.0 CERAMIC DOME AND INSULATING RING STRUCTURAL ANALYSIS

5.1 Ceramic Dome Stresses

Prior to the selection of the mechanical contact seal as the preferred seal approach, methods were developed for analyzing the stresses in a variety of ceramic dome/seal configurations including free-standing and clamped-hermispherical and shallow-dome seals. Both analytical and finite-element analyses were used to detemine the combined pressure and thermal stresses in spherical-dome-segment, heat-exchanger units. Thermal stresses in the dome arise from the temperature gradient through the thickness of the dome for the conduction of heat. Dome stresses were calculated for a four-atmosphere pressure differential across the dome and a maximum temperature gradient through the dome of 400°C/inch. Calculations were performed for dome thicknesses in the range from 1/16 to 1/4 inch and dome spans from 6 to 36 inches using material properties representative of Norton NC-430 silicon carbide (SiC) material. A complete explanation of the methods and results may be found in Appendix C. Some examples of those results follow.

An example of the combined pressure and thermal stresses in a 1/8-inch-thick, 12-inch-hemispherical, SiC dome with free edges as predicted by the analytical treatment is shown in Fig. 31. Variations in dome compressive and tensile stresses as a function of polar angle, $\emptyset$, are illustrated and show that a maximum hoop stress of $\sigma_{\theta top} = 9000$ psi occurs in this example on the outside of the dome at its edge, $\emptyset/\emptyset_{max} = 1$.

Maximum stress levels have been determined, from stress profiles of the type shown in Fig. 31, for free and clamped domes with shapes that vary from hemispherical to shallow forms and the results are summarized in Table IV. Based on these structural analyses, the free hemispherical-dome seal and the clamped shallow-dome ($h/b = 0.20$) seal were selected for design, fabrication and test in one-foot-diameter sizes. The maximum stress levels for these configurations are 9000 and 5950 psi, respectively, and these stresses are small in comparison with the strengths of the silicon carbide material. As shown earlier, Norton NC-430 SiC and MTC CVD SiC have MOR at 2200°F (1200°C) temperature of 38,000 to 52,000 psi and 52,000 to 68,000 psi, respectively.

C71-949

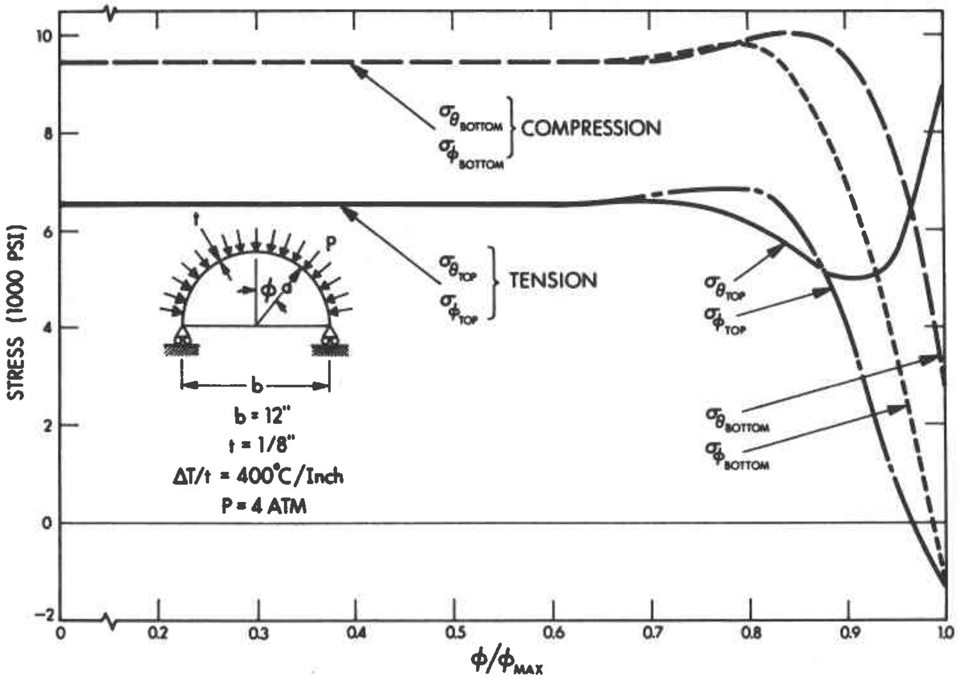

Figure 31. Combined pressure and thermal stresses in a 12-inch hemispherical dome.

C71-948

TABLE IV

SiC DOME STRESSES

		HEMISPHERICAL DOME		SHALLOW DOME H/B*= 0.2	
DOME THICKNESS (INCHES)	DOME SPAN (INCHES)	CLAMPED	FREE (TROLLEY)	CLAMPED	FREE (TROLLEY)
1/16	6	+2,400	+3,900	+1,950	+24,000
	12	+1,000	+2,500	- 100	+64,300
	36	-4,900	NC⁺	-8,800	NC⁺
1/8	6	+9,700	+10,000	+9,400	+15,500
	12	+6,500	+9,000	+5,950	+28,700
	36	+3,900	+5,800	+1,700	+118,000
1/4	6	+15,700	+20,500	+15,400	+20,000
	12	+14,600	+20,000	+14,300	+24,900
	36	+12,800	+19,000	+11,900	+54,500

* Ratio of dome mid-height to span.

⁺ Not calculated.

Note: Plus signs (+) indicate tensile stress and minus signs (-) indicate compressive stress.

5.2 Insulating Ring Stresses

Stresses in the insulating ring arising from the dome pressure loads on the dome/ring interface (200 pounds per linear inch), from a 400°F temperature difference across the ring and a clamping force of 150 pounds per linear inch, have been calculated by infinite element methods and have been found low in comparison to ceramic material strengths (Appendix C). Results for a SiC insulating ring are shown in Fig. 32. Based on these analyses, SiC and Al_2O_3 insulating ring ceramic pieces of one-foot diameter were purchased for the seal proof tests.

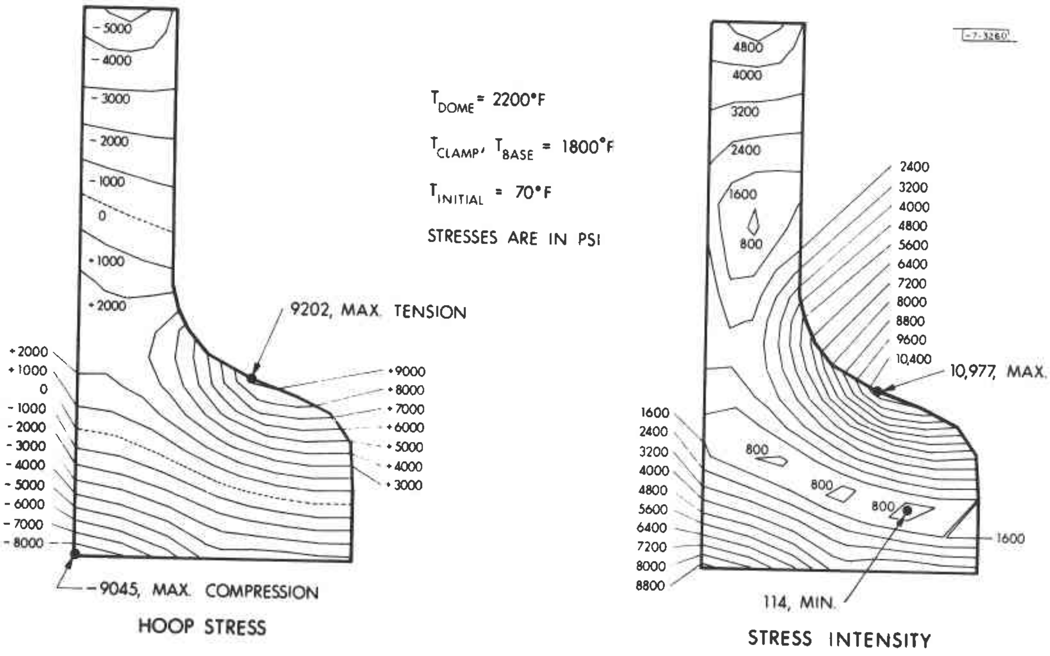

HOOP STRESS

STRESS INTENSITY

Figure 32. Stresses in a 12-inch-diameter SiC insulating ring--clamped edge condition.

6.0 ONE-FOOT-DIAMETER SEAL TESTS

6.1 Introduction

The one-foot-diameter contact-seal-leakage measurement tests reported below were undertaken after promising results were obtained in experimental leak tests using two-inch-diameter ceramic hardware and after analytical and finite-element structural analyses of ceramic dome units demonstrated that ceramic domes can be designed to support the pressure, thermal stress and temperature load encountered. The goal of the one-foot-diameter seal tests was to demonstrate a seal with a leakage rate which is 1% (or less) of the total flow impinging on the dome for heat-transfer purposes, with the seal operating in the desired temperature range from 1000°C to 1200°C (1800°F to 2200°F) and with a pressure differential of four atmospheres (60 psi). Experimental testing of the impingement heat-transfer design in combination with the high-temperature seal was not part of contract ET-78-5-02-4878. Verification of the impingement-jet design approach was considered by DOE to be of secondary importance to the development of a seal, and impingement cooling tests were deferred.

6.2 Experimental Apparatus

The one-foot-diameter, ceramic-to-ceramic contact seal tests were performed by constructing a dome-seal test unit and mounting it on the top of an existing cylindrically shaped, electrically heated radiant furnace as shown in the cross-sectional view, Fig. 33, and in the photograph, Fig. 34. The dome test fixture houses the dome, dome-insulating support ring and metal support structure. The space above the dome could be pressurized and the dome was radiantly heated to the desired temperature from below by the radiant furnace. Seal tests were conducted at the correct seal pressure differential and temperature, but without impingement cooling and heat transfer through the dome.

C74-268A

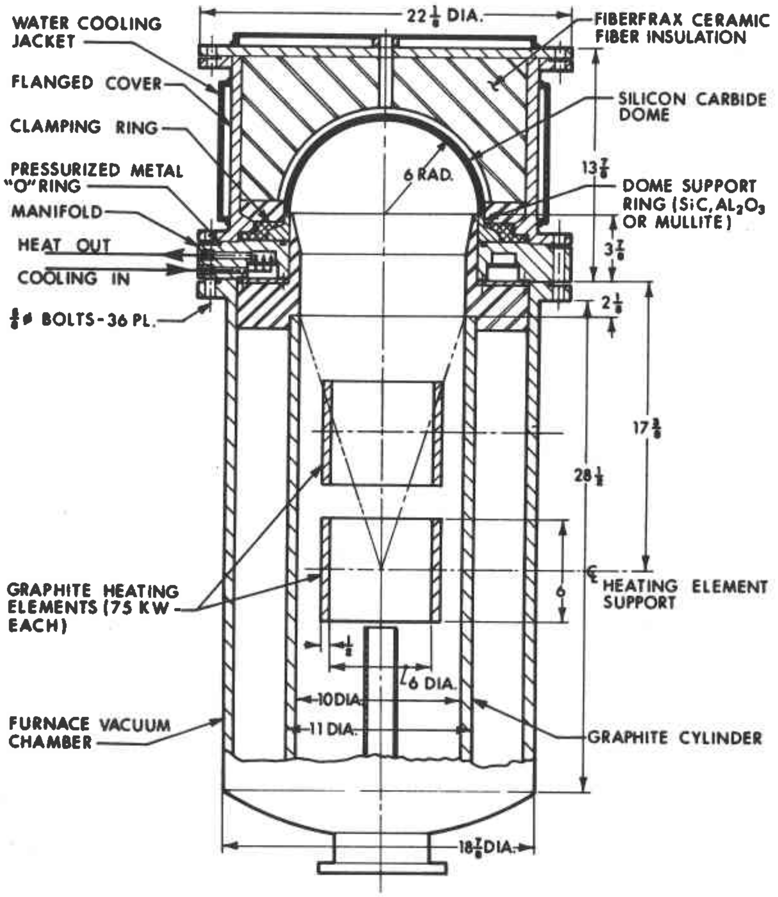

Figure 33. Dome seal/radiant furnace test unit, cross-sectional view.

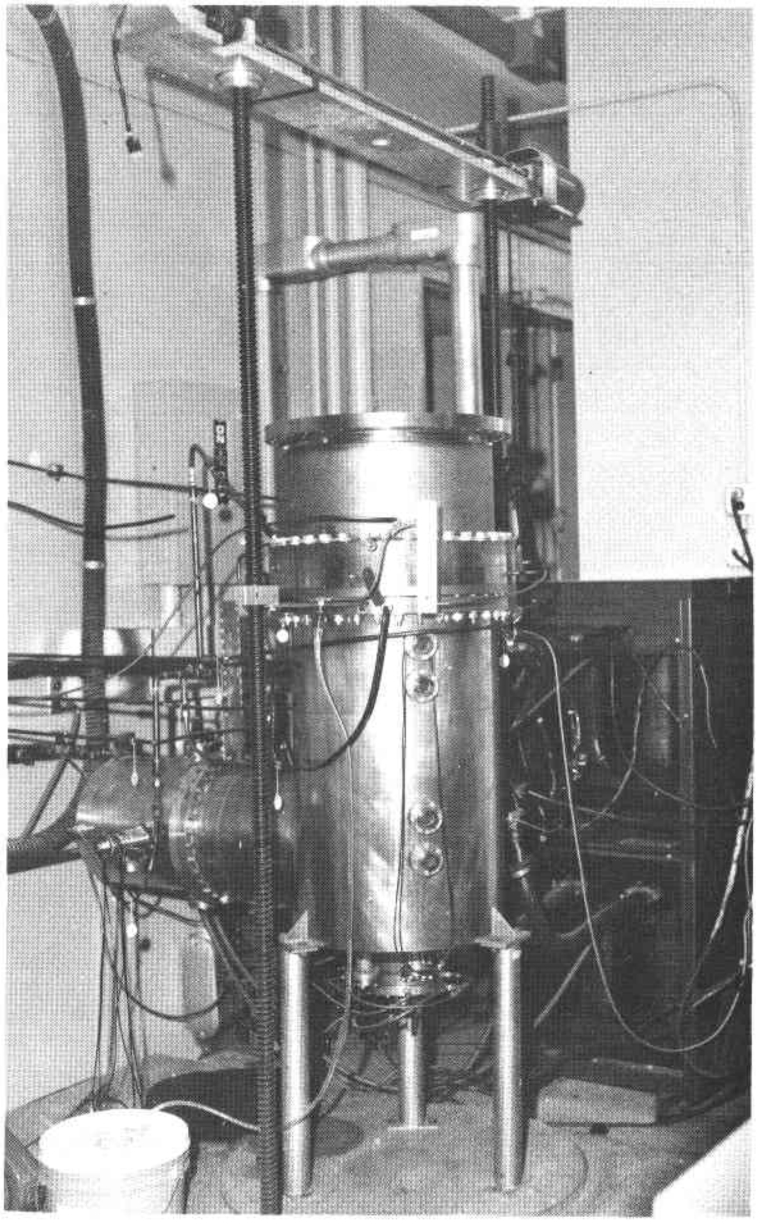

Figure 34. Dome seal/radiant furnace test equipment.

The furnace contained two graphite resistance heating elements which could consume up to 75 kW of electrical power each. The upper furnace electrode is shown in Fig. 35, and the furnace control console in Fig. 36. Instrumentation for the experiment consisted of pressure transducers, temperature measurement equipment, and flowmeter measurement units for leakage tests. Thermocouples were mounted at various locations on the ceramic dome, ceramic insulating ring, and metal support structure. The radiation flux profile from the radiant furnace to the dome surface was measured prior to the experiments using a water-cooled flux gage that translated along a hemispherical surface coincident to that which was later occupied by the installed dome.

CP267-4579

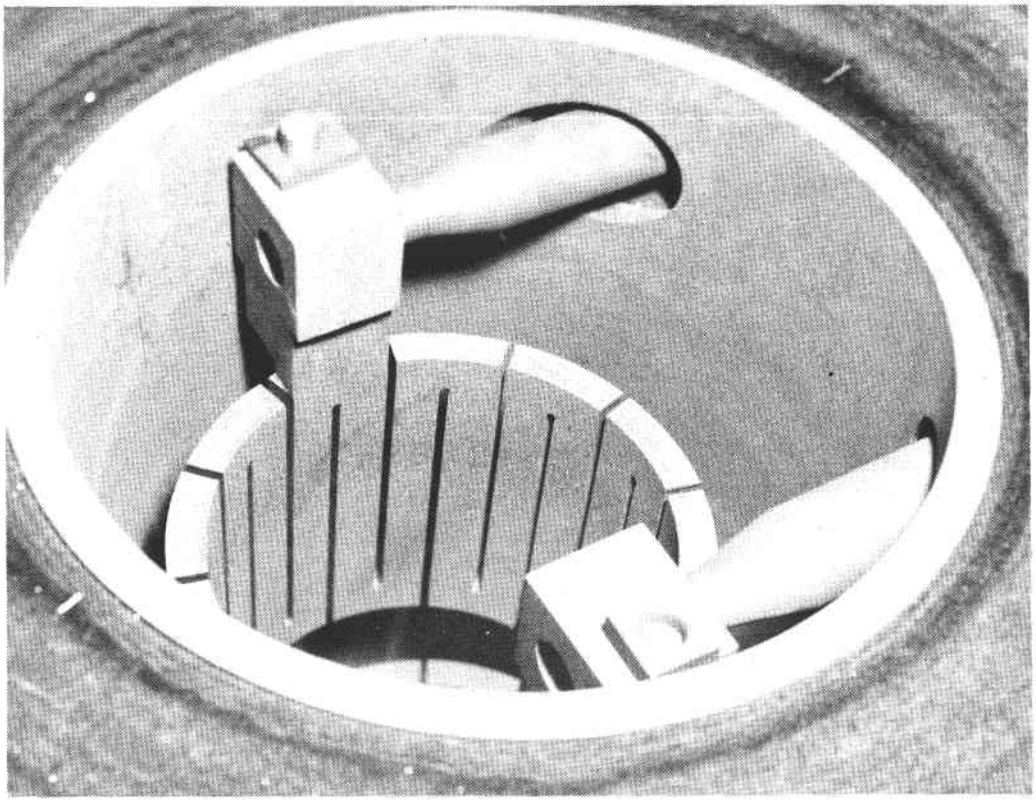

Figure 35. Upper furnace electrode.

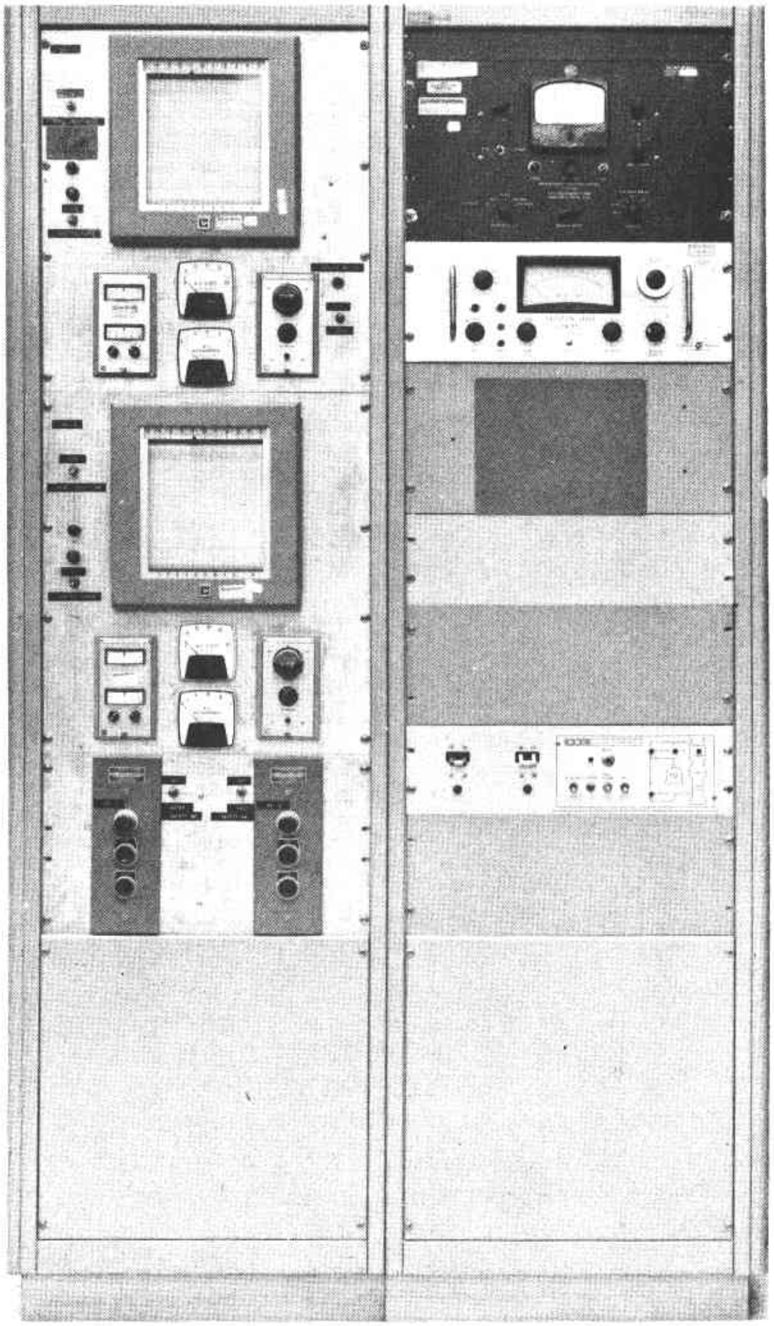

Figure 36. Radiant furnace control console.

Subcontracts were let with industrial ceramic manufacturers for the manufacture of the ceramic hardware required for the seal tests. One-foot-diameter silicon carbide (SiC) insulating rings were delivered by Materials Technology Corporation (MTC) Dallas, Texas (Fig. 37) and by Norton Company, Worcester, Massachusetts (Fig. 38). The MTC insulating rings were constructed by CVD deposition of a layer of silicon carbide on a graphite mandrel while those from Norton were solid SiC, prepared by a process which employs slip casting, firing and siliconization of the piece. The finished material is designated as NC-430 SiC by the Norton Company. One-foot-diameter NC-430 SiC shallow domes and one-foot-span NC-430 SiC hemispherical domes were delivered by Norton Company (Fig. 39). Aluminium oxide (Al_2O_3) ceramic hardware in the form of disks and insulating rings (Fig. 40) were procured from Western Gold and Platinum (WESGO) Company. An assembled hemispherical dome seal test unit is shown in Fig. 41 and a shallow-dome seal test unit in Fig. 42.

CP267-4866

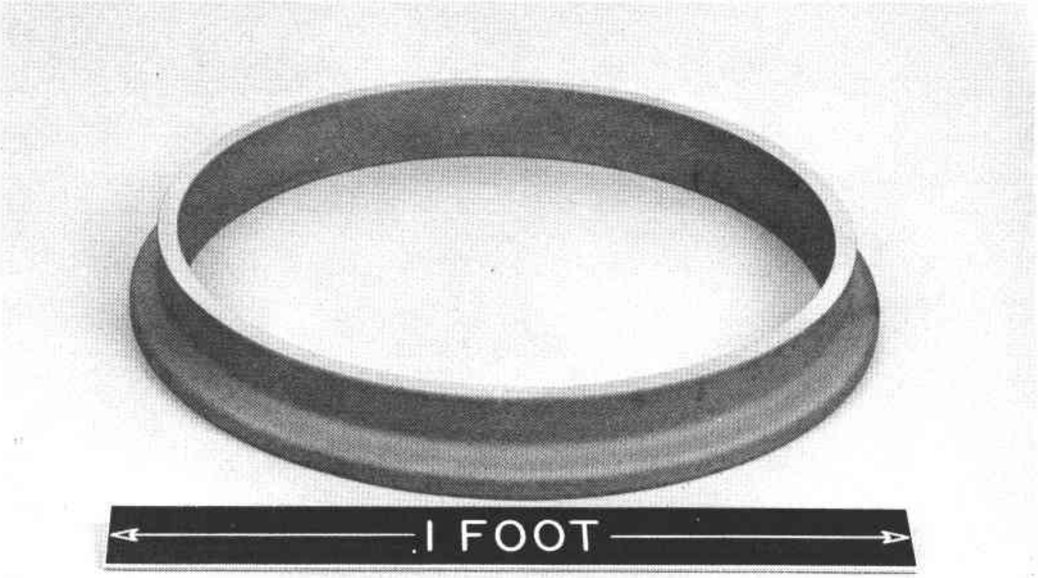

Figure 37. One-foot-diameter MTC CVD silicon carbide insulating ring.

CP267-5038

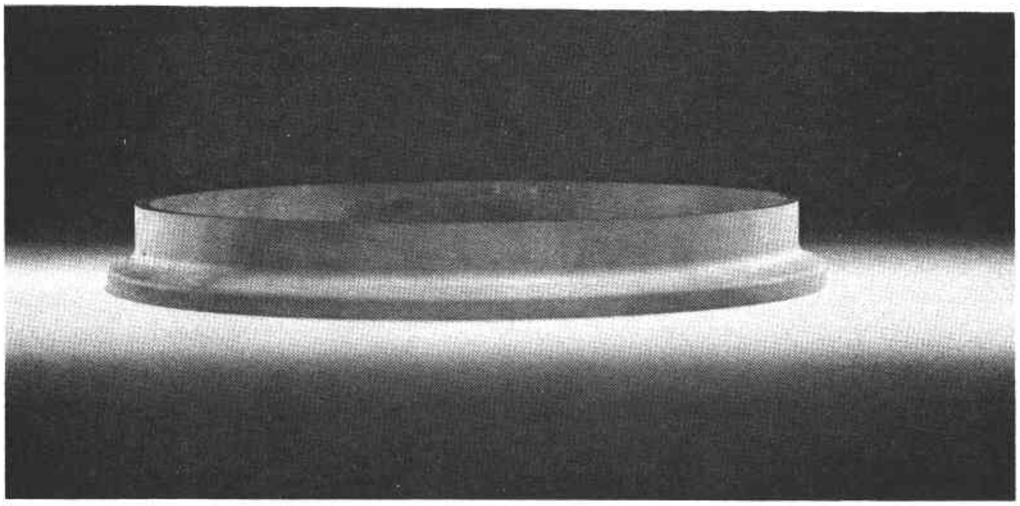

Figure 38. One-foot-diameter Norton NC-430 silicon carbide insulating ring.

CP267-5034

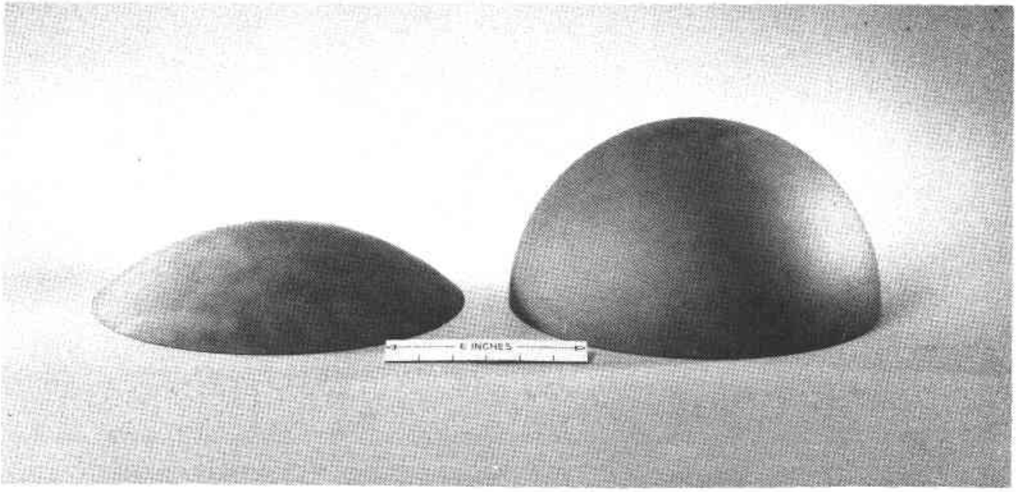

Figure 39. Shallow and hemispherical silicon carbide NC-430 ceramic dome hardware.

CP267-4948

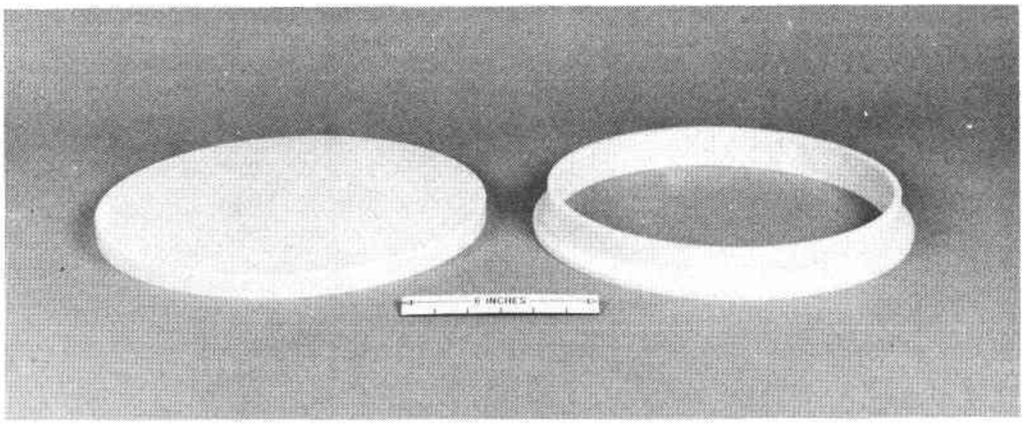

Figure 40. One-foot-diameter alumina ceramic disk and insulating ring seal unit.

CP267-4921

Figure 41. NC-430 silicon carbide hemispherical dome and insulating ring seal unit.

Figure 42. NC-430 silicon carbide shallow dome and insulating ring seal unit.

6.3 Radiation Flux Measurements

Hemispherical dome radiant flux measurements were made using the radiation flux distribution test unit shown in Figs. 43 and 44. In this apparatus, a water-cooled radiation flux gauge can be moved along the hemispherical dome profile and/or rotated in the azimuthal direction. Experimental measurements of the radiation flux profile are offered in Fig. 45 and show that the flux was constant from the center of the dome to a location half-way toward the edge (i.e., between $\phi = 0$ and $\phi = 45°$). As the edge of the dome is approached (i.e., between $45° \leq \phi \leq 90$), the radiation flux decreases slightly and at $\phi = 70°$, a 20% reduction in flux is observed. Measurements of the flux pattern were also made as a function of azimuthal angle and two measurements made 90° apart are compared in Fig. 45. The agreement between the two patterns indicates that the flux pattern is symmetrical in azimuth angle, as expected.

C74-606

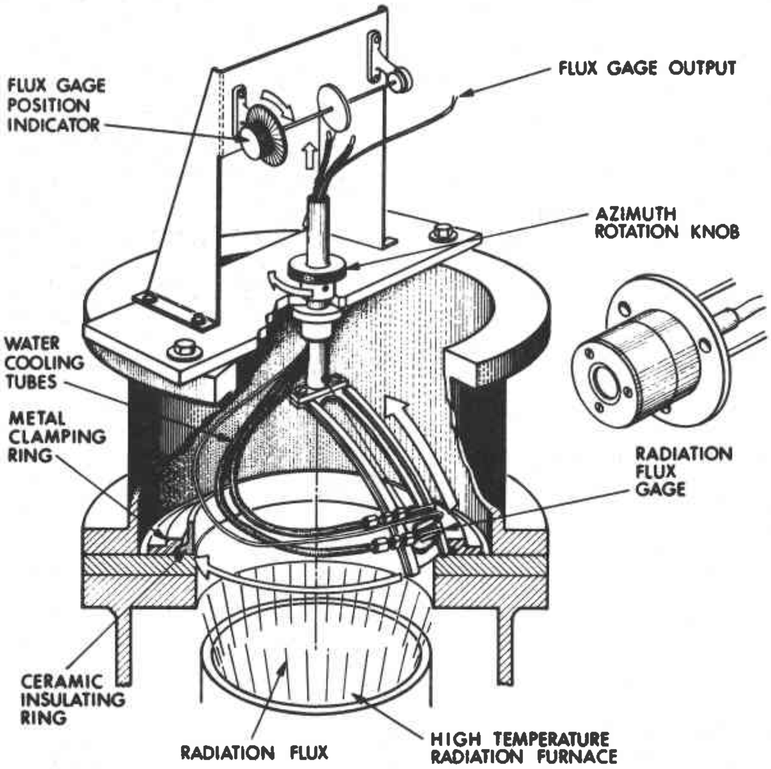

Figure 43. Radiation flux distribution flux unit.

CP267-4927

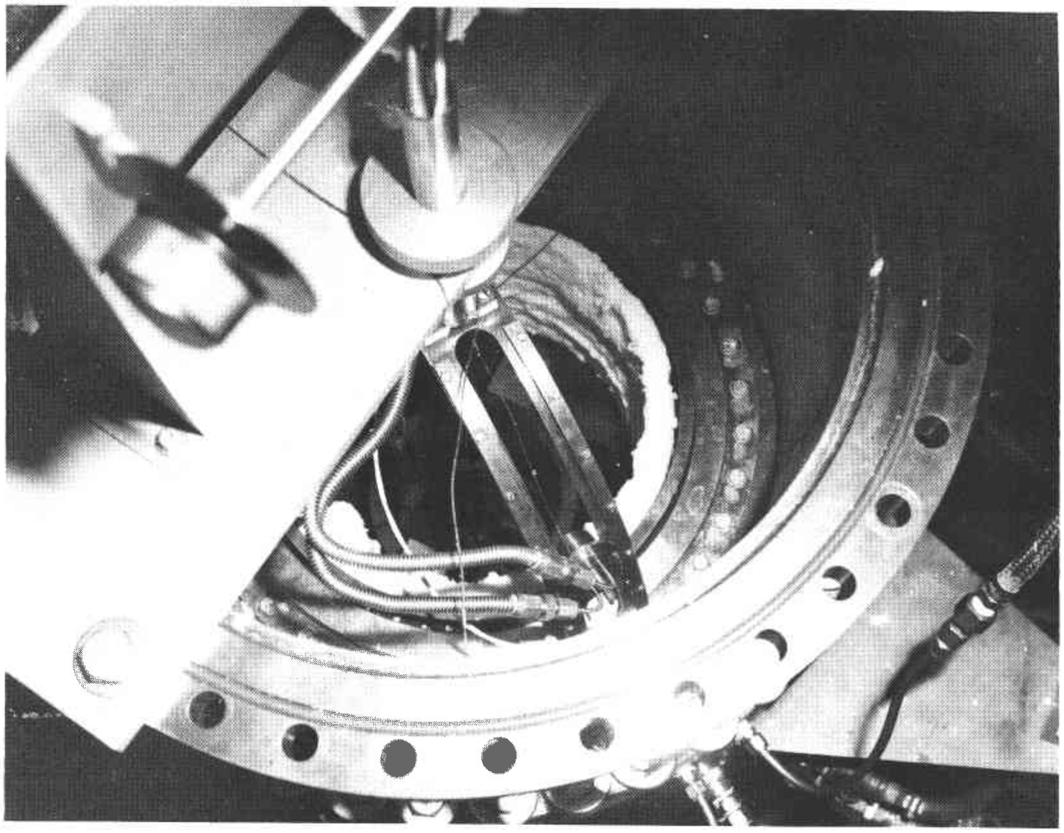

Figure 44. Radiation flux gauge installed in radiant furnace.

C74-550

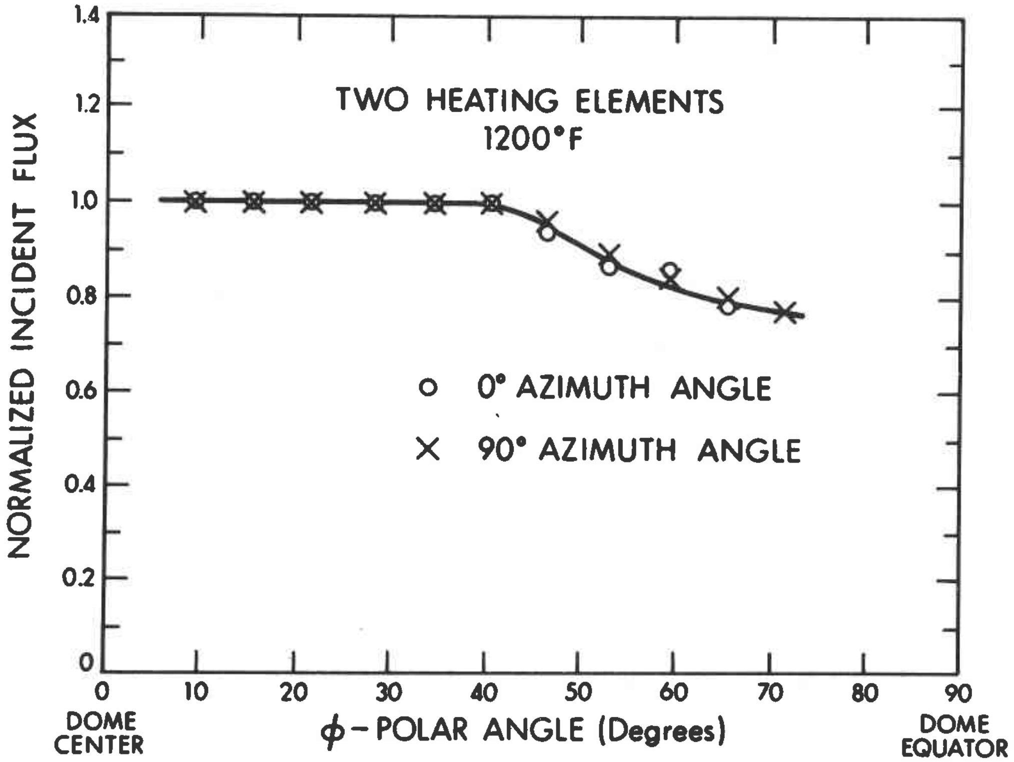

Figure 45. Incident radiant flux distribution in furnace on a hemispherical surface.

The measured flux pattern was deemed acceptable for the planned seal tests because the absolute dome operating temperature level, rather than details of the flux distributions, was the driving experimental variable. The flux distribution on the dome could have been made more uniform, if desired, by inverting the top furnace element toward the dome. This would improve the view factor between the radiating furnace element and the dome area near the dome equator, thus smoothing the flux distribution. However, for the present test program this was not deemed necessary.

6.4 Seal Leakage Measurements

Leakage tests were performed on a number of candidate seal configurations with the baseline seal configuration consisting of a hemispherical dome sitting freely on a clamped insulating ring with a clean copper gasket for the secondary seal. A schematic view of the high-temperature seal test setup is shown in Fig. 46 and a view of a hemispherical dome seal unit mounted in the furnace, before insulating materials are placed in the space above the dome, is offered in Fig. 47. The clamping system for the insulating ring was designed to have translational freedom in the vertical direction in order to avoid any buildup of temperature stresses related to differential thermal expansion between the ceramic and metal support units. Vertical freedom was achieved by placing conical-shaped washers under each clamping bolt. Forces generated by the clamping bolt and ring system seated the insulating ring down against the copper gasket or metal O-ring secondary seal. The conical washers maintained constant seating force during the heating cycle. The pressure forces acting on the dome during the leakage tests then provided additional seating forces on the secondary seal.

C74-717

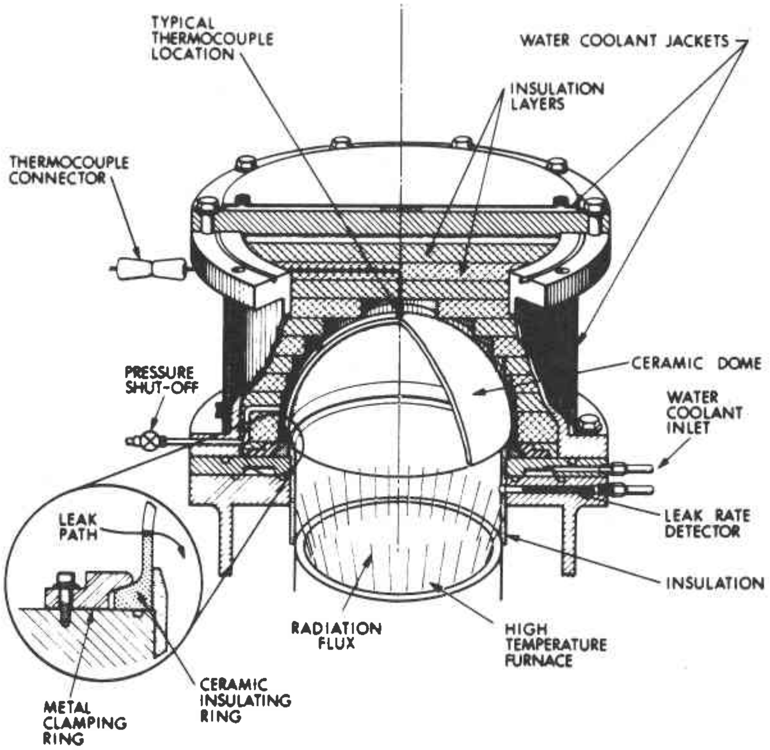

Figure 46. High-temperature seal test setup.

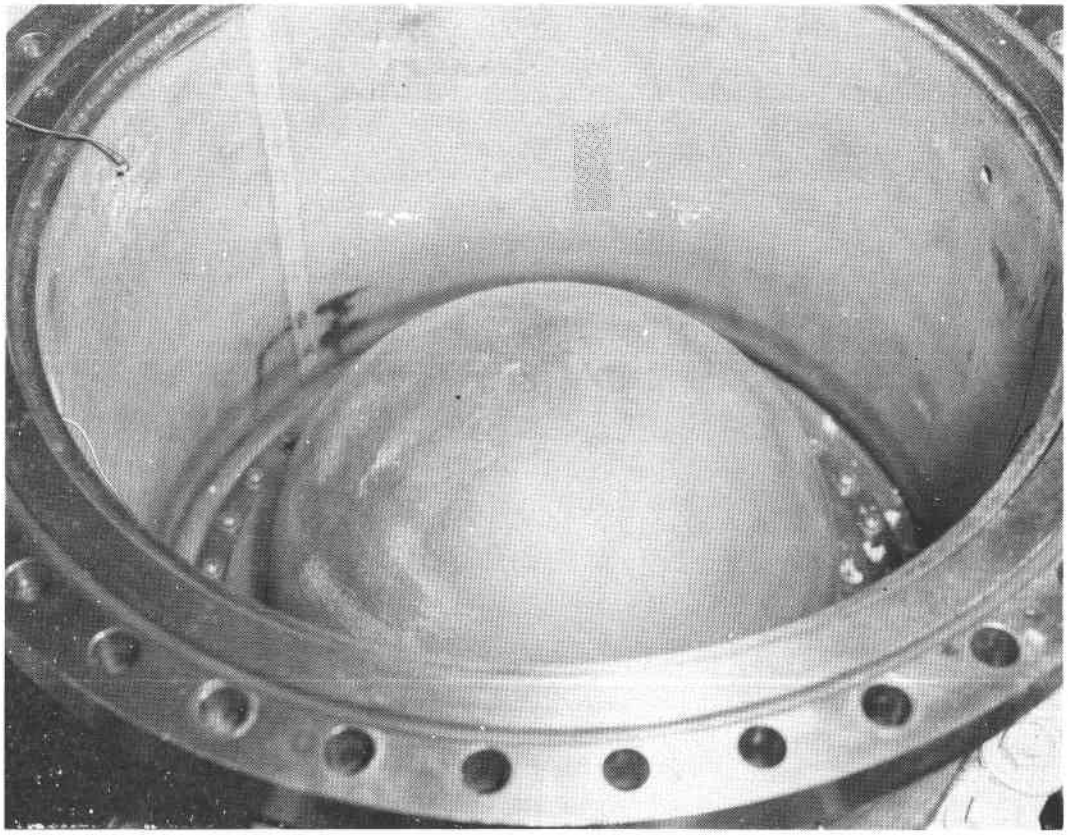

Figure 47. Hemispherical dome seal unit installed in test fixture.

The same test gas was used in both the upper dome seal test unit and in the radiant furnace enclosure and gas leakage through the dome seal system into the furnace space was measured by flowmeters connected to the furnace space. Leakage gas exiting from the furnace was water-cooled to room temperature before passing through the flowmeter measurement unit. The flowmeter equipment consisted of three standard float-type gas flowmeters, covering the measurement range of 0 to 0.18 SCFH, 0 to 2.0 SCFH and 4 to 190 SCFH, and a highly accurate Matheson mass flowmeter for the leak range from 0.004 to 0.2 SCFM.

6.4.1 Baseline Seal

Experimental seal leakage rates for a one-foot-diameter baseline ceramic dome seal (Fig. 48) are illustrated in Fig. 49. The seal leak rate was found to decrease rapidly with temperature (also observed in the earlier test series using two-inch-diameter ceramic hardware) and essentially zero leak rate ($< .004$ SCFH) was measured for seal temperatures above 1000°F. The rapid decrease in leakage rate with increasing temperature is due to the increase in viscosity of gases with increasing temperature and is predicted by the leakage formula, Section 4.1. The surface finishes on the dome and ring were 10 and 6 μ inches, respectively, and were prepared by a local ceramic grinding house using standard diamond-grinding techniques. Diamond-ground surfaces were more than adequate for the tests and smoother lapped surfaces were not needed. Constant leak rate levels as a fraction of the 1% leakage goal are superimposed on Fig. 49 and a comparison of the experimental leak rate data with these values shows that the baseline seal leak rate at temperature 500°F is substantially below the 1% goal. For temperatures above 1000°F, the leak rate was less than 1/1000 of the 1% goal.

6.4.2 Baseline Seal with Sealant on the Copper Gasket

As part of the test program, methods were explored to further reduce the component of leakage through the secondary seal, even though the leak rate goal had been bettered by a sizable amount in the baseline seal configuration. These efforts were fostered by a desire to determine the real potential of the contact seal approach and by the desire to isolate the leak rate contribution through the primary seal by eliminating all other potential leak paths. A commercially available, high-temperature antiseize lubricating compound, consisting of finely divided nickel particles in a hydorcarbon carrier, with an advertised maximum-use temperature of 1425°C (2600°F), was applied to the copper gasket to reduce leakage through that path. Leak tests of this seal configuration showed substantially reduced leakage rates. For example, room-temperature leak rate data for this configuration (see Fig. 50) shows that addition of the sealant to the copper gasket reduced the overall

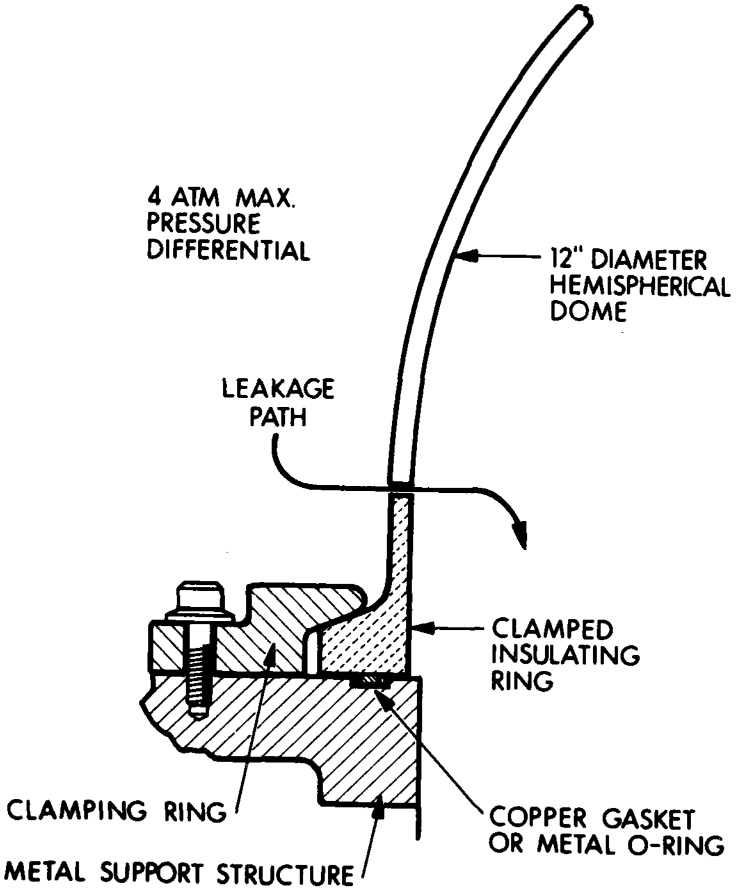

Figure 48. Clamped-ring leak test configuration 12-inch-diameter domes.

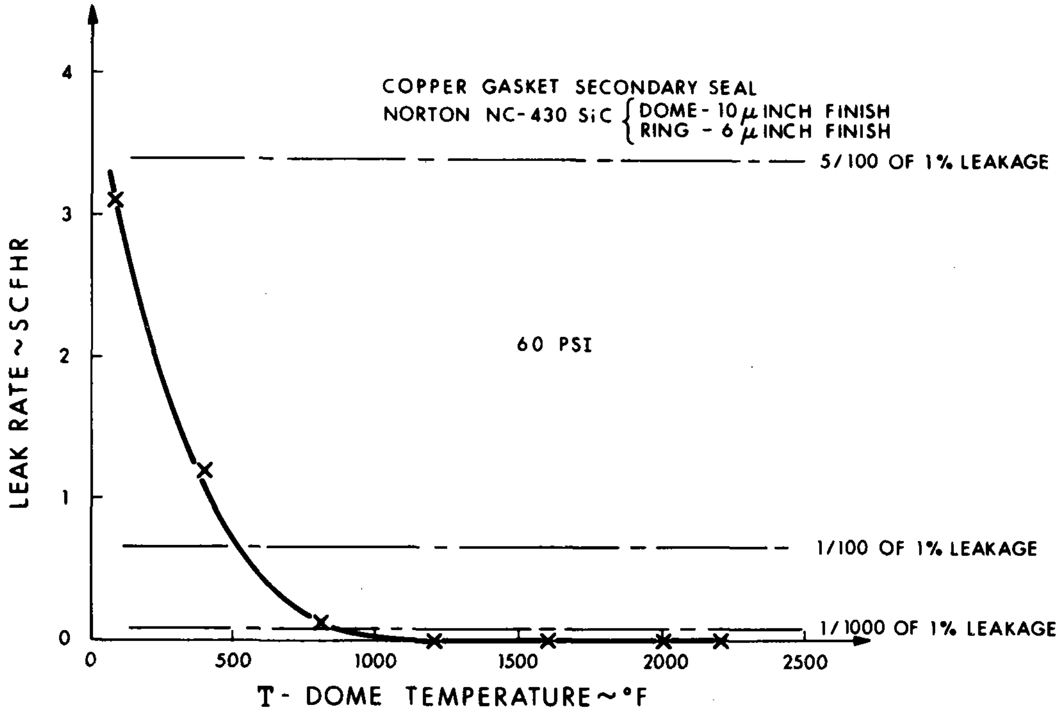

Figure 49. Seal leak rates versus temperature--12-inch-diameter hemispherical dome on clamped ring.

leak rate to 0.016 SCFH at 60 PSI pressure differential in comparison to the 3.1 SCFH leak rate experienced by the clean gasket test unit. The leak rate of 0.016 SCFH measured at room temperature corresponds to a 2/10000 fraction of the 1% leakage goal. A separate test series in which the ceramic dome was replaced by a flat metal plate supported on a gasket was carried out and showed zero leakage at room temperature and at temperatures to 500°F, the maximum operating temperature of the gasket material. It can be concluded from the supplementary tests that the addition of sealant eliminated all leaks through the secondary seal and that the leakage values shown in Fig. 50 may be attributed solely to the contact seal between the ceramic parts. A reduction of the leakage with temperature was also measured as expected for this seal configuration. At temperatures above 500°F, the leakage had decreased below the minimum mass flowmeter measurement capability of 0.004 SCFH, corresponding to 1/60000 of the 1% goal, and measurements were suspended.

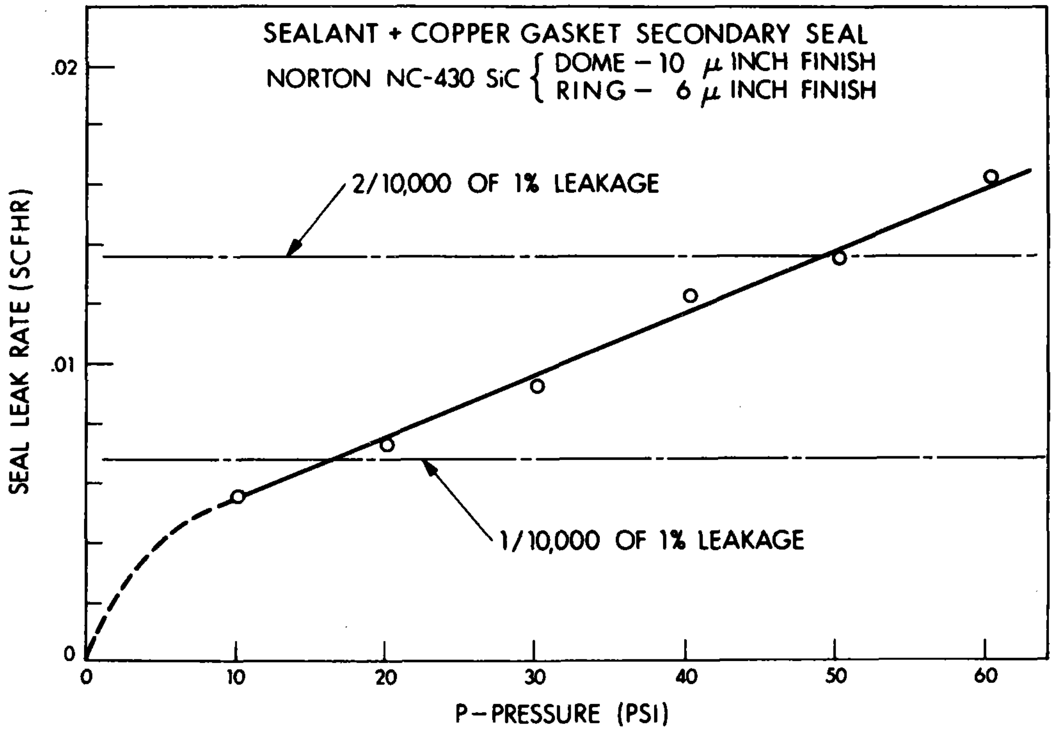

Figure 50. Seal leak rate--12-inch-diameter hemispherical dome on clamped ring--room temperature with sealant.

6.4.3 Baseline Seal with Unclamped Insulating Ring

The exceptional performance of the baseline mechanical contact seal, as exemplified by its low leakage rate in comparison to the 1% leakage goal, raised the possibility that the seal design approach could be simplified while maintaining the leakage at or below the design goal. One approach that was investigated in the test series was the possible elimination of the metal clamping ring and bolt system.

Tests were run on the baseline seal configuration with an unclamped insulating ring (Fig. 51) to determine the leakage rate as a function of temperature and pressure. Leakage data at 2000°F and 2200°F are shown in Fig. 52 for pressures to 60 PSI (4 atmospheres). At 2000°F, the seal leak rate is 1/10th of the goal while at 2200°F it is 1/100th of that goal. The variation of the leakage with temperature, for temperatures between room temperature and 2200°F, was also measured and is shown in Fig. 53. These data illustrate that even at room temperature, when the leak is the greatest, the magnitude of the leakage is still less than that 1% leakage goal.

C74-604

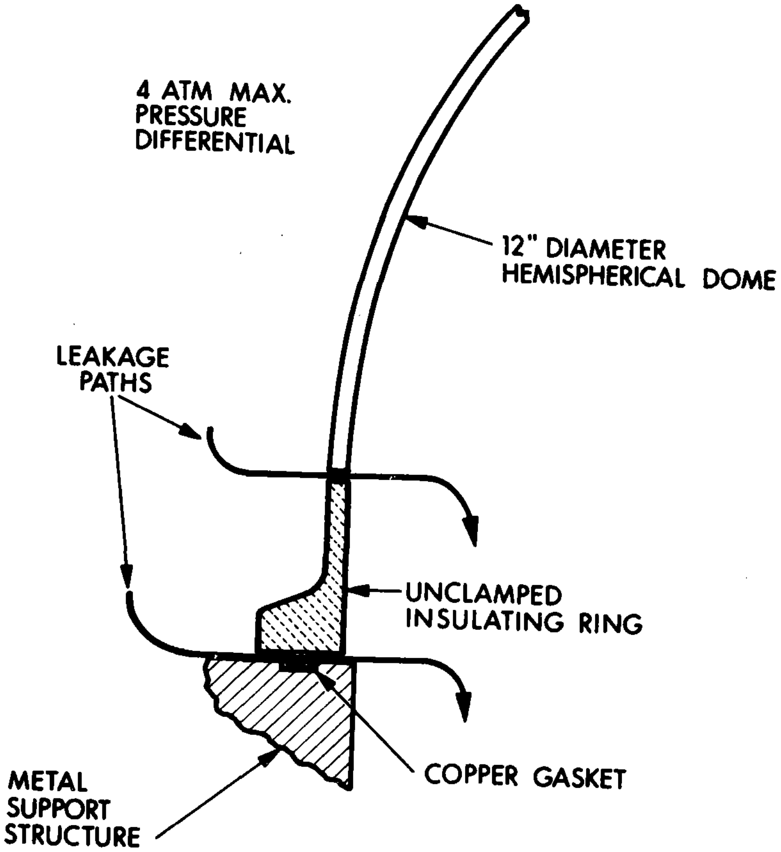

Figure 51. Unclamped ring leak test configuration 12-inch-diameter domes.

C74-597

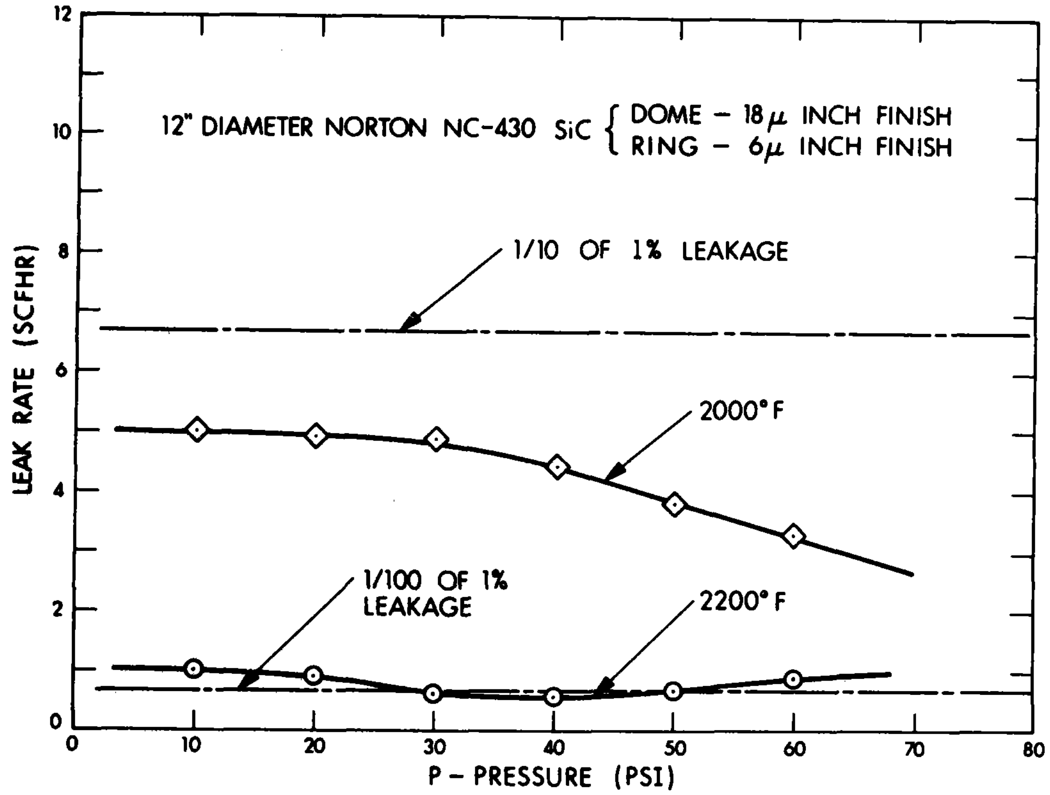

Figure 52. Leakage rate of free hemispherical dome on unclamped ring.

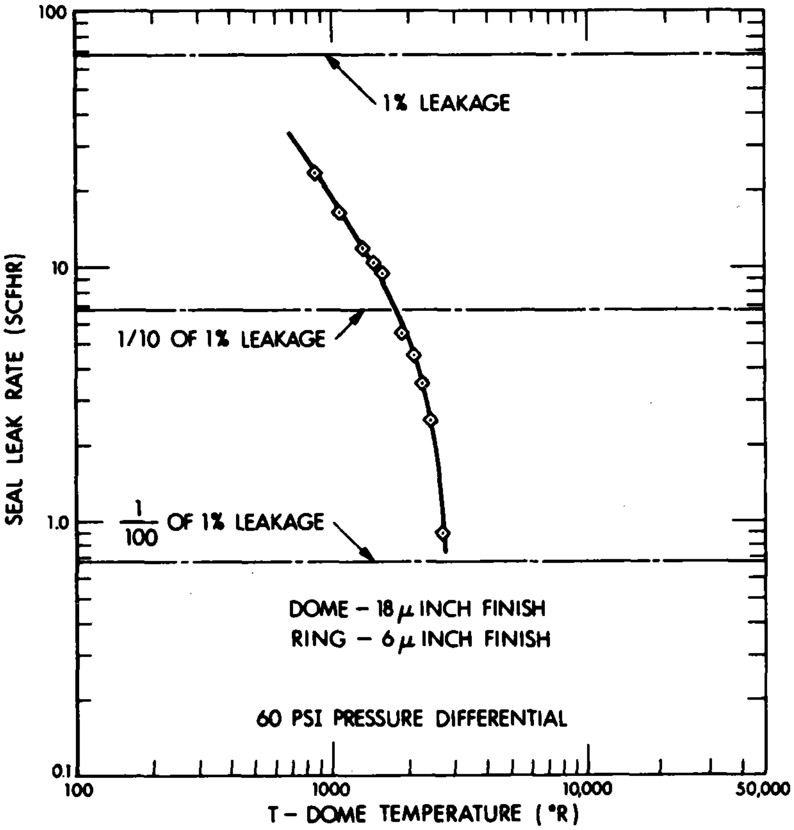

Figure 53. Effect of dome temperature on leak rate--
free 12-inch-diameter hemispherical SiC dome on unclamped SiC ring.

It should be noted that the ceramic dome and insulating ring finishes for the example data shown in Fig. 53 were 18 μ-inches and 6 μ-inches, respectively (12 μ-inch average finish), and that the leak rate could be improved substantially by utilizing a smoother surface finish on the ceramic dome part (a 10 μ-inch finish being readily obtainable with diamond grinding). The leak rate is known to vary as the average roughness to the Nth power, where $N = 1.6$. Thus a change in the average surface roughness, from the 12 μ-inch average for the data in Fig. 53 to an 8 μ-inch average finish consistent with the data of Figs. 49 and 50, would decrease the unclamped ring leak data shown in Fig. 53 by a factor of 1.9.

6.4.4 Comparison of Seal Leak Data

The leak data measured on the baseline mechanical contact seal, baseline seal with gasket sealant, and baseline seal with unclamped insulating ring are compared with each other and to fractions of the leak leakage goal in Fig. 54. The baseline seal with sealant has the lowest leak rate, the baseline seal the next highest leakage and, finally, the baseline seal with unclamped ring has the highest rate. However, all three seal configurations tested have leak rates at all temperatures which are below the 1% leakage goal. The data in Fig. 54 show that the mechanical contact seal approach is quite flexible in that leakage rates may be varied over at least four orders of magnitude by making controlled changes in the overall design approach used for the seal.

C74-766

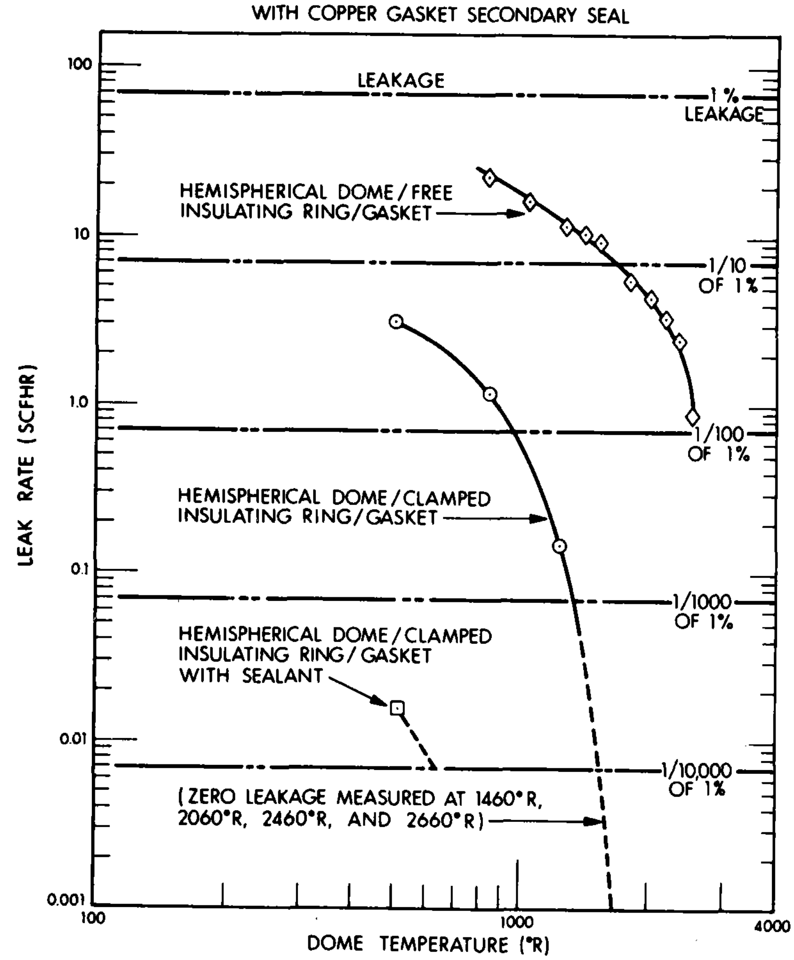

Figure 54. Comparison of the leakage rate of various configurations.

7.0 CONCLUSIONS

A mechanical contact seal has been successfully demonstrated on one-foot-diameter, silicon-carbide, ceramic-dome hardware at pressure differentials to four atmospheres and at temperatures to 2200°F. Experimental measurements of the leakage of such seals have been carried out and the results compared with the goal of developing a seal with a leakage which is 1% (or less) of the heat-transfer airflow impinging on the dome. For all seal configurations tested and for all test temperatures between room temperature and 2200°F, the experiment leak data demonstrated that the contact seal approach easily bettered the 1% leakage goal. In fact, the baseline seal arrangement demonstrated leakage which was but a fraction of the goal: a leak rate less than 1/10000th of the goal at typical seal-operating temperatures. Measured leakage rates on the baseline seal were so low that the metal clamping ring and bolt system could be eliminated from the baseline design with the measured leakage still remaining below the desired level. The mechanical contact seal which has been tested and proven provides a solution to the high-temperature seal question which was thought to be the technologically pacing element in the development of the Solar Heated-Air Ceramic Dome Cavity Receiver (SHARE) concept. A number of receiver configurations appear to be likely candidates for application of the developed dome heat exchanger technology.

8.0 REFERENCES

1. "Solar Heated-Air Gas Turbine Generating Systems," 10th Intersociety Energy Conversion Engineering Conference, University of Delaware, Newark, Delaware, 18-22 August 1975.
2. "Solar Heated-Air Receivers," Solar Energy, Vol. 19, pp. 139-147, Pergamon Press, 1977.
3. "Combined Cycle Solar Central Receiver Hybrid Power Systems Study," Bechtel National Laboratory, Inc., Report No. DOE/ET/21050-1, November 1979.

COO-4878-9

SOLAR RADIATION FLUX DISTRIBUTIONS IN CAVITY RECEIVERS

N.I. Hamilton
P.O. Jarvinen

Massachusetts Institute of Technology
Lincoln Laboratory
Lexington, Massachusetts 02173

28 November 1979

Prepared For

THE U.S. DEPARTMENT OF ENERGY

UNDER CONTRACT NO. ET-78-S-02-4878

Additional copies available from the National Technical Information Service, U.S. Department of Commerce, Springfield, Virginia 22161.

Price: Paper Copy $4.50
Microfiche $3.00

COO-4878-9

SOLAR RADIATION FLUX DISTRIBUTIONS IN CAVITY RECEIVERS

N.I. Hamilton
P.O. Jarvinen

28 November 1979

Massachusetts Institute of Technology
Lincoln Laboratory
Lexington, Massachusetts 02173

ABSTRACT

Analyses of solar radiation flux distribution in cavity receivers for various cavity geometries are summarized. Simple analytical techniques to calculate the incident solar flux distribution inside the cavities are derived for several cavity shapes to provide a quick, but reasonably accurate analysis of temperature profiles along the walls and backs of cavities. Design strategies to couple a dome-capped ceramic receiver to a dish/Brayton or dish/Stirling engine are also discussed.

A steady-state analysis of cavity receivers shows that direct heat-transfer concepts, where heat is drawn off directly to the load, are more efficient than indirect heat-transfer concepts, where heat is withdrawn from a cavity area that does not receive incident solar flux.

CONTENTS

SUMMARY AND CONCLUSIONS

A program is underway to develop a ceramic heated-air receiver for advanced-Brayton central tower and dispersed-dish solar-thermal-electric applications at MIT/Lincoln Laboratory. The ceramic receiver converts solar energy to high-temperature heat and the heated airstream from the receiver drives a gas turbine/generator unit to produce electrical energy. To date, ceramic dome units designed to withstand the pressure and thermal stresses encountered in operation along with a high-temperature seal between the pressurized gas and ceramic dome material – silicon carbide – have been developed and tested.[1]

This report summarizes the analyses performed and solar radiation flux distributions in cavity receivers for various wall shapes and outlines the essential design strategy in coupling a dome-capped ceramic receiver to a dish/Brayton or dish/Stirling engine by a sample design calculation. It is shown that this analytical approach, which minimizes the use of cumbersome numerical techniques, can be used in the analysis of flux distribution in the receiver and heat transfer to a load, and the subsequent design of a parabolic dish/cavity receiver system capable of supplying heat uniformly over a wide temperature range to the load.

Sample analytical techniques for calculating the incident solar distribution inside cavities heated by parabolic concentrators are thus derived for several cavity geometries where individual cavity sides differ in their shapes. It is shown that the required degree of flux uniformity in the cavity can be controlled by selecting the proper cavity dimensions and form. Concave surfaces having an elliptical, part-hemispherical or hemispherical shape on the cavity sides and rear enables flux uniformity in the cavity to be achieved, and hence the desired geometry can be chosen for a specific heat-transfer application.

Form factors within the cavity are calculated for representative receiver configurations and are verified by experimental measurements using the unit-sphere method. These view factors may then be used in a mathematical model developed to provide a more rigorous analysis that simulates the steady state condition in the cavity by including radiation and reflection through the aperture. A receiver configuration for a 65-kW_t regenerative, open-cycle Brayton, dispersed solar system, presented as a sample application of the methodology, is modeled on a digital computer and the results of the final flux distribution presented. In this case, the receiver used a dome-capped cylinder combination in which the length-to-diameter (L/D) ratio of the cavity is selected to achieve uniform flux over the dome and the L/D and aperture combination is selected to provide high-receiver-energy conversion efficiency.

The analysis is then extended to include consideration of two different direct and indirect heat-transfer-receiver configurations for large-scale systems on the order of 100 kW_t or larger. The direct concepts were found to provide more efficient energy conversion than indirect concepts.

Calculations are also presented that predict a relatively uniform incident flux in a 12-inch-diameter dome with ceramic-to-ceramic contact seals in an experimental test fixture designed at MIT/Lincoln Laboratory to confirm the leakage predictions for a high-temperature, pressurized dome seal.

SOLAR RADIATION FLUX DISTRIBUTIONS IN CAVITY RECEIVERS

1. Introduction

Solar cavity receivers are being considered by MIT/Lincoln Laboratory for a solar thermal, heated-air, Brayton power system. In this concept, dome-shaped-ceramic receiver elements heat pressurized gas to 1800°F (1000°C) for use with gas turbine units. Figure 1 shows the method of sealing the dome to the cavity and the impingement heat-transfer technique in a cross-sectional arrangement of a single, shallow dome. Ceramic dome units, designed to withstand the pressure and thermal stresses encountered in operation, along with a high-temperature seal between the pressurized gas and ceramic dome material – silicon carbide – have been developed and tested.[1]

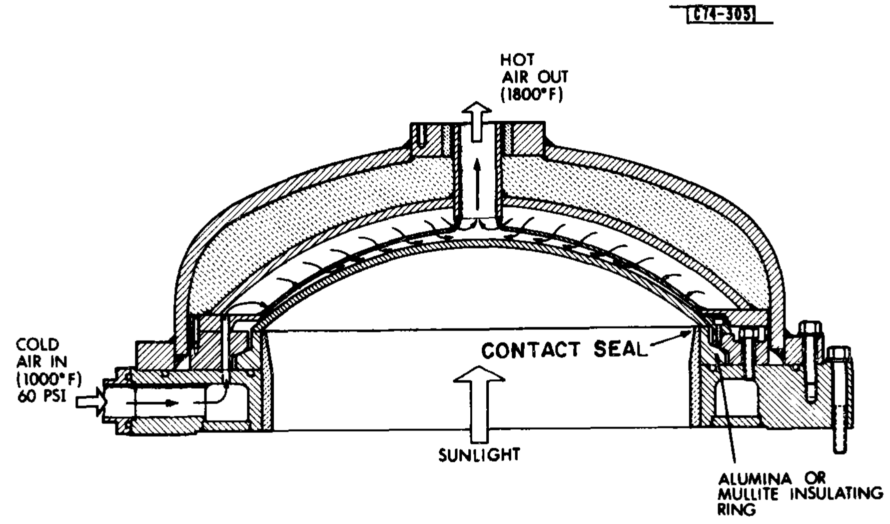

Fig. 1. Ceramic, impingement-cooled shallow dome module.

Figure 2 shows the hemispherical ceramic elements covering the interior walls of a 1-MW_t bench-model-size receiver. Another concept uses a ceramic dome as the rear section of a cylindrical cavity receiver in a dispersed dish/receiver system. The receiver in this instance supplies heat to a free-piston Stirling engine (Fig. 3). The design of the receiver is a pacing item in the development of the approach and requires knowledge of the flux distribution within the receiver. Thus as a first step, tools for the analysis and design of the receiver, and the matching requirements for the cavity receiver/engine combination will be presented.

Existing methods for analyzing flux distributions inside cavities in a parabola-dish/cavity-receiver combination involve Monte Carlo and Ray Vector techniques that are cumbersome and time consuming. Thus simple analytical methods have been developed to describe the incident solar flux distributions in cavity receivers heated by parabolic concentrators for a variety of cavity geometries including elliptical, parabolic, hemispherical and part-hemispherical cavity forms. Mirror imperfections in the 0-10 milliradians range may also be accounted for in the mathematical equations by including a mirror error constant and numerically integrating the resulting equations. The accuracy of the analytical techniques has been shown to be comparable to the numerical approach, and since mirror errors affect only the leading edge of the flux profile, a quick, fairly accurate solution may be arrived at by assuming perfect optics.

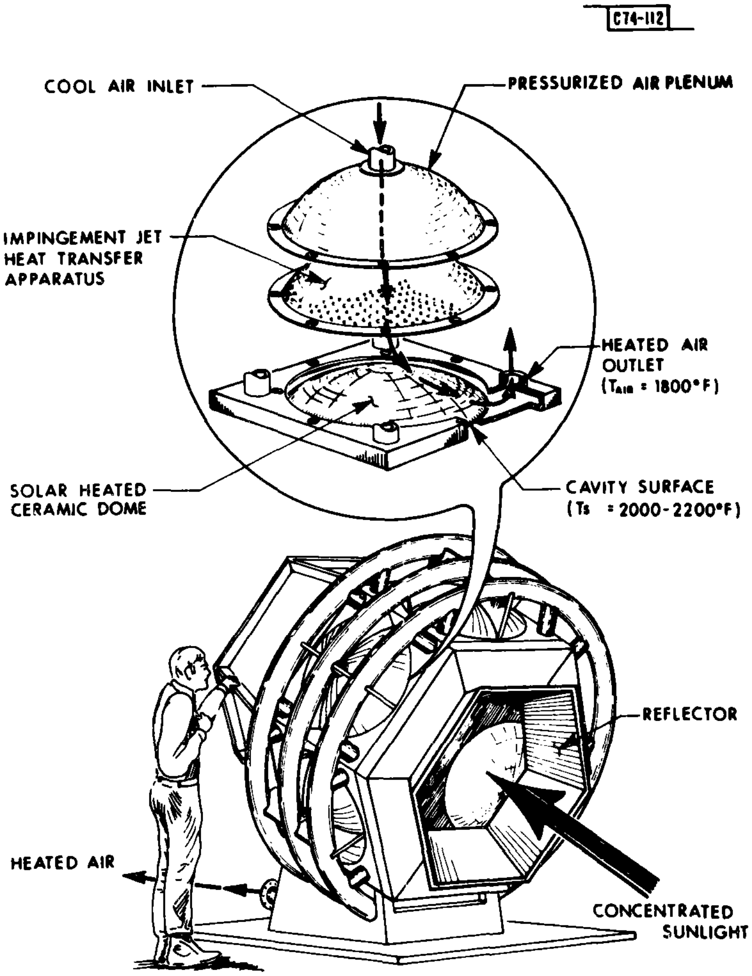

Fig. 2. Conceptual design of a 1-MW$_t$ ceramic dome, heated-air receiver.

The incident flux concentration ratio in the cavity interior is thus first calculated using simple equations developed to describe the cavity shape. A suitable geometry may then be chosen to ensure a relatively uniform flux density along the side and bottoms while retaining as high a cavity efficiency (ratio of the integral resultant cavity flux to the incident collector flux) as possible. The design may then be optimized once the entire set of radiative exchange and reradiation processes have been taken into account.

2. Cavity Configurations

The cylindrical cavity is one of the most commonly considered cavity receiver configurations. Variations in cavity geometry are also possible, for example, with cavity shapes ranging from spherical to cylinder/dome combinations suitable for use in the solar-thermal heated-air Brayton power concept. In such cases, incident flux may fall on the wall or back or be spread over the interior of the cavity, depending on the receiver design and desired flux distribution.

3. Incident Flux on the Back Plane of a Cylindrical Cavity

Figure 4 shows the incident solar flux focussed from a parabolic concentrator to the back plane of a cylindrical cavity. The back plane of the cavity may be treated as an off-focal plane.

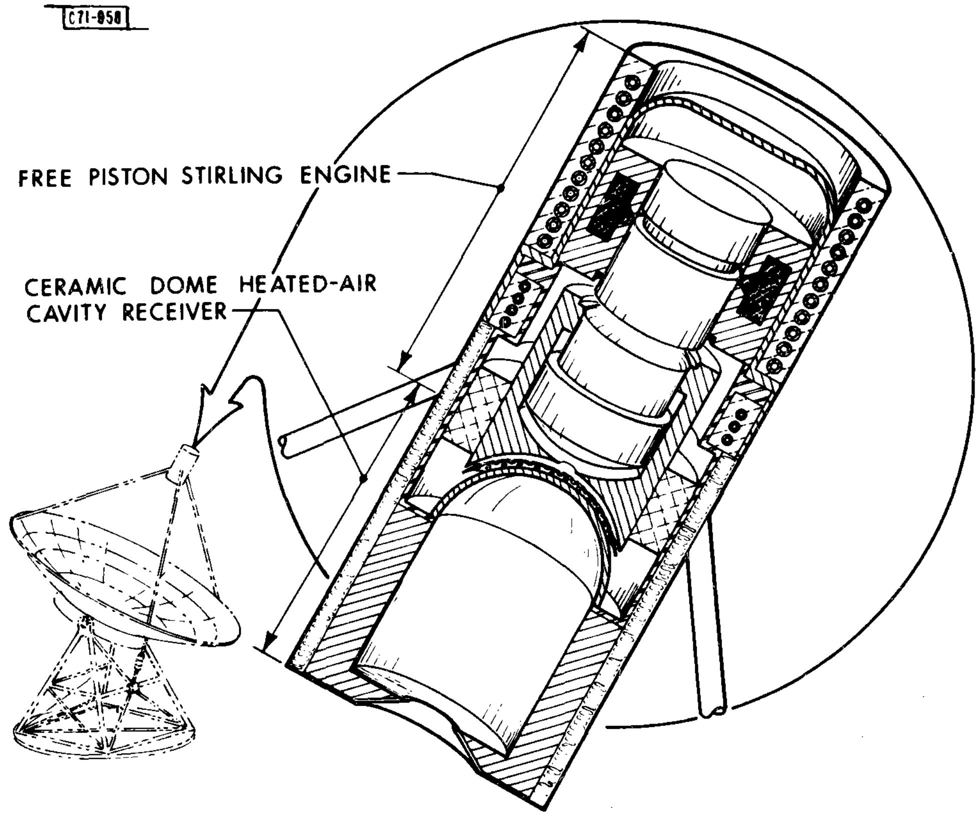

Fig. 3. Ceramic dome receiver for dispersed-dish applications.

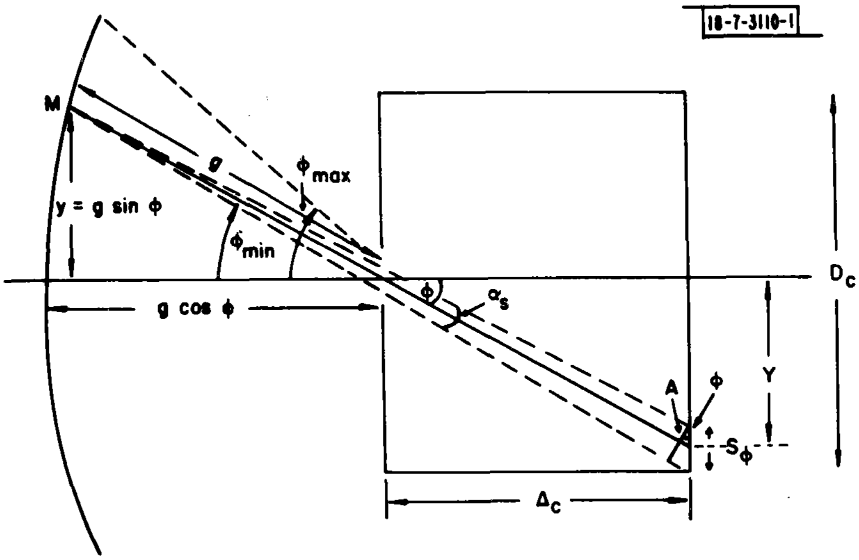

Fig. 4. Incident flux on back plane of cylindrical cavity.

It is assumed that the aperture is at least as large as the width of the solar beam entering the cavity. A ring on the parabola at point M projects an image on the cavity back of thickness, S_ϕ.

Now,

$$A = S_\phi \cos\phi$$

where $A = (g + \Delta_c/\cos\phi)\alpha_s$. So,

$$S_\phi = (g + \frac{\Delta_c}{\cos\phi}) \frac{\alpha_s}{\cos\phi} \quad . \tag{1}$$

C00-4878-9-8

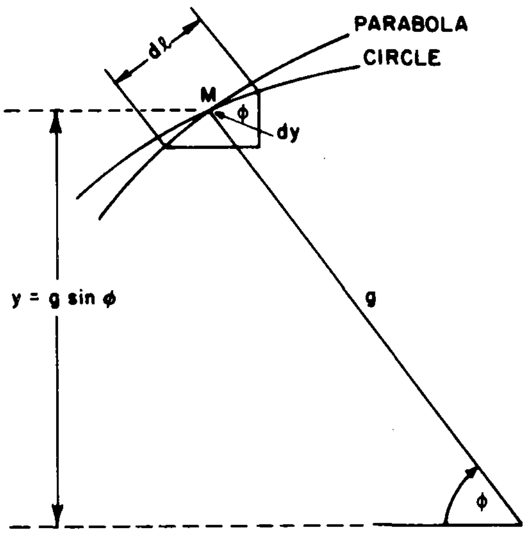

Fig. 5. Thickness of image at M on parabolic dish.

The thickness of the annulus at M, $d\ell$, is shown in Fig. 5. As $y = g \sin\phi$, $dy = g \cos\phi d\phi$, and area of the annulus at M is $2\pi y d\ell$ where $dy \approx d\ell \cos\phi$ assuming $d\ell = g d\phi$.

So $d\ell = dy/\cos\phi$ and the area of the ring becomes:

$$\begin{aligned} & 2\pi g \sin\phi(dy/\cos\phi) \\ = \; & 2\pi g \sin\phi(\frac{g \cos\phi d\phi}{\cos\phi}) \\ = \; & 2\pi g^2 \sin\phi d\phi \quad . \end{aligned}$$

Thus if all the points at the same radial distance as M are considered, the average concentration ratio, C_y, on the back plane is at a radial distance, Y:

$$d(C_y) = \eta_M \frac{2\pi g \sin\phi g d\phi}{2\pi Y S_\phi} \tag{2}$$

where

$$Y = \Delta_c \tan\phi \quad .$$

Therefore,

$$d(C_y) = \eta_M \frac{g^2 \sin \phi d\phi}{\Delta_c \tan \phi S_\phi} \quad .$$

The limits of integration of the ring thickness, ϕ_{max} and ϕ_{min}, are given by:

$$Y = \Delta_c \tan \phi \pm \frac{\alpha_s}{2} \tag{3}$$

$$C_y = \eta_M \int_{\phi_{min}}^{\phi_{max}} g^2 \left(\frac{\sin \phi}{\Delta_c \tan \phi S_\phi} \right) d\phi \quad . \tag{4}$$

If:

$$\frac{||\phi_{max} - \phi_{min}||}{\phi} << 1$$

then

$$C_y = \eta_M \frac{g^2 \sin \phi (\Delta \phi)}{\Delta_c \tan \phi S_\phi} \quad . \tag{5}$$

Now

$$(\Delta \phi)/S_\phi \approx d\phi/dY$$

and since $Y = \Delta_c \tan \phi$

$$\frac{d\phi}{dY} = \frac{\cos^2 \phi}{\Delta_c} \quad .$$

Substituting in Eq. (5):

$$\begin{aligned} C_y &= \eta_M g^2 \sin \phi \frac{\cos^2 \phi}{\Delta_c} \frac{1}{\Delta_c \tan \phi} \\ &= 4\eta_M \left[\frac{F_p}{\Delta_c (\cos \phi + 1)} \right]^2 \cos^3 \phi \end{aligned}$$

where g = distance between a point on the mirror and the focus = $2F_p/(1 + \cos \phi)$. Therefore,

$$C_y = 4\eta_M \left(\frac{F_p}{\Delta_c} \right)^2 \frac{\cos^3 \phi}{(1 + \cos \phi)^2} \quad . \tag{6}$$

This result agrees with the stated equation contained in Ref. 2.

To account for mirror imperfections, Eq. (4) may be integrated numerically and the substitution, $\alpha = \alpha_s + 4\gamma$ may be made, where γ is the surface slope error of the mirror in milliradians.

Equations will now be developed for the flux on the back plane of cavity geometries other than the flat-ended cylindrical cavity.

4. Incident Flux on a Hemispherical Dome-Shaped Back Plane

The back plane of the cylinder (with diameter D_c) is replaced by a dome with the same diameter as shown in Fig. 6. Using the same approach as just described, the equation for the concentration ratio follows:

$$A = \sin\phi S_\phi$$

and

$$A = \left(g + \Delta \cos\phi + \sqrt{R_c^2 - \Delta^2 \sin^2\phi}\right) \alpha_s \quad .$$

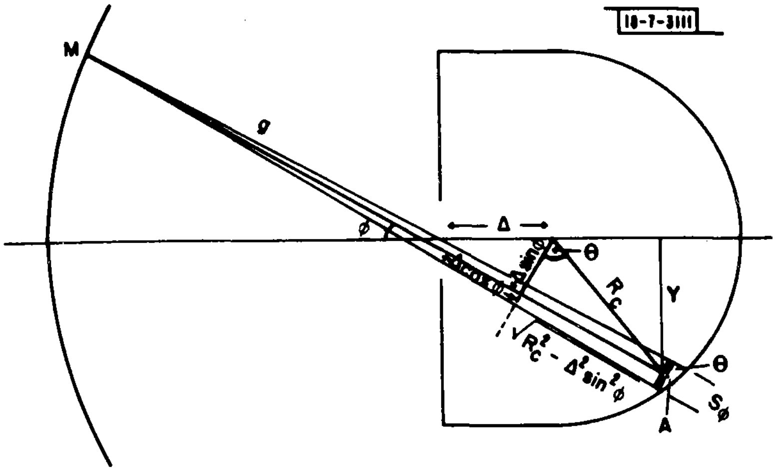

Fig. 6. Incident flux on cavity back of a hemispherically backed cavity.

Therefore

$$S_\phi = \left(\frac{g + \Delta \cos\phi + \sqrt{R_c^2 - \Delta^2 \sin^2\phi}}{\sin\phi}\right) \quad . \tag{7}$$

Thus the concentration ratio on the dome is given by:

$$dC_\phi = \eta_M (2\pi g \sin\phi g d\phi / 2\pi t \sin\phi S_\phi)$$

where

$$t = \Delta \cos\phi + \sqrt{R_c^2 - \Delta^2 \sin^2\phi} \quad .$$

Simplifying,

$$dC_\phi = \eta_M g^2 \left(\frac{d\phi}{tS_\phi}\right)$$

$$= \eta_M 4 \frac{F_p^2}{(1 + \cos\phi)^2} \frac{1}{t} \frac{d\phi}{S_\phi} \quad .$$

Now since $A \approx td\phi$, therefore

$$S_\phi \sin\phi = td\phi$$

and therefore

$$\frac{d\phi}{S_\phi} = \frac{\sin\phi}{(\Delta \cos\phi + \sqrt{R_c^2 - \Delta^2 \sin^2\phi})} \quad .$$

Therefore

$$C_\phi = \eta_M \int_{\phi_{min}}^{\phi_{max}} \frac{g^2 d\phi}{\left(\Delta \cos \phi + \sqrt{R_c^2 - \Delta^2 \sin^2 \phi}\right) S_\phi} \tag{8}$$

where ϕ_{max} and ϕ_{min} are given by:

$$y = \{\Delta \cos (\phi \pm \frac{\alpha}{2}) + \sqrt{R_c^2 - \Delta^2 \sin^2 (\phi \pm \frac{\alpha}{2})}\} \sin (\phi \pm \frac{\alpha}{2}) \tag{9}$$

and

$$\alpha = \alpha_s + 4\gamma \quad .$$

Assuming perfect optics and that $(||\phi_{max} - \phi_{min}||/\phi) << 1$, Eq. (8) can be simplified (using the same assumption as in Section 3) to:

$$C_\phi = 4\eta_M \frac{F_p^2}{(1 + \cos \phi)^2} \frac{\sqrt{R_c^2 - \Delta^2 \sin^2 \phi}}{R_c \left(\Delta \cos \phi + \sqrt{R_c^2 - \Delta^2 \sin^2 \phi}\right)^2} \quad . \tag{10}$$

5. Incident Flux on the Cavity Back that has an Elliptical or Spherically Shaped Segment

If the back of the cavity is elliptical the formula given in Eq. (10) is applicable, but R_c, the cavity radius, is replaced by the equation for the ellipse:

$$\frac{x^2}{a^2} + \frac{y^2}{e^2} = 1 \tag{11}$$

where a, the semi-minor axis, is equal to the cavity radius. The value of e, the semi-major axis (see Fig. 6) may be selected, and the values of R_c, which is the cavity radius in Eq. (10), now becomes the distance from the center of curvature of the ellipse corresponding to selected values of ϕ, and may be calculated using Eq. (11).

If the back of the cavity is a shallow dome (part hemisphere), each value of R_c corresponding to ϕ can be calculated knowing the radius of curvature of the rear segment and the cavity radius, and then substituted into Eq. (10). Similarly, the incident flux on the back of a cavity that has a hyperbolic or parabolic surface may be calculated using the equations for the hyperbola and parabola, respectively.

6. Incident Flux on the Cavity Walls (Other Than the Back Plane)

The equation for the incident flux on the cavity walls is derived in Ref. 2, but a more complete derivation is included here for clarity (Fig. 7).

A point at M projects an image on the walls of the cylindrical cavity of thickness, S_ϕ, where

$$A = S_\phi \sin \phi$$

and

$$A = \left(g + \frac{D_c}{2 \sin \phi}\right) \alpha_s \quad .$$

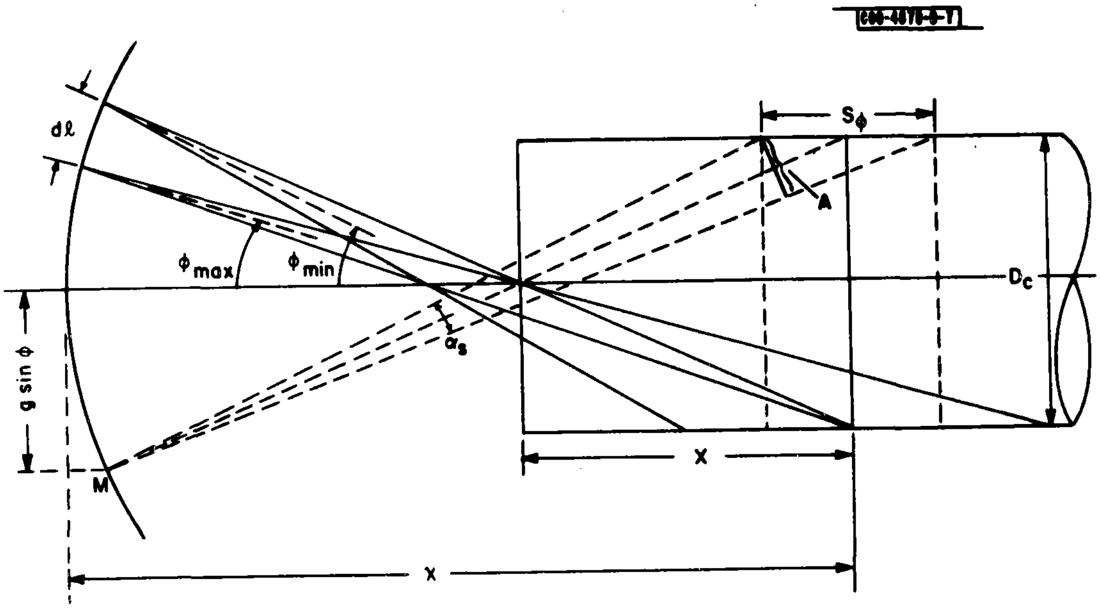

Fig. 7. Incident flux on walls of a cylindrical cavity.

Therefore

$$S_\phi = \left(g + \frac{D_c}{2\sin\phi}\right)\frac{\alpha_s}{\sin\phi} \quad .$$

Considering all other points on the mirror at the same radial distance at M the average concentration ratio inside the cavity is at a distance X,

$$dC_x = \eta_M(2\pi y d\ell/\pi D_c S_\phi) \tag{12}$$

Now since $y = g \sin\phi$ and assuming that $d\ell = g\,d\phi$,

$$y\,d\ell = g^2 \sin\phi\, d\phi$$

and

$$dC_x = 2\eta_N g^2 \sin\phi \frac{d\phi}{D_c S_\phi}$$

The limits of integration, ϕ_{max} and ϕ_{min}, are obtained from:

$$\chi = (g\sin\phi + R_c)/\tan(\phi \pm \frac{s}{2}) - g\cos\phi \tag{13}$$

where

$$\tan\phi = g\sin\phi + R_c/X \quad .$$

Therefore:

$$C_x = 2\eta_M \int_{\phi_{min}}^{\phi_{max}} \left(g^2 \frac{\sin\phi}{D_c S_\phi}\right) d\phi \quad . \tag{14}$$

Assuming

$$||\phi_{max} - \phi_{min}||/\phi << 1$$

$$C_x = 2\eta_M g^2 \sin\phi \frac{d\phi}{D_c S_\phi} \quad . \tag{15}$$

Now

$$\frac{d\phi}{S_\phi} \approx \frac{d\phi}{dx}$$

and since

$$X = R_c/\tan\phi$$

$$dx = -R_c d(\cot\phi)$$

where a positive change in x corresponds to a negative change in angle ϕ. So,

$$\frac{dx}{d\phi} = \frac{R_c}{\sin^2\phi}$$

and

$$\frac{d\phi}{S_\phi} \approx \frac{2\sin^2\phi}{D_c} \quad .$$

Substituting in Eq. (15):

$$C_x = 2\eta_M g^2 \frac{\sin\phi}{D_c} \frac{2\sin^2\phi}{D_c}$$

$$= 16\eta_M \left(\frac{F_p}{D_c}\right)^2 \frac{\sin^3\phi}{(1+\cos\phi)^2} \quad . \tag{16}$$

The minimum length into the cavity before any radiation is incident and the minimum distance into the cavity for Eq. (16) to be valid is given by:

$$X_{min}, X_{max} = \frac{D_c}{2} \tan\phi_{min} \pm (S_{\phi_{min}}/2) \quad . \tag{17}$$

Mirror errors can be accounted for in Eqs. (13) and (14) by substituting $\alpha = \alpha_s + 4\gamma$.

7. Incident Flux on Other Wall Shapes (Other Than the Back Plane)

Figure 8 shows a cylindrical cavity with spherical walls where the section NN' in Fig. 8(a) has been rotated clockwise by 90 degrees and turned on its side, NO'. The equation for the concentration ratio follows:

$$A = S_\phi \sin\Theta$$

where

$$B = \Delta \cot\phi$$

$$C = (R - B)\cos\phi$$

$$D = (R - B)\sin\phi$$

and

$$A \approx \left(g + \frac{\Delta}{\sin\phi} + C + \sqrt{R_c^2 - D^2}\right) d\phi$$

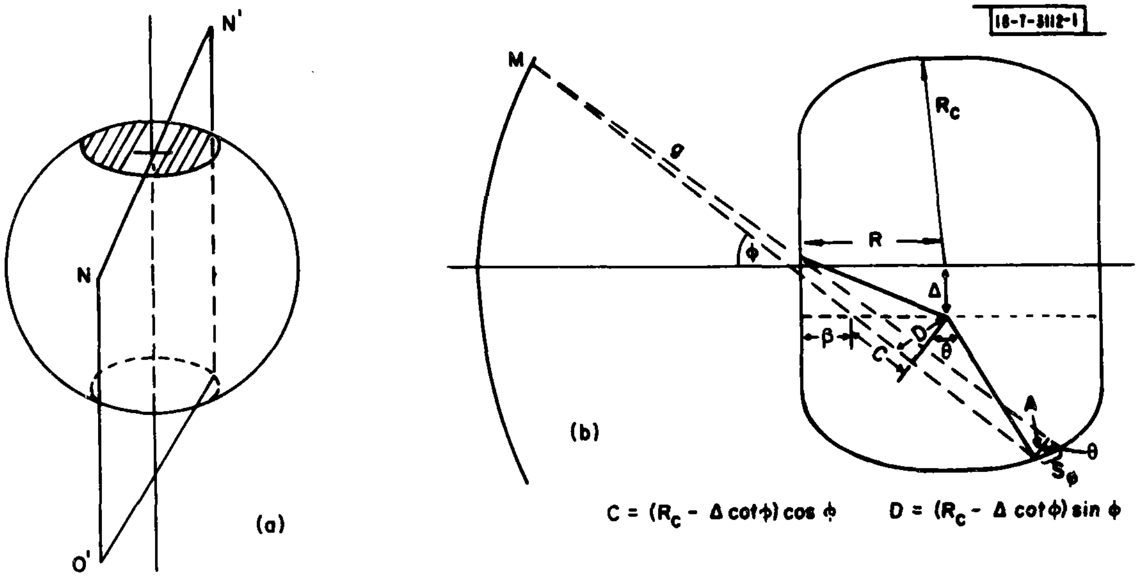

Fig. 8. Incident flux on spherical walled cavity.

Therefore:

$$S_\phi = \frac{(g + \frac{\Delta}{\sin\phi} + (R - B)\cos\phi + \sqrt{R_c^2 - D^2})\,\alpha_s}{\sin\Theta} \quad .$$

So,

$$dC_x = \eta_M 2\pi y\,dy/2\pi(C + \sqrt{R_c^2 - D^2})\sin\phi S_\phi$$

$$= \eta_M g^2 \frac{d\phi}{(C + \sqrt{R_c^2 - D^2})\,S_\phi} \quad \text{using the approximation illustrated in Fig. 4.}$$

$$= 4\eta_M \frac{F_p^2}{(1 + \cos\phi)^2} \frac{1}{(C + \sqrt{R_c^2 - D^2})} \frac{d\phi}{S_\phi} \quad . \tag{18}$$

Now

$$A = (\frac{\Delta}{\sin\phi} + C + \sqrt{R_c^2 - D^2})\, d\phi$$

so,

$$S_\phi \sin\Theta = (\frac{\Delta}{\sin\phi} + C + \sqrt{R_c^2 - D^2})\, d\phi$$

therefore,

$$\frac{d\phi}{S_\phi} = \frac{\sin\Theta}{(\frac{\Delta}{\sin\phi} + C + \sqrt{R_c^2 - D^2})} \quad .$$

Assuming $||\phi_{max} - \phi_{min}||/\phi << 1$, Eq. (18) can be simplified to:

$$C_\phi = 4\eta_M \frac{F_p^2}{(1 \div \cos\phi)^2} \frac{\sin\Theta}{(\frac{\Delta}{\sin\phi} + C + \sqrt{R_c^2 - D^2})\,(C + \sqrt{R_c^2 - D^2})}$$

$$= 4\eta_M \frac{F_p^2}{(1 + \cos\phi)^2} \frac{\sqrt{R_c^2 - D^2}}{R_c\,(\frac{\Delta}{\sin\phi} + C + \sqrt{R_c^2 - D^2})\,(C + \sqrt{R_c^2 - D^2})}$$

where

$$\sin\Theta = \sqrt{R_c^2 - D^2}\,/R_c$$

that is:

$$C = 4\eta_M \frac{F_p^2}{(1 + \cos\phi)^2}$$

$$\times \frac{\sqrt{R_c^2 - (R - \Delta\cot\phi)^2 \sin^2\phi}}{R_c[\frac{\Delta}{\sin\phi} + (R - \Delta\cot\phi)\cos\phi + \sqrt{R_c^2 - (R - \Delta\cot\phi)^2 \sin^2\phi}][(R - \Delta\cot\phi)\cos\phi + \sqrt{R_c^2 - (R - \Delta\cot\phi)^2 \sin^2\phi}]} \quad .$$

If $\Delta = 0$, the cavity becomes a sphere and, $R_c = R$:

$$C_\phi = 4\eta_M \frac{F_p^2}{(1 + \cos\phi)^2} \frac{1}{R_c^2 \cos\phi} \qquad (20)$$

For wall geometries other than spherical, i.e., part spherical, ellipsoidal, parabolic or hyperbolic the appropriate analytical equation is used to calculate R_c as described for incident flux on the cavity back.

8. Design Strategies and Incident Flux Calculations

8.1 Sizing of the Parabolic Dish

As it is desirable to have a high concentration ratio at the cavity aperture, the sizing of the parabolic dish is important. The average concentration ratio at the cavity aperture is given by:

$$C_{av} = \eta_M(D_p^2/d_{max}^2) \qquad (21)$$

and in the general case,

$$d_{max} = 2F_p\alpha_s\,[f(\phi_{min}) + 4\gamma/\alpha_s]/[(1 + \cos\phi_{min})\cos\phi_{min}]$$

where

$$f(\phi_{min}) = [(\sin\phi_{min} + 2\gamma/\cos\phi_{min})^2 + \cos^2\phi]^{1/2} \quad .$$

Using a value of γ = 2.3 mrad for the surface slope error of the mirror, and β = 0.0097 rad, the ratio F_p/D_p and the average flux concentration ratio, C_{av}, are plotted against ϕ in Fig. 9, where D_p is the diameter of the parabolic dish. As can be seen in Fig. 9, there is a 26-percent drop in F_p/D_p corresponding to a 38-percent drop in C_{av} as ϕ goes from 45 to 60 degrees, respectively. The ratio F_p/D_p determines the beamwidth, and hence the aperture size of the cavity, which basically determine the cavity reradiation losses, is important. Thus lower radiation losses are associated with a larger F_p/D_p. However, as Fig. 9 shows that a per unit change in C_{av} has a greater effect than a per unit change in F_p/D_p on the cavity efficiency, a dish with a 45-degree rim angle will, overall, give a higher cavity efficiency than a 60-degree dish, and the former is preferred. Further, it is shown in Ref. 2 that a 45-degree dish, with a higher mirror surface error than a 60-degree dish, can consistantly achieve a higher C_{av}, and therefore, a higher cavity efficiency than the 60-degree dish. Since the mirror cost increases with surface accuracy, the 45-degree dish will be the more economical of the two. Based on this discussion, a 45-degree dish will be selected for the example calculations.

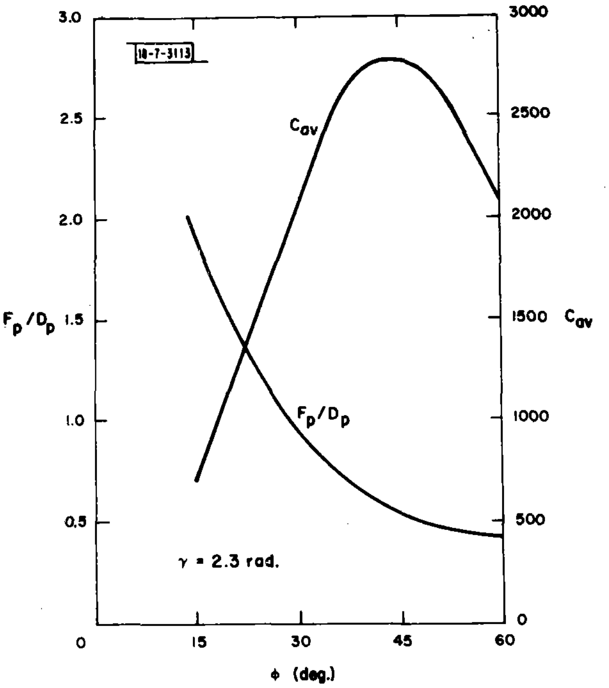

Fig. 9. Variation of concentration ratio with angle of incidence beam.

8.2 Cavity Flux Distribution: Effect of L/D Ratio and Cavity Geometry

Figure 10 shows the effect of altering the cavity length for a hemispherically backed cavity if the flux distribution is spread over the back of the cavity only (i.e., ϕ lies between $\phi = \pm 45$ degrees over the cavity back). The shorter the cavity length, the smaller the relative variation in flux density. Decreasing the cavity radius so that the flux on the back falls between $\phi = \pm 22.5$ degrees and the wall flux lies between ϕ = 22.5 and 45 degrees, causes a greater proportion of the flux to be distributed over the side walls, and vice versa. This does smooth the energy distribution across the dome, but since the majority of flux now falls on the cavity walls (which contribute the major portion of cavity radiation loss; radiation losses from the dome are small) cavity efficiency is reduced. Hence it is desirable to catch most of the incident flux across the dome. Thus, cavity length determines the intensity of the flux and relative variation in intensity over the interior while the cavity radius apportions the flux between the walls and back of the cavity receiver. If peaks on the cavity walls are desirable, for example, so that the walls reradiate to the back of the cavity and increase the flux intensity there, then the cavity radius is decreased until the correct cavity flux level is reached. If less flux variation or lower intensities at the walls or back are required, then the cavity length and cavity geometry should be adjusted. Varying the cavity wall shapes will alter the position and intensity of the peaks on the walls. For example, spherically shaped walls will flatten the flux distribution there and the peaks will be minimized.

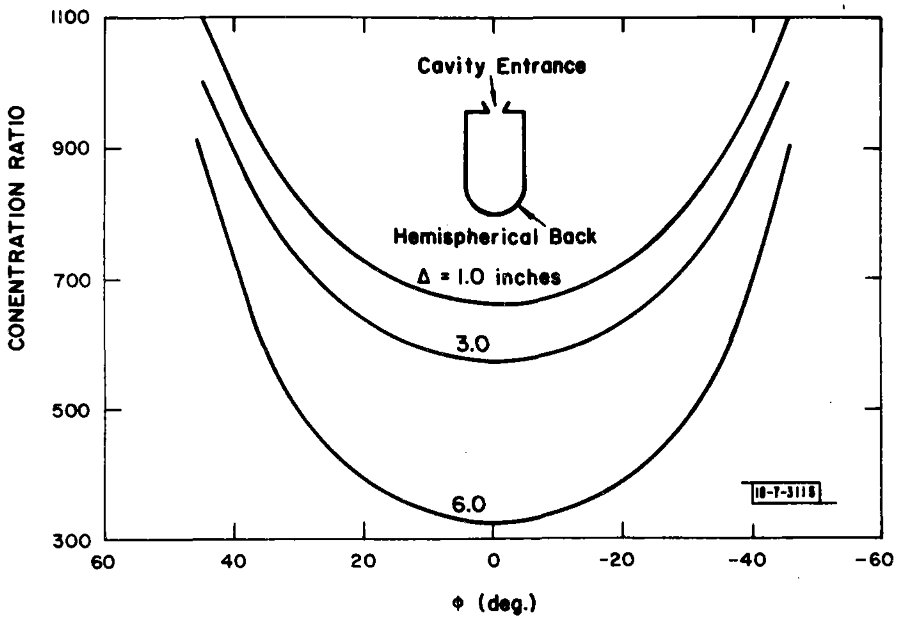

Fig. 10. Variation of concentration ratio with degrees for a hemispherically backed cavity. Cavity length = Δ feet.

Figure 11 shows the effect of the cavity length/diameter (Δ/D) ratio for a slightly larger cavity radius of .6 feet and larger values of Δ/D. Hence it is possible to effectively equalize the flux distribution across a hemispherical dome. The dotted curve ① defines the incident flux angle (ϕ) limits if a 1-percent variation in flux response (C_ϕ) for Δ = 1.2, 1.5 or 1.8 feet is desired. ② defines the 10-percent limit.

In Fig. 12 the flux distributions of three different geometries for the rear cavity section are shown; i.e., for an ellipse, part hemisphere, and hemisphere. The same cavity in Fig. 10 (R_c = .5 feet, Δ = .2 feet) has been chosen for the hemispherical shape. Clearly, the ellipse has the flattest flux distribution, but the curve for the part hemispherical shape is nearly as even and would be a good substitute if the former shape is impractical to manufacture. By comparison with the foregoing shapes, the same size cavity with a flat back plane shows such a large variation in flux distribution at the back that the resulting curve went off the scale in Figs. 10 and 11; i.e., at $\phi = 0$ degree, $C_\phi = 1201$ and at $\phi = 45$ degrees, $C_\phi = 146.4$. It should be noted that each geometry will suit a particular design. For example, although the dome shows more variation in distribution than the ellipse, the peaks on the cavity will tend to fill out the distribution, whereas the ellipsoidal back would register a more uneven distribution once the peaks on the walls are taken into account. Secondly, the response of the hemisphere is similar to the part hemisphere if part of the flux is designed to fall on the back; i.e., $\phi = \pm 25$ degrees corresponds to the dome edge, and the remainder, between $\phi = 25$ and 45 degrees falls on the walls as shown in the sketch of the hemispherical back. Thus the ellipse shape is more suitable (should a flat distribution be desired) for the case where no flux falls on the cavity walls.

9. Radiative View Factors

To simulate the steady state or equilibrium condition, a more detailed examination of the flux distribution within the cavity is necessary and the entire set of radiative exchange and

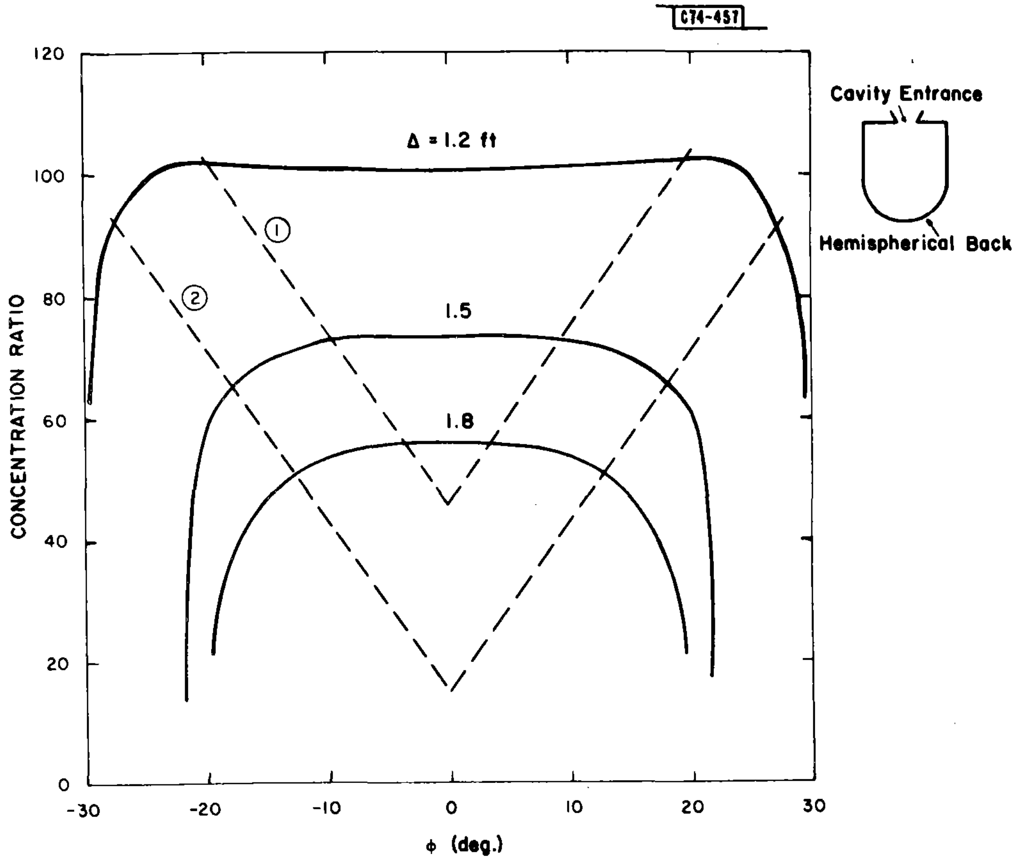

Fig. 11. Variation of concentration ratio with degrees for a hemispherically backed cavity centroid. $R_C = 0.6$ feet.

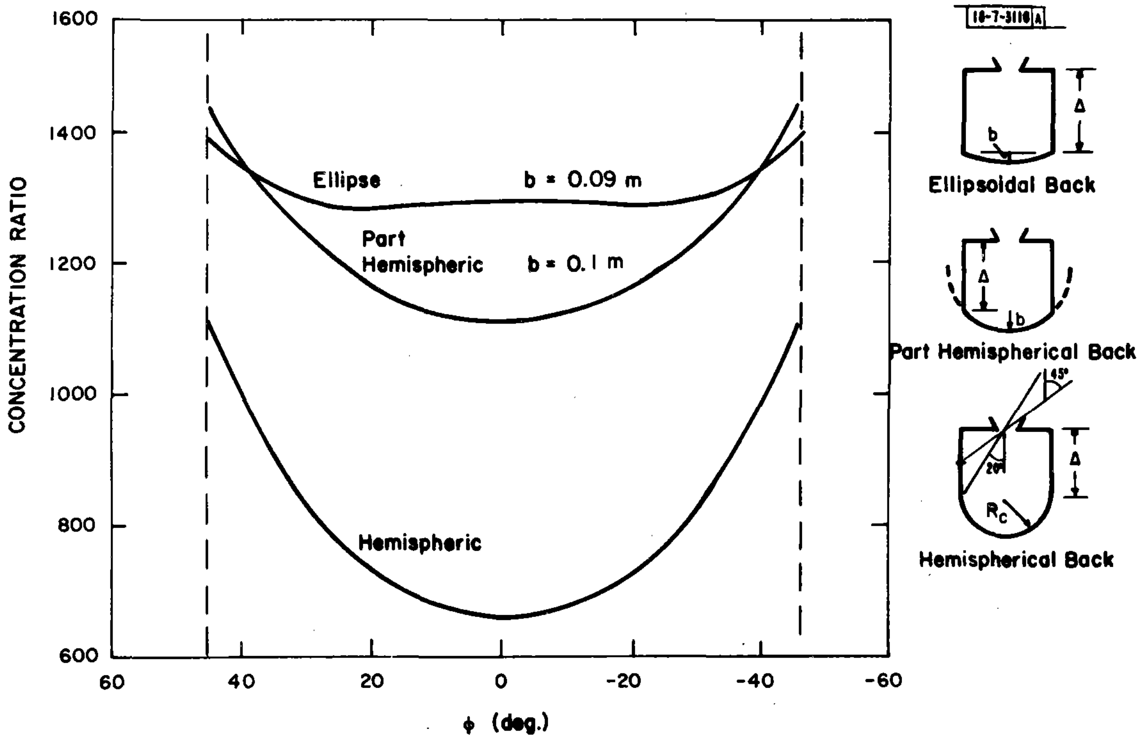

Fig. 12. Variation of concentration ratio with degrees for different cavity geometries. $R_C = 0.5$ feet, $\Delta = 0.2$ feet.

reradiation processes must be included. However, as view factor algebra was used to determine the view factors, a short summary note on the subject is included.

All energy that leaves one surface, designated i, in an enclosure must reach all surfaces in the enclosure that it can "see." The enclosure will be considered to have n surfaces, with any surface that receives energy from i designated j. (Note that in the case of a concave surface, $F_{ii} \neq 0$.) This concept may be expressed formally as:

$$\sum_{j=1}^{n} F_{ij} = 1 \quad . \tag{23}$$

The reciprocity relation is:

$$A_iF_{ij} = A_iF_{ji} \quad . \tag{24}$$

These two expressions comprise the basis for view-factor algebra.

Simplified notation will be used by introducing the symbol, G_{ij}, defined as:

$$G_{ij}A_iF_{ij} \quad . \tag{25}$$

This definition permits Eqs. (23) and (24) to be written as:

$$\sum_{j=1}^{n} G_{ij} = A_i \tag{26}$$

and

$$G_{ij} = G_{ji} \quad . \tag{27}$$

The quantity symbolized by G_{ij} is designated the geometric flux. Relations involving geometric fluxes are provided by energy conservation requirements.

Some special symbolism must now be explained. Between surface 1 and two other surfaces "seen" by 1, designated 2 and 3,

$$G_{1-(2+3)} = G_{1-2} + G_{1-3} \quad . \tag{28}$$

Equation (28) is reduced quite easily as follows:

$$A_1F_{1-(2+3)} = A_1F_{1-2} + A_1F_{1-3}$$

or

$$F_{1-(2+3)} = F_{1-2} + F_{1-3}$$

that is, the energy leaving surface 1 and striking both surfaces 2 and 3 is the total of that striking each separately.

A second expression, involving four surfaces is written as $F_{(1+2)-(3+4)}$, which is interpreted as:

$$G_{(1+2)-(3+4)} = G_{1-(3+4)} + G_{2-(3+4)} \quad . \tag{29}$$

The reciprocity relation for Eq. (29) can be obtained easily; it is:

$$G_{(3+4)-(1+2)} = G_{(3+4)-1} + G_{(3+4)-2} \quad . \tag{30}$$

The third relation to be given here is a decomposition of Eq. (29):

$$G_{(1+2)-(3+4)} = G_{1-3} + G_{1-4} + G_{2-3} + G_{2-4} \tag{31}$$

which is a direct result of Eqs. (28) and (29).

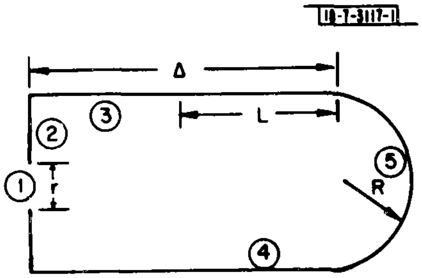

Fig. 13. Surfaces inside the cylinder/dome cavity.

Four basic equations are needed to determine the 56 view factors for the configuration given in Fig. 13. Side 4 is subdivided into four equal sections. (The equations were taken from Ref. 3 and modified to suit the cavity geometry.)

1. The view from side 1 to sides 3 + 4 is:

$$F_{\textcircled{1}-\textcircled{3}+\textcircled{4}} = \frac{1}{2}\left[1 - \frac{R^2 + \Delta^2}{r^2} + \sqrt{\left(1 + \frac{R^2 + \Delta^2}{r^2}\right)^2 - 4\,\frac{R^2}{r^2}}\right]$$

2. View from ② to ③ + ④ is:

$$F_{\textcircled{2}-\textcircled{3}+\textcircled{4}} = \frac{1}{2}\left[1 + \left(\frac{1}{R^2 - r^2}\right)\left(\Delta\sqrt{4R^2 + \Delta^2} - \sqrt{(r^2 + F^2 + \Delta^2)^2 - (2Rr)^2}\right)\right]$$

3. View from ③ to ③ is:

$$F_{\textcircled{3}-\textcircled{3}} = 1 - \frac{1}{2}\left[\sqrt{4 + \frac{(\Delta - L)^2}{-R^2}} - \frac{(\Delta - L)}{R}\right]$$

4. View from ③ to ④ is:

$$F_{\textcircled{3}-\textcircled{4}} = \frac{1}{2R} + \frac{1}{4}\left[\sqrt{4 + \frac{(\Delta - L)^2}{R^2}} + \frac{L}{(\Delta - L)}\sqrt{4 + (\frac{L}{R})^2} - (\frac{\Delta}{\Delta - L})\sqrt{4 + (\frac{\Delta}{R})^2}\right]$$

Using inverse area ratios and view factor algebra all the view factors may be calculated. The view of the dome may be calculated by view factor algebra or by treating the dome as a cylinder of length 0.636R tagged onto the cylinder of length Δ.

Configuration factors between the cavity walls were determined theoretically and verified experimentally. The numbered surfaces in Fig. 13 are represented by subscripts in the symbol for view factor; e.g., F_{12} represents the view factor from surface 1 to surface 2. The equations for the view factors required follow:

$$F_{13} = \frac{1}{2}\left\{1 - \frac{R^2 + (\Delta - L)^2}{r^2} + \sqrt{\left[1 + \frac{R^2 + (\Delta - L)^2}{r^2}\right] - \frac{4R^2}{r^2}}\right\} \tag{32}$$

$$F_{15} = \frac{1}{2} \quad 1 + \frac{R^2 + (\Delta + 0.7071R)^2}{r^2} - \sqrt{\left[1 + \frac{R^2 + (\Delta + 0.7071R)^2}{r^2}\right] - \frac{4R^2}{r^2}}$$

$$= 1 - F_{(3+4)} \tag{33}$$

$$F_{23} = \frac{1}{2} \left[1 + \frac{1}{R^2 - r^2} \quad (\Delta - L) \sqrt{4R^2 + (\Delta - L)^2} - \sqrt{[r^2 + R^2 + (\Delta - L)^2]^2 - (2Rr)^2}\right] \tag{34}$$

$$F_{25} = 1 - \frac{1}{2} \left[1 - \frac{R^2 + \Delta^2}{r^2} + \sqrt{1 + \frac{R^2 + \Delta^{2\ 2}}{r^2} - \frac{4R^2}{r^2}}\right] \tag{35}$$

$$F_{32} = \frac{R^2 - r^2}{2D(\Delta - L)} \left\{1 + \left(\frac{1}{R^2 - r^2}\right) (\Delta - L)^2 - \sqrt{4R^2 + (\Delta - L)^2}\right.$$

$$\left. - \sqrt{[r^2 + R^2 + (\Delta - L)^2]^2 - (2Rr)^2}\right\} \tag{36}$$

$$F_{33} = 1 - \frac{1}{2} \left[\sqrt{4 + \frac{(\Delta - L)^2}{R^2}} - \frac{(\Delta - L)}{R}\right] \tag{37}$$

$$F_{35} = \frac{1}{4} \left[\frac{\Delta + 0.636R}{\Delta - L} \sqrt{4 + (\frac{\Delta + 0.636R}{R})^2} - \frac{\Delta + L + 1.272R}{R}\right.$$

$$\left. - (\frac{L + 0.636R}{\Delta - L}) \sqrt{4 + (\frac{L + 0.636R}{R})^2}\right] \tag{38}$$

$$F_{41} = \frac{r^2}{2DL} \left\{\frac{L^2 - 2L\Delta}{r^2} + \sqrt{\left(1 + \frac{R^2 + \Delta^2}{r^2}\right)^2 - \frac{4R^2}{r^2}} - \sqrt{\left[1 + \frac{R^2 + (\Delta - L)^2}{r^2}\right]^2 - \frac{4R^2}{r^2}}\right\} \tag{39}$$

$$F_{42} = \frac{1}{2} \left\{\frac{1}{R^2 - r^2} [\Delta \sqrt{4R^2 + \Delta^2} - (\Delta - L) \sqrt{4R^2 + (\Delta - L)^2} - \sqrt{(r^2 + R^2 + \Delta^2) - (2Rr)}\right.$$

$$\left. + \sqrt{(r^2 + R^2 + (\Delta - L)^2 - (2Rr)^2}\right\} \tag{40}$$

$$F_{43} = \frac{\Delta - L}{D} + \frac{1}{4} \left[\sqrt{4 + \frac{L^2}{R^2}} + \frac{\Delta - L}{L} \sqrt{4 + \frac{(\Delta - L)^2}{R^2}} - \frac{\Delta}{L} \sqrt{4 + \frac{\Delta^2}{R^2}}\right] \tag{41}$$

$$F_{45} = 0.313 + \frac{1}{4} \left[\sqrt{4 + \frac{L^2}{R^2}} + \frac{1.335R}{L} - \frac{4L}{R} (\frac{L + 0.636R}{R})^2 - \frac{1.86L}{R}\right]$$

$$+ (L + 0.636R) \sqrt{4 + (\frac{L + 0.636R}{R})^2} \left(\frac{L}{R^2} - \frac{1}{4L}\right) \tag{42}$$

$$F_{52} = \frac{(R^2 - r^2)}{2R^2} \left\{ 0.5 + \left[\frac{R^2 + \Delta^2}{r^2} - \frac{1}{2} \sqrt{1 + \frac{R^2 + \Delta^2}{r^2}{}^2 - \frac{4R^2}{r^2}} \right] \right\} \quad (43)$$

$$F_{53} = \frac{(\Delta - L)}{2D} \left[\frac{\Delta + 0.636R}{\Delta - L} \sqrt{4 + \left(\frac{\Delta + 0.636R}{R}\right)^2} - \frac{\Delta + L + 1.272R}{R} \right.$$

$$\left. - \left(\frac{L + 0.636R}{\Delta - L}\right) \sqrt{4 + \left(\frac{L + 0.636R}{R}\right)^2} \right] . \quad (44)$$

The radiation view factors just cited may be verified experimentally using a simple graphical procedure developed by Herman and Nusselt known as the unit-sphere method.[4] Some experimental measurements, $F_{5-(1+2)}$ and $F_{5-(3+4)}$ were determined using the apparatus shown in Fig. 14.

P267-473

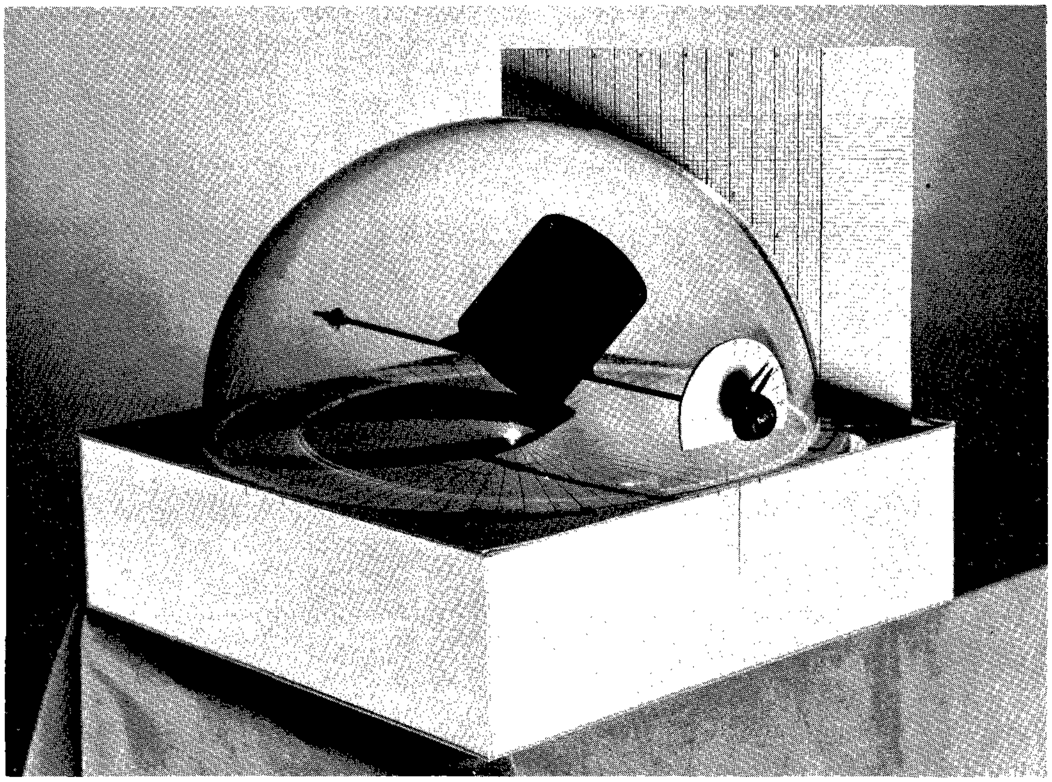

Fig. 14. Apparatus to determine view factors in cylinder/dome combination.

An open-sided cylinder is mounted on a metal bar, supported at either end by the glass dome, and rotated by the dial at one end of the bar. A small glass bulb acts as a point source of radiation from the center of the circular base to the cylinder. The area of the shadow produced at the base may be estimated by rotating a graduated disk around the glass dome and measuring the horizontal coordinates of the shadow produced on the dome. By rotating the cylinder through ±90 degrees the value of the view factor from the hemisphere to cylinder may be obtained. The ratio of a given shadow area to the base area gives the required view factor. Two shadows were produced, one representing the view factor between the hemisphere and the bottom of the cylinder; the other, between the hemisphere and the cylinder walls. The results for two Δ/D ratios are given in Fig. 15.

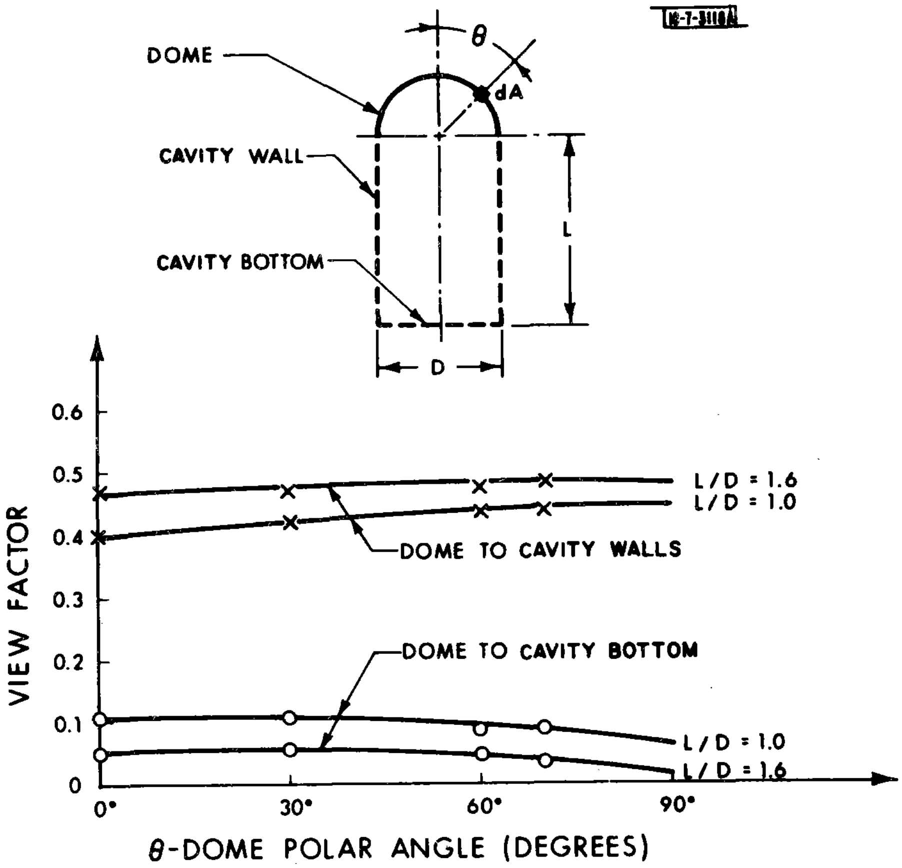

Fig. 15. View factors between a hemispherical dome and a cylindrical radiating cavity as a function of position on dome.

The view factor from the hemisphere to the cylinder wall seems a little high, as the combined view factor from the hemisphere to the walls and the bottom is 0.52, whereas it should be 0.5, since the view factor for the hemisphere itself is 0.5. Using the foregoing equations, the predicted view factors are given in Table 1. Thus the experimental and predicted values agree within 10 percent.

TABLE 1

VIEW FACTORS

Location	Theoretical		Experimental		Percent Difference
	Δ/D = 1	Δ/D = 1.6	Δ/D = 1	Δ/D = 1.6	
Hemisphere to Walls	0.39154	0.4419	0.42	0.47	6
Hemisphere to Bottom	0.1084	0.0581	0.10	0.0513	9

10. A Mathematical Model

Consider an enclosure of N isothermal surfaces with constant properties, the radiosity, J_i, or total radiant energy per unit time per unit area leaving a surface is:

$$J_i = \rho_i G_i + \epsilon_i E_{bi} \tag{45}$$

where

G_i = surface irradiation is the rate at which radiant energy reaches a surface per unit time per unit area

E_{bi} = radiant energy emitted.

If the surface being considered has a uniform temperature, t_i, then

$$\rho_i = \rho_i(T_i) \quad \text{and} \quad \alpha_i = \epsilon_i \quad .$$

If the enclosure is a cavity receiver the interior may be treated as a closed system of surfaces; the inlet aperture is treated as one of the surfaces, possessing the properties of a black body with respect to reflection and absorption, and the properties at a temperature of 0°R with respect to radiation. The remainder of the cavity interior surface is considered to be grey and diffuse. By subdividing the interior of the cavity up into a number of surfaces such that the temperature and optical properties of each surface remain constant, a set of simultaneous equations (incorporating the necessary view factors) which express the radiation and radiation interchange between surfaces can be solved using the Gauss-Seidel iteration technique until equilibrium is established within the cavity.

The surface i is irradiated by each surface K in the enclosure that has a view of it and by incident solar flux. Thus for surface i,

$$G_i = \frac{1}{A_i} \sum_{K=1}^{N} J_K F_{Ki} A_K + E_i$$

where E_i represents the incident solar flux

$$= \frac{1}{A_i} \sum_{K=1}^{N} J_K F_{iK} A_i + E_i$$

since $A_K F_{Ki} = A_i F_{iK}$

$$= \sum_{K=1}^{N} J_K F_{iK} + E_i \quad . \tag{46}$$

Substituting Eq. (46) in Eq. (45):

$$J_i = \rho_i \left(\sum_{K=1}^{N} J_K F_{iK} + J_i F_{ii} + E_i \right) + \epsilon_i E_{bi} \tag{47}$$

where $\rho_i J_i F_{ii}$ = irradiation of surface i by itself.

Thus

$$J_i(1 - \rho_i F_{ii}) = \rho_i\left(\sum_{\substack{K=1\\K\neq i}}^{N} J_K F_{iK} + E_i\right) + \epsilon_i E_{bi}$$

or

$$J_i = \frac{\rho_i}{(1 - \rho_i F_{ii})} \sum_{\substack{K=1\\K\neq i}}^{N} J_K F_{iK} + E_i) + \frac{\epsilon_i}{1 - \rho_i F_{ii}} E_{bi} \tag{48}$$

The incident solar flux is also absorbed by surface i and reradiated. The E_{bi} represents the total energy arriving at surface i that is absorbed and reemitted; i.e.,

$$E_{bi} = E_i + \sum_{K=1}^{N} J_K F_{Ki}$$

therefore Eq. (48) becomes:

$$J_i = \left[\rho_i\ E_i + \sum_{\substack{K=1\\K\neq i}}^{N} J_K F_{Ki} + \epsilon_i\left(E_i + \sum_{K=1}^{N} J_K F_{Ki}\right)\Big/(1 - \rho_i F_{ii})\right] . \tag{49}$$

Now a fraction, F_{i1} of the radiant energy per unit time per unit area leaving surface i escapes through the entrance aperture (surface 1) as Eq. (49) has to be modified accordingly:

$$J_i = \left[\rho_i\left(E_i + \sum_{\substack{K=1\\K\neq i}}^{N} J_K F_{Ki}\right) + \epsilon_i\left(E_i + \sum_{K=1}^{N} J_K F_{Ki}\right)\right]\left[\frac{1 - F_{i1}}{1 - \rho_i F_{ii}}\right] . \tag{50}$$

The incident radiation E_i is first calculated from Eqs. (2) through (8). Strictly speaking, the specular reflection component of incident flux should be accounted for in the model as a fraction of the component will pass out through the aperture after several bounces inside the cavity.

11. Sample Design Calculations

A sample design calculation for the concept of coupling a dome-capped cylindrical receiver to a Brayton or Stirling engine follows. The cavity is sized to receive 65 kW_t from a parabolic concentrator and to supply 60 kW_t (78 hp) to a Brayton or Stirling engine at 1800°F. Normally, the Brayton cycle would run at around 2000°F and the Stirling at around 1500°F, so for convenience sake, 1800°F was chosen as a mean, although the cavity can easily operate at 1500° or 2000°F. Assuming perfect optics, a 30-foot-diameter parabolic dish, which has a rim angle of 45 degrees, considered optimum for this dish/receiver combination,[3] gives a 2-inch beamwidth at the focal point. An entrance reflector is added to the 2-inch aperture to enable the solar beam to enter the cavity from 0-45 degrees. The calculations assume no conduction or convention losses.

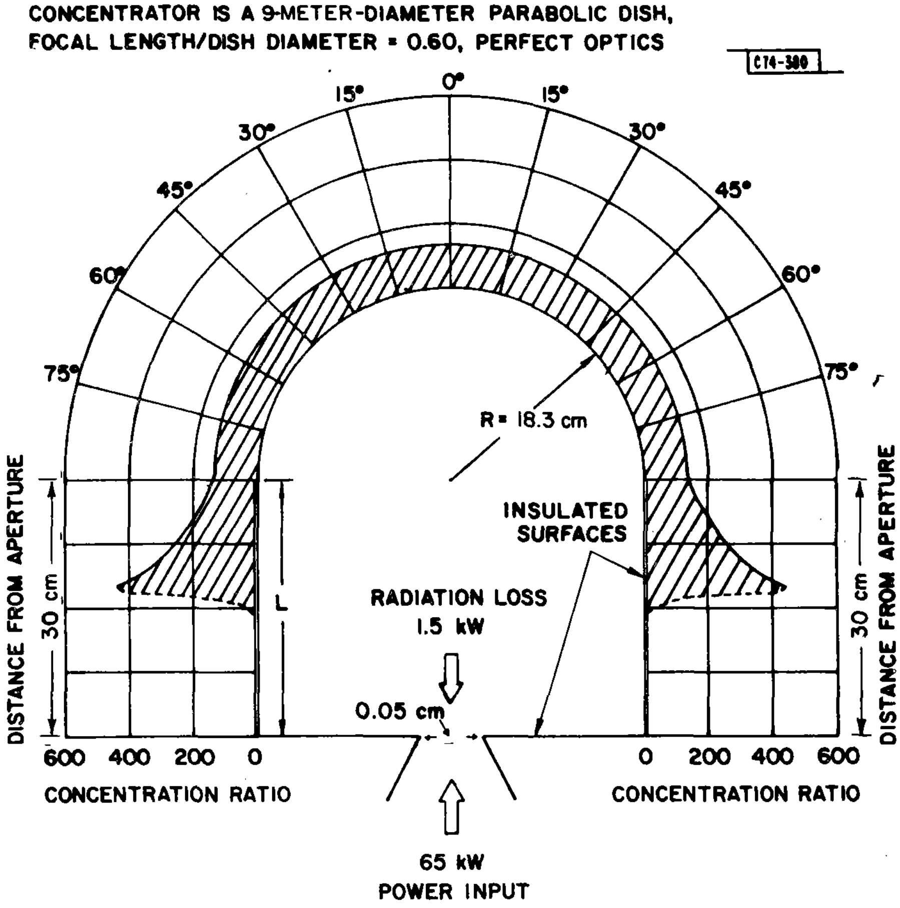

Fig. 16. Incident solar flux distribution in dome-capped cylindrical receivers.

Using Eqs. (10) and (16) plus the design strategy discussed in Section 8, the initial cavity flux distribution was calculated and an appropriate length/diameter ratio chosen. Figure 16 shows the incident energy on the interior of a 14.4-inch-diameter, 12-inch-long cavity placed at the focus of the parabolic trough. Flux impinging on the hemispherical back is almost constant over the dome with flux peaks on the walls of the cylinder. The uniform flux on the dome will ensure that very low thermal stresses are generated from the incident flux field.

Given the initial flux distribution, Eq. (50) can now be modeled on a computer to determine the final flux and temperature profiles in the cavity. The model treats the cavity as having eight separate regions including four equidistant cylindrical strips between the wall length, 7.2 and 12 inches.

The flow chart for the computer program is shown in Fig. 17. The procedure for arriving at a solution is to assume values for J_i, $i \neq 1$, and solve for J_1. The incident flux arriving at the walls and cavity back should be included in the value of J_i. Each successive iteration takes into account the incident solar flux. With the new value of J_1 and assumed values of J_i, the solution for J_2 is obtained. This procedure is repeated, using the most recent values for J_i, until

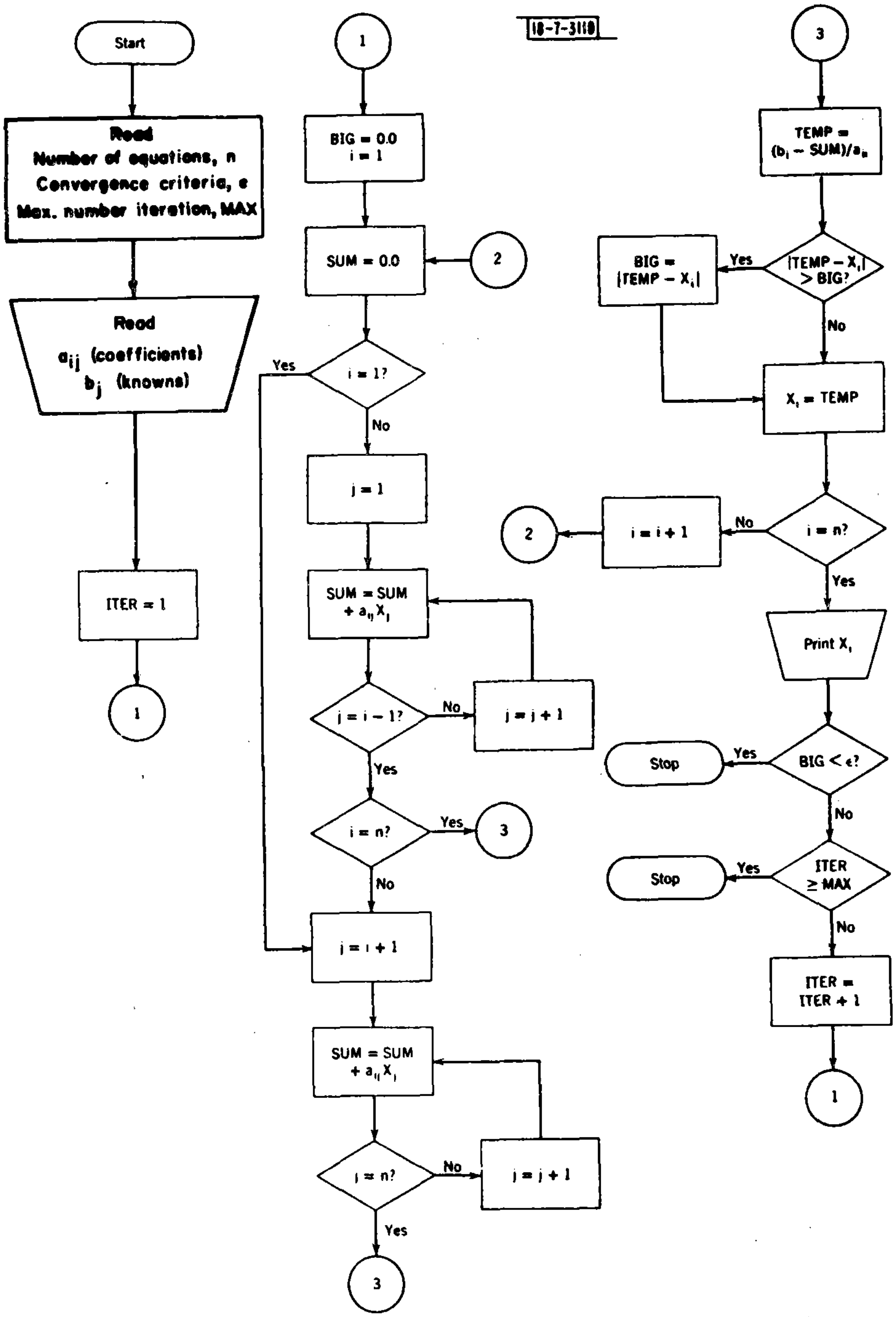

Fig. 17. Flow chart for Gauss-Seidel iteration.

the energy arriving at each surface is approximately equal to the energy leaving that surface; i.e.,

$$\sum_{i=1}^{N} (G_i - J_i) A_i = \Delta$$

where Δ = arbitrary constant. The flow chart (Fig. 17) is a standard chart for a Gauss-Seidel iteration solution of equations of the form:

$$a_{11}x_1 + a_{12}x_2 \cdot \cdot \cdot \cdot \cdot = b_1$$

$$a_{21}x_1 + a_{22}x_2 \cdot \cdot \cdot \cdot \cdot = b_2$$

$$a_{n1}x_1 \cdot \cdot \cdot \cdot \cdot \cdot \cdot \cdot \cdot \cdot = b_n$$

Figure 18 shows the internal and external cavity radiation profiles in ① and ③. Together, items ①, ②, and ③ illustrate all the radiation components that interact in the equilibrium condition. Figure 19 shows the cavity receiver's internal equilibrium temperature profile. The exact surface temperatures are shown in Table 2. As in Fig. 16, the peak (2980°F) still occurs at 7.2 inches along the cavity wall, but there is little variation in temperature over the cavity interior. The results show a smoothing out of the flux distribution from the incident flux condition to the equilibrium condition, although the position of the peaks on the walls does not change.

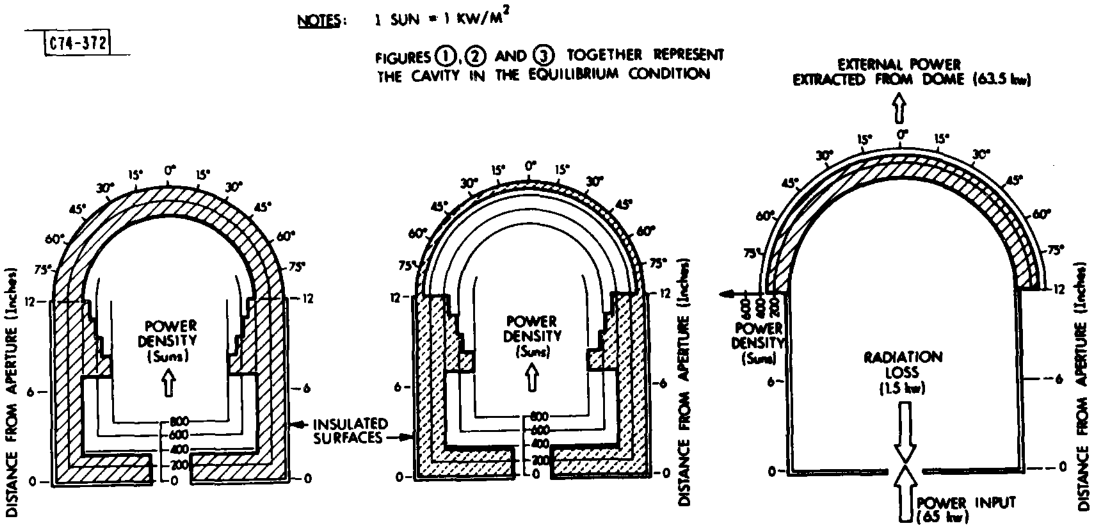

NOTES: 1 SUN = 1 KW/M²

FIGURES ①, ② AND ③ TOGETHER REPRESENT THE CAVITY IN THE EQUILIBRIUM CONDITION

① INTERNAL PROFILE INCLUDING INCIDENT RADIATION, RERADIATION AND SELF-IRRADIATION (FLUX INCIDENT AT EACH SURFACE)

② INTERNAL RERADIATION PROFILE (FLUX LEAVING EACH SURFACE)

③ POWER TRANSFERRED TO AND FROM CAVITY (FLUX EXTRACTED EXTERNALLY AT EACH SURFACE)

Fig. 18. Cavity receiver radiation equilibrium conditions.

In practice, the high receiver efficiency (97 percent) will be reduced as a larger cavity aperture is necessary to accommodate a broader beamwidth (caused by mirror error), thereby increasing the losses through the aperture. In addition, specular reflection is estimated to reduce the efficiency by about 2 percent, but even when this and mirror errors up to 10 milliradians are

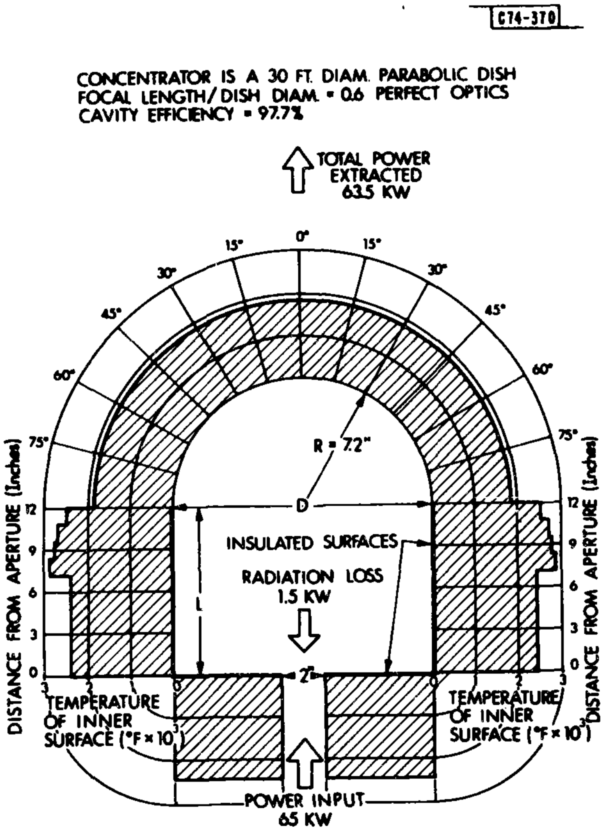

Fig. 19. Cavity receiver equilibrium temperature profile.

TABLE 2

TEMPERATURE AND FLUX DISTRIBUTIONS IN THE DOME-CAPPED CYLINDRICAL RECEIVER

Node	Incident Energy (Btu)	Energy (Btu/hr) Arriving	Energy (Btu/hr) Leaving	Temperature (°F)
1	–	221,700	5,100	–
2	–	132,850	132,850	2426
3	–	280,000	280,000	2446
4	45,500	92,300	92,300	2980
5	33,779	79,200	79,200	2860
6	25,515	69,403	69,403	2752
7	19,604	61,000	61,000	2647
8	97,200	333,300	116,060 internal 216,600 external	1870

included, the cavity efficiency still exceeds 90 percent. Conduction and convection losses will reduce the efficiency further but it is expected that receiver efficiencies in the range from 85 to 90 percent may be achieved in an actual receiver.

12. Design Considerations for Dome-Capped Cylindrical Receiver

a. Radiation loss is most effectively controlled by incorporating an entrance reflector and reducing the aperture size. Increasing the cavity length will reduce the radiation loss to a certain extent, but in doing so the desired flux distribution within the cavity is affected.

b. Wall temperatures should not exceed 3000°F (to avoid materials problems), but should operate at least 400°-600°F hotter than the dome to transfer sufficient indirect heat to it. The wall temperature, which is a major contributor to radiation loss, may be controlled by varying the cavity diameter.

c. Dome temperature may be controlled by varying the cavity length. The dome does not contribute significantly to radiation loss at Δ/D ratios close to unity. The dome flux distribution is smoothed by decreasing dome depth and cavity length.

d. Optimum heat transfer across the dome is achieved by designing for the minimum dome area required to transfer heat to the load. In the dish/Stirling concept the dome diameter is slightly larger than the Stirling engine's cylinder bore.

13. Larger Scale Receiver Concepts

Large-scale solar-conversion-receiver concepts of the order of 1 MW_t are being considered for operating a Brayton engine (Fig. 2). Individual dome units line the interior walls of the receiver providing a sufficiently large heat-transfer area for the impinging jets to transfer heat to the load. Heat flux may reach the domes directly (incident solar flux strikes the dome) or indirectly via other interior cavity surfaces. The object of the exercise is to determine whether direct or indirect energy conversion is the most efficient of the two approaches and whether the individual domes should be placed at the top, side walls or bottom of the cavity receiver. In all, four receiver concepts were evaluated.

To simplify the comparison, the small ceramic dome units were "lumped together" and considered as a single, large heat-transfer area with a shallow dome shape. The area of this heat-transfer section is the same for all four concepts. A 75-kW_t receiver input was chosen, and each design concept optimized for maximum energy-conversion efficiency. The dome-operating temperature is 1800°F. A 5-inch aperture was chosen; the smallest size possible for an entrance aperture/reflector combination that would still admit the incoming beam and minimize the radiation loss. The view factors necessary for the equilibrium flux calculation were obtained using the equations given in Section 9. Radiation was considered as the only heat exchange mode inside the receiver.

Table 3 summarizes and compares the four basic concepts considered. Clearly, direct concepts are more efficient than indirect concepts. However, it would be premature to rank the concepts before a more complete analysis is made that includes reflections, convection and conduction losses, and considers the heat-transfer surfaces (surface number ② of concepts ② and ③) as being made up of several individual dome elements. Such an analysis should produce a great spread of results with larger differences in efficiencies between each concept.

TABLE 3

SOLAR CONVERSION RECEIVER CONCEPTS SUMMARY

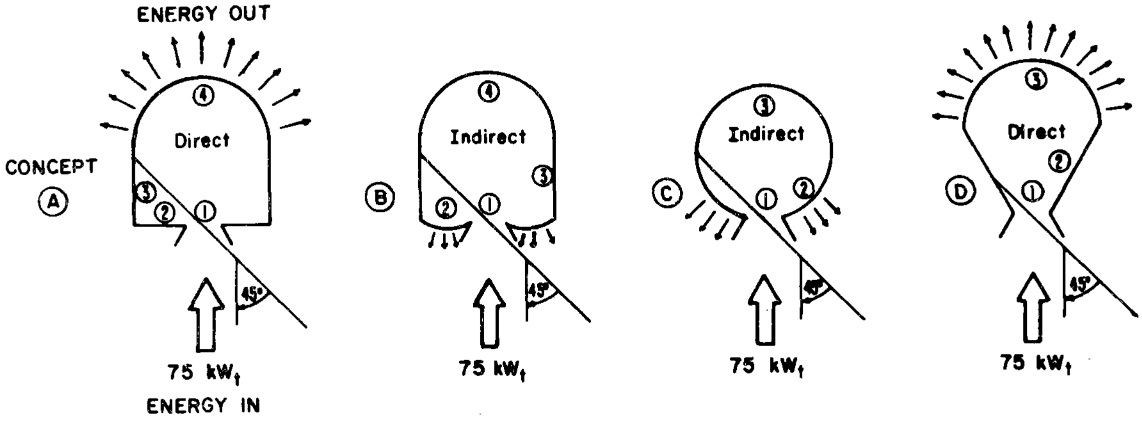

	Ⓐ	Ⓑ	Ⓒ	Ⓓ
Cavity Length (in.)	8	11.6	8	8
Cavity Diameter (in.)	21	23.2	21	21
Δ/D	0.38	0.5	0.38	0.38
Temperature (°F)				
Node 1				
2	1798	1800	1800	
3	1790	2350	2609	1800
4	1800	2701	–	1794
Radiation Loss (kW$_t$)	1.799	5.586	4.5	1.802
Cavity Efficiency (%)	97.6	92.7	94.17	97.66

Two factors account for the difference between direct and indirect concepts. First, direct concepts operate on the principle that most of the incident flux falls onto and is conducted through the ceramic dome. Part of this incident flux is reflected and reradiated to the cavity walls, however, as Table 3 indicates, the wall temperatures run cooler than the dome. Now as the dome does not contribute significantly to the radiation loss, and the wall temperatures are below 1800°F, the radiation loss is minimized. Secondly, as the heat-transfer surface area is fixed, the configuration in concept ② requires a larger cavity diameter, and a larger cavity length. This causes the conversion efficiency of concept ② to be slightly lower than concept ③.

Table 4, concept ①, shows that increasing cavity length and aperture size lower the cavity efficiency where the latter has by far the greater effect. This is confirmed when the cavity length is increased in concept ③.

TABLE 4
DIRECT VS. INDIRECT CONCEPTS

Concept	Cavity Size			Aperture Diameter (in.)	Ceramic Shape	Wall Temperature (°F)			Dome Top Temperature (°F)	Cavity Eff. (%)	Radiation Loss (kW_t)
	Diameter (in.)	L (in.)	Δ/D (in.)			Bottom	Side (Indirect)	Side (Direct)			
1 Direct	21	8	0.38	5	Hemisphere	1798	1790	–	1800	97.68	1.74
1 Direct	16	16	1.0	5	Hemisphere	2473	2482	2780	1800	93.0	5.25
1 Direct	16	24	1.5	5	Hemisphere	2620	2573	2764	1780	84.7	11.48
1 Direct	16	24	1.5	5.5	Hemisphere	2575	2540	2747	1780	82.5	13.12
3 Indirect	23.2	11.6	0.5	5	Hemispherical Toroid	1800	2350	–	2701	92.7	5.48
3 Indirect	23.2	23.2	1.0	5	Hemispherical Toroid	1800	2345	2707	2666	90.97	6.77

14. Furnace Experiment

Tests are being undertaken at MIT/Lincoln Laboratory to confirm the leakage predictions for a 12-inch-diameter, ceramic-to-ceramic contact seals using the experimental test fixture shown in Fig. 20 (Ref. 1). A 12-inch hemispherical silicon carbide ceramic dome is mounted on the top of a cylindrical vacuum furnace unit that heats the ceramic dome/seal module to 1800°-2000°F temperatures. The dome is then subjected to a 4-atmospheres pressure differential and the leakage through the contact area is measured with a mass flow meter.

An important aspect of the experiment is to simulate the condition of a uniform flux distribution across the dome. Thus the test fixture has to be sized to approach a uniform incident radiation profile across the dome as closely as possible. By calculating the view factors inside the furnace an estimate of the distribution of flux and number of suns can be made. Assuming two furnace elements are present, the furnace walls, bottom, and cone surface will all be at roughly the same temperature. Hence the flux contributions from each section, including the furnace elements may be added separately and calculated at different locations on the dome. When one furnace element is present (the lower one), it is assumed that only the walls and bottom of the furnace are at the same temperature as the element, and that these items radiate to the cone, determining the temperature of the cone. Of course, in the equilibrium condition, the whole inner furnace, including the dome, will be at the same temperature, but it is important to know the temperatures and flux distributions initially and so avoid the possibility of excessive thermal stresses being set up in the dome.

Referring to Fig. 20, the radiation received by the dome may be considered to be composed of four basic components:

a. Upper furnace element. Only the inside of the element sees the dome. The outer surface sees the cylinder and the cone.

b. Lower furnace element. Only the inside of the element sees the dome. The outer surface sees the cylinder and the cone.

c. Cylinder (body of furnace). This is assumed to have the same temperature as the furnace element(s). Its view of the dome is partially obscured by the furnace elements.

d. Cone. This has the best view of the dome. If two elements are used, the cone is assumed to be at the same temperature as the cylinder. If one element is used, the cone temperature is determined by the view that the cylinder and the furnace elements have of it; i.e., the cone will be at a lower temperature than the cylinder.

Formulas for the view factors given hereafter were taken from Ref. 3 and modified according to the furnace geometry. See Fig. 21 for its notation.

View factor from sphere to cylinder

$$F = \left\{ \frac{1}{4R_c^2(\cos\Theta_{m-1} - \cos\Theta_m)} \right\} \Big\{ 2R_c(a_n - a_{n-1})(\cos\Theta_{m-1} - \cos\Theta_m) \\ + \overset{①}{f_{14}\, a_{n-1}, \Theta_{m-1}} - \overset{②}{f_{14}\, a_{n-1}, \Theta_m} + \overset{③}{f_{14}\, a_n, \Theta_m} - \overset{④}{f_{14}\, a_n, \Theta_{m-1}} \Big\} \qquad (51)$$

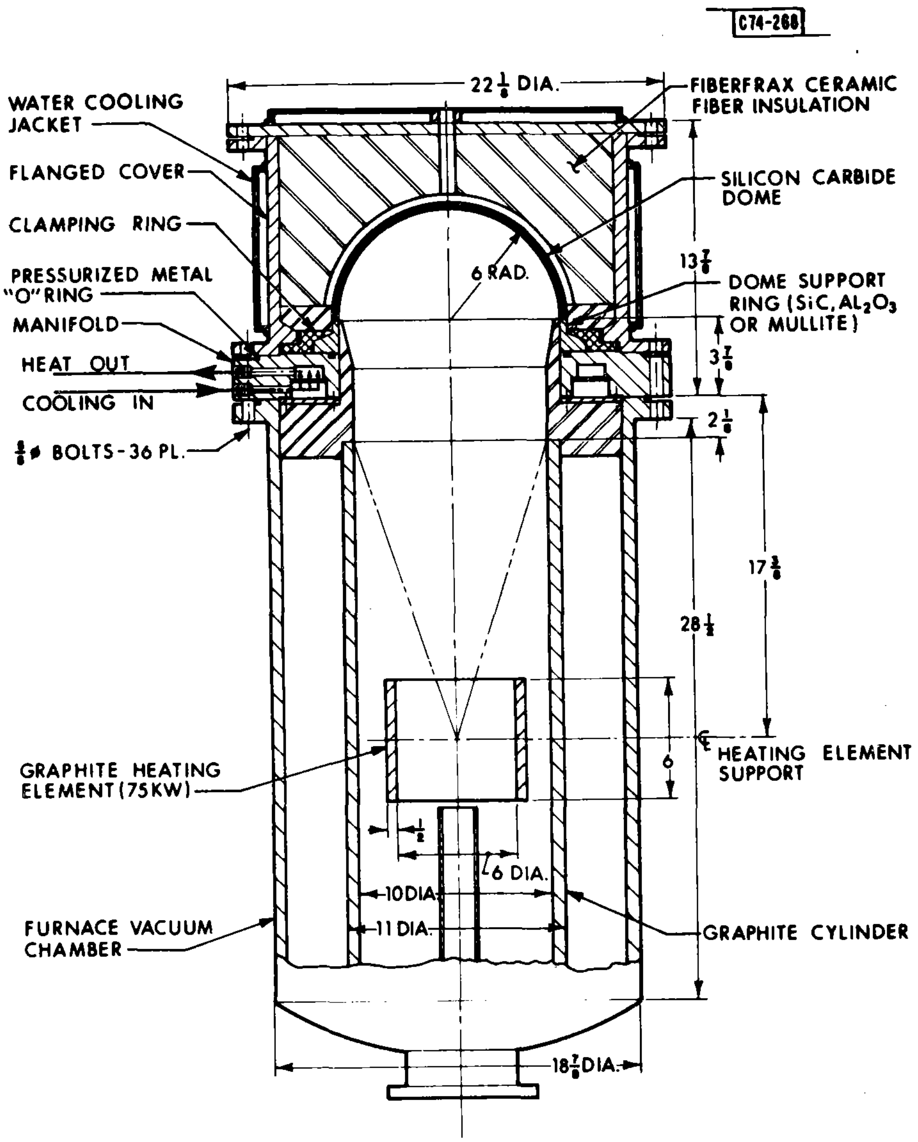

Fig. 20. Twelve-inch dome/seal text fixture.

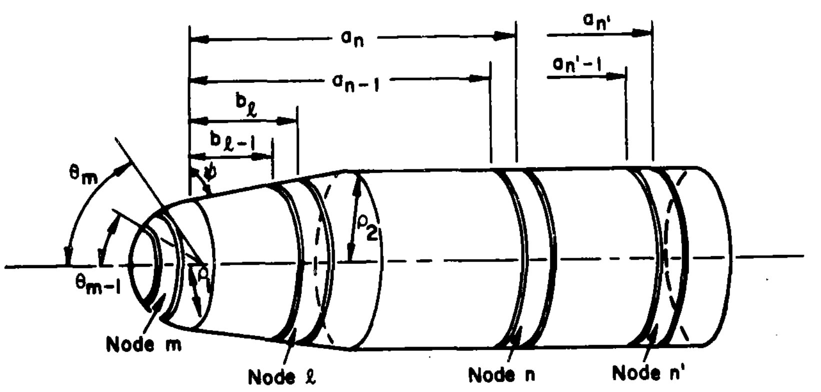

Fig. 21. Sphere-cone-cylinder configuration.

where

$$f_{14}(\lambda, \omega) = \Bigl\{\Bigl([\lambda + R_c(\cos\omega + \sin\psi)]^2 + \rho_2^2 + R_c^2 \sin^2\omega\Bigr)^2 - (2R_c\rho_2 \sin\omega)^2\Bigr|^{1/2}$$

and R_c = dome radius = $\rho_1/\sin\psi$

View factor from dome to cone

$$\begin{aligned} F = &\left\{\frac{1}{4R_c^2(\cos\Theta_{m-1} - \cos\Theta_m)}\right\} \{2R_c(b_\ell - b_{\ell-1})\,(\cos\Theta_{m-1} - \cos\Theta_m) \\ &+ f_{15}(b_{\ell-1}, \Theta_{m-1}) - f_{15}(b_{\ell-1}, \Theta_m) + f_{15}(b_\ell, \Theta_m) - f_{15}(b_\ell, \Theta_{m-1})\} \end{aligned} \tag{52}$$

where

$$\begin{aligned} f_{15}(\zeta, \omega) = \{[\zeta &+ R_c(\cos\omega + \sin\psi)^2 + (\rho_1 + \frac{\zeta}{\tan})^2 + R_c^2 \sin^2\omega\}^2 \\ &- [2R_c \sin\omega\,(\rho_1 + \frac{\zeta}{\tan})]^2\}^{1/2} \end{aligned}$$

View factor from cone to cylinder

$$\begin{aligned} F_{(\ell,n)} = &\left[\frac{\frac{1}{2}\cos\psi}{2\rho_1(b_\ell - b_{\ell-1}) - \dfrac{(b_\ell)^2 - (b_{\ell-1})^2}{\cot 4}}\right] [2(b_\ell - b_{\ell-1})\,(a_n - a_{n-1}) \\ &+ f_{16}(a_{n-1}, b_{\ell-1}) - f_{16}(a_{n-1}, b_\ell) + f_{16}(a_n, b_\ell) - f_{16}(a_n, b_{\ell-1}) \end{aligned}$$

where

$$f_{16}(\zeta, \omega) = \left\{\left[(\zeta - \omega)^2 + \rho_2^2 + (\rho_1 - \frac{\omega}{\cot\psi})^2\right]^2 - \left[2\rho_2(\rho_1 - \frac{\omega}{\cot\psi})\right]^2\right\}^{1/2}$$

Using the inverse area ratio law [Eq. (24)] and view factor algebra – the view factors from the furnace elements – the cylinder and the cone to the dome were calculated (Table 5). The contribution from the bottom of the furnace is neglected.

In Table 5, selected strips (radial thickness 1 deg.) every 15 degrees over the dome were chosen as calculation points so that the dome flux distribution could be determined. Clearly, the cone has the best view of the dome. This pattern does not change significantly when only the lower furnace element is present.

In Table 6, the flux density (suns) and temperature (°R) at each radial strip is presented. The total energy arriving at each strip due to two furnace elements is given by:

$$\begin{aligned} Q_{\text{strip}} &= Q_{\text{cone}} + Q_{\text{cylinder}} + Q_{\text{elements}} \\ &= \sigma T^4(A_{\text{cone}}\,F_{\text{cone-strip}} + A_{\text{cylinder}}\,F_{\text{cylinder-strip}} \\ &\qquad + A_{\text{element}_1\text{-strip}} + A_{\text{element}_2\text{-strip}}) \end{aligned}$$

where A_{element_1}, A_{element_2} are the inner surface areas of the top and bottom furnace elements, respectively.

TABLE 5

VIEW FACTORS FROM SECTIONS OF FURNACE TO SELECTED DOME STRIPS

View Factor to Dome Strip	Upper and Lower Furnace Elements Present							Lower Furnace Element Only						
	0	15	30	45	60	75	90	0	15	30	45	60	75	90
	(degrees)							(degrees)						
Cone	0.0111	0.0124	0.0115	0.0097	0.00699	0.00353		0.001199	0.00134	0.00124	0.001048	0.000755	0.000381	
Cylinder	0.000612	0.000916	0.0007616	0.000585	0.000451	0.0002718		0.000877	0.000709	0.000579	0.0004286	0.000283	0.000164	
Top Element	0.000425	0.00041	0.000385	0.000328	0.000236	0.000121								
Bottom Element	0.000105	0.000103	0.0001	0.00009	0.000074	0.0000464		0.000105	0.000103	0.0001	0.00009	0.000074	0.0000464	
Bottom														
Total	0.01224	0.01383	0.0127	0.0106	0.007751	0.00397		0.00297	0.00215	0.00205	0.001567	0.001112	0.000591	

TABLE 6

FLUX AND TEMPERATURE DISTRIBUTION ACROSS THE DOME INCLUDING CONTRIBUTIONS FROM FURNACE ELEMENTS, CYLINDER AND CONE

Flux Density Due to	Upper and Lower Furnace Elements						Lower Furnace Element					
	0	15	30	45	60	75	0	15	30	45	60	95
	(degrees)						(degrees)					
Cone	26,380 83 suns	80,501 96	31,548 100	32,590 103	32,642 103	31,357 99	2849 8.99	3297 10.4	3401 10.73	3525 11.12	3528 11.13	3385 10.68
Cylinder	2268 7.15	4698 14.82	4290 13.53	4620 14.57	4387 13.84	4248 13.4	4933 15.56	4642 14.64	4784 15.09	4942 15.59	5053 15.94	4963 15.66
Top Element	542 1.71	543 1.71	569 1.8	592 1.87	591 1.87	578 1.82						
Bottom Element	135 0.42	136 0.43	149 0.47	162 0.51	186 0.59	222 0.7	135 0.42	136 0.43	149 0.47	162 0.51	186 0.59	322 0.7
Total	29,335 92.28	35,878 112.96	36,556 115.8	37,203 117.55	37,806 119.3	36,405 114.84	7917 24.97	8075 25.47	8334 26.29	8629 27.22	8767 27.66	8570 27.04
Strip Temperature (°R)	2035	2140	2150	2180	2168	2148	1467	1494	1486	1499	1505	1496

To calculate the number of suns falling on each strip due to the cylinder,

$$\frac{Q_{strip}}{A_{strip}} = \text{No. of suns of strip} = \frac{Q_{strip}}{A_{cylinder}} + \frac{A_{cylinder}}{A_{strip}}$$

The furnace element temperature is 1800°F. Again the cone contributes most of the energy to the dome. However, the distribution across the dome is fairly uniform, whether considering the individual contributions or the total contribution.

When considering the lower furnace element only, the cone temperature is given by

$$T_{cone}^{4} = \frac{(F_{element_2\text{-}cone}\, A_{element_1} + F_{cylinder\text{-}cone}\, A_{cylinder})\, T^4}{A_{cone}}$$

where T^4 = furnace temperature raised to the fourth power.

Using view factors in Table 5 and the furnace dimensions,

$$T_{cone} = 0.573\, T \quad .$$

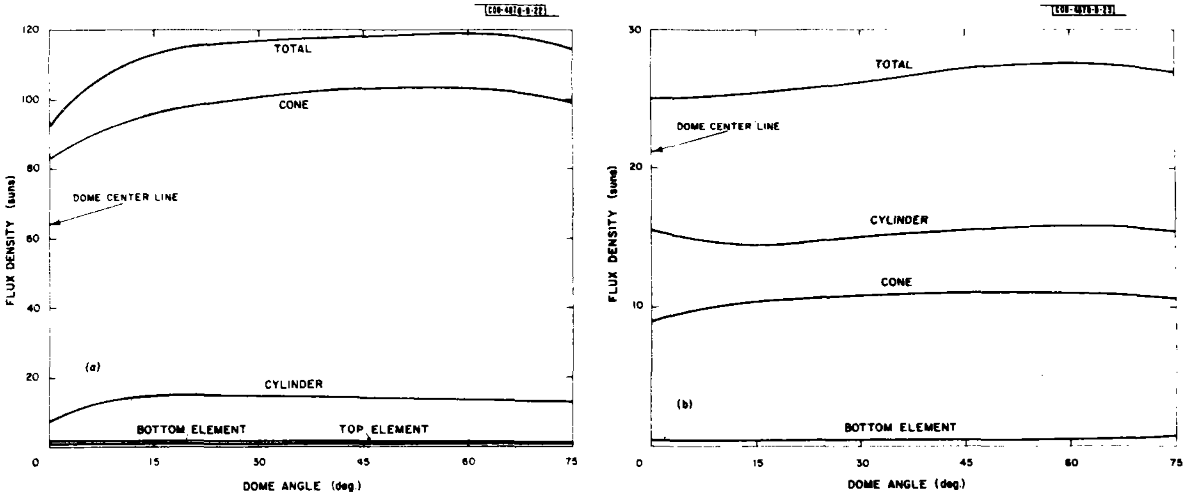

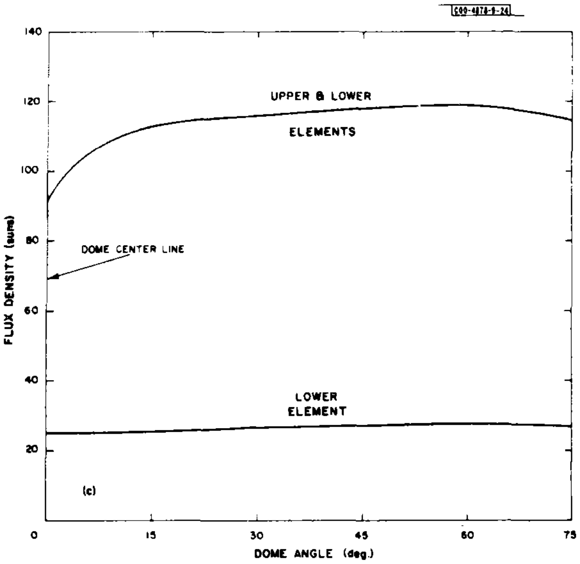

Fig. 22. Furnace component flux density (suns) being radiated to individual dome strips starting from dome side (0°) to dome top (90°) for a given furnace temperature of 1800°F (a) 2 elements, (b) lower element, and (c) summary of (a) and (b).

If the lower furnace element is present only, the cone does not provide most of the radiation to the dome, and the energy radiated to the dome from all sections is considerably less. However, as with the furnace elements case, the dome flux distribution is fairly homogeneous.

To convert the number of suns calculated over the dome for a given furnace temperature to another furnace temperature, multiply by the inverse ratio of temperatures raised to the fourth power; i.e., say T_1 = furnace temperature = 2260°R (used for present calculation) and the number of suns on dome for a furnace temperature = T_2 = 1520°R is desired. Multiply the number of suns at each radial strip by

$$(T_2/T_1)^4 = 0.2 \quad .$$

The results shown in Table 6 have been plotted in Fig. 22. In practice, the real emissivity of each surface should be taken into account, which will give a lower number of suns received on the dome, but the relative distribution across the dome, which is uniform in this case (1800°F furnace temperature) will not change. To include the emissivities, multiply the number of suns by the surface emissivity for each surface.

REFERENCES

1. Jarvinen, P.O., "Ceramic Receivers for Solar Power Conversion," AIAA Terrestrial Energy Systems Conference, Orlando, Florida (June 4-6, 1979).
2. Dasgupta, S.; Mauke, E., and Hildebrandt, A., "Flux Distributions Inside and Thermal Efficiencies of Solar Cavities Heated by Parabolic Dishes," Proc. International Solar Energy Society, American Section 2, 1, Denver, Colorado (1978).
3. Stevenson, J.A. and Grafton, J.C., "Radiation Heat Transfer Analysis for Space Vehicles," Technical Report SID-61-91, North American Aviation (AF ASD TR 61-119, pt. 1) (September 9, 1961).
4. Jakob, M., Heat Transfer, II (Wiley, New York, 1959).

NOMENCLATURE

A_i, A_j	Areas of surfaces i, j
b	Dome depth
C	Concentration ratio
D_c, R_c	Cavity diameter, radius
D_p	Parabolic dish diameter
d_{max}	Maximum diameter of illuminated zone of focal plane
E_i	Incident solar flux
E_{bi}	Radiant energy emitted by surface i
F_{ij}	View factor from surface i to j
F_p	Focal length of parabolic dish
g	Distance between a point on the dish and focus $= 2F_p/(1 + \cos\phi)$
L	Length of incident flux distribution on cylindrical cavity wall
r	Aperture radius
T_i	Temperature of surface i
X	Distance from cavity bottom (located at aperture) to wall flux peak
α_s, α	Solar disk diameter, corrected solar disk diameter
γ	Surface slope error of mirror
Δ	Cavity length
ϵ, ρ	Emissivity, reflectivity of cavity
ϕ_{rim}	Rim angle of mirror
θ	Angle subtended on dome measured from center of curvature
η_M	Reflectivity of mirror surface
χ	Distance from base of parabolic dish to center of image in cavity generated by a point M on the dish

APPENDIX B

CERAMIC/METAL TEST COUPONS

Ceramic	Metal Coating (thickness)	Test Temperatures	Comments
SiC	W (0.5μ)	600°C, 800°C, 1000°C 1200°C	Excellent coating adhesion to 1200°C
SiC	W (1.0μ) RT	600°C, 800°C, 1000°C 1200°C	Excellent coating adhesion to 1200°C
SiC	W (5μ)	600°C, 800°C, 1000°C 1200°C	Excellent coating adhesion to 1200°C
SiC	W (1μ), Ni (200 in.)	600°C, 800°C, 1000°C 1050°C, 1100°C, 1150°C, 1250°C	Excellent coating adhesion to 1250°C
SiC	W (1μ), Ni (5μ), D	600°C, 800°C, 1000°C, 1100°C, 1150°C, 1250°C	Extrodeposited coating, good adhesion to 800°C
SiC	W (5μ), Ni (200μ in)	600°C, 800°C, 1050°C, 1100°C, 1150°C, 1250°C	Good coating adhesion to 800°C
SiC	W (5μ), Ni (5μ), D	600°C, 800°C, 1000°C, 1100°C, 1150°C, 1300°C	Electrodeposited coating; good coating adhesion to 800°C
SiC	W (.5μ), Ni (.5μ)	600°C, 800°C, 1000°C, 1050°C, 1150°C, 1300°C	Coating oxidized off on 1050°C cycle
SiC	W (.5μ), Ni (.5μ), Rh (2.5μ)	600°C, 800°C, 1000°C, 1050°C	Coatings cracked and chipped after 1000°C cycle
Al_2O_3	Ni (.8μ)	600°C, 800°C, 1000°C, 1050°C, 1150°C, 1300°C	Excellent coating adhesion to 1300°C

Appendix B (con'd)

Ceramic	Metal Coating (thickness)	Test Temperatures	Comments
Al_2O_3	Nb (.22 μ), Ni .78μ	600°C, 800°C, 1000°C 1050°C	Coatings show some cracks at room temperature, large areas of Al_2O_3 exposed by 600°C
Al_2O_3	Nb (.5 μ), Ni (.5 μ)	600°C, 800°C	Same as above
Al_2O_3	Nb (.5 μ)	600°C, 800°C	Excellent coating quality at room temperature, good to 800°C
Al_2O_3	Nb (1 μ)	600°C, 800°C, 1100°C	Same as above, coating gone after 1100°C cycle
Al_2O_3	Nb (5 μ)	600°C, 800°C, 1100°C	Same as above
Al_2O_3	Nb (.5 μ), Ni (5 μ)	600°C, 800°C, 1050°C, 1100°C, 1150°C, 1300°C	Excellent coating adhesion to 1150°C
Al_2O_3	Nb (1 μ), Ni (5 μ)	600°C, 800°C, 1050°C, 1100°C, 1150°C, 1300°C	Excellent coating adhesion to 1300°C
Al_2O_3	Nb (5 μ), Ni (5 μ)	600°C, 800°C, 1050°C, 1100°C, 1150°C, 1250°C	Excellent coating adhesion to 600°C
Mullite	W (.5μ)	600°C, 800°C, 1050°C, 1100°C, 1300°C	Excellent coating adhesion to 1050°C
Mullite	W (1 μ)	600°C, 800°C, 1050°C, 1100°C, 1250°C	Excellent coating adhesion to 1100°C
Mullite	W (5 μ)	600°C, 800°C, 1050°C, 1100°C, 1250°C	Excellent coating adhesion to 1250°C

Appendix B (con'd)

Ceramic	Metal Coating (thickness)	Test Temperatures	Comments
Mullite	Nb (.5μ), Ni (5μ)	600°C, 800°C, 1050°C, 1100°C, 1250°C	Excellent coating adhesion to 1250°C
Mullite	W (1μ), Ni (5μ)	600°C, 800°C, 1050°C, 1100°C, 1250°C	Excellent coating adhesion to 1250°C
Mullite	W (5μ), Ni (5μ)	600°C, 800°C, 1050°C	Excellent coating adhesion to 800°C

APPENDIX C

COO-4878-11

EDGE STRESSES IN SPHERICAL-SHELL SOLAR RECEIVERS

18 January 1980

Duncan B. Sheldon

Massachusetts Institute of Technology
Lincoln Laboratory
Lexington, Massachusetts 02173

Prepared For

THE U.S. DEPARTMENT OF ENERGY
UNDER CONTRACT NO. ET-78-S-02-4878

Additional copies available from the National Technical
Information Service, U.S. Department of Commerce,
Springfield, Virginia 22161.

Price: Paper Copy $5.25
Microfiche $3.00

COO-4878-11

EDGE STRESSES IN SPHERICAL-SHELL SOLAR RECEIVERS

18 January 1980

Duncan B. Sheldon

Massachusetts Institute of Technology
Lincoln Laboratory
Lexington, Massachusetts 02173

Prepared For
THE U.S. DEPARTMENT OF ENERGY
UNDER CONTRACT NO. ET-78-S-02-4878

SUMMARY

The suitability of using spherical silicon carbide shells as heat exchangers in solar energy receivers is investigated. The responses of several such shells to the required thermal and pressure loads are examined quantitatively. Shells of different edge diameters, depths, and thicknesses are considered. Numerical data are presented which describe the maximum tensile and compressive stresses arising from heat-transfer requirements and the shells' nominal diurnal temperature cycle. These data describe the stresses resulting from a range of edge conditions. Relatively simple minimum-stress boundary conditions are identified. The characteristics of a pressure seal and edge-support mechanism that permit these minimum-stress boundary conditions to be realized are discussed. The temperature of the middle surface of each shell and the temperature gradient through its thickness are assumed to be uniform over the entire shell.

It is assumed that the shells' nominal diurnal temperature cycle ranges between 20° and 1000°C, and that heat-transfer requirements are fulfilled if the pressure and temperature differences across the thicknesses of the shells are four atmospheres (60 psi) and 400°C/inch. Under these conditions, the minimum-stress boundary conditions produce tensile and compressive stresses of the order of 10,000 psi in a 12-inch edge-diameter shell whose thickness is 1/8 inch (0.125 inch). Calculations show that the maximum stresses in a spherical shell can be much larger if the shell's boundary conditions deviate from the minimum-stress boundary conditions. Such deviations can result from constraining the rotation or expansion of the shell's edge when the shell is subjected to thermal diurnal cycling.

Two design approaches avoid large deviations from the minimum-stress boundary conditions:

1. Hemispherical shells can be freely supported, and
2. Shallow shells can be restrained by a clamp that accommodates changes in the diameter and rotation of a shell's edge.

These designs are compatible with minimizing the effects of thermal transients whose time scale is substantially shorter than the diurnal cycle. A nominal shell thickness of 1/8 inch facilitates manufacturing. This thickness is substantially greater than the minimum thickness required for stability in this application.

This work was performed in conjunction with the Solar Heated Air Receiver Experiment (SHARE). Other publications associated with this project are listed among the references at the end of this report.

CONTENTS

NOMENCLATURE

a	Radius of spherical shell, inch
b	Diameter of circular edge, inch
C	Constant derived from boundary conditions, lb/inch
D	$Eh^3/(12(1 - \nu^2))$, lb-inch
da	Differential expansion of shell radius, inch
E	Young's modulus, psi
H	Total horizontal force at the edge of the shell (positive inward, lb/inch
H_α	Horizontal force at the edge of the shell exclusive of the horizontal force reacting against the membrane force induced by the pressure difference across the shell (positive inward), lb/inch
$\hat{H}_\alpha$	Horizontal component of the membrane force due to the pressure, p, at the edge of the shell; also the value H corresponding to the minimum-stress boundary conditions (positive inward), lb/inch
h	Shell thickness (uniform), inch
h_t	Shell height, inch
M	Total bending moment at the edge of the shell, perpendicular to the local meridional plane, per unit meridional length, inch-lb/inch
M_α	Value of M at the edge of the shell exclusive of the bending moment induced by the thermal moment, M_t; also the value of M corresponding to the minimum-stress boundary conditions, inch-lb/inch
$\hat{M}_\alpha$	Value of M corresponding to the minimum-stress boundary conditions, inch-lb/inch
M_ϕ	Bending moment perpendicular to the local meridional plane, per unit circumferential length, inch-lb/inch
M_θ	Bending moment tangent to the local meridian, per unit meridional length, inch-lb/inch

NOMENCLATURE (Continued)

M_t	Uniform thermal moment throughout the shell, inch-lb/inch
N_ϕ	Membrane force in a meridional direction, lb/inch
N_θ	Membrane force in a circumferential direction, lb/inch
p_1	Pressure on the concave surface of the shell, psi
p_2	Pressure on the convex surface of the shell, psi
p	$p_2 - p_1$, psi
Q_ϕ	Shear force in a meridional plane, per unit length perpendicular to the meridional plane, lb/inch
r_o	Parallel circle radius, $r_o = a \sin \phi$, inch
T_1	Uniform temperature on the concave surface of the shell, °C
T_2	Uniform temperature on the convex surface of the shell, °C
$T_o(\phi)$	Temperature of the middle surface of the shell expressed as a function of the colatitude angle, °C
$T(\phi)$	Temperature gradient through the thickness of the shell expressed as a function of the colatitude angle, °C/inch
U	aQ_ϕ, lb
V	Rotation (deflection) in the plane of the meridian of the tangent to the local meridian (positive rotation closes shell), radian
V_α	V at $\phi = \alpha$, radian
$\hat{V}_\alpha$	Edge rotation corresponding to the minimum-stress boundary conditions, radian
v	Displacement of shell along the local meridian (positive as ϕ increases), inch
w	Displacement (deflection) of the shell along the local normal (positive inward), inch

NOMENCLATURE (Continued)

z	Distance from the middle surface of the shell, inch
α	Colatitude angle of the shell's edge, radian or degree
α_e	Thermal coefficient of linear expansion, $(°C)^{-1}$
γ	Constant determined from boundary conditions, radian
δ	Increase (deflection) in the parallel circle radius, inch
δ_α	δ at $\phi = \alpha$, inch
$\hat{\delta}_\alpha$	Horizontal edge displacement corresponding to minimum-stress boundary conditions
λ	$\sqrt{\frac{a}{h}}$, no units
λ_o	$\sqrt[4]{3(1 - \nu^2)(a/h)^2}$, no units
ΔT	Temperature difference, $T_1 - T_2$, across thickness of shell, °C
θ	Azimuthal angle, radian or degree
ν	Poisson's ratio (no units)
σ	Stress, psi
σ_p	Membrane stress due to uniform pressure, psi
σ_t	Thermal stress due to ΔT, psi
σ_θ	Stress in circumferential direction due to $(V_\alpha, \delta_\alpha)$, psi
σ_ϕ	Stress in meridional direction due to $(V_\alpha, \delta_\alpha)$, psi
σ_θ^t	Total stress in circumferential direction due to all effects: pressure, thermal gradient, and edge deformation $(V_\alpha, \delta_\alpha)$, psi
σ_ϕ^t	Total stress in meridional direction due to all effects: pressure, thermal gradient, and edge deformation $(V_\alpha, \delta_\alpha)$, psi
ϕ	Colatitude angle, radian or degree
$\hat{\phi}$	Normalized colatitude angle, radian or degree
ψ	$(\alpha - \phi)$, radian or degree

Edge Stresses in Spherical-Shell Solar Receivers

1.0 INTRODUCTION

M.I.T. Lincoln Laboratory is evaluating the use of ceramic domes in a solar heated air receiver. One area being investigated is a method of sealing these domes around their edges to prevent leakage of the high-pressure air supply that is being heated. Another area requiring investigation and the subject of this work is the question of how ceramic domes of different depths should be supported mechanically to minimize the tensile and compressive stresses as these domes pass from room temperature to operating temperature near 1000°C. A solution to this problem requires consideration of the deflections and stresses in domes with fixed, free, pinned or other edge conditions. The dome is subjected to stresses arising from pressure loads and thermal loads due to temperature gradients through the thickness of the dome and radial temperature profiles along the surface of the dome. It is well known that ceramics prefer to operate under compressive rather than tensile forces.

1.1 Scope of Investigation

The object of this investigation is to perform calculations that will provide insight into the expected stresses in the dome under a variety of conditions. Primary attention is directed toward describing the deflections and stresses in spherical domes of uniform thickness subjected to uniform pressure loads and thermal gradients. No material other than silicon carbide was considered in the analyses. The results are used to design supports for spherical ceramic domes that will minimize stress levels encountered during operation.

1.2 Analytical Methods

The deflections and stresses experienced by a spherical dome are treated in detail in Timoshenko's Theory of Plates and Shells.[1] The methods and approximations given are used to fulfill most of the analytical requirements of this investigation. Timoshenko describes a spherical shell's response to uniform pressure and temperature differences acting across the thickness of the shell. He also describes the shell's response to a uniform horizontal force and moment acting at its edge. Finally, a combined response is obtained by superposition. These steps form the basis of the analytical procedure adopted in this work. Timoshenko's approximations for the deflections and stresses are relatively simple, and they were coded for machine calculation.

Substantial care was exercised to validate the resulting computer program. This was done by reproducing the results of the two examples in Ref. 1., and by confirming the results of hand calculations describing the stresses at the edge of a shell nominally identical to those under consideration. Each example in Ref. 1 provides an exact description of the tensile and compressive stress distributions over an entire spherical shell. The results of the machine calculations were within ±1 percent of the exact results thoroughout the region of applicability of the approximations (Section 2.1.2). The program was also used to perform a parametric study that considered several families of spherical shells and different boundary conditions. The results of these calculations are used to identify the significant structural requirements and limitations of the proposed dome.

Time allocations for the study did not permit a detailed examination of the deflections and stresses generated in shells with nonuniform temperature gradients over their surfaces. However, an appropriate reference providing such information is identified—Ref. 2—and the methods of the approach are outlined.

The temperature distribution of a spherical shell can be expressed in the form:

$$T(z,\phi) = T_0(\phi) + z\ T(\phi) \tag{1}$$

where z is the distance (either positive or negative) from the middle surface of the shell, and ϕ is the colatitude angle with respect to the shell's axis of symmetry. The functions $T_0(\phi)$ and $T(\phi)$ are each represented by a series of associate spherical functions of the first kind. The resulting normal and meridional displacements are represented by a series of Legendre polynomials. The relevant material given in Ref. 2 could be applied directly to the present problem of determining the maximum tensile and compressive stresses in the shell. The only important modification would be that of changing the variable ϕ (colatitude angle) to:

$$\hat{\phi} = \phi \frac{\alpha}{(\pi/2)} \tag{2}$$

where α is the colatitude angle of the circular edge. This would be necessary because the equations given in Ref. 2 are specialized to $\alpha = \pi/2$. The Gaussian quadrature formula used in wing theory (Ref. 3) would be very helpful in evaluating the required integrals. Neglecting the meridional variation in the shell's temperature sets aside questions concerning the thermal leakage (heat losses) through its supports, and its detailed response to thermal transients.

2.0 STRESS ANALYSIS

2.1 Theory and Limitations

The shell material is assumed to be perfectly elastic and to undergo deformations that are small compared to its thickness (nominally 0.125 inch). Young's modulus expresses the linear relationship between stress and strain, and the coefficient of thermal expansion expresses the linear relationship between temperature increase and linear expansion. Additional approximations are discussed as they are used. Unless stated otherwise, the shell is understood to have a nominal edge diameter of 12 inches.

It is convenient to begin the stress analysis of the shell by thinking of the stress as arising from two sources:

a. Pressure and temperature differences across the shell

b. Edge conditions that produce significant deformation.

The former is discussed in Section 2.2, the latter in Section 2.3. Superposing these sources of stress is discussed in Section 2.4. Several of the terms used in these Sections are illustrated in Fig. 1 whose terms are defined in the Nomenclature.

2.1.1 Minimum-Stress Boundary Conditions

It should be recognized at the beginning of the analysis that for specified temperature and pressure difference ($\Delta T, p$) across the thickness of the shell, there exist boundary conditions ($\hat{M}_\alpha, \hat{H}_\alpha$) at the edge of the shell that minimize both the tensile and compressive stresses in the shell (Figs. 2, 3). These boundary conditions are referred to as the minimum-stress boundary conditions. The minimum-stress boundary condition for the edge moment is:

$$\hat{M}_\alpha = \frac{-\alpha_e D(1 + \nu)}{h} \Delta T = M_t \tag{3}$$

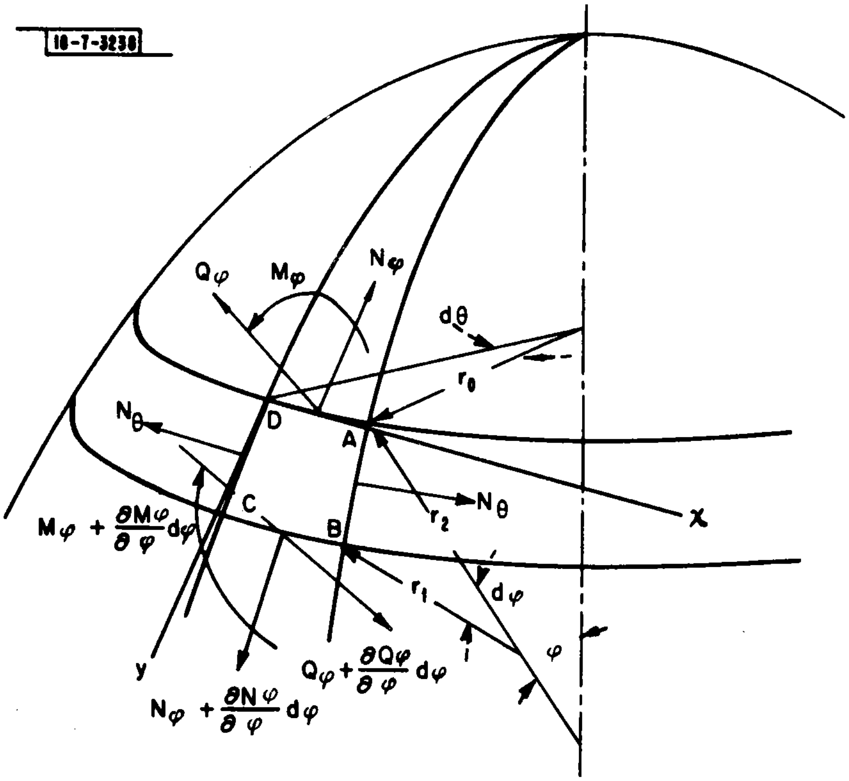

Fig. 1. Forces and moments acting on an elemental shell area: $r_1 = r_2 = a$.

where α_e = Thermal coefficient of linear expansion

h = Shell thickness

$D = Eh^3/\left\{12(1 - \nu^2)\right\}$

ΔT = Temperature difference across the thickness of the shell. ($T_{\text{outer surface}} < T_{\text{inner surface}}$)

$\hat{M}_t$ = Uniform thermal moment throughout the shell.

The minimum-stress boundary condition for the uniform horizontal force at the edge is:

$$\hat{H}_\alpha = \frac{pa}{2} \cos \alpha \tag{4}$$

where a = Radius of the spherical shell

p = Pressure difference across the thickness of the shell

α = Colatitude angle of the shell's edge.

Before showing why these boundary conditions are indeed minimum-

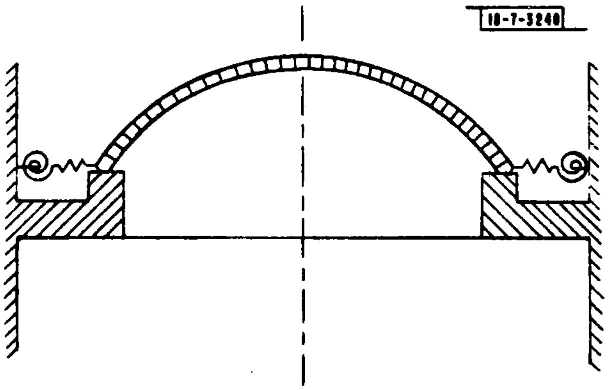

Fig. 3. (left) Shell support mechanism.

Fig. 2. (below) Summary of shell conditions and sign conventions from Ref. 1.

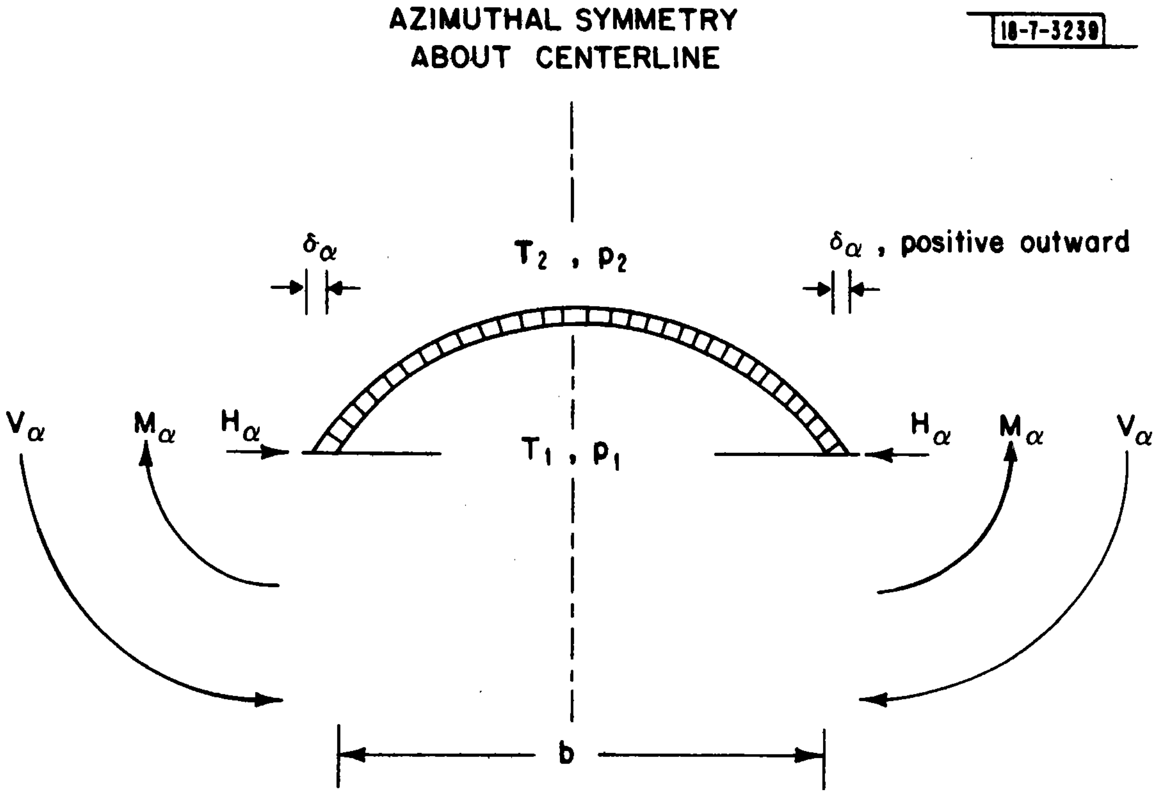

$T_1 - T_2 = \Delta T$

$p_2 - p_1 = p$

b = Edge diameter

V_α = Rotation at shell edge

M_α = Applied moment at shell edge

H_α = Discontinuity in horizontal component of membrane force at shell edge

δ_α = Increase of edge radius, b/2 stress boundary conditions, it is first necessary to discuss how these conditions are related to the uniform stresses in a complete, closed, spherical shell. Imagine a complete, closed, spherical shell whose polar cap has the same shape and thickness as the actual shell (Fig. 4a). Unlike the real shell, the polar cap has no edge, only a boundary specified by $\phi = \alpha$. $(\Delta T, p)$ are applied and the temperature of the shell's middle surface is not changed. The uniform bending moments throughout this complete spherical shell are:

$$M_\phi = M_\theta = \frac{-\alpha_e D(1+\nu)}{h} \Delta T \qquad (5)$$

The shell's uniform membrane force is given by:

$$N_\phi = N_\theta = -\frac{pa}{2} \qquad (6)$$

In response to the outside pressure, p, the radius of the shell contracts by an amount:

$$\begin{aligned} da &= \frac{a}{Eh}(N_\theta - \nu N_\phi) \\ &= -\frac{pa^2(1-\nu)}{2Eh} \end{aligned} \qquad (7)$$

A change in the radius of the shell induced by a uniform temperature elevation is not considered. It is merely assumed that the shell radius, a, is the unrestrained radius [except for the pressure, p] of the shell when its middle surface is at a uniform temperature. The maximum tensile stress occurs at the outer surface of the closed shell and is given by:

$$(\sigma_{\text{tensile}})_{\max} = -\frac{pa}{2h} + \frac{6\alpha_e D(1+\nu)}{h^2} \Delta T \qquad (8)$$

The maximum compressive stress occurs at the inner surface of the closed shell and is given by:

$$(\sigma_{\text{compression}})_{\max} = -\frac{pa}{2h} - \frac{6\alpha_e D(1+\nu)}{h^2} \Delta T \qquad (9)$$

In spite of the application of ΔT and p, the complete shell remains perfectly spherical, and the polar cap corresponding to the actual shell remains identified by $\phi \le \alpha$.

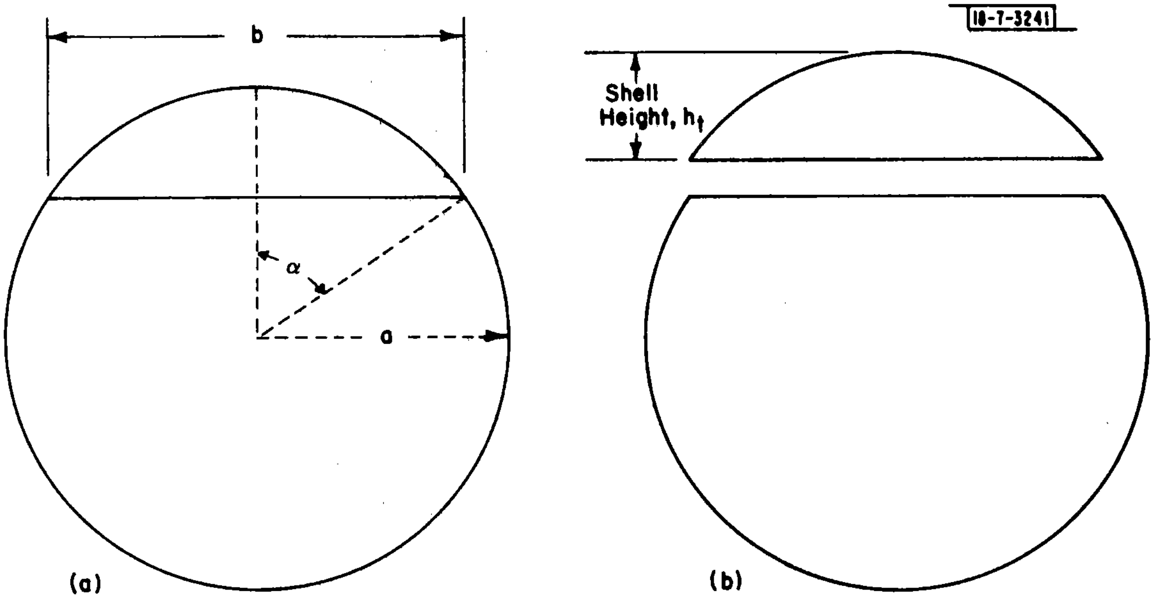

Fig. 4. Polar cap of closed spherical shell with no edge as opposed to real shell.

Imagine now that the polar cap is separated, without deformation, from the remainder of the shell by:

a. Maintaining the temperature and pressure differences across the surface of the new shell (formerly the polar cap of the complete shell).

b. Applying the uniform moment

$$\hat{M}_\alpha = \frac{-\alpha_e D(1 + \nu)}{h} \Delta T \qquad (3)$$

around the edge of the new shell

c. Applying the membrane force

$$N_\phi = -\frac{pa}{2} \qquad (4)$$

around the edge of the new shell; this membrane force must be tangent to the shell at its edge; i.e.,

$$\hat{H}_\alpha = \frac{pa}{2} \cos \alpha$$

If this is done, the stress distribution in the separated shell will be identical to the stress distribution in the polar cap of the entire spherical shell. Furthermore, this stress distribution is uniform. The forces at the edge are shown in Fig. 5.

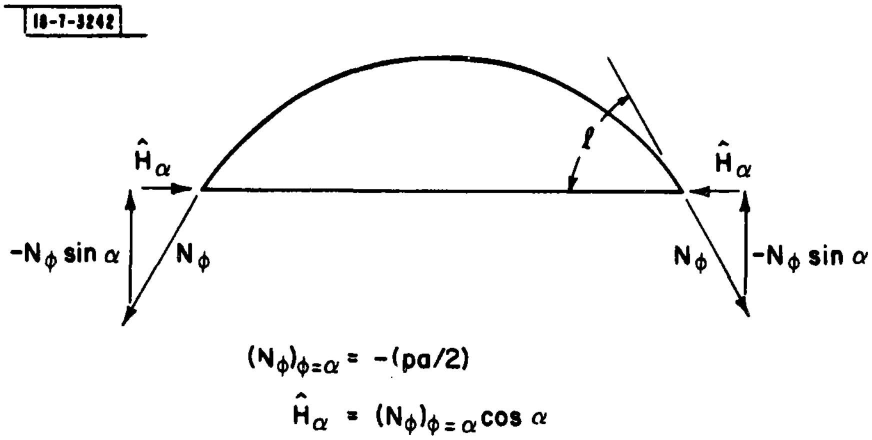

Fig. 5. Edge-reaction forces for the minimum-stress boundary conditions.

The question now is: Why are the foregoing boundary conditions minimum-stress boundary conditions? A rigorous proof is not offered, but the rhetorical question is confirmed by the results of the parametric study. It is also observed that any other boundary conditions will induce a nonuniform deformation of the shell; i.e., the shell does not remain a perfectly spherical dome.

Now that the minimum-stress boundary conditions have been identified, how can they be used to aid in the design of the shell's edge support? In particular, is not the boundary condition, $H = \hat{H}_\alpha$, relatively easy to apply? Unfortunately, no. For H to equal $\hat{H}_\alpha$, the supporting reaction force must be tangent to the shell and follow exactly the horizontal expansion and contraction of the edge throughout the thermal cycle of the shell. The shell's edge must also contract by the amount (Eq. 7):

$$-\frac{pa^2(1 - \nu)}{2EH} \quad \sin \alpha \qquad (10)$$

Although minimum-stress boundary conditions may not be easy to achieve, they are significant to this analysis because:

a. Minimum-stress boundary conditions represent an optimum; stresses given by Eqs. (8) and (9) must be acceptable.

b. They provide a basis for the parametric study. After allowing for the contraction given by Eq. (10), a shell's maximum tensile and compressive stresses are conveniently expressed as functions of the horizontal and rotational motion of its edge.

c. All subsequent stresses are understood to be superposed on the minimum stresses.

In the next Section, the responses of a spherical shell to the general boundary conditions (M_α, H_α) are discussed. At any point in the shell, the total tensile or compressive stress can then be obtained from:

$$\sigma_{total} = \sigma_{(\hat{M}_\alpha, \hat{H}_\alpha)} + \sigma_{(M_\alpha, H_\alpha)} \tag{11}$$

2.1.2 Timoshenko's Approximation

In Chapter XII of Ref. 1, the following system of linear differential equations is derived:

$$\begin{aligned} L(U) + \frac{\nu}{a} U &= EhV \\ L(V) - \frac{\nu}{a} V &= -\frac{U}{D} \end{aligned} \tag{12}$$

where $U = aQ_\phi$

$$V = \frac{1}{a}\left(v + \frac{dw}{d\phi}\right)$$

and the differential operation $L(\ldots)$ is given by:

$$L(\ldots) = \frac{1}{a}\left[\frac{d^2}{d\phi^2}(\ldots) + \cot\phi \frac{d}{d\phi}(\ldots) - \cot^2\phi\,(\ldots)\right]$$

The remainder of the terms are defined in the Nomenclature. This system of equations is derived from the equations of equilibrium describing the forces and moments acting on a differential element (Fig. 1) of a spherical shell of constant thickness. Using the notation:

$$\mu^4 = \frac{Eh}{D} - \frac{\nu^2}{a^2} \tag{13}$$

both equations can be reduced to the form:

$$LL(U) + \mu^4 U = 0 \tag{14}$$

This equation can be rewritten:

$$z^{IV} + \alpha_2 z^{II} + \alpha_1 z^{I} + (\beta^4 + \alpha_o) = 0 \tag{15}$$

where $z = Q_\phi \sqrt{\sin\phi}$

$$a_o = -\frac{63}{16\sin^4\phi} + \frac{9}{8\sin^2\phi} + \frac{9}{16}$$

$$a_1 = \frac{3\cos\phi}{\sin^3\phi}$$

$$a_2 = -\frac{3}{2\sin^2} + \frac{5}{2}$$

$$4\beta^4 = (1 - \nu^2)(1 + \frac{12a^2}{h^2})$$

Now approximations are applied. For thin shells, $\frac{a}{h} \gg 1$ and $4\beta^4$ are very large compared to a_o, a_1, and a_2 if the angle ϕ is not small. Applying this approximation, it is found that:

$$z^{IV} + 4\beta^4 z = 0 \tag{16}$$

whose general solution is:

$$Q_\phi = \frac{1}{\sqrt{\sin\phi}} e^{\beta\phi}(C_1\cos\beta\phi + C_2\sin\beta\phi) + e^{-\beta\phi}(C_3\cos\beta\phi + C_4\sin\beta\phi)$$

In the case of a sphere without a hole at the top, it is permissible to set C_3 and C_4 equal to zero; i.e., Q_ϕ must remain finite as ϕ approaches zero. Based on similar consideration, Timoshenko introduces the simplified system of equations:

$$\begin{aligned} \frac{d^2Q_1}{d\phi^2} &= EhV_1 \\ \frac{d^2V_1}{d\phi^2} &= -\frac{a^2}{D}Q_1 \end{aligned} \tag{17}$$

where $Q_1 = Q_o \sqrt{\sin \phi}$

$V_1 = V \sqrt{\sin \phi}$

and then Timoshenko obtains the equations that are used in the computer program:

$$\begin{aligned} Q_\phi &= C \frac{e^{-\lambda_o\psi}}{\sqrt{\sin(\alpha - \psi)}} \sin (\lambda_o\psi + \gamma) \\ V &= \frac{2\lambda_o^2}{Eh} C \frac{e^{-\lambda_o\psi}}{\sqrt{\sin(\alpha - \psi)}} \cos (\lambda_o\psi + \gamma) \\ N_\phi &= -\cot (\alpha - \psi)\ C \frac{e^{-\lambda_o\psi}}{\sqrt{\sin(\alpha - \psi)}} \sin (\lambda_o\psi + \gamma) \\ N_\theta &= C \frac{\lambda_o\ e^{-\lambda_o\psi}}{2\sqrt{\sin(\alpha-\psi)}}[2\cos(\lambda_o\psi+\gamma)-(k_1+k_2)\sin(\lambda_o\psi+\gamma)] \\ M_\phi &= \frac{a}{2\lambda_o} C \frac{e^{-\lambda_o\psi}}{\sqrt{\sin(\alpha-\psi)}}[k_1\cos(\lambda_o\psi+\gamma)+\sin(\lambda_o\psi+\gamma)] \\ M_\theta &= \frac{a}{4\nu\lambda_o} C \frac{e^{-\lambda_o\psi}}{\sqrt{\sin(\alpha-\psi)}}[1+ \nu^2)(k_1+k_2)-2k_2]\cos(\lambda_o\psi+\gamma) \\ &\quad + 2\nu^2\sin(\lambda_o\psi+\gamma)] \\ \delta &= \frac{a\ \sin(\alpha-\psi)}{Eh} C \frac{\lambda_o\ e^{-\lambda_o\psi}}{\sqrt{\sin(\alpha-\psi)}}[\cos(\lambda_o\psi+\gamma)-k_2\sin(\lambda_o\psi+\gamma)] \end{aligned} \tag{18}$$

where $\psi = \alpha - \phi$

C and γ are integration constants

$$\lambda_o = \left\{3(1 - \nu^2)\left(\frac{a}{h}\right)^2\right\}^{1/4}$$

$$k_1 = 1 - \frac{1 - 2\nu}{2}\cot(\alpha - \psi)$$

$$k_2 = 1 - \frac{1 + 2\nu}{2}\cot(\alpha - \psi)$$

Applying first the boundary conditions:

$$\begin{aligned} (M_\phi)_{\phi=\alpha} &= M \\ (N_\phi)_{\phi=\alpha} &= 0 \end{aligned} \qquad (19)$$

then the boundary conditions (Fig. 6):

$$\begin{aligned} (M_\phi)_{\phi=\alpha} &= 0 \\ (N_\phi)_{\phi=\alpha} &= -H_\alpha \cos\alpha \end{aligned} \qquad (20)$$

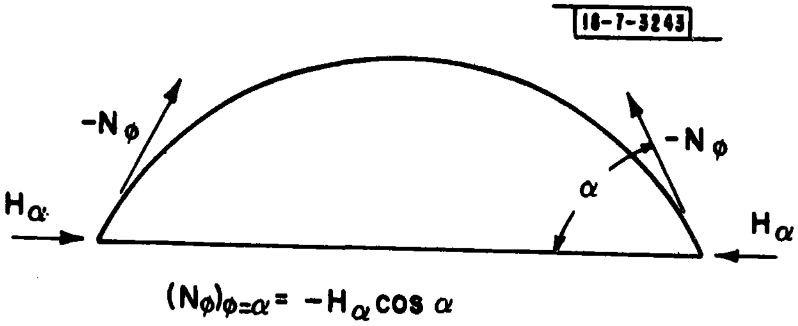

Fig. 6. Edge-reaction force that causes a discontinuity in the membrane force across the shell-support interface.

and using the reciprocity theorem, the following matrix equation is obtained that applies only at the edge of the shell:

$$\begin{bmatrix} \frac{-4\lambda_o^3}{Eahk_1} & \frac{2\lambda_o^2 \sin\alpha}{Ehk_1} \\ \frac{2\lambda_o^2 \sin\alpha}{Ehk_1} & -\frac{\lambda_o a \sin^2\alpha}{Eh}\left(k_2 + \frac{1}{k_1}\right) \end{bmatrix} \begin{Bmatrix} M_\alpha \\ H_\alpha \end{Bmatrix} = \begin{Bmatrix} V_{\psi=0} \\ \delta_{\psi=0} \end{Bmatrix} \qquad (21)$$

The edge conditions, $V_{\psi=0}$ and $\delta_{\psi=0}$, are used to evaluate the integration constants:

$$\gamma = \tan^{-1}\frac{1}{k^2}\left(1 - \frac{C_3}{C_1}\right)$$

$$C = \frac{C_1}{\cos\gamma}$$

where $C_3 = \delta_{\psi=0}\,\dfrac{Eh}{a\lambda_o\sqrt{\sin\alpha}}$

$$C_1 = -V_{\psi=0}\,\frac{Eh\sqrt{\sin\alpha}}{2\lambda_o^2}$$

The boundary condition, $(N\phi)_{\phi=\alpha} = -H_\alpha\cos\alpha$, is not to be confused with the minimum-stress boundary condition, $\hat{H}_\alpha = (N\phi)_{\phi=\alpha}\cos\alpha$. Following the notation of Ref. 1, the quantity, $(N\phi)_{\phi=\alpha}$, has quite different meanings in the two cases. The membrane force that keeps the shell in vertical equilibrium is:

$$(N\phi)_{\phi=\alpha} = -\frac{pa}{2} \tag{22}$$

The horizontal force, $\hat{H}_\alpha$, simply maintains the continuity of the membrane force across the shell-support interface. The horizontal force, H_α, appearing in Eq. (20) induces a discontinuity, $H_\alpha\cos\alpha$, in the membrane force at the shell-support interface; i.e., the total membrane force at the edge of the shell is:

$$\left[(N\phi)_{\phi=\alpha}\right]_{\text{total}} = -\frac{pa}{2} + \left[(N\phi)_{\phi=\alpha}\right]_{\text{due to }(M_\alpha,H_\alpha)} \tag{23}$$

The total horizontal force at the shell edge is:

$$H = \hat{H}_\alpha + H_\alpha \tag{24}$$

Similarly, the total moment at the edge is:

$$M = \hat{M}_\alpha + M_\alpha \tag{25}$$

The superposition of the membrane force that maintains the shell's vertical equilibrium and the membrane force arising from the moment and force (M_α,H_α) at the shell edge is discussed in the next Section; the superposition of $\hat{M}_\alpha$ and M_α is also discussed. The boundary conditions that maintain the continuity of the membrane forces across the shell-support interface are the minimum-stress boundary conditions, and the effect of any deviation (V_α, δ_α) from these maximum-stress boundary conditions is described by Eqs. (18). Equations (18) become less accurate as ϕ tends to zero. For example, results obtained by the computer program begin to deviate from exact [Eqs. (18)] results shown in Fig. 7 when $\phi < 7.5°$. At $\phi = 1°$, the deviation is as high as a factor of 2. The important point, however, is this: For the shells under consideration ($a/h \gg 1$), the effect of the edge moment and force always "damps out" as ϕ tends to zero, and the maximum values of the tensile and compressive stresses usually lie in the region of applicability of Eqs. (18). The values of the stresses are obtained from the following equations:

$$
\begin{aligned}
(\sigma_\theta)_{\text{top surface}} &= \frac{N_\theta}{h} - \frac{6M_\theta}{h^2} \\
(\sigma_\theta)_{\text{bottom surface}} &= \frac{N_\theta}{h} + \frac{6M_\theta}{h^2} \\
(\sigma_\phi)_{\text{top surface}} &= \frac{N_\phi}{h} - \frac{6M_\phi}{h^2} \\
(\sigma_\phi)_{\text{bottom surface}} &= \frac{N_\phi}{h} + \frac{6M_\phi}{h^2}
\end{aligned}
\qquad (26)
$$

2.1.3 Superposition of Minimum-Stress Boundary Conditions and Timoshenko's Approximation

Equations (18) in Section 2.1.2 and the minimum-stress boundary conditions discussed in Section 2.1.1. are two separate and distinct considerations. Equations (18) describe the moments and membrane forces resulting from some specified rotation and horizon-

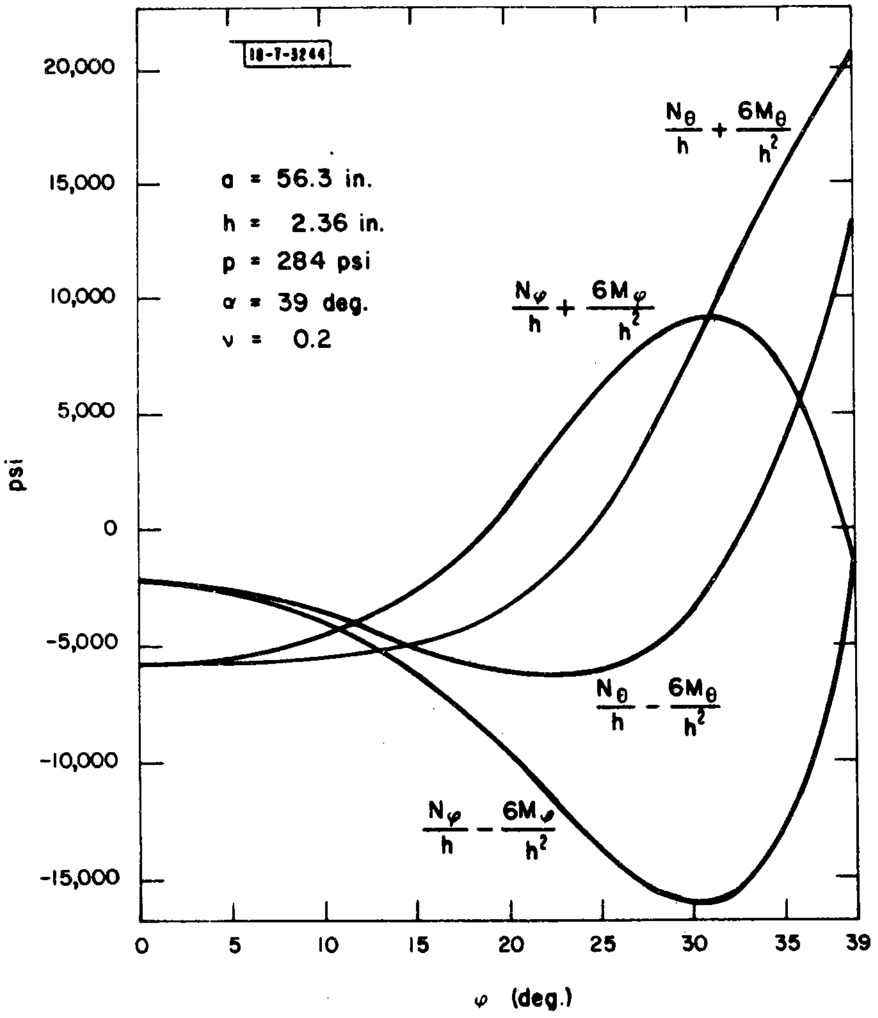

Fig. 7. "Exact" data from Ref. 1 for free-edge boundary condition.

tal displacement (V_α, δ_α) at the edge of the shell. The minimum-stress boundary conditions ($\hat{M}_\alpha$, $\hat{H}_\alpha$) are the boundary conditions that minimize the maximum values of the tensile and compressive stresses in a shell having a uniform thermal and pressure gradient (ΔT,p) across its thickness. The steps in the superposition procedure are as follows:

1. The spherical shell is initially assumed to be undeformed with no forces or moments acting anywhere.
2. Uniform thermal and pressure gradients (ΔT,p) are applied to the shell. The temperature of the shell's middle surface is unchanged. The edge of the shell is unrestrained. Applying (ΔT,p) deforms the shell in some unspecified manner.

3. Minimum-stress boundary conditions ($\hat{M}_\alpha$, $\hat{H}_\alpha$) are applied, and the resulting maximum stress determined using:

$$(\sigma_\theta)_{max} = (\sigma_\phi)_{max} = \frac{6\hat{M}_\alpha}{h^2} + \frac{pa}{2h} \tag{27}$$

Applying ($\hat{M}_\alpha$,$\hat{H}_\alpha$) restores the shell to its initial spherical shape, but its initial radius, a, is decreased due to the application of p (Section 2.1.2). All subsequent deformations of the shell are measured with respect to its shape after the application of p and the minimum-stress boundary conditions, i.e.,

$$\begin{Bmatrix} \hat{V}_\alpha \\ \hat{\delta}_\alpha \end{Bmatrix} = \begin{Bmatrix} 0 \\ 0 \end{Bmatrix} \tag{28}$$

after these conditions are applied. In most subsequent work, it is assumed that the decrease in the shell's initial radius due to the application of p is negligible. This decrease is included in the printed output of the computer program so that it can be compared to subsequent horizontal displacements of the edge.

4. Equations (18) are used to compute the stress distributions over the shell resulting from the prescribed edge deformation $\{V_\alpha,\delta_\alpha\}$ (Section 2.1.2). These stress distributions are unrelated to the minimum-stress boundary conditions. Usually, the reduction in the shell's radius due to p is negligible. If it is not, a small adjustment in the prescribed value of δ_α is made to account for this reduction.
5. Each uniform stress calculated in step 3 is added to the corresponding stress distribution calculated in step 4.

Step 5 provides the tensile and compressive stress distributions from which the maximum values are obtained.

The value of the prescribed edge deformation $\{V_\alpha,\delta_\alpha\}$ depends on the edge conditions. The effect of a uniform temperature elevation on a shell with a fixed edge (displacement and rotation) can be fully accounted for by setting δ_α equal to the horizontal displacement of the shell's middle surface which is <u>prevented</u> by the fixed-edge boundary conditions. For example, if a uniform temperature elevation implies that the unrestrained middle surface of the shell would expand horizontally by 0.030 inch, the fixed-boundary conditions imply that the shell is subjected to a displacement, δ_α, of -0.030 inch. Reference 1 contains other examples of how edge conditions can be applied by adjusting $\{V_\alpha, \delta_\alpha\}$. Frequently, the edge conditions are prescribed by $\{M_\alpha, H_\alpha\}$ rather than $\{V_\alpha, \delta_\alpha\}$. When this is done, $\{V_\alpha, \delta_\alpha\}$ can be obtained from Eq. (21).

2.2 Computer Program

A computer program was written that calculates the maximum values of the tensile and compressive stresses occurring in spherical shells. The program begins by using the boundary values (M_α, H_α) or $(V_\alpha, \delta_\alpha)$ to calculate $\sigma_\theta(\phi_i)$ and $\sigma_\phi(\phi_i)$ for $i = 1, 2, \ldots i_{max}$. Equations (18) and (26) are used to do this. Next, the thermal moment is calculated using Eq. (3), and the pressure stress, σ_p, is calculated using:

$$\sigma_p = -\frac{pa}{2h} \tag{29}$$

The thermal stresses are calculated using:

$$\begin{aligned} \sigma_{t,\text{ lower surface}} &= -\frac{6M_t}{h^2} \\ \sigma_{t,\text{ upper surface}} &= \frac{6M_t}{h^2} \end{aligned} \tag{30}$$

The total stresses at colatitude angle ϕ_i, and on the upper surface of the shell, are calculated using

$$\begin{aligned} \sigma^t_{\theta,\text{upper surface}}(\phi_i) &= \sigma_\theta(\phi_i) + \sigma_p + \sigma_{t,\text{ upper surface}} \\ \sigma^t_{\phi,\text{upper surface}}(\phi_i) &= \sigma_\phi(\phi_i) + \sigma_p + \sigma_{t,\text{ upper surface}} \end{aligned} \tag{31}$$

The total stresses at ϕ_i, and on the lower surface of the shell, are calculated using

$$\sigma^t_{\theta,\text{ lower surface}}(\phi_i) = \sigma_\theta(\phi_i) + \sigma_p + \sigma_{t,\text{ lower surface}}$$

$$\sigma^t_{\phi,\text{ lower surface}}(\phi_i) = \sigma_\phi(\phi_i) + \sigma_p + \sigma_{t,\text{ lower surface}} \qquad (32)$$

The program determines the maximum tensile and compressive stresses in the shell by selecting the maximum and minimum values from the total stresses:

$$\left.\begin{array}{l} \sigma^t_{\theta,\text{ upper surface}}(\phi_i) \\ \sigma^t_{\phi,\text{ upper surface}}(\phi_i) \\ \sigma^t_{\theta,\text{ lower surface}}(\phi_i) \\ \sigma^t_{\phi,\text{ lower surface}}(\phi_i) \end{array}\right. \quad i = 1,2,\ldots i_{max} \qquad (33)$$

2.2.1 Computer Program Inputs

The following variables are required by the computer progarm:

a. Shell height in inches [HH]

b. Edge diameter in inches [B]

c. Shell thickness in inches [H]

d. Young's modulus in psi [E]

e. Poisson's ratio [PR]

f. Coefficient of thermal expansion in (centigrade degrees)$^{-1}$ [ALPHAT]

g. Pressure difference across the thickness of the shell in psi [PRESS]

h. Temperature difference across the thickness of the shell in degrees centigrade [GRADT]

i. Horizontal edge displacement, δ_α,[DZ]

j. Edge rotation, V_α,[DV]

k. Number of colatitude angles, ϕ, at which the stresses are to be calculated [IPHI]. The maximum value of IPHI is 101.

In addition to this basic list, the user has the following options:

a. The geometry of the shell can be defined by the colatitude angle of the edge and the shell's radius rather than the shell's height and edge diameter [controlled by IFIX].

b. A sequence of values of the horizontal edge displacement, δ_α, and edge rotation, V_α, can be accommodated during one execution. Consequently, a matrix of combinations of V_α and δ_α can be accommodated. The number of different values of V_α is specified by JPMAX, and the number of different values of δ_α is specified by IPMAX. The incremental value of V_α is DVZ, and the incremental value of δ_α is DDZ.

c. (M_α,H_α) rather than (V_α,δ_α) can be specified. The program does not accommodate a sequence of values of either M_α or H_α.

All of these variables are discussed further in Section 2.2.5, which gives a card-by-card description of the data deck.

2.2.2 Computer Program Output

The complete output of a sample problem is given in Appendix B. This output consists of three pages, and most of the labels are self-explanatory. Further explanation may be appropriate in the following cases:

SIGMA(P) is the stress throughout the shell due only to the pressure, p; it is positive in tension.

HOR. MEM. FORCE is the horizontal component of the membrane force, N_ϕ, at the edge of the shell due only to the pressure, p; it is positive inward.

DELTA(P) is the horizontal displacement of the edge of the shell due only to the pressure, p, when H_α is zero. DELTA(P) is positive outward.

THERMAL MOMENT is the uniform thermal moment throughout the shell due only to the THERMAL DIFFERENCE, ΔT, across the thickness of the shell.

SIGMA(T) is the maximum thermal stress experienced by the shell due only to the THERMAL DIFFERENCE, ΔT. This maximum stress occurs at the inner (compression) and outer (tension) surfaces of the shell.

The program requires that the shell's support conditions be specified in the input data. The required support conditions are either (M_α,H_α) or (V_α,δ_α). If (M_α,H_α) is specified in the input data, the calculated values of V_α and δ_α are printed. Alternatively, if (V_α,δ_α) is specified, the values of M_α and H_α are printed. The printed output states that support conditions were specified in the input data and were obtained by using Eq. (21). The support conditions (V_α,δ_α) are also the shell's rotation and displacement boundary conditions; the support conditions (M_α,H_α) are, however, not the shell's moment and horizontal membrane force boundary values. H_α is the horizontal force at the edge of the shell exclusive of the horizontal force reacting against the membrane force induced by the pressure difference [Eq. (23)]. M_α is the difference between the total edge moment, M, and the edge moment that effects the minimum-stress boundary conditions [Eq. (25)]. For example, if $T \neq 0$, and the edge is free to rotate, the boundary value of M is $(M)_{\phi=\alpha} = 0$ whereas $M_\alpha = -M_{\text{thermal}}$. If $(M)_{\phi=\alpha} = 0 = M_{\text{thermal}}$, then $M_\alpha = 0$, Regardless of which pair of variables is specified in the input data, the shell's stress distribution is determined by using (V_α,δ_α). Sometimes it is simply more convenient to enter (M_α,H_α) rather than (V_α,δ_α); an example is the free-edge boundary condition mentioned in Section 2.2.3. The remaining variables on the first page of printed output [C,GAMMA,LAMBDA,C1, C3,K1,K2] are intermediate results that are useful if one wishes to check hand calculations.

The data on the second page of the printed output give the values of the following variables as a function of the colatitude angle, ϕ: Q_ϕ, V_ϕ, N_ϕ, N_θ, M_ϕ, M_θ, and δ. The data on the third pages give σ_θ and σ_ϕ on the top and bottom surfaces of the shell as a function of the colatitude angle, ϕ. The maximum and minimum values of all these stresses are printed at the bottom of the third page.

If several cases are submitted at the same time, the output corresponding to each case is printed separately.

2.2.3 Computer Program Validation

The computer program was validated by checking the program's results against sample data given in Ref. 1 and the results of hand calculations. The two cases of sample data obtained from Ref. 1 are given in Figs. 7, 8, and 9. Figure 7 shows σ_θ and σ_ϕ at the top and bottom surfaces of a spherical shell subject only to a pressure difference across its thickness. The boundary conditions are (Fig. 10):

$$H_\alpha = -\frac{pa}{2}\cos\alpha, \quad M_\alpha = 0 \qquad (34)$$

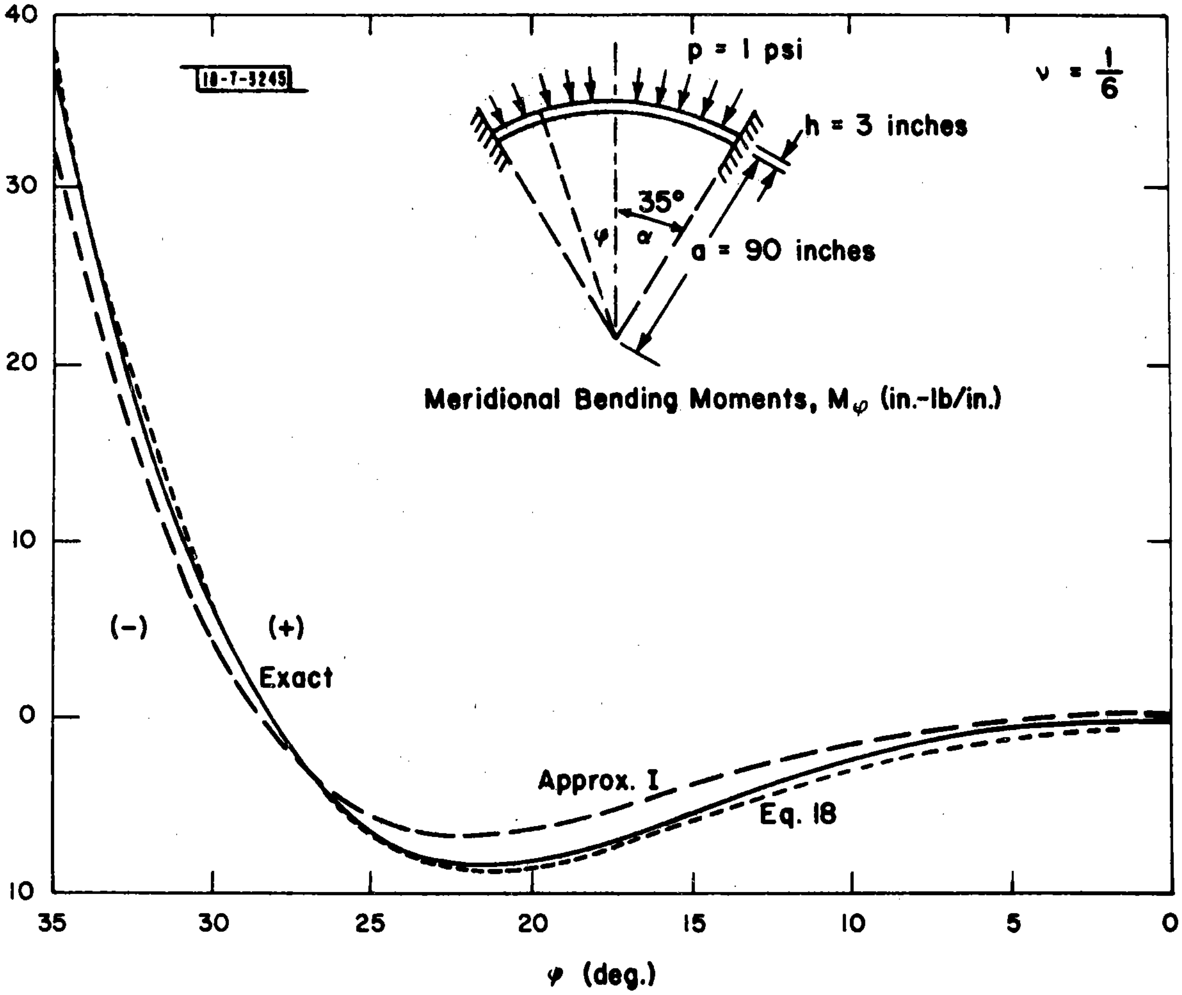

Fig. 8, "Exact" and approximate data from Ref. 1 for fixed-edge boundary condition.

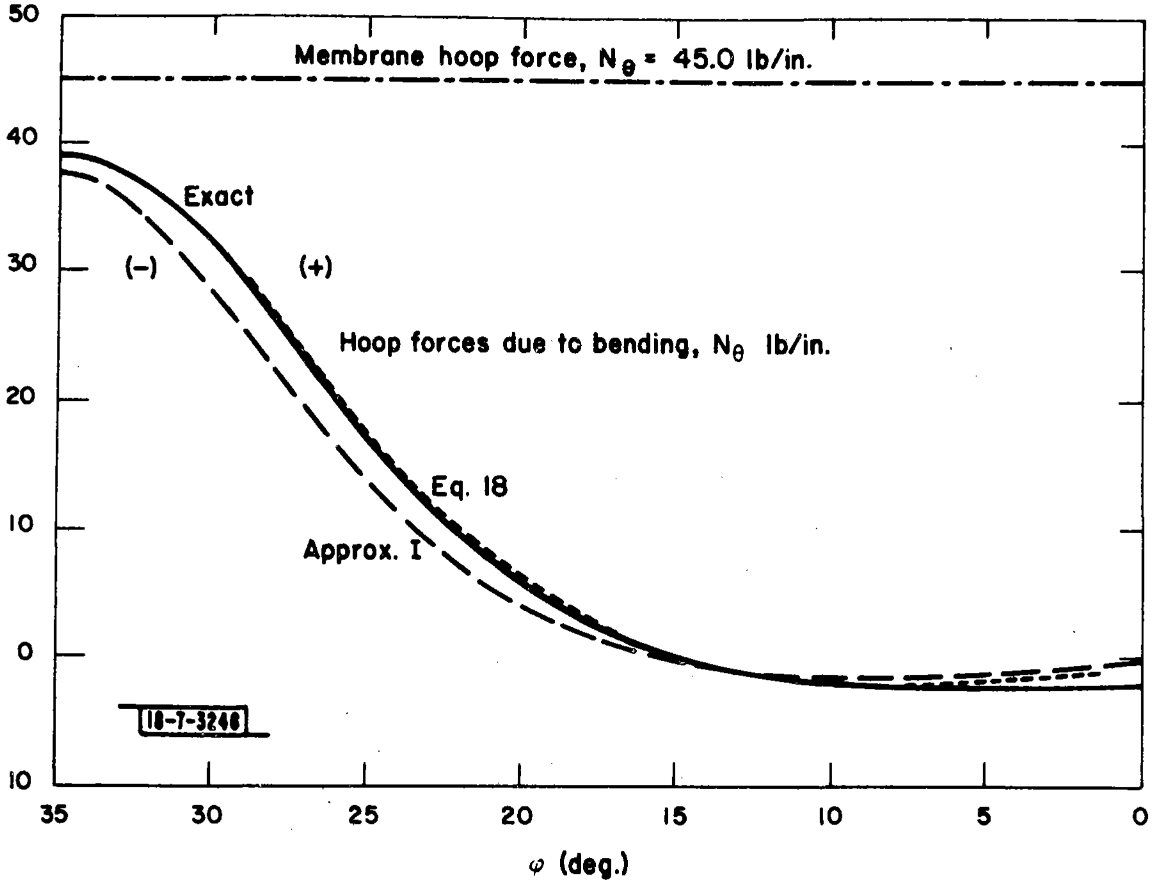

Fig. 9. "Exact" and approximate data from Ref. 1 for fixed-edge boundary condition.

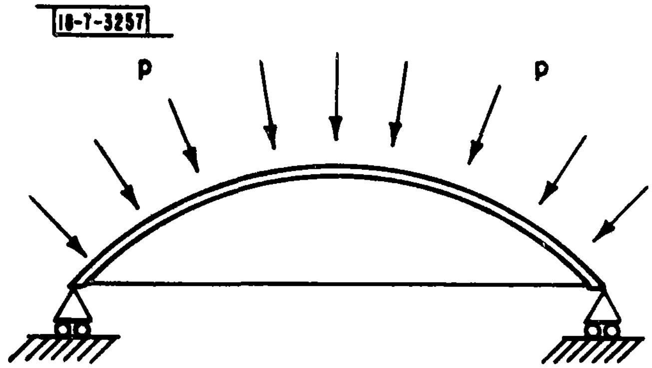

Fig. 10. Free-edge boundary condition.

The edge of the shell is free to expand and rotate as a result of the uniform pressure, p, until the edge support of the shell exerts only a vertical force on the shell (Ref. 1). The data given in Fig. 7 are for an "exact" solution, not the approximate solution obtained by the computer program (Section 2.1.2). The data given in Fig. 7 are in agreement with the computer program's output to within one percent over the range, $\phi > 7.5°$. For $\phi < 7.5°$, the lack of agreement between the approximate and "exact" solution can be accounted for by the nature of the approximate solution. Figures 8 and 9 show values of M_ϕ and N_ϕ for a different spherical shell, again subject only to a pressure difference across the thickness; the boundary conditions are now (Fig. 8):

$$\delta_\alpha = 0, \; V_\alpha = 0 \tag{35}$$

In this case, the approximate solutions for M_ϕ and N_ϕ are shown along with the "exact" solutions. The agreement of the published approximate solutions and the calculated approximate solutions was within 1/2 percent over the entire range of the colatitude angle (0 to 35°). No published solution was found for a shell subjected to both a uniform pressure and temperature difference across its thickness. Consequently, the edge conditions $[N_\theta, M_\theta, \sigma_\theta]$ for a silicon carbide shell with differences $(p, \Delta T)$ equal to (60 psi, -222°C) were calculated by hand and are in satisfactory agreement with the output of the computer program. The calculation was for the free-edge boundary condition shown in Fig. 10. The input data were:

$$\begin{aligned} HH &= 1.8 \text{ inches} \\ B &= 12 \text{ inches} \\ H &= 0.25 \text{ inch} \\ E &= 5.4 \times 10^{7} \text{ psi} \\ PR &= 0.10 \\ ALPHAT &= 5.6 \times 10^{-6} \text{ per °C} \\ PRESS &= 60 \text{ psi} \\ GRADT &= -222\text{°C} \\ H &= -2.73 \times 10^{+2} \text{ pounds/inch} \\ M &= -3.88 \times 10^{+2} \text{ inch-pounds/inch} \end{aligned} \tag{36}$$

The temperature difference across the shell is negative; this is immaterial to the purpose of comparing machine and hand calculations. H_α is obtained from Eq. (29) and M_α from Eq. (5). Neglecting uniform pressure and thermal stresses, the following results were obtained:

$$(N_\theta)_{\phi=\alpha} = -3.16 \times 10^{+3} \text{ pound/inch}$$

$$(M_\theta)_{\phi=\alpha} = -9.35 \times 10^{+1} \text{ inch-pound/inch}$$

$$\sigma_{\theta,\text{upper edge}} = \frac{(N_\theta)_{\phi=\alpha}}{h} - \frac{6(M_\theta)_{\phi=\alpha}}{h^2} \tag{37}$$

$$= -3.5 \times 10^3 \text{ psi}$$

$$\sigma_{\theta,\text{lower edge}} = \frac{(N_\theta)_{\phi=\alpha}}{h} - \frac{6(M_\theta)_{\phi=\alpha}}{h^2}$$

$$= -2.5 \times 10^4 \text{ psi}$$

Superposing the values of σ_p and σ_t,

$$\sigma_p = - \frac{pa}{2h} = -1.3 \times 10^{+3} \text{ psi} \tag{38}$$

$$\sigma_{t, \text{ upper edge}} = -3.73 \times 10^4 \text{ psi}$$

$$\sigma_{t, \text{ lower edge}} = 3.73 \times 10^4 \text{ psi}$$

on these values of σ_θ, the following final results were obtained:

$$\begin{aligned} \sigma_{\theta, \text{ upper edge}} &= -4.23 \times 10^4 \text{ psi} \\ \sigma_{\theta, \text{ lower edge}} &= -1.44 \times 10^4 \text{ psi} \end{aligned} \tag{39}$$

The negative temperature difference across the thickness of the shell illustrates an interesting result. Using Eq. (21) to calculate $\delta\alpha$, the horizontal displacement at the edge, H_α is found to contribute to opening the shell at its edge by an amount equal to 1.14 mils, and M_α to closing the shell by an amount equal to 2.55 mils. The net result is a negative horizontal displacement of 1.4 mils; i.e., the thermal effect dominates the pressure effect. In the case of a positive temperature difference, the thermal and pressure effects each contribute to opening the shell.

2.2.4 Advantages and Disadvantages of Computer Program With Respect to Finite-Element Programs

The advantages of the computer program written in connection with this investigation include its very low cost of execution and the simplicity of its input data. The cost of obtaining output for one case is about ten cents. Only eleven input variables are required to execute an unlimited number of cases. This makes the program ideally suited for parametric studies.

The disadvantage of the program is that spherical shells with either a nonuniform thickness or temperature distribution cannot be considered. NASTRAN is an example of a finite-element program that permits these nonuniformities to be considered.

2.2.5 Card-by-Card Description of the Input Data Deck

Card 1

READ(5,2) IPMAX, JPMAX, IFIX FORMAT(10I5)

IPMAX is the number of different values of δ_α, the horizontal displacement of the shell at its circular edge, for which the program will calculate stress distributions.

JPMAX is the number of different values of V_α, the angular displacement of the shell at its circular edge, for which the program will calculate stress distributions.

Card 2

READ(5,1) HH,B,H FORMAT(4E15.4)

HH is the height of the shell in inches, B is the diameter of the circular edge of the shell in inches (Fig. 4).

H is the uniform thickness of the shell in inches.

Card 3

READ(5,1)VZ,DZ,MOMA,HZTL,DVZ,DDZ

FORMAT (4E15.4)

VZ is the initial value of V_α, the angular displacement of the shell at its circular edge, in radians. The program calculates first a stress distribution for V_α = VZ, and then repeats the calculation for increased values of V_α if required. The number of different values of V_α is specified by JPMAX; the program calculates the values of V according to V=VZ+(I-1)*DVZ where I=1, JPMAX.

DZ is the initial value of δ_α, the horizontal displacement of the shell at its circular edge, in inches. The program calculates first a stress distribution for δ_α = DZ, and then repeats the calculation for increased values of δ_α. The number of different values of δ_α is specified by IPMAX; the program calculates the values of δ_α according to δ_α = DZ+(I-1)*DDZ where I=1, IPMAX.

MOMA is the value of the edge, moment, M_α, in inch-pounds/inch.

HZTL is the value of the horizontal force, H_α, at the edge, in pounds/inch.

Note: Only (VZ,DZ) or (MOMA,HZTL) should be specified. The unspecified pair should be set to (0.,0.) in the input data. The value of the unspecified pair is calculated by the program using Eq. (21), and the results are printed.

DVZ is the incremental value of V_α, the angular displacement of the shell at its circular edge, in radians. The program calculates a stress distribution for an initial value of V_α and for successive increments, DVZ.

DDZ is the incremental value of δ_α, the horizontal displacement of the shell at its circular edge, in inches. The program calculates a stress distribution for an initial value of δ_α and for successive increments, DDZ.

Card 4

READ(5,1) PRESS FORMAT(4E15.4)

PRESS is the uniform pressure difference across the shell, p, in psi. A positive difference means the greater pressure acts on the upper surface (Fig. 2).

Card 5

READ(5,1) GRADT,ALPHAT   FORMAT(4E15.4)

GRADT is the uniform temperature difference across the shell, ΔT, in centigrade degrees. A positive difference means the lower surface is hotter (Fig. 2).

ALPHAT is the thermal expansion coefficient of the shell material in (centigrade degrees)$^{-1}$.

Card 6

READ(5,1) E, PR   FORMAT(4E15.4)

E is the young's modulus for the shell material in psi.

PR is Poisson's ratio for the shell material, no units.

Card 7

READ(5,2)IPHI   FORMAT(1015)

IPHI is the number of values of the colatitude angle, ϕ, for which the program will calculate moments and stresses. The program extracts maximum values of the shell's tensile and compressive stresses from the set of stresses calculated for the IPHI values of ϕ:

$$\frac{\alpha}{IPMI}, \frac{2\alpha}{IPHI}, \ldots\ldots, \frac{(IPHI-1)\alpha}{IPHI},$$

where α is the colatitude angle of the shell's circular edge.

3.0 RESULTS

3.1 Stress Distribution

Calculations were performed for shell thicknesses in the range from 1/16 to 1/4 inch and shell edge diameters from 6 to 36 inches using properties representative of Norton silicon carbide material. An example of the combined pressure and thermal stresses in a 1/8-inch-thick, 12-inch-diameter, hemispherical, silicon carbide shell with free edges as described by the analytical treatment is shown in Fig. 11. Variations in dome compressive and tensile stresses as a function of colatitude angle, ϕ, are illustrated and show that a maximum hoop stress of $\sigma_{\theta_{top}}$ = 9000 psi occurs in this example on the outside of the shell at its edge, ϕ/ϕ_{max} = 1. An

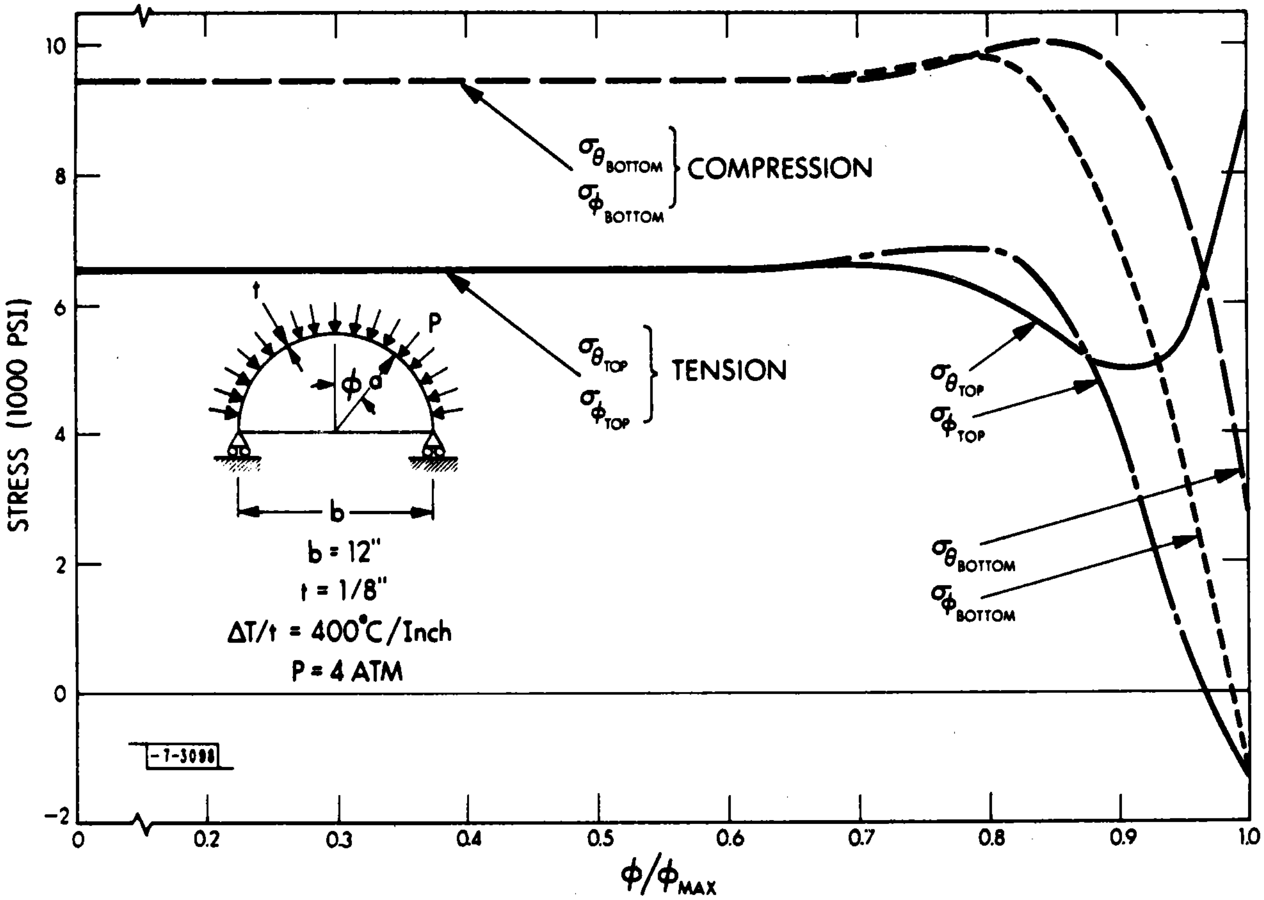

Fig. 11. Combined pressure and thermal stresses in a 12-inch-diameter, hemispherical silicon carbide shell with free edges.

example of the combined pressure and thermal stresses in a similar but shallower shell is shown in Fig. 12. The edge diameter is again 12 inches, but the height-to-edge-diameter ratio is now 0.2, and the shell's radius is 8.70 inches. Otherwise this example is the same as the previous one.

There is a substantial increase in the horizontal component of the membrane force at the edge of the shell, and the stresses are now more severe. The stress distribution is shown in Fig. 13. Again, the maximum stress is a hoop stress occurring along the

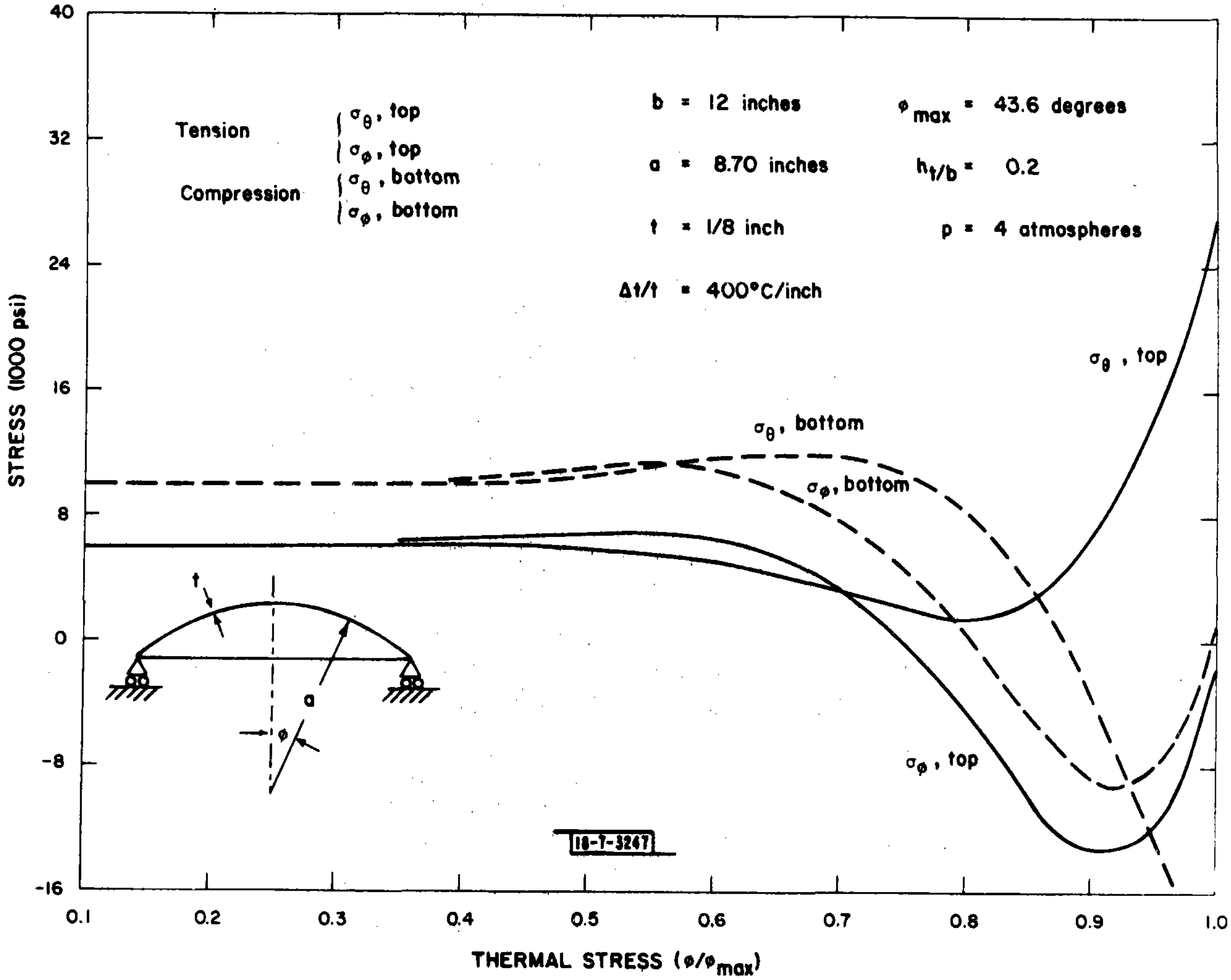

Fig. 12. Combined pressure and thermal stresses in a shallow 12-inch edge-diameter shell.

upper edge of the shell. In this case, the maximum stress is 28,000 psi. The results of applying the minimum-stress boundary conditions to similar shells of varying depth are shown in Fig. 13. When the minimum-stress boundary conditions are applied, the stress distribution is uniform over the surfaces of the shell, i.e., $\sigma_{\Delta T}$ and σ_p are independent of ϕ (Section 2.1.1). The thermal stress, $\sigma_{\Delta T}$, has a linear profile along a radius of the shell, and reaches its maximum tensile and compressive values at the outer and inner surfaces, respectively. In Fig. 13 the ordinate—maximum stress—is the tensile stress at the outer surface of the family of shells of varying λ.

In Fig. 13 the depth of the shell is characterized by the

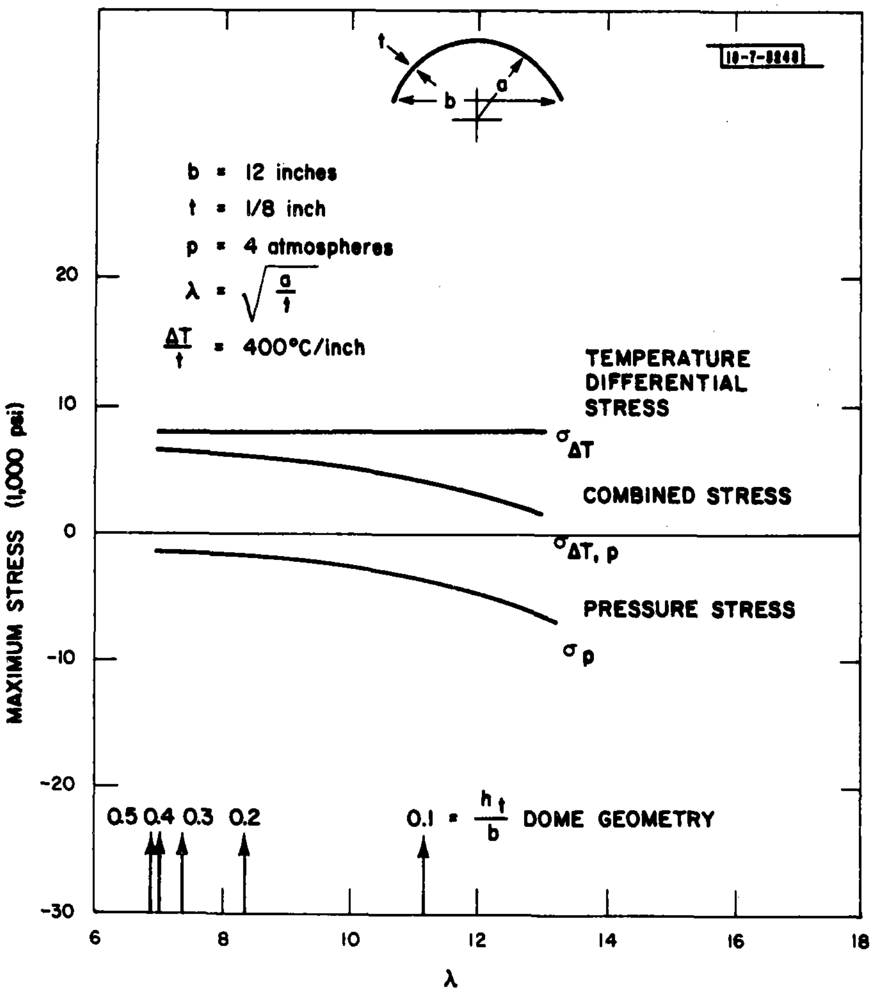

Fig. 13. Silicon carbide spherical shell stresses as a function of shell depth for the minimum-stress boundary condition.

variable

$$\lambda = \sqrt{\frac{a}{h}} \tag{40}$$

which is nearly equal to the variable λ_o appearing in Eqs. (18); λ and λ_o differ by a factor of about 1.3 depending on the value of Poisson's ratio. The tensile stress corresponding to the minimum-stress boundary conditions decreases as the shell becomes shallower. The reverse is true for the free-edge boundary condition. In the former case, the membrane stress always acts to reduce the thermal tensile stress, and in the latter case, the horizontal component of the membrane stress increases as the shell becomes shallower. The horizontal component of the membrane stress acts to open the shell, and the resulting deformation increases as the shell becomes shallower.

3.2 Maximum Stresses for the Free-Edge Boundary Condition

Maximum tensile stresses for the free-edge boundary condition were determined for a range of shell depths. These maximum stress levels were obtained from calculated stress distributions similar to those shown in Figs. 11 and 12. The results are shown in Fig. 14; the depth of the shell is again characterized by λ. The maximum pressure stress, σ_p, and the maximum temperature differential stress, $\sigma_{\Delta T}$, do not necessarily add to equal the combined maximum stress, $\sigma_{\Delta T,p}$. This is because the maximum stresses σ_p, $\sigma_{\Delta T}$, and $\sigma_{\Delta T,p}$ do not necessarily occur at a common colatitude angle, ϕ; also, each of these maximum stresses corresponds to quite different (ΔT,p) conditions (as indicated in the upper left-hand corner of Fig. 14). The pressure, p, acts to open the shell and produce positive (tensile) stresses at the inner surface of the shell.

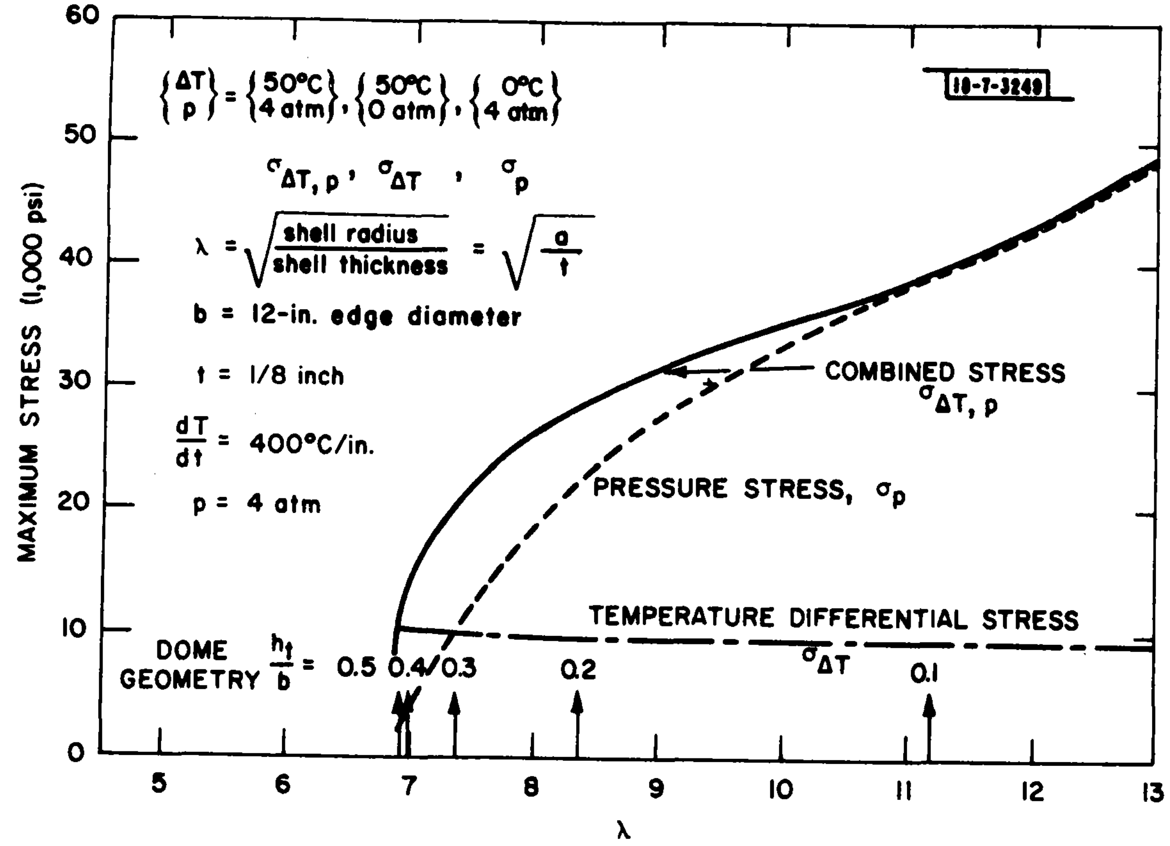

Fig. 14. Silicon-carbide, spherical-shell maximum stresses as a function of shell depth for the free-edge boundary condition.

3.3 Comparison of Maximum Stresses for Different Boundary Conditions

Maximum stresses in silicon carbide domes over a range of thicknesses and edge diameters are shown in Table I for two boundary conditions.

Table I

Maximum Stresses in Different SiC Spherical Shells

SHELL THICKNESS (inches)	EDGE DIAMETER (inches)	HEMISPHERICAL SHELL		SHALLOW SHELL $(h_t^*/b) = 0.2$	
		Clamped‡	Free (Trolley)	Clamped‡	Free (Trolley)
		(psi)			
1/16	6	+2400	+3900	+1950	+24,000
	12	+1000	+2500	-100	+64,300
	36	-4900	nc	-8800	nc
1/8	6	+9700	+10,000	+9400	+15,500
	12	+6500	+9000	+5950	+28,700
	36	+3900	+5800	+1700	+118,000
1/4	6	+15,700	+20,500	+15,400	+20,000
	12	+14,600	+20,000	+14,300	+24,900
	36	+12,800	+19,000	+11,900	+54,500

* Ratio of dome mid-height to span.
\+ Tensile stress.
\- Compressive stress.
nc Not calculated.

‡ No edge deformation. Minimum-stress boundary conditions, V_α and δ_α, both equal zero.

3.4 Limits on Edge Rotation and Displacement

Stress distributions were also calculated for a range of edge deformations. V_α and δ_α were assigned values between ±5 milliradians and ±5 mils, respectively. The computer program [Eqs. (18)] was used to calculate the resulting stresses. The results showed that combined deformations of the order of ±1 milliradian and ±1 mil produce a maximum tensile stress of the order of 30,000 psi in the 12-inch edge-diameter, silicon carbide shell discussed in Section 3.3. This result is only moderately affected by the depth of the shell and the thickness of the shell [as long as the temperature difference across the shell is unchanged]. The reader is cautioned that this is an approximate result. Positive values of V_α and δ_α of less than 1 milliradian and 1 mil will produce a maximum tensile stress in excess of 30,000 psi. Furthermore, this approximation <u>does</u> <u>not</u> include the stresses associated with minimum-stress boundary conditions. For completeness, the uniform stresses corresponding to null values of V_α and δ_α should be added to the stresses induced by any edge deformation (Section 2.1.3). These uniform stresses can act to increase or decrease resulting maximum tensile stress. The computer program is available to investigate specific cases.

4.0 CONCLUSIONS

The principal conclusion of this work is that it is possible to maintain the maximum tensile stress in a silicon carbide shell below an acceptable limit during the application under consideration. This application consists of using the shell to transfer heat from a solar radiation cavity-receiver to air impinging on the shell's outer (convex) surface. This conclusion applies to a nominal spherical shell whose thickness is 1/8 inch and whose edge diameter is 12 inches or less.

Minimum-stress boundary conditions exist when there are no edge deformations. Then the temperature of the middle surface of the shell is uniform, and its shape remains spherical. Under these circumstances the maximum tensile stress in the nominal shell described above is of the order of 10,000 psi. The computer program described herein can be used to calculate the maximum tensile stress occurring in a spherical shell of any dimensions (except very shallow or unstable shells). This computer program calculates the constitutive stresses arising from: (1) pressure and temperature differences across the thickness of the shell, and (2) edge deformations of the shell.

One approach to the design objective of achieving the minimum stress conditions consists of using a hemispherical shell. In this case, the free-edge boundary conditions do not produce edge deformations which introduce additional stress. However, the maximum stress occurring in a hemispherical shell is larger than the maximum stress occurring in a shallower shell (for the same edge diameter, shell thickness, etc.). This suggests that it is advantageous to use a shallow shell provided edge deformations can be suppressed. The higher membrane compressive stress of shallower shells results in a lower maximum tensile stress unless stresses introduced by any edge deformations negate this improvement. It may be possible to introduce a clamp at the edge of the shell that accommodates changes in the edge diameter [as a result of the diurnal temperature cycle]. The success of such a clamp depends on how well it maintains the spherical shape of the shell throughout the diurnal temperature cycle.

Appendix A
Computer Program Listing

The computer program discussed in Section 2.2 is as follows:

```
C      PROGRAM DOME(OUTPUT,TAPE21,INPUT,TAPE5=INPUT,TAPE6=OUTPUT)
       COMMON/QQ/E,H,LAM,AA,PRA,A,K1,K2,C1,C3
       DIMENSION THETAP(101),THETAM(101),PHIP(101),PHIM(101)
       COMMON/VE/A11,A12,A22
       COMMON/SC/ADUM(404)
       EQUIVALENCE (ADUM(1),THETAP(1)),(ADUM(102),THETAM(1)),
     1 (ADUM(203),PHIP(1)),(ADUM(304),PHIM(1))
       DIMENSION Q(101),V(101),NP(101),NT(101),MP(101),MT(101),DL(101),
     1 PHI(101)
       REAL MOMT
       REAL NP,NT,MP,MT
       REAL LAM,K1,K2,MOMA
     1 FORMAT(4E15.4)
     2 FORMAT(10I5)
       IGRAD=0
       PI=3.14159265
       PI2=PI*0.5
       EPSL = 1.E-6
       CRDEG = 180./PI
       CDEGR = 1./CRDEG
       HZTL=0.
       MOMA=0.
       WRITE(6,601)
   601 FORMAT(1H,////,15X,25H*************************,
     1 //,20X,15HSPHERICAL DOME ,//,20X,
     2 15HSTRESS ANALYSIS,//,15X,25H*************************,//)
C
C WHEN READ (HH,B) CAN BE EITHER (HEIGHT,DIAMETER OF CIRCULAR EDGE)
C OR (ANGLE ALPHA IN DEGREES,SHELL RADIUS)
C
       READ(5,2) IPMAX,JPMAX
       READ(5,1) HH,B,H
       READ(5,1) VZ,DZ,MOMA,HZTL,DVZ,DDZ
       READ(5,1) PRESS
       READ(5,1) GRADT,ALPHAT
       READ(5,1) E,PR
       READ(5,2) IPHI
       IF(HH.LT.10.) GO TO 840
       HH=HH*CDEGR
       XB=2.*B*SIN(HH)
       HH=B*(1.-COS(HH))
       B=XB
   840 CONTINUE
```

```
C
      DO 1001 IPM=1,IPMAX
      DZ=DZ+DDZ
      IF(IPM.GT.1) VZ=VZ-DVZ*FLOAT(JPMAX)
      DO 1002 JPM=1,JPMAX
      VZ=VZ+DVZ
      WRITE(6,501)
  501 FORMAT(1H1)
C
C HH IS HEIGHT
C B IS DIAMETER OF CIRCULAR EDGE
C H IS THICKNESS
C
      WRITE(6,201) HH
  201 FORMAT(10X,21H               HEIGHT = ,F5.2    ,17H        INCHES      )
      WRITE(6,203) B
  203 FORMAT(10X,21H        EDGE DIAMETER = ,F5.2    ,17H        INCHES      )
      WRITE(6,205) H
  205 FORMAT(10X,21H      SHELL THICKNESS = ,F5.2    ,17H        INCHES      )
C
C CALCULATE RADIUS, A,  AND ANGLE ALPHA, AA.
C
      X=B*0.5/HH
      CA2=ATAN(X)
      A2=PI2-CA2
      AA=2.*A2
      A=B*0.5/SIN(AA)
      WRITE(6,204) A
  204 FORMAT(10X,21H         SHELL RADIUS = ,F5.2    ,17H        INCHES      )
      AA = AA*CRDEG
      WRITE(6,202) AA
      AA = AA*CDEGR
  202 FORMAT(10X,21H          ANGLE ALPHA = ,F5.2    ,17H        DEGREES     )
      WRITE(6,206) E
  206 FORMAT(10X,21H       YOUNGS MODULUS = ,1PE10.3,05H  PSI)
      WRITE(6,207) PR
  207 FORMAT(10X,21H       POISSONS RATIO = ,F5.2    ,17H        NO UNITS    )
C
C CALCULATE ELASTIC AND GEOMETRICAL CONSTANTS
C
      REH=1./(E*H)
      PRS=PR*PR
      X1=1.-PRS
      X=3.*X1*(A/H)**2
      LAM=SQRT(X)
      LAM=SQRT(LAM)
      XPR1=(1.-2.*PR)*0.5/LAM
      XPR2=(1.+2.*PR)*0.5/LAM
      D=E* H**3/(12.*X1)
      WRITE(6,901) PRESS
```

```
  901 FORMAT(10X,20H            PRESSURE = ,F6.2    ,17H        PSI        ) DOM00940
      RCPH=1./H                                                              DOM00950
      SIGMA=-PRESS*A*RCPH*0.5                                                DOM00960
      WRITE(6,902) SIGMA                                                     DOM00970
  902 FORMAT(10X,21H            SIGMA(P) = ,1PE10.3,17H  PSI               ) DOM00980
      HMFCE=PRESS*A*0.5*COS(AA)                                              DOM00990
      HMFC=-HMFCE                                                            DOM01000
      WRITE(6,806) HMFCE                                                     DOM01010
  806 FORMAT(10X,21H   HOR. MEM. FORCE = ,1PE10.3,17H  LBS/INCH          ) DOM01020
      DELP=-PRESS*A*A*(1.-PR)*SIN(AA)*0.5*REH                                DOM01030
      WRITE(6,807) DELP                                                      DOM01040
  807 FORMAT(10X,21H            DELTA(P) = ,1PE10.3,17H  INCHES            ) DOM01050
      WRITE(6,801) GRADT                                                     DOM01060
  801 FORMAT(10X,21HTHERMAL DIFFERENCE = ,1PE10.3,17H  CENTIGRADE DEGS) DOM01070
      WRITE(6,802) ALPHAT                                                    DOM01080
  802 FORMAT(10X,21HTHERMAL COEF. EXP. = ,1PE10.3,17H  PER CENT. DEG   ) DOM01090
      THRM =-ALPHAT*GRADT*D*(1.+PR)*RCPH                                     DOM01100
      WRTIE(6,805) THRM                                                      DOM01110
  805 FORMAT(10X,21H      THERMAL MOMENT = ,1PE10.3,17H  INCH-LBS/INCH   ) DOM01120
      SIGT=6.*THRM*RCPH*RCPH                                                 DOM01130
      WRITE(6,803) SIGT                                                      DOM01140
  803 FORMAT(10X,21H            SIGMA(T) = ,1PE10.3,17H  PSI              ,/DOM01150
     1/,43X,48HSIGMA(T) IS BASED ON THE THERMAL DIFFERENCE ONLY,             DOM01160
     2/,43X,54HSIGMA(T) IS NEGATIVE ON THE INSIDE SURFACE OF THE DOME,       DOM01170
     3/,43X,35HAND POSITIVE ON THE OUTSIDE SURFACE,/)                        DOM01180
C                                                                            DOM01190
CC IPHI IS THE NUMBER OF COLATITUDE ANGLES AT WHICH                          DOM01200
C THE STRESSES ARE REQUIRED.                                                 DOM01210
C                                                                            DOM01220
      XPHI=AA/FLOAT(IPHI)                                                    DOM01230
      SINAL = SN(AA)                                                         DOM01240
      COTA = COS(AA)/SINAL                                                   DOM01250
      K1 = 1. -XPR1*COTA                                                     DOM01260
      K2 = 1. -XPR2*COTA                                                     DOM01270
      RK1 = 1./K1                                                            DOM01280
      SK = K2+RK1                                                            DOM01290
      REHK1 = REH*RK1                                                        DOM01300
      A11 =-4.*LAM**3*REHK1/A                                                DOM01310
      A12 =2.*LAM*LAM*SINAL*REHK1                                            DOM01320
      A22 =-LAM*A*SINAL*SINAL*REH*SK                                         DOM01330
C                                                                            DOM01340
C CALCULATE EDGE DISPLACEMENT AND ROTATION IF REQUIRED.                      DOM01350
C                                                                            DOM01360
      IF((ABS(MOMA).LT.EPSL).AND.(ABS(HZTL).LT.EPSL)) IBC=1                  DOM01370
      IF (IBC.EQ.1) GO TO 21                                                 DOM01380
      WRITE(6,251) MOMA                                                      DOM01390
  251 FORMAT(10X,21H        EDGE MOMENT = ,1PE10.3,15H  INCH-LBS/INCH,     DOM01400
     13X,29H(POSITIVE MOMENT OPENS SHELL))                                   DOM01410
      WRITE(6,252) HZTL                                                      DOM01420
```

```
252 FORMAT(10X,21H  HORIZONTAL FORCE = ,1PE10.3,15H  LBS/INCH      ,
   18X,17H(POSITIVE INWARD))
    VZERO = A11*MOMA + A12*HZTL
    DZERO = A12*MOMA + A22*HZTL
    VZ = VZERO
    DZ = DZERO
 21 CONTINUE
    VZMR=1000.*VZ
    WRITE(6,253) VZMR
253 FORMAT(10X,21H      EDGE ROTATION = ,F5.1,5X,15H  MILLIRADIANS ,
   19X,32H(POSITIVE ROTATION CLOSES SHELL))
    DZMR=1000.*DZ
    WRITE(6,254) DZMR
254 FORMAT(10X,21H EDGE DISPLACEMENT = ,F5.1,5X,15H MILS           ,
   19X,18H(POSITIVE OUTWARD))
    IF(IBC.EQ.1) CALL VERT(VZ,DZ,MOMT,HORF)
    CALL BDRY(VZ,DZ,C,GAM)
    COEFQ=C
    COEFV=C*2.*LAM*LAM*REH*(-1.)
    COENP=C
    COENT=C*LAM*0.5
    PRTLAM=PR*LAM
    CTA=C*A
    COEMP=CTA*0.5/LAM
    COEMT=CTA*0.25/PRTLAM
    COEFD=CTA*REH*LAM
    DO 20 I=1,IPHI
    XI=I
    PHI(I)=XPHI*XI
    PSI=AA-PHI(I)
    CTPSI=COS(PSI)
    SPS =SIN(PSI)
    CTPHI=COS(PHI(I))
    SPHI=SIN(PHI(I))
    CTPHI=CTPHI/SPHI
    K1=1.-XPR1*CTPHI
    K2=1.-XPR2*CTPHI
    EMPSI=EXP(-LAM*PSI)
    ERSIN=EMPSI/(SQRT(SPHI))
    XARG=LAM*PSI+GAM
    SF=SIN(XARG)
    CF=COS(XARG)
    Q(I) = COEFQ*ERSIN*SF
    V(I) = COEFV*ERSIN*CF
    NP(I)= COENP*ERSIN*(-1.)*CTPHI*SF
    NT(I)= COENT*ERSIN*(2.*CF-(K1+K2)*SF)
    MP(I) =COEMP*ERSIN*(K1*CF+SF)
    MT(I)= COEMT*ERSIN*(((1.+PRS)*(K1+K2)-2*K2)*CF+2.*PRS*SF)
    DL(I)  =COEFD*ERSIN*SPH*(CF-K*SF)
```

```
   20 CONTINUE                                                            DOM01920
      WRITE(6,213)                                                        DOM01930
      WRITE(6,211) C                                                      DOM01940
  211 FORMAT(10X,21H                   C = ,1PE10.3,17H      LBS/INCH    ) DOM01950
      WRITE(6,212) GAM                                                    DOM01960
  212 FORMAT(10X,21H               GAMMA = ,1PE10.3,17H      RADIANS     ) DOM01970
      WRITE(6,213)                                                        DOM01980
  213 FORMAT(//)                                                          DOM01990
      WRITE(6,700)                                                        DOM02000
  700 FORMAT(10X,15HOTHER CONSTANTS)                                      DOM02010
      WRITE(6,213)                                                        DOM02020
      WRITE(6,701) LAM                                                    DOM02030
  701 FORMAT(10X,21H              LAMBDA = ,1PE10.3,18H      RADIANS**(-1)) DOM02040
      WRITE(6,702) C1                                                     DOM02050
  702 FORMAT(10X,21H                  C1 = ,1PE10.3)                      DOM02060
      WRITE(6,703) C3                                                     DOM02070
  703 FORMAT(10X,21H                  C3 = ,1PE10.3)                      DOM02080
      WRITE(6,704) K1                                                     DOM02090
  704 FORMAT(10X,21H          K1 AT EDGE = ,1PE10.3)                      DOM02100
      WRITE(6,705) K2                                                     DOM02110
  705 FORMAT(10X,21H          K2 AT EDGE = ,1PE10.3)                      DOM02120
      WRITE(6,677)                                                        DOM02130
  677 FORMAT(1H1)                                                         DOM02140
      WRITE(6,301)                                                        DOM02150
  301 FORMAT(3X,5HANGLE,8X,5HSHEAR,4X,11HROTATION OF,12H  MEMBRANE  ,    DOM02160
     112H  MEMBRANE  ,9H  BENDING,5X,7HBENDING,5X,10HHORIZONTA-,/,        DOM02170
     24X,3HPHI,9X,5HFORCE,7X,5HLOCAL,6X,6HSTRESS,6X,6HSTRESS,5X,          DOM02180
     36HMOMENT,6X,6HMOMENT,6X,10HDEFLECTIN,/,                             DOM02190
     416X,5H(PHI),5X,8HMERIDIAN,5X,5H(PHI),7X,7H(THETA) ,5X,5H(PHI),      DOM02200
     56X,7H(THETA),//,2X,7HRADIANS,6X,8HLBS/INCH,3X,7HRADIANS,5X,         DOM02210
     68H-BS/INCH,4X,8HLBS/INCH,3X,09HIN-LBS/IN,3X,9HIN-LBS/IN,6X,         DOM02220
     76HINCHES)                                                           DOM02230
      WRITE(6,213)                                                        DOM02240
      DO 316 I=1,IPHI                                                     DOM02250
  316 WRITE(6,315)PHI(I),Q(I),V(I),NP(I),NT(I),MP(I),MT(I),DL(I)          DOM02260
  315 FORMAT(1PE11.3,1P7E12.3,/)                                          DOM02270
C                                                                         DOM02280
C CALCULATE SIGMA(THETA) AND SIGMA(PHI) AT THE TO AND BOTTOM SURFACES     DOM02290
C OF THE SHELL. SIGMA IS THE UNIFORM PRESSURE STRESS.                     DOM02300
C                                                                         DOM02310
      DO 333 I=1,IPHI                                                     DOM02320
      MT(I)=MT(I) + THRM                                                  DOM02330
      MP(I)=MP(I) + THRM                                                  DOM02340
      THETAP(I)=RCPH*(NT(I)+6.*MT(I)*RCPH)  +SIGMA                        DOM02350
      THETAM(I)=RCPH*(NT(I)-6.*MT(I)*RCPH)  +SIGMA                        DOM02360
      PHIP(I)   =RCPH*(NP(I)+6.*MP(I)*RCPH)  +SIGMA                       DOM02370
      PHIM(I)   =RCPH*(NP(I)-6.*MP(I)*RCPH)  +SIGMA                       DOM02380
  333 CONTINUE                                                            DOM02390
      WRITE(6,907)                                                        DOM02400
```

```
 907 FORMAT(1H1)                                                      DOM02410
     WRITE(6,376)                                                     DOM02420
 376 FORMAT(5X,3HPHI,9X,11HSIGMA THETA,5X,11HSIGMA THETA,             DOM02430
    16X, 9HSIGMA PHI,6X,9HSIGMA PHI,/,17X,11HTOP SURFACE,4X,          DOM02440
    214HBOTTOM SURFACE,3X,11HTOP SURFACE,4X,14HBOTTOM SURFACE,/,      DOM02450
    33X,7HRADIANS,11X,3HPSI,13X,3HPSI,13X,3HPSI,13X,3HPSI)            DOM02460
     WRITE(6,213)                                                     DOM02470
     DO 334 I=1,IPHI                                                  DOM02480
 334 WRITE(6,115) PHI(I),THETAM(I),THETAP(I),PHIM(I),PHIP(I)          DOM02490
 115 FORMAT(1PE12.3,4(3X,1PE12.3),/)                                  DOM02500
     CALL SORT(IPHI)                                                  DOM02510
1002 CONTINUE                                                         DOM02520
1001 CONTINUE                                                         DOM02530
     END                                                              DOM02540
     SUBROUTINE BDRY(VZ,DZ,C,GAM)                                     DOM02550
     COMMON /QQ/E,H,LAM,AA,PR,A,K1,K2,C1,C3                           DOM02560
     REAL LAM,K1,K2,K2P                                               DOM02570
     SAL=SIN(AA)                                                      DOM02580
     CAL=COS(AA)                                                      DOM02590
     COTAL=CAL/SAL                                                    DOM02600
     SSAL=SQRT(SAL)                                                   DOM02610
     C1=-VZ*E*H*SSAL/(2.*LAM*LAM)                                     DOM02620
     IF(ABS(C1).LT.1.E-08) C1 = 1.E-08                                DOM02630
     C3=DZ*E*H/(A*SSAL*LAM)                                           DOM02640
     K2P=1. - (1.*2.*PR)*COTAL/(2.*LAM)                               DOM02650
     ARG =(1.-C3/C1)/K2P                                              DOM02660
     GAM=ATAN(ARG)                                                    DOM02670
     C = C1/COS(GAM)                                                  DOM02680
     RETURN                                                           DOM02690
     END                                                              DOM02700
     SUBROUTINE SORT(IPHI)                                            DOM02710
     COMMON/SC/ADUM(404)                                              DOM02720
     XMAX=ADUM(1)                                                     DOM02730
     XMIN=ADUM(1)                                                     DOM02740
     DO 1 K=1,4                                                       DOM02750
     DO 1 I=1,IPHI                                                    DOM02760
     IDEX = 101*(K-1) + I                                             DOM02770
     IF(ADUM(IDEX).GT.XMAX) XMAX=ADUM(IDEX)                           DOM02780
   1 IF(ADUM(IDEX).LT.XMIN) XMIN=ADUM(IDEX)                           DOM02790
     WRITE(6,213)                                                     DOM02800
     WRITE(6,903) XMAX                                                DOM02810
     WRITE(6,213)                                                     DOM02820
     WRITE(6,904) XMIN                                                DOM02830
 903 FORMAT(10X,21H    MAXIMUM STRESS = ,1PE10.3,17H        PSI      ) DOM02840
 904 FORMAT(10X,21H    MAXIMUM STRESS = ,1PE10.3,17H        PSI      ) DOM02850
 213 FORMAT(//)                                                       DOM02860
     RETURN                                                           DOM02870
     END                                                              DOM02880
```

```
      SUBROUTINE VERT(CC1,CC2,MOMT,HORF)                                DOM02890
      COMMON/VE/A11,A12,A22                                             DOM02900
      REAL MOMT                                                         DOM02910
      DET=A11*A22-A12*A12                                               DOM02920
      RDET=1./DET                                                       DOM02930
      MOMT=(CC1*A22-CC2*A12)*RDET                                       DOM02940
      HORF=(CC2*A11-CC1*A12)*RDET                                       DOM02950
      WRITE(6,1)                                                        DOM02960
    1 FORMAT(//,10X,32HCALCULATED EDGE FORCE AND MOMENT,                DOM02970
     146H DUE TO APPLIED DISPLACEMENT AND ROTATION ONLY)                DOM02980
      WRITE(6,251) MOMT                                                 DOM02990
      WRITE(6,252) HORF                                                 DOM03000
  251 FORMAT(10X,21H       EDGE MOMENT = ,1PE10.3,15H  INCH-LBS/INCH,   DOM03010
     13X,29H(POSITIVE MOMENT OPENS SHELL))                              DOM03020
  252 FORMAT(10X,21H  HORIZONTAL FORCE = ,1PE10.3,15H  LBS/INCH     ,   DOM03030
     18X,17H(POSITIVE INWARD))                                          DOM03040
      RETURN                                                            DOM03050
      END                                                               DOM03060
```

Appendix B

Sample Output

```
             HEIGHT =  6.00         INCHES
      EDGE DIAMETER = 12.00         INCHES
    SHELL THICKNESS =   .25         INCHES
       SHELL RADIUS =  6.00         INCHES
        ANGLE ALPHA = 90.00         DEGREES
     YOUNGS MODULUS =  5.400E+07    PSI
     POISSONS RATIO =   .10         NO UNITS
           PRESSURE = 60.00         PSI
           SIGMA(P) = -7.200E+02    PSI
    HOR. MEM. FORCE = -6.462E-07    LBS/INCH
           DELTA(P) = -7.200E-05    INCHES
 THERMAL DIFFERENCE =  1.110E+02    CENTIGRADE DEGS
 THERMAL COEF. EXP. =  5.600E-06    PER CENT. DEG
     THERMAL MOMENT = -1.943E+02    INCH-LBS/INCH
           SIGMA(T) = -1.865E+04    PSI

        SIGMA(T) IS BASED ON THE THERMAL DIFFERENCE ONLY
        SIGMA(T) IS NEGATIVE ON THE INSIDE SURFACE OF THE DOME
        AND POSITIVE ON THE OUTSIDE SURFACE


      EDGE ROTATION =  -4.0  MILLIRADIANS  (POSITIVE ROTATION CLOSES SHELL)
  EDGE DISPLACEMENT =   1.0  MILS          (POSITIVE OUTWARD)


CALCULATED EDGE FORCE AND MOMENT
DUE TO APPLIED DISPLACEMENT AND ROTATION ONLY

        EDGE MOMENT =  4.458E+02  INCH-LBS/INCH (POSITIVE MOMENT OPENS SHELL)
   HORIZONTAL FORCE =  3.029E+02  LBS/INCH      (POSITIVE INWARD)


INTEGRATION CONSTANTS OF HOMOGENEOUS SOLUTION

              C =  7.197E+02      LBS/INCH
          GAMMA =  4.345E-01      RADIANS

OTHER CONSTANTS

          LAMBDA =  6.431E+00      RADIANS**(-1)
              C1 =  6.528E+02
              C3 =  3.499E+02
      K1 AT EDGE =  1.000E+00
      K2 AT EDGE =  1.000E+00
```

ANGLE PHI RADIANS	SHEAR FORCE (PHI) LBS/INCH	ROTATION OF LOCAL MERIDIAN RADIANS	MEMBRANE STRESS (PHI) LBS/INCH	MEMBRANE STRESS (THETA) LBS/INCH	BENDING MOMENT (PHI) IN-LBS/IN	BENDING MOMENT (THETA) IN-LBS/IN	HORIZONTAL DEFLECTION INCHES
7.854E-02	-9.951E-02	8.785E-07	1.254E+00	-9.143E-01	-6.045E-02	-1.369E-01	-3.629E-08
1.571E-01	-2.078E-02	1.249E-06	1.312E-01	-1.242E+00	-6.742E-02	-9.912E-02	-8.729E-08
2.356E-01	1.091E-01	1.565E-06	-4.544E-01	-2.118E+00	-3.743E-02	-8.018E-02	-2.150E-07
3.142E-01	3.156E-01	1.508E-06	-9.714E-01	-3.127E+00	5.441E-02	-4.894E-02	-4.161E-07
3.927E-01	5.886E-01	5.713E-07	-1.421E+00	-3.675E+00	2.376E-01	7.598E-03	-6.008E-07
4.712E-01	8.524F-01	-1.895E-06	-1.673E+00	-2.657E+00	5.243E-01	9.600E-02	-5.026E-07
5.498E-01	9.211E-01	-6.466E-06	-1.583E+00	1.614E+00	8.719E-01	2.108E-01	4.096E-07
6.283E-01	4.617E-01	-1.311E-05	-6.355E-01	1.111E+01	1.128E+00	3.242E-01	2.918E-06
7.069E-01	-9.950E-01	-2.024E-05	1.165E+00	2.706E+01	9.647E-01	3.742E-01	7.778E-06
7.854E-01	-3.922E+00	-2.345E-05	3.922E+00	4.787E+01	-1.553E-01	2.593E-01	1.492E-05
8.639E-01	-8.444E+00	-1.421E-05	7.211E+00	6.561E+01	-2.914E+00	-1.492E-01	2.193E-05
9.425E-01	-1.367E+01	2.024E-05	9.935E+00	6.173E+01	-7.850E+00	-9.574E-01	2.184E-05
1.021E+00	-1.674E+01	9.405E-05	1.026E+01	3.796E+00	-1.469E+01	-2.145E+00	1.050E-06
1.100E+00	-1.170E+01	2.139E-04	5.963E+00	-1.522E+02	-2.122E+01	-3.399E+00	-6.050E-05
1.178E+00	1.082E+01	3.611E-04	-4.482E+00	-4.463E+02	-2.173E+01	-3.926E+00	-1.831E-04
1.257E+00	6.204E+01	4.637E-04	-2.016E+01	-8.756E+02	-5.647E+00	-2.330E+00	-3.692E-04
1.335E+00	1.490E+02	3.636E-04	-3.577E+01	-1.322E+03	4.224E+01	3.201E+00	-5.697E-04
1.414E+00	2.616E+02	-2.032E-04	-4.143E+01	-1.448E+03	1.373E+02	1.411F+01	-6.340E-04
1.492E+00	3.511E+02	-1.573E-03	-2.763E+01	-5.936E+02	2.829E+02	2.974E+01	-2.618E-04
1.571F+00	3.029E+02	-4.000F-03	-1.087E-06	2.250E+03	4.458E+02	4.458E+01	1.000E-03

```
    PHI            SIGMA THETA      SIGMA THETA       SIGMA PHI        SIGMA PHI
                   TOP SURFACE     BOTTOM SURFACE    TOP SURFACE     BOTTOM SURFACE
  RADIANS             PSI               PSI              PSI              PSI


 7.854E-02         1.794E+04        -1.938E+04       1.794E+04       -1.937E+04

 1.571E-01         1.793E+04        -1.938E+04       1.793E+04       -1.937E+04

 2.356E-01         1.793E+04        -1.938E+04       1.793E+04       -1.937E+04

 3.142E-01         1.792E+04        -1.939E+04       1.792E+04       -1.937E+04

 3.927E-01         1.791E+04        -1.938E+04       1.790E+04       -1.935E+04

 4.712E-01         1.791E+04        -1.937E+04       1.787E+04       -1.932E+04

 5.498E-01         1.791E+04        -1.934E+04       1.784E+04       -1.929E+04

 6.283E-01         1.794E+04        -1.929E+04       1.782E+04       -1.926E+04

 7.069E-01         1.800E+04        -1.922E+04       1.784E+04       -1.927E+04

 7.854E-01         1.809E+04        -1.915E+04       1.796E+04       -1.937E+04

 8.639E-01         1.820E+04        -1.912E+04       1.824E+04       -1.962E+04

 9.425E-01         1.827E+04        -1.921E+04       1.872E+04       -2.008E+04

 1.021E+00         1.815E+04        -1.956E+04       1.938E+04       -2.074E+04

 1.100E+00         1.765E+04        -2.030E+04       1.999E+04       -2.138E+04

 1.178E+00         1.652E+04        -2.153E+04       2.000E+04       -2.147E+04

 1.257E+00         1.465E+04        -2.309E+04       1.839E+04       -1.999E+04

 1.335E+00         1.233E+04        -2.435E+04       1.373E+04       -1.546E+04

 1.414E+00         1.078E+04        -2.381E+04       4.577E+03       -6.349E+03

 1.492E+00         1.270E+04        -1.889E+04      -9.345E+03        7.684E+03

 1.571E+00         2.265E+04        -6.087E+03      -2.487E+04        2.343E+04



              MAXIMUM STRESS =  2.343E+04        PSI


              MINIMUM STRESS = -2.487E+04        PSI
```

Appendix C

Diagrams of Constituent Stress Distributions and their Superposition

There are four total stress distributions of interest:

σ^t_θ, top surface (ϕ)

σ^t_θ, bottom surface (ϕ)

σ^t_ϕ, top surface (ϕ)

σ^t_ϕ, bottom surface (ϕ)

where the top and bottom surfaces refer, respectively, to the convex and concave surfaces shown in Fig. 2. The shell's maximum tensile and compressive stresses will occur somewhere on these surfaces. Each of these total stress distributions is obtained by superposing the following constituent stress distributions:

1. σ_p, the membrane pressure stress due to the uniform pressure, p.
2. $\sigma_t(\pm h/2)$, the thermal stress due to ΔT at the top or bottom surface of the shell.

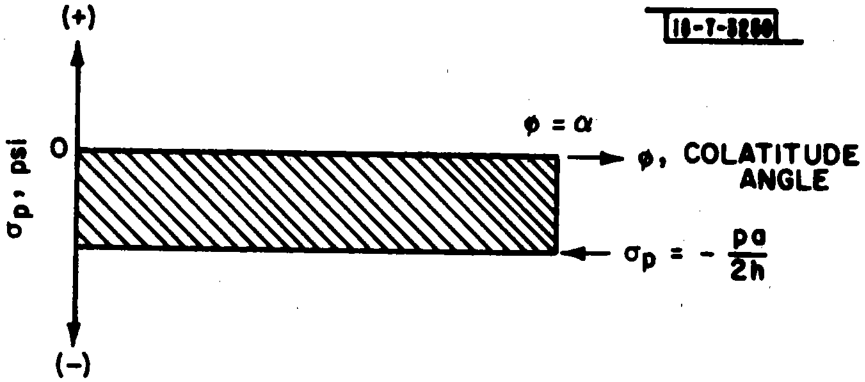

Fig. C-1. Uniform σ_p distribution throughout the shell.

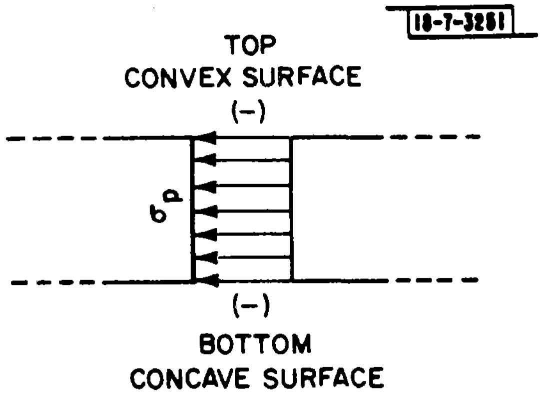

Fig. C-2. Uniform σ_p distribution over any cross section of the shell.

3. σ_θ, top surface (ϕ), σ_θ, bottom surface (ϕ), σ_ϕ, top surface (ϕ), or σ_ϕ, bottom surface (ϕ) where

$$\sigma_\theta,\ \text{top surface}\ (\phi) = \frac{N_\theta(\phi)}{h} - \frac{6M_\theta(\phi)}{h^2}$$

$$\sigma_\theta,\ \text{bottom surface}\ (\phi) = \frac{N_\theta(\phi)}{h} + \frac{6M_\theta(\phi)}{h^2}$$

$$\sigma_\phi,\ \text{top surface}\ (\phi) = \frac{N_\phi(\phi)}{h} - \frac{6M_\phi(\phi)}{h^2} \qquad \text{(C-1)}$$

$$\sigma_\phi,\ \text{bottom surface}\ (\phi) = \frac{N_\phi(\phi)}{h} + \frac{6M_\phi(\phi)}{h^2}$$

and $N_\theta(\phi)$, $N_\phi(\phi)$, $M_\theta(\phi)$, and $M_\phi(\phi)$ are the membrane forces and bending moments resulting from the edge deformation $(V_\alpha, \delta_\alpha)$. Any deformation of the shell resulting from its uniform temperature elevation is assumed to be caused by an edge condition that produces the edge deformation $(V_\alpha, \delta_\alpha)$.

The membrane pressure stress, σ_p, is derived from the membrane pressure forces N_ϕ and N_θ:

$$\sigma_p = \frac{N_\phi}{h} = \frac{N_\theta}{h} = -\frac{pa}{2} \qquad \text{(C-2)}$$

The membrane pressure stress is uniform over the surface of the shell and across its thickness.

The thermal stress due to ΔT is uniform over the surface of the shell, but varies linearly across its thickness. $\sigma_t(z)$ is independent of the uniform temperature elevation of the shell.

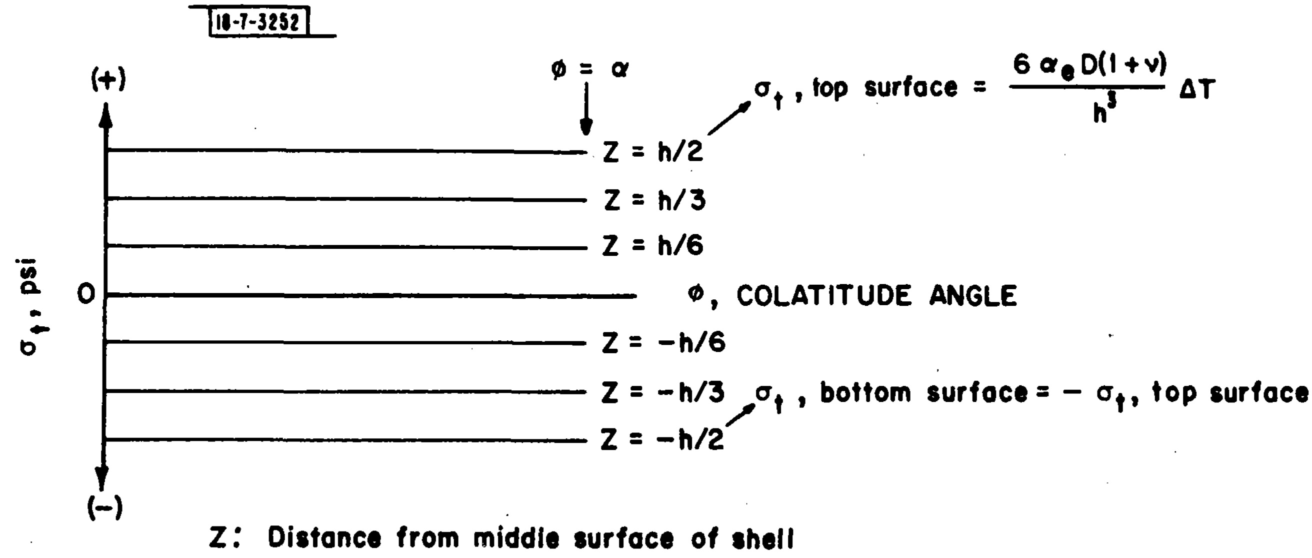

Fig. C-3. Uniform $\sigma_t(z)$ distributions at different distances from middle surface of the shell.

The circumferential and meridional stresses, $\sigma_\theta(z,\phi)$ and $\sigma_\phi(z,\phi)$, vary along both the surface of the shell and across its thickness. Typical stress distributions at the top and bottom surfaces are shown in Fig. C-5. These particular distributions are based on the free-edge boundary condition shown in Fig. 10 of Section 2.2.3 and the shell parameters shown in Fig. 7 of the same Section.

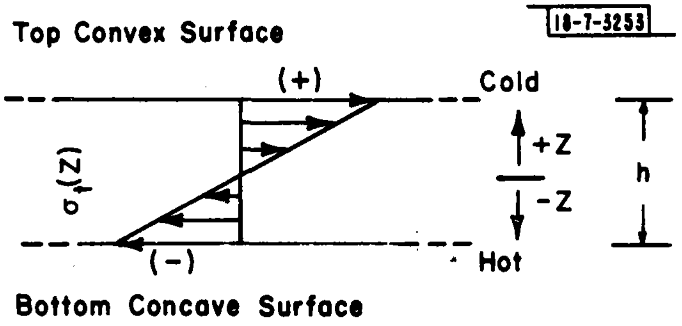

Fig. C-4. Linear $\sigma_t(z)$ distribution over any cross section of the shell.

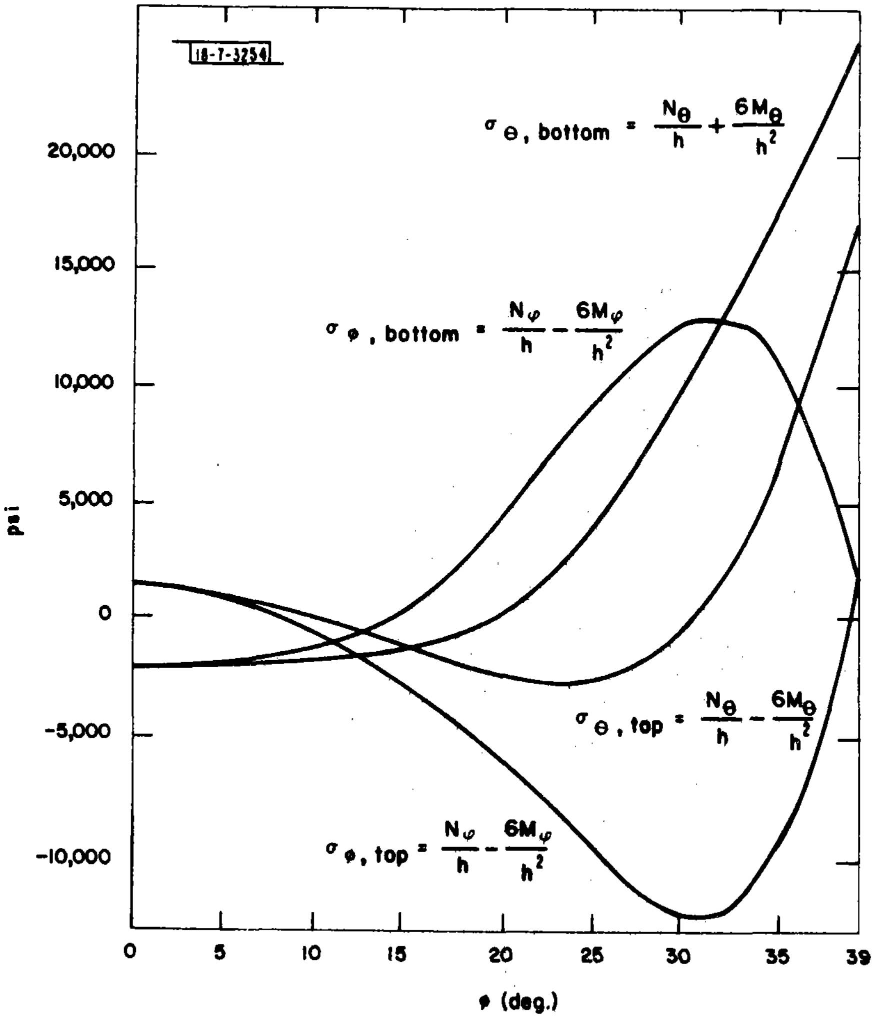

Fig. C-5. Typical stress distributions due to $(V_\alpha, \delta_\alpha)$ at the top and bottom surfaces of the shell.

The pressure and edge supports cause deformations $(V_\alpha, \delta_\alpha)$ at the edge of the shell. Only stresses due to the edge deformation $(V_\alpha, \delta_\alpha)$ are represented in Fig. C-5; the membrane pressure stress, σ_p, and the thermal stress due to ΔT, $\sigma_t(z)$, are not included. The membrane forces and bending moments, $N_\theta(\phi)$, $N_\phi(\phi)$, $M_\theta(\phi)$, and $M_\phi(\phi)$ are calculated using Eqs.(18). Figures C-6 and -7 show the $\sigma_\theta(\phi, z)$ and $\sigma_\phi(\phi, z)$ stress distributions at $\phi = 31$ degrees corresponding to the surface stress distributions shown in Fig. C-5.

The stresses σ_p and $\sigma_t(z)$ are determined by the shell's

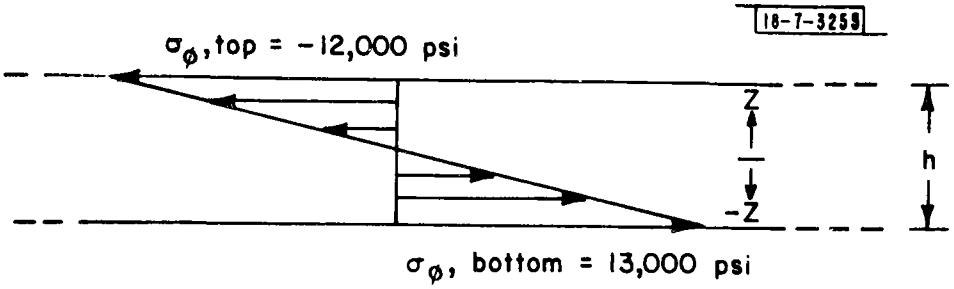

Fig. C-6. Linear $\sigma_\phi(z,\phi)$ distribution over a meridional cross section at ϕ = 31 degrees for surface distribution per Fig. C-5.

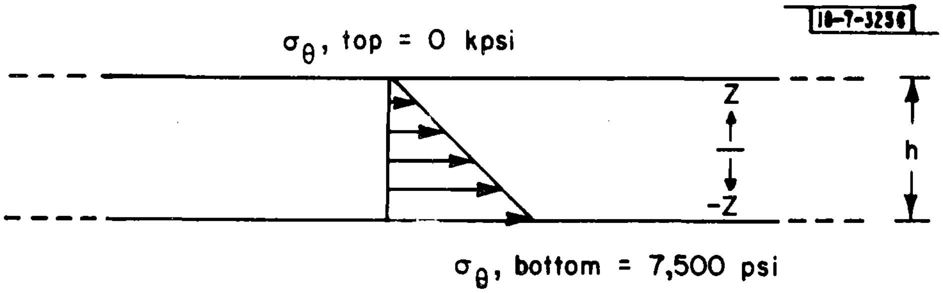

Fig. C-7. Linear $\sigma_\theta(z,\phi)$ distribution over circumferential cross section at ϕ = 31 degrees for surface distribution per Fig. C-5.

surface conditions and are uniform over the entire surface of the shell, even out to its edge, for all edge conditions. Only the stresses $\sigma_\theta(z,\phi)$ and $\sigma_\phi(z,\phi)$ are determined by referring to the shell's edge conditions, which are expressed as either (V_α,δ_α) or (M_α,H_α). These edge conditions are related to p, ΔT, and the shell's uniform temperature elevation as discussed in Section 2.1.3.

Appendix D
Insulating Ring Structural Analysis

One method of reducing the thermal gradients at the edge of the spherical shell consists of inserting an insulating ring between the shell and its supporting structure. A finite-element analysis was performed to determine if the stresses experienced by such an insulating ring are acceptable. The ring is assumed to have the following dimensions:

Height	3 inches
Inner diameter	11-1/2 inches
Outer diameter, top	12 inches
Outer diameter, bottom	13 inches.

A 400°F temperature difference is assumed between the top of the ring and the isothermal contact regions at the base of the ring. A compressive force of 200 psi is assumed to act in the vertical direction at the dome-ring interface. In two of the cases considered a 150-psi clamping force is assumed to act in the vertical direction at the shoulder of the ring. The resulting forces and moments are balanced by vertical reaction forces acting at two ring-supporting interfaces. Both interfaces are annular regions; one is near the middle of the base, the other includes the outer corner of the ring. The location and relative sizes of these regions as well as temperature distributions in the rings are indicated on radial cross sections (Fig. D-1). In Fig. D-1(a) a clamp is assumed to be present at the shoulder of the ring. A heat-conduction path exists through the clamp-ring interface.

These temperature distributions depend only on the steady-state boundary conditions and the shape of the rings; the temperature distributions are independent of the thermal conductivity of the ring material. Stress contours are available for the clamped and unclamped cases. Ring materials of aluminum oxide and silicon

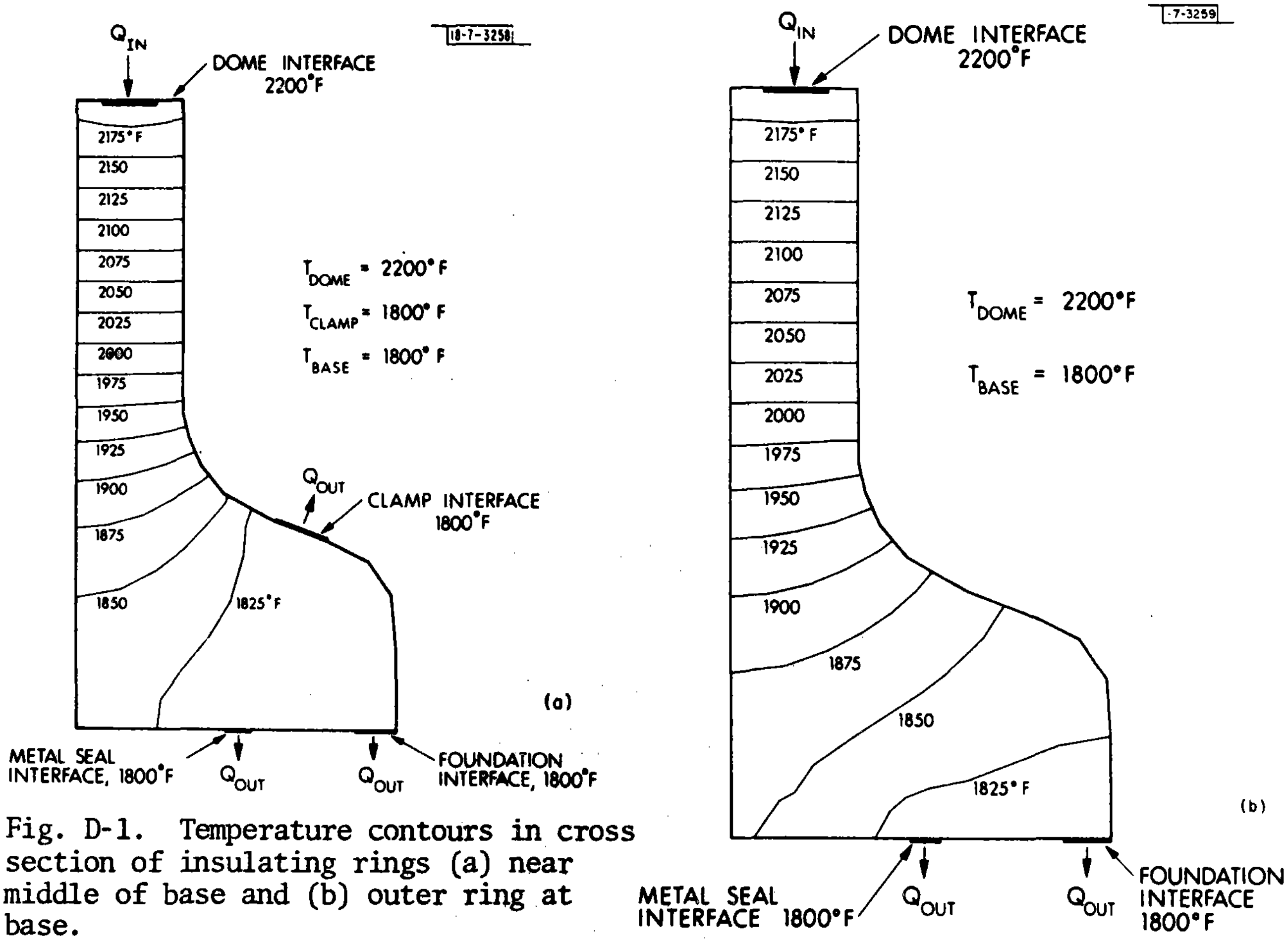

Fig. D-1. Temperature contours in cross section of insulating rings (a) near middle of base and (b) outer ring at base.

carbide are considered. The two clamped cases are shown in Figs. D-2 and -3, and the two unclamped cases are shown in Figs. D-4 and -5. The stress intensity is equal to twice the absolute value of the maximum local shear stress. The stress intensity is larger than the absolute value of any component of the stress tensor. Nuclear regulatory standards concerning permissible stress levels are usually based on stress intensity limits.

In the four cases considered here the combined pressure and thermal loadings are within the limits of the ceramic materials' strengths.

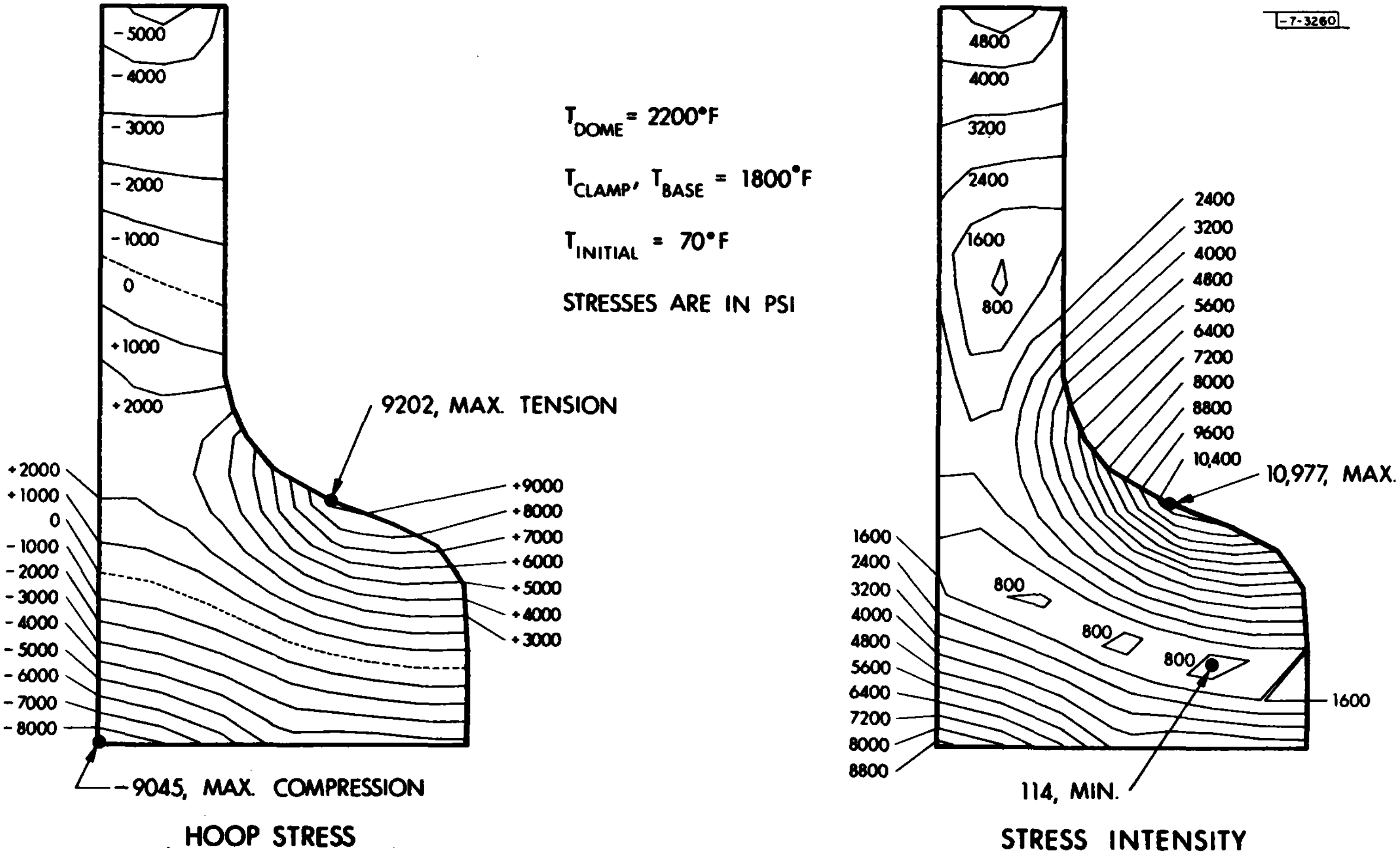

Fig. D-2. Stress contours in cross section of silicon carbide insulating ring, clamped.

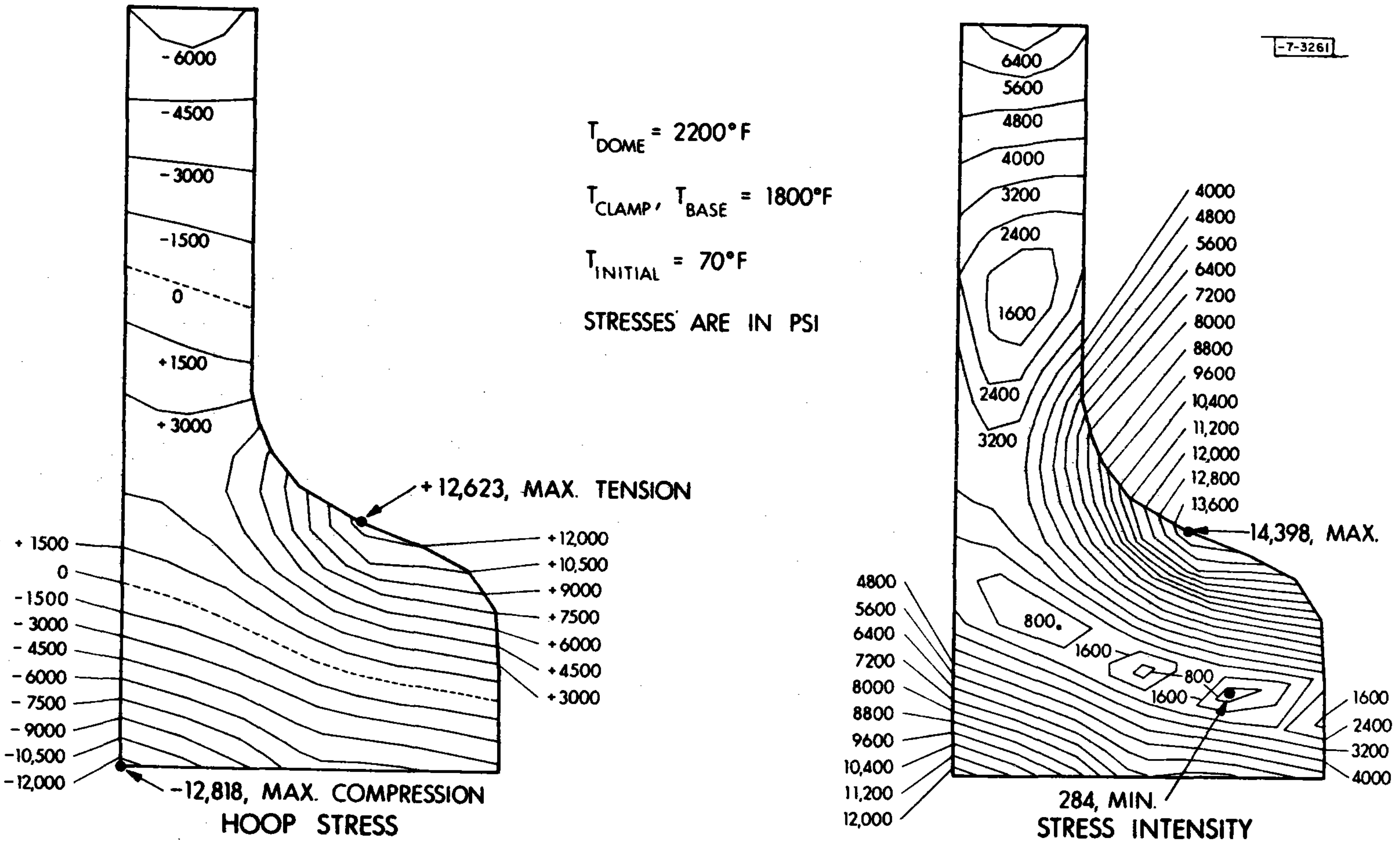

Fig. D-3. Stress contours in cross section of aluminum oxide insulating ring, clamped.

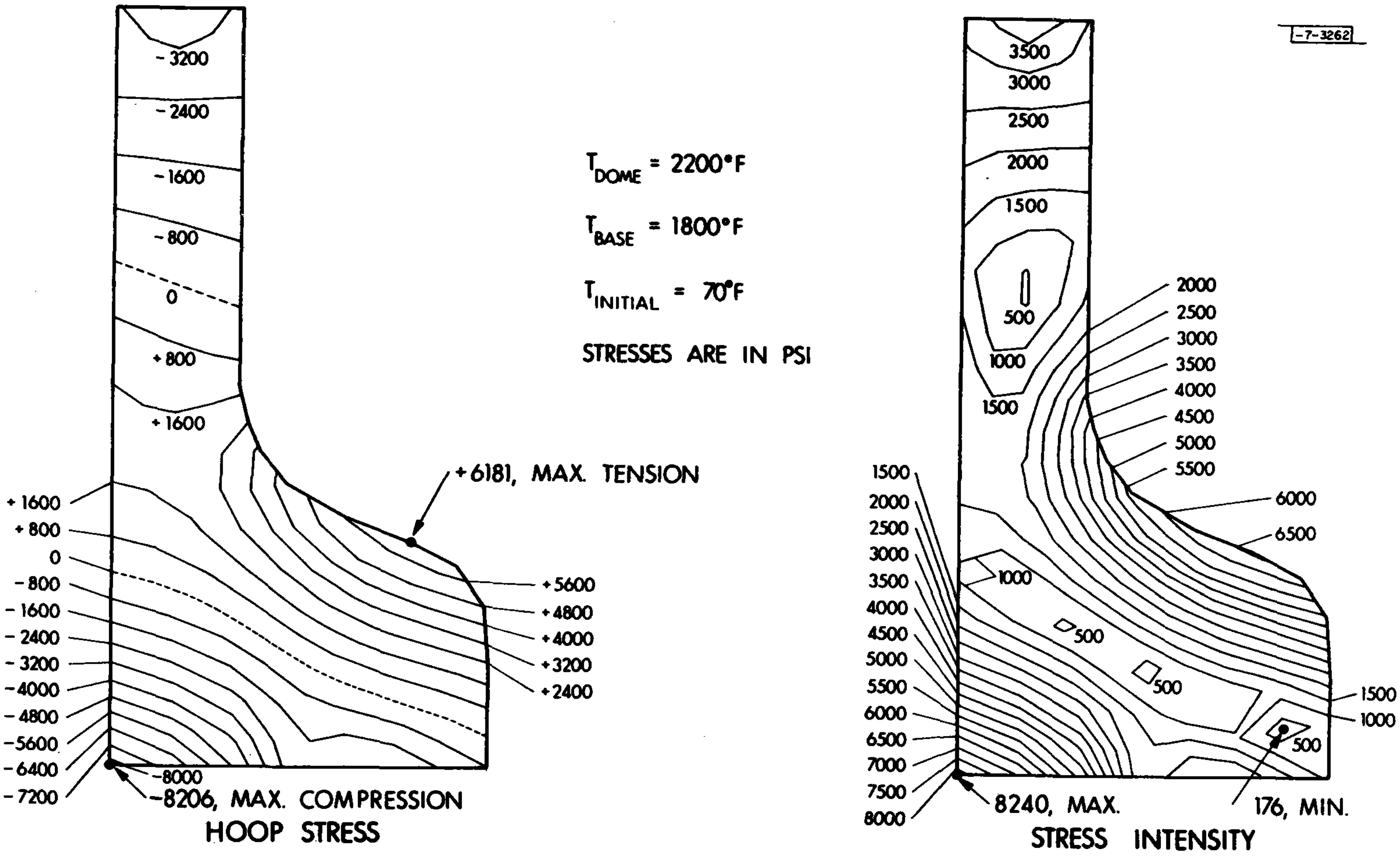

Fig. D-4. Stress contours in cross section of silicon carbide insulating ring, unclamped.

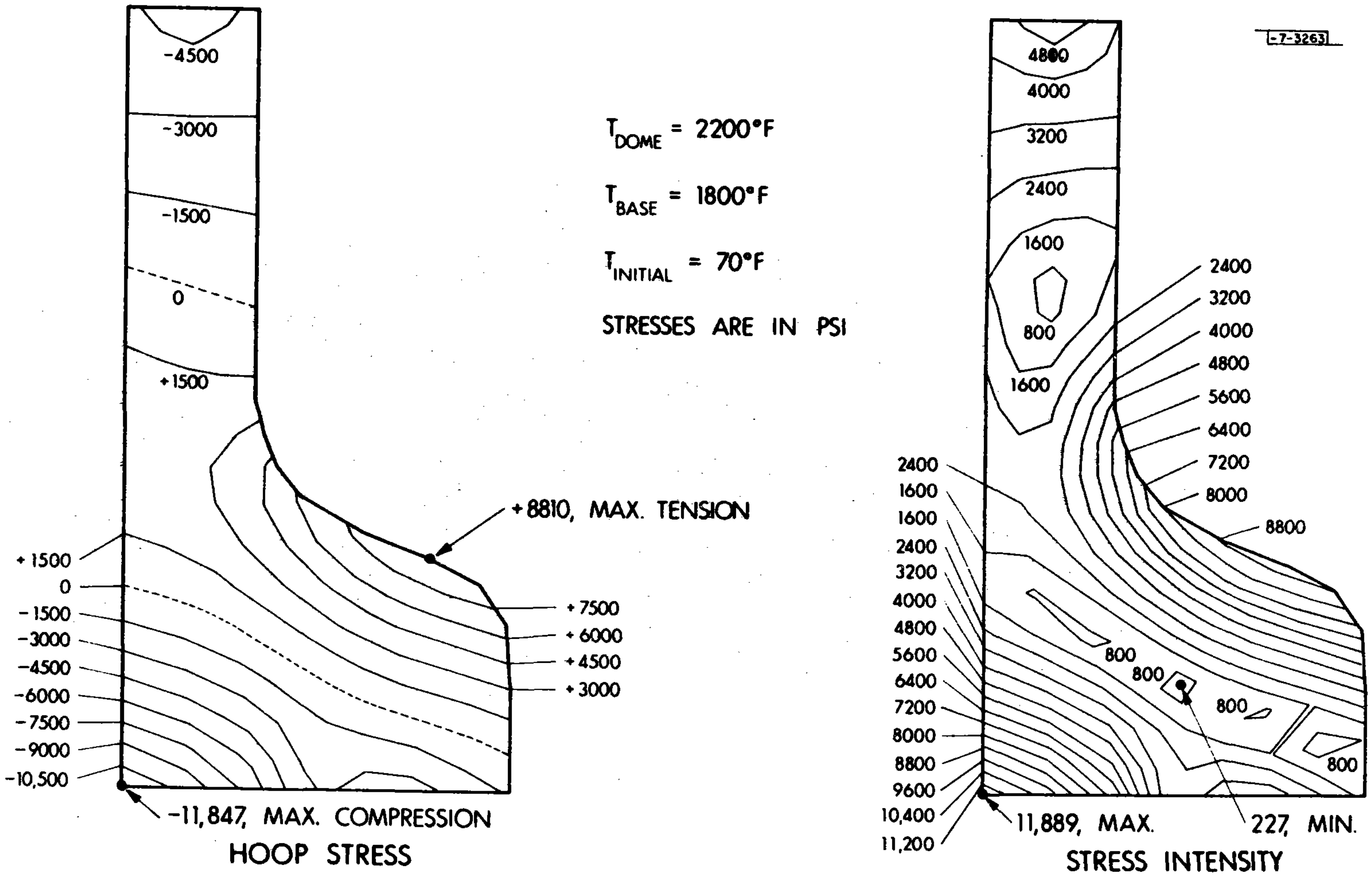

Fig. D-5. Stress contours in cross section of aluminum oxide insulating ring, unclamped.

REFERENCES

1. Timoshenko, S., Theory of Plates and Shells (McGraw-Hill, New York, 1959).

2. Nowacki, W., Thermoelasticity, International series of monographs on Aeronautics and Astronautics, (Addison-Wesley; Reading, Massachusetts.

3. DeYoung, J. and Harper, C. W., "Theoretical Symmetric Span Loading at Subsonic Speeds for Wings Having Arbitrary Plan Form," NACA Report No. 921 (1950).

The following references are publications discussing related work associated with the Solar Heated Air Receiver Experiment:

4. Jarvinen, P. O., "Novel Ceramic Receiver for Solar Brayton Systems," 1979 International Gas Turbine Conference and Product Show (12-15 March 1979).

5. Jarvinen, P. O., "Ceramic Receivers for Solar Power Conversion," AIAA Terrestrial Energy Systems Conf. (4-6 June 1979).

6. Jarvinen, P. O., "Ceramic Solar Receivers," 14th Intersociety Energy Conf. (5-10 August 1979).

7. Jarvinen, P. O., "Advanced Solar Receiver Development," International Solar Energy Society Congress and Silver Jubilee, Atlanta, Georgia (28 May – 1 June 1979).

8. Hamilton, N. I. and Jarvinen, P. O., "Conceptual Design of a Solar Heated Air Receiver Coupled to a Brayton or Stirling Engine," ISES Silver Jubilee International Solar Exhibition, Atlanta, Georgia (28 May – 1 June 1979).

9. Hamilton, N. I. and Jarvinen, P. O. "Solar Radiation Flux Distributions in Cavity Receivers for Various Wall Shapes," COO-4878-9, Technical Report, Lincoln Laboratory, Lexington, Massachusetts (15 November 1979).

REFERENCES (Continued)

10. Jarvinen, P. O., "Solar Heated Air Cavity Receiver Development (SHARE)," Review of Advanced Solar Thermal Power Systems, DOE/JPL 1060-78/5 (15-17 November 1979).

UNITED STATES DEPARTMENT OF ENERGY
P.O. BOX 62
OAK RIDGE, TENNESSEE 37830

OFFICIAL BUSINESS
PENALTY FOR PRIVATE USE $300

POSTAGE AND FEES PAID
UNITED STATES
DEPARTMENT OF ENERGY

U S MAIL

FS- 1

SANDIA NATIONAL LABORATORIES
ATTN A. C. SKINROOD
DIVISION 8452
LIVERMORE, CA 94550